International Journal of Photoenergy

New Environmentally Friendly Solar Energy and Hydrogen Storage Materials

Lead Guest Editor: Jiangwei Liu
Guest Editors: Qiang Fu, Xuelong Hao, Jinlong Liu, and Yimin Wu

New Environmentally Friendly Solar Energy and Hydrogen Storage Materials

International Journal of Photoenergy

New Environmentally Friendly Solar Energy and Hydrogen Storage Materials

Lead Guest Editor: Jiangwei Liu
Guest Editors: Qiang Fu, Xuelong Hao, Jinlong Liu, and Yimin Wu

Contents

Structural Defects of Graphene Oxidation Reduction and Its High-Efficiency Structural Reforming Technology
Junwei An, Chen Wen, Chuping Chen, and Xiaolin Qiu
Research Article (7 pages), Article ID 8894830, Volume 2021 (2021)

Corrosion Reason Analysis of 13Cr110 Tubing in an Injection and Production Well of the Suqiao Gas Storage Group
Rui Cai, Jie Gui, Mingxing Li, Binbin Zhao, Xiaohong Bai, and Guangxu Cheng
Research Article (12 pages), Article ID 6639179, Volume 2021 (2021)

Influence of Retrogression and Reaging Treatment on Microstructure and Microhardness of the 3A21/7075 Aluminum Alloy Cladding Material
Ming Hu, Xiaoxue Ren, Jianbo Sun, and Yunlong Zhang
Research Article (9 pages), Article ID 6647271, Volume 2021 (2021)

Study on the Influence of Introducing Al Transition Layer on Deuterium Resistance of Al_2O_3 Coating
Weijing Wang, Qinghe Yu, Xiaopeng Liu, Lei Hao, Jing Mi, Shijie Li, Shuai Li, Zheng Lu, Shanshan Li, and Hao Liu
Research Article (7 pages), Article ID 6687288, Volume 2021 (2021)

Fabrication of SiC@Cu/Cu Composites with the Addition of SiC@Cu Powder by Magnetron Sputtering
Zhang Yunlong, Li Wenbo, Hu Ming, Yi Hongyong, Zhou Wei, Ding Peiling, and Tang Lili
Research Article (8 pages), Article ID 6623776, Volume 2021 (2021)

The Effect of Graphite and Fe_2O_3 Addition on Hydrolysis Kinetics of Mg-Based Hydrogen Storage Materials
Kun Yang, Hongyun Qin, Junnan Lv, Rujun Yu, Xia Chen, Zengdian Zhao, Yongjie Li, Fang Zhang, Xianchang Xia, Qiang Fu, and Ming Wang
Research Article (8 pages), Article ID 6651541, Volume 2021 (2021)

Simulation of the Residual Stress of the Y_2O_3/Al_2O_3 Composite Deuterium Permeation Barrier under Thermal Shock
Kezhi Huang, Weijing Wang, Qinghe Yu, Lei Hao, Jing Mi, Shijie Li, Hao Liu, Shanshan Li, Juan Liu, and Jianwei Wang
Research Article (12 pages), Article ID 6684802, Volume 2021 (2021)

Investigation on Mechanical Properties of GH4720Li at High Strain Rates at Wider Temperature Range
Jie Chen, Haifeng Zhang, Yunlong Zhang, Hongtao Zhang, Qingxiang Yang, and Longhai Ye
Research Article (12 pages), Article ID 8839411, Volume 2021 (2021)

Prototype of an Expert System for the Selection of Aircraft Structural Materials
Xuelong Hao, Chen Wen, Ning Zhao, Lu Lu, Kai Zhang, and Donghui Zhang
Research Article (7 pages), Article ID 8891541, Volume 2020 (2020)

Study on Hydrolysis of Magnesium Hydride by Interface Control
Yanyan Chen, Ming Wang, Fenggang Guan, Rujun Yu, Yuying Zhang, Hongyun Qin, Xia Chen, Qiang Fu, and Zeyao Wang
Research Article (8 pages), Article ID 8859770, Volume 2020 (2020)

Effect of Stress on Creep Behavior of Single Crystal Alloy IC6SX at 980°C
Liwu Jiang, Xuezheng Dou, and Meiling Wu
Research Article (5 pages), Article ID 8844874, Volume 2020 (2020)

Experimental Study on the Distribution Trends of Fouling on a Compressor Blade
Jie Tang, Dianrong Gao, Liwen Wang, and Jinjian Huo
Research Article (7 pages), Article ID 8885737, Volume 2020 (2020)

Effects of Initial Nitrate Concentrations and Photocatalyst Dosages on Ammonium Ion in Synthetic Wastewater Treated by Photocatalytic Reduction
Orawan Rojviroon, Sanya Sirivithayapakorn, Thammasak Rojviroon, and Chalermraj Wantawin
Research Article (9 pages), Article ID 8893816, Volume 2020 (2020)

Preparation of Graphene-Modified Anticorrosion Coating and Study on Its Corrosion Resistance Mechanism
Peng Wang and Dayong Cai
Research Article (9 pages), Article ID 8846644, Volume 2020 (2020)

Study of the Protection of Aluminum Alloy Surfaces by a Graphene-Modified Fluorocarbon Anticorrosive Coating
Peng Wang and Dayong Cai
Research Article (8 pages), Article ID 8835737, Volume 2020 (2020)

Study on the Creep Behavior of a Ni_3Al-Based Single Crystal Alloy at 850°C/450 MPa
Liwu Jiang, Yu Yang, Meiling Wu, and Min Cai
Research Article (7 pages), Article ID 8818136, Volume 2020 (2020)

Dynamical Properties of the New Ternary Fission in Collisions of $^{197}Au+^{197}Au$ at 15 *MeV/Nucleon*
Xian Li, Chengqian Wang, and Yaohui Xu
Research Article (9 pages), Article ID 8896666, Volume 2020 (2020)

Elastic, Mechanical, and Phonon Behavior of Orpiment Arsenic Trisulfide under Pressure
Liwu Jiang, Meiling Wu, Peng Shi, and Chuanhui Zhang
Research Article (6 pages), Article ID 8852665, Volume 2020 (2020)

Hindawi
International Journal of Photoenergy
Volume 2021, Article ID 8894830, 7 pages
https://doi.org/10.1155/2021/8894830

Research Article

Structural Defects of Graphene Oxidation Reduction and Its High-Efficiency Structural Reforming Technology

Junwei An,[1] Chen Wen,[2] Chuping Chen,[3] and Xiaolin Qiu[1]

[1]*Nanchang Institute of Technology, Nan Chang, China 330013*
[2]*Beijing Spacecrafts, China Academy of Space Technology, Beijing, China*
[3]*School of Material Science and Engineering, Beijing Institute of Petrochemical Technology, Beijing, China*

Correspondence should be addressed to Chen Wen; 13552907280@163.com

Received 14 August 2020; Accepted 18 August 2021; Published 13 October 2021

Academic Editor: Juan Manuel Peralta-Hernández

The Hummers' method is used to prepare graphene oxide and graphene powder, and the obtained powder material contains a large amount of oxygen-containing groups. Due to the effect of strong oxidants, there are many defects on the graphene body. Although a large number of oxygen-containing groups are reduced by the reduction reaction, the defects of the graphene body are numerous, which has a great influence on the conductivity of graphene and also limits the high carrier transport capability and application of graphene itself. Using industrial means, the graphene powder is highly reduced, and the ultrathin graphene powder is obtained, the graphene powder has extremely low impurity content, and the defects are substantially completely reduced. Then, these lay the foundation for its application in the battery industry.

1. Introduction

Graphene is a two-dimensional crystal composed of closely packed carbon atoms. It was taught by Prof. A. Geim and Novoselov of the University of Manchester in the UK. A single layer of graphene was obtained by stripping off the graphite [1]. At the same time, graphene has also become a research hotspot in the field of materials and physics. With the "Graphene+" strategic platform, it can provide strong support for the performance improvement and application expansion of a large number of traditional materials, and at the same time, a series of new generation functional components with excellent performance will be derived [2], and the application in many traditional fields and emerging fields will cause revolution in related industries and become a strategic emerging industry leading a new generation of industrial technology. Graphene is the most disruptive new material in the 21st century. At present, the graphene industry is in a critical period of evolution from technology to business, and large-scale application is coming soon.

Graphene is a honeycomb two-dimensional crystal composed of a single layer of hexagonal cellular carbon atoms. Due to the special structure of graphene, it also exhibits specific property that many other materials do not have. In excellent electrical conductivity [3], carrier electrons and holes in graphene are continuous, and the mobility can reach $1 \times 10^5\ cm^2 \cdot Vs^{-1}$. In ultrahigh transmittance [4], the transmittance of single-layer graphene reaches 97.7%. In ultrahigh strength, graphene was found to be the material with the highest modulus of elasticity and strength after carbon nanotubes. Its strength is 100 times stronger than the best steel in the world. The hardness is higher than the hardest diamond in nature, and it has excellent flexibility and can be bent at will. In ultrahigh thermal conductivity, because of its low-dimensional physics and unique honeycomb structure [5, 6], graphene also has a very high thermal conductivity. The free-state single-layer graphene has a thermal conductivity of $5000\ W \cdot mK^{-1}$ at room temperature. Graphene is the currently known material with the highest thermal conductivity. In ultralarge specific surface area, since the thickness of graphene is only one carbon atom thick, single-layer graphene has an ultralarge specific surface area, which can reach $2630\ m^2 \cdot g^{-1}$ [7], which is much larger than the specific surface area of ordinary activated carbon. If

you look at these properties alone, graphene is simply perfect. But the only imperfection is that there are more defects on the graphene body, and properties of graphene can be significantly changed by defects [6].

At present, the preparations of graphene are mainly based on graphite. The main preparation methods include mechanical exfoliation method [8], liquid phase stripping [9], oxidation-reduction method [10], and chemical vapor deposition [11], and oxidation reduction is one of the most widely used methods. The main idea of oxidation reduction is to treat graphite with strong oxidant, such as sulfuric acid and potassium permanganate, adding a large amount of oxidizing groups between the graphite layer and the layer, so that the spacing between the layers is increased to form graphite oxide. Then, by reducing means, such as hydrazine hydrate [12], sodium borohydride [13], and other reducing agents or heat treatment under protective or reducing atmosphere, the surface groups are removed, making it a single layer of graphite, which is graphene. Commonly used preparation methods for graphene oxide are the Brodie method [14], the Staudenmaier method [15], and the Hummers' method [16]. The Hummers' method, named after the inventor Hummer, was reported as early as the middle of the last century and has been used by people until now. However, the biggest problem with this method is that chemical means cannot completely separate the single layer of graphite. It is not possible to remove the surface groups 100% and leave more lattice defects, thereby affecting the electrical and thermal properties of graphene. Therefore, graphene made by this method is difficult to apply to devices. In this paper, the graphene powder material was prepared by the modified Hummers' oxidation method, and then, the ultrathin graphene powder was obtained by industrial reduction method. The impurity content was extremely low, and the defects were almost completely reduced, and the conductivity was improved, which lay the foundation for its application in the battery industry.

2. Experimental Part

2.1. Preparation of Experimental Materials. Hummers' redox method graphene powder manufacturing method is a modification of the Hummers' method. The typical method is the first stage: 5.5 kg of 1000 mesh high-purity flake graphite (99.95%) is put into the reaction kettle, and then, 3 kg industrial sodium nitrate is added in 210 L of concentrated sulfuric acid, keep stirring at equal speed, use the coolant to the reaction kettle, and lower the temperature to below 10°C; continue to maintain the stirring, then add 2.42 kg of potassium permanganate in batches; when the temperature reaches below 10°C, start to add potassium permanganate to the reactor in batches, and put it into the reactor every 5 minutes, each time to put 96.68 g, 25 times in total; keep the temperature not exceeding 15°C, keep the temperature below 10°C, and keep the temperature constant for 2 hours. First, the temperature of the reaction kettle is raised to 35°C and then constant temperature for 0.5 hours; after the end of the constant temperature, add water in three stages: add 89.6 L water in one hour; add 89.6 L water in half an hour; add 179.2 L water in half an hour; first, raise the temperature to 93°C, then keep the temperature constant for 2 hours; raised to 98°C and then constant temperature treatment for 2 hours; discharged the slurry in the reactor, naturally cooled for 0.5 hours; discharged the slurry in the reactor, naturally cooled for 0.5 hours; added concentrated hydrochloric acid 136.25 L and then reacted for 1 hour. Tap water is 1692 L, settling for 12 hours. The second stage is drain the supernatant of the liquid after standing, add 4241.67 L of water, stir evenly, put the 320 mesh filter cloth into the centrifuge, rinse with a proper amount of water, and then add the feed liquid several times. Until there is no filtration droplets, take the liquid, put the 380 mesh filter cloth into the centrifuge, rinse with a proper amount of water, and then add the liquid several times until no liquid droplets are removed, and the liquid is taken; the filtrate is poured along in a three-reactor, electric heating, reflux with a condenser until the liquid boils for 150-300 min; place the 2000 mesh filter cloth in the centrifuge, rinse with a proper amount of water, and then add the liquid several times until there is no filtrate. Drip out, take the filter cake, scrape the filter cake on the filter cloth, add 121 L hydrochloric acid in the container, stir evenly, pour into the three-reactor, heat it, condense and reflux, monitor the liquid temperature until the temperature of the liquid after reaching 85°C, and continuing the reaction for 2 h; add the purified slurry to 2401.67 L of water, stir evenly, then put the 2000 mesh filter cloth into the centrifuge, rinse with a proper amount of water, and then add the feed solution several times. Until there is no filter drop out, cake. For the third stage, first take the filter cake into the tray, then put the tray into the oven, set the temperature of the oven to 80°C, and dry for 12 h; pulverize the dried material with a pulverizer and put it into a closed device. The fourth stage is weigh the crushed graphite oxide to 100 g per bag; cut the graphite paper according to the crucible structure and lay it into the crucible, cover it, and transfer the graphite paper paved crucible to the workshop carbonization Kiln production line; use the robot hand, take off the lid of the crucible, and spread the graphite oxide of the good bag evenly to the middle of the crucible; cover the lid and restore it to the kiln for 24 hours; after the carbonization treatment, take off the crucible the lid; the product was collected, and the graphene oxide powder was obtained by the Hummers' method, followed by test preparation.

The preparation process of graphitized graphene is as follows: The Hummers' method graphene powder prepared above is placed in a special graphite crucible; each crucible is filled with 800 g of graphene powder and then placed in a graphitization furnace. The reaction temperature curve is increased from 20°C to 2000°C at a rate of 15°C/hour, then from 2000°C to 2800°C at a rate of 10°C/hour, held for 48 h, and then increased from 2800°C at 5°C/hour to 3200°C, hold for 48 h, then reduce the temperature to 50°C at 10°C; open the crucible, take out the material powder, get graphene powder, and test.

2.2. Test Procedure. The surface structure of graphene and graphitized graphene was characterized by HITACHI S4800

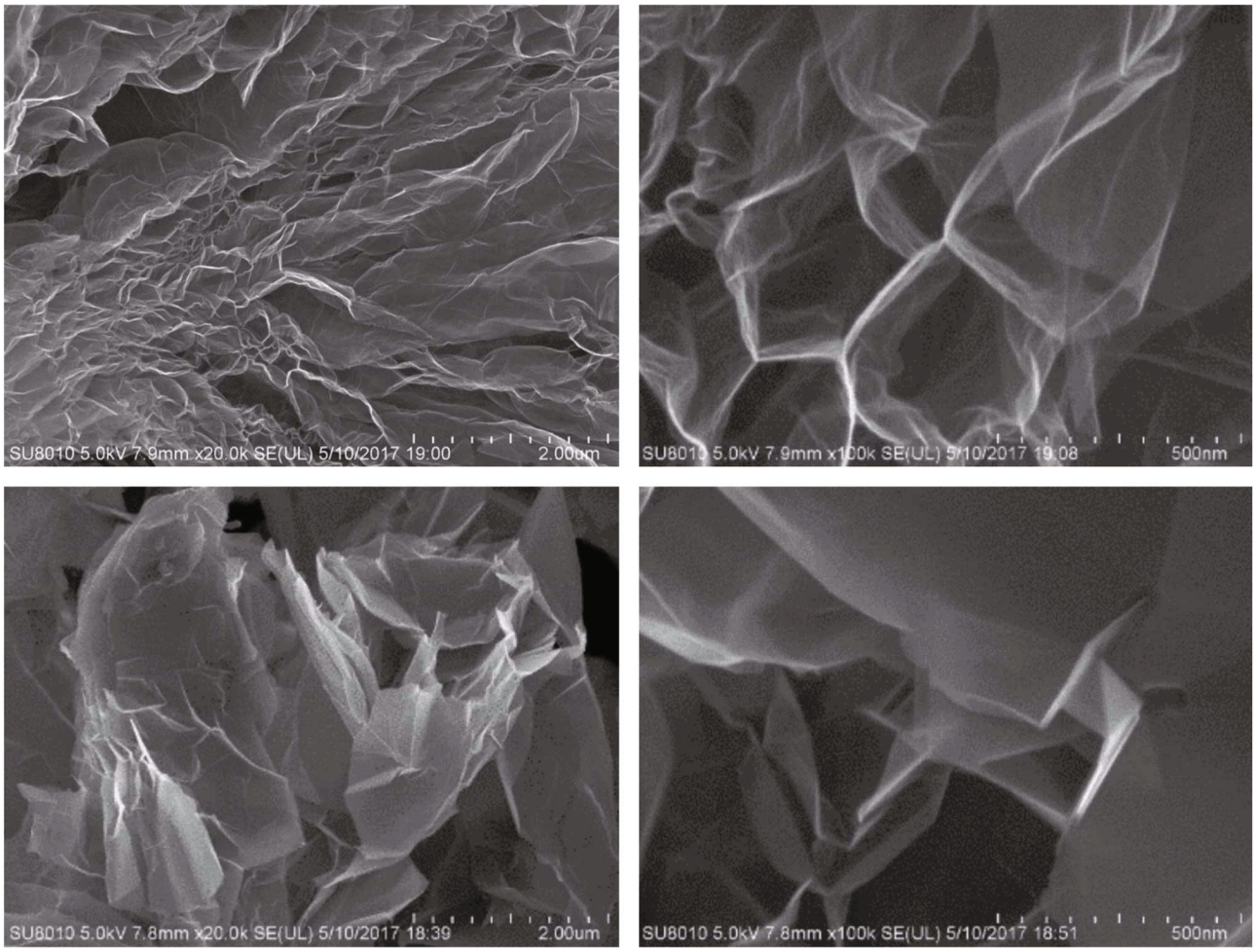

Figure 1: SEM surface topography of graphene and graphitized graphene.

field emission scanning electron microscope according to JY/T010-1996 analytical scanning electron microscopy method; using FEI Tecnai G2F30 transmission electron microscope, the structure and high resolution morphology of graphene and graphitized graphene were characterized by the JY/T011-1966 transmission electron microscopy method. Graphene and graphitized graphite were prepared according to the conventional treatment method using HORIBA LabRAM HR800 Raman spectrometer. The Raman spectrum structure of the olefin was characterized; the specific surface area of graphene and graphitized graphene was determined by using the Micromeritics ASAP2020 surface porosity and chemisorber according to the GB/T19587-2004 gas adsorption BET method for determining the specific surface area of solid materials. The RIGAKU D/max2500 X-ray diffractometer was used to test the layer spacing unit cell parameters of graphene oxide, graphene, and graphitized graphene; using Thermo Nicolet iS50 FTIR infrared spectrometer, according to GB/T 6040-2002 Infrared Spectroscopy General Rules for Graphene and Graphitized Graphene Infrared, band organic functional groups were analyzed; using Perkin Elmer Optima 7300 DV inductively coupled plasma spectrometer, according to GB/T 23942-2009 chemical reagent inductively coupled plasma atomic emission spectrometry for graphene, graphitized graphene metal and nonmetal elemental content was analyzed. The MCP-PD51 powder conductivity test systems were used to test the conductivity of graphene and other conductive materials.

The main equipments used for graphene and graphitized graphene are as follows: 5 1000 liter reactors, Zhejiang Wenzhou Zhao Flulon Co., Ltd., lined with PTFE; 1 chiller, Nanjing Hengbiao Srei Refrigeration Machinery Manufacturing Co., Ltd.; 20 sets of transfer pumps, Zhejiang Ligao Pump Industry Technology Co., Ltd.; 6 centrifuges, model SS600, Jiangsu Zhangjiagang Weilong Machinery Equipment Manufacturing Co., Ltd.; 4 plate rolling roller kiln, China Electronics Technology Group Co., Ltd. Forty-eighth Research Institute; Acheson Graphitization Furnace 1, Homemade; High Purity Water Water Machine, Qingdao Haiyue Company; and oven, CT-C-1, Nanjing Zhuoxin Drying Equipment Co., Ltd.

Drugs used in the experimental preparation are as follows: flake graphite, 1000 mesh, carbon content 99.96%, Inner Mongolia Ruisheng New Energy Co., Ltd.; concentrated sulfuric acid, 98%, industrial grade; potassium

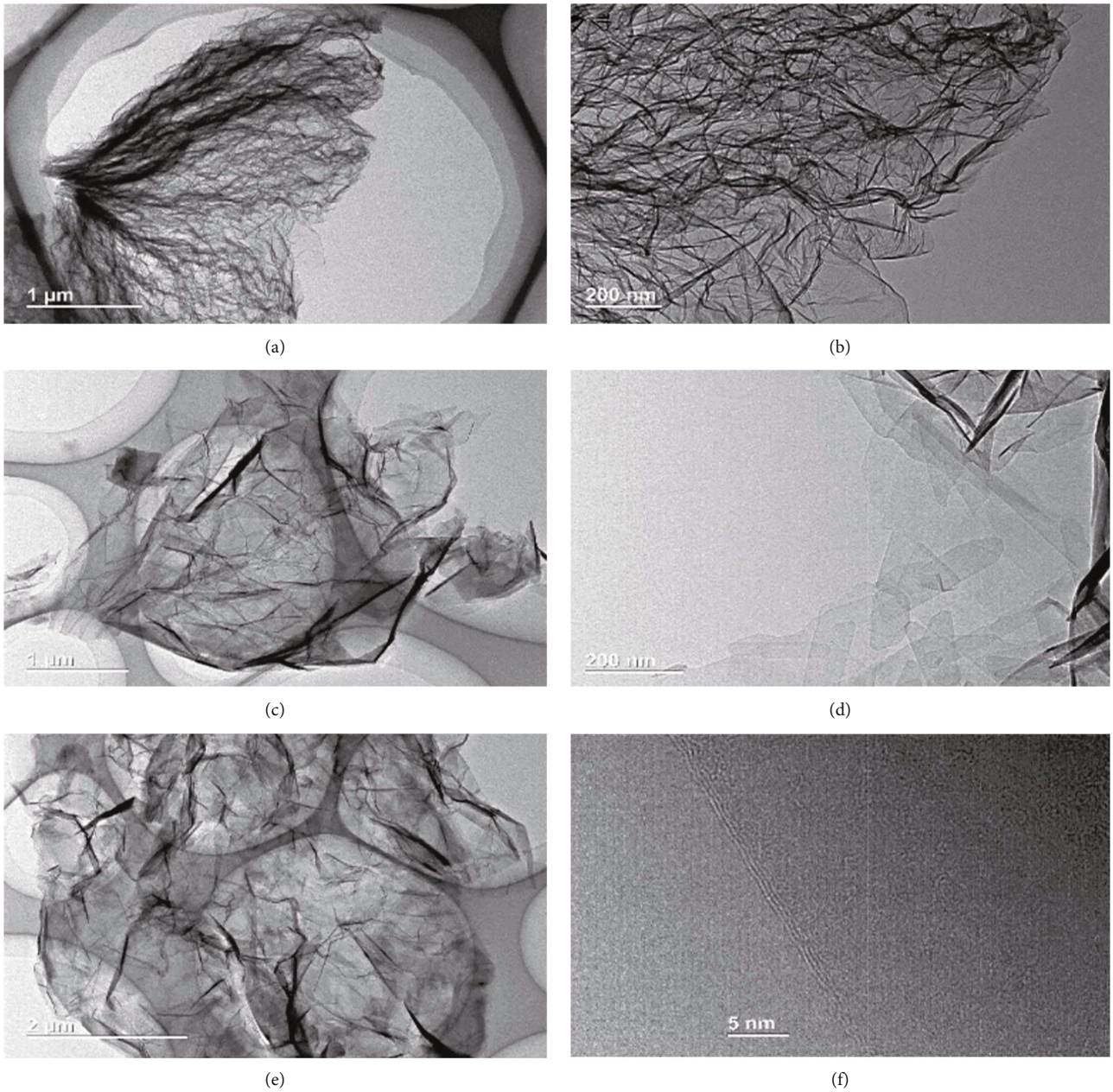

(a) (b) (c) (d) (e) (f)

Figure 2: TEM morphology and HRTEM structure of graphene and graphitized graphene.

permanganate, Tianjin company; sodium nitrate, industrial grade, a company in Tianjin; concentrated hydrochloric acid, 35%, Tianjin Membrane Company; hydrogen peroxide, 30%, a company in Tianjin; and high purity water, 17 megohms.

3. Results and Discussion

The surface morphology of graphene and graphitized graphene was characterized and compared by field emission electron scanning microscopy. It is found from Figure 1 that the surface of graphene manufactured by the modified Hummers' method exhibits a remarkable wrinkle morphology, which may be related to its chemical oxidation and reduction during chemical separation and stripping, and the porous structure indicates that it is significantly high. The specific surface area is similar to the surface structure of the graphene powder prepared by the typical chemical method reported in the literature. The surface morphology of the graphene powder after graphitization is observed, and the structure is found to exhibit less obvious folds. At the same time, its high-magnification photographs show that its structure is thicker than the graphene produced by the redox chemistry of the Hummers' method, suggesting that it may undergo significant agglomeration and back-up and also indicates that it has a small specific surface area.

The structure of graphene powder and graphitized graphene powder produced by Hummers' redox chemical method was characterized by high-rate field emission

transmission electron microscopy, as shown in Figure 2. Observations show that Figures 2(a) and 2(b) show a typical pleat structure feature, corresponding to the surface topography in Figures 1(a) and 1(b), showing a thinner sheet structure, indicating that the peeling is more thorough; the layer is thinner, indicating a larger specific surface area. Figures 2(c) and 2(d) are structural diagrams of graphitized graphene. It is found by Dolby that the structure of graphene which has been graphitized by high temperature has no obvious wrinkles, and the higher magnification of the transmission electron micrograph is shown in Figure 2(d), showing that it is relatively transparent. The characteristics of the graphite sheet layer indicate that the thickness may be thicker than the thickness of the graphene method for the Hummers' method redox chemistry. By high magnification of the portion of Figure 2(e), as shown in Figure 2(f), it can be found that the thickness of the thinnest portion is about 1.5 nm, indicating that the overlap between the graphene sheets occurs, and the thickness may be between 3and 5 layers.

Figure 3 is the XRD spectrum of the graphene precursor graphene oxide powder, graphene, and high temperature graphitized graphene powder in the Hummers' process redox chemistry. The Hummers' method redox chemical method graphite can be seen from the figure. The precursor graphene oxide powder of the olefin powder has a 2θ angle of 11°, a layer spacing of 0.804 nm, and a graphite layer spacing of 0.35 nm. Bragg equation is as follows: $2d \sin \theta = n\lambda$, where d is the crystal plane distance (that is, the layer spacing you want), θ is the readout on the graph (note that 2θ is on the graph), λ is the X-ray wavelength, and $n = 1$ (first order diffraction) Cu target Ka ray ($\lambda = 0.15406$ nm).

The 2θ angle of graphene and graphitized graphene in the Hummers' method is 26.5°, and the layer spacing is 0.336 nm, indicating that the interlayer spacing has been consistent with the graphite layer spacing, indicating that it is not a single layer of graphene.

Figure 4 is a Raman spectrum of the Hummers' method redox method graphene powder and graphitized graphene. Figure 4(a) shows the Raman spectrum of the redox method graphene showing a distinct D peak and a weak 2D peak with a small G/D peak, showing the redox method of graphene powder, the structure being strongly oxidized. Destruction, this structural damage may affect the π-π conjugated structure of the redox graphene of the Hummers' method, which affects the transport of free electrons therein and has a decisive influence on its conductivity. The Raman spectrum of graphene produced by high-temperature graphitization is shown in Figure 4(b). In the structure, the D peak disappears almost completely, the G peak is sharp, and the 2D peak is more obvious and significant, indicating that the π-π conjugate structure has been fixed. This will better embody the intrinsic properties of the prepared graphene, so that it can be applied to fields requiring high conductivity properties such as lithium ion battery conductive agents and conductive inks.

The electrical conductivity comparison in Table 1 shows that the electrical conductivity of the graphitized graphene sheet powder is not improved but is slightly lower than that of the original nongraphitized graphene. This seems unreasonable, but from its tap density, it can be found that the tap density of graphene after graphitization is only 0.0505, and the tap density of graphene without graphitization is 0.0768. This low tap density may be due to its larger specific surface area and repulsion of electrostatic charges, which makes its density lower under the same pressure, and the contact between the lamellae is not close, which affects its powder conductivity lower than the conductivity of ordinary graphene powder that has not been graphitized. In addition, it can be seen from the element content in Table 2 that it

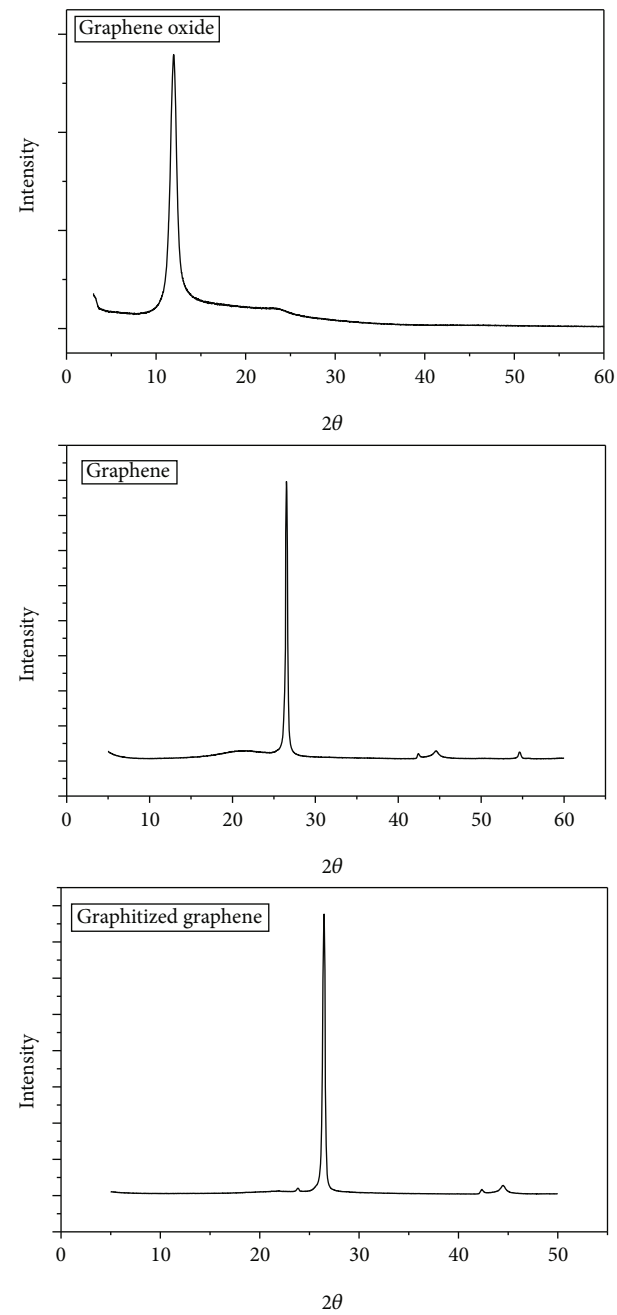

Figure 3: XRD structure of graphene oxide, graphene, and graphitized graphene.

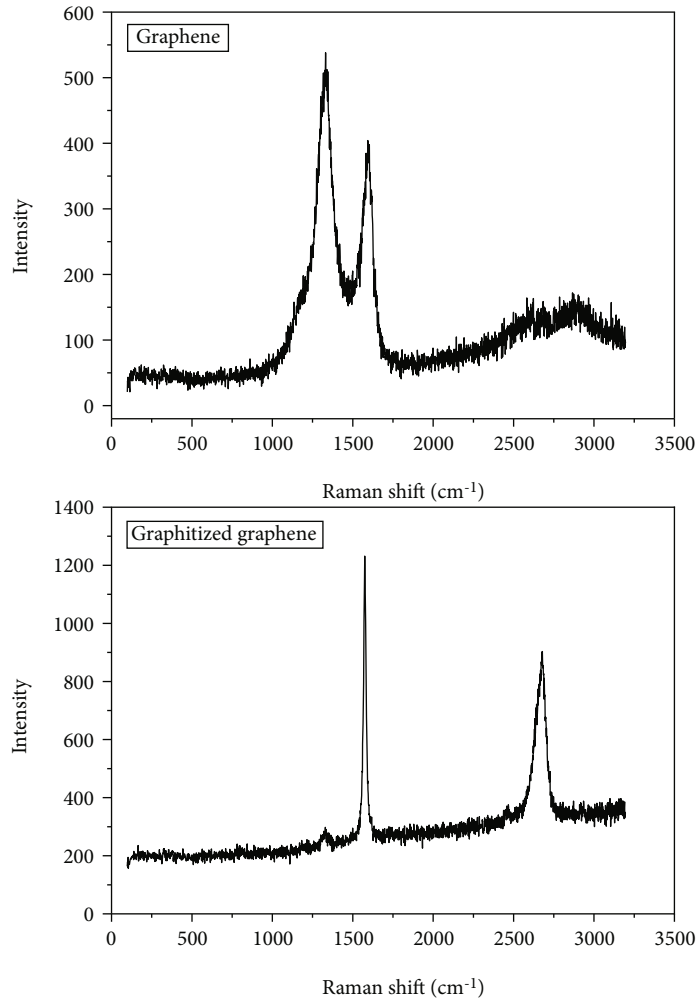

Figure 4: Raman spectrum of graphene and graphitized graphene.

Table 1: Comparison of conductivity between graphene and other conductive agents.

Sample	Conductivity (S/cm)	Conductivity (g/cm^3)
Graphitized graphene	587.3	0.0505
Graphitized graphene-purification	427.3	0.0539
Graphene	858.7	0.0768
BTR-1	400	
GC-325	773.6	0.6335
CNT	95	
KA	1210	0.4121
SP-1	20.07	0.4454
SP-2	35	0.4454

may also be due to the large amount of metal ions contained in ordinary graphene, which causes the overall conductivity of ordinary graphene powder to show greater conductivity, but its electrical conductivity may contribute more to the influence of a large amount of metal or metal oxide impurities.

Table 2: Element content in graphene powder.

Sample	Content	
	Graphene	Graphitized graphene
Fe	452.8	42.22
Mn	17730	1.19
Cu	7210	0.24
Ni	8448	1.9
Cr	103.3	3.79
Co	0.875	0.24
Mo	0	0.24
Zn		8.3
S		184.04
Cl		8

4. Conclusion

The structure and morphology of Hummers' graphene were studied by SEM, TEM, XRD, Raman, and FTIR methods. At the same time, the graphene after industrialization was compared, and the treated graphene was found to have reduced defects. Big tests on its conductivity and impurity content

show that it has high purity and impurity content, which has great prospects for its application in the battery field.

Data Availability

All data in this paper are true and valid and has not been published in other journals.

Conflicts of Interest

The authors declare that they have no conflicts of interest.

References

[1] S. K. Tiwari, R. K. Mishra, S. K. Ha, and A. Huczko, "Evolution of gGraphene Ooxide and Ggraphene: fFrom iImagination to Iindustrialization," *ChemNanoMat*, vol. 4, pp. 598–620, 2018.

[2] J. Wang, X. Jin, C. Li, W. Wang, H. Wu, and S. Guo, "Graphene and graphene derivatives toughening polymers: toward high toughness and strength," *Chemical Engineering Journal*, vol. 370, pp. 831–854, 2019.

[3] C. Chen, L. Pan, S. Jiang et al., "Electrical conductivity, dielectric and microwave absorption properties of graphene nanosheets/magnesia composites," *Journal of the European Ceramic Society*, vol. 38, no. 4, pp. 1639–1646, 2018.

[4] D. T. Thanh, K. B. Ko, Z. Khurelbaatar, C.-J. Choi, C.-H. Hong, and T. V. Cuong, "Transparent and flexible ultraviolet photoconductors based on solution- processed graphene quantum dots on reduced graphene oxide films," *Materials Research Bulletin*, vol. 91, pp. 49–53, 2017.

[5] B. S. Lee, "Thermal conductivity and scattering models for graphene: from intrinsic scattering of pristine graphene to strong extrinsic scattering of functionalized graphene," *Applied Surface Science*, vol. 497, pp. 143739.1–143739. 9, 2019.

[6] K. R. Pyun and S. H. Ko, "Graphene as a material for energy generation and control: Recent progress in the control of graphene thermal conductivity by graphene defect engineering," *Materials Today Energy*, vol. 12, pp. 431–442, 2019.

[7] S. Ren, P. Rong, and Q. Yu, "Preparations, properties and applications of graphene in functional devices: a concise review," *Ceramics International*, vol. 44, no. 11, pp. 11940–11955, 2018.

[8] K. S. Novoselov, A. K. Geim, S. V. Morozov et al., "Electric field effect in atomically thin carbon films," *Science*, vol. 306, no. 5696, pp. 666–669, 2004.

[9] Y. Hernandez, V. Nicolosi, M. Lotya et al., "High-yield production of graphene by liquid-phase exfoliation of graphite," *Nature Nanotechnology*, vol. 3, no. 9, pp. 563–568, 2008.

[10] S. Stankovich, D. A. Dikin, R. D. Piner et al., "Synthesis of graphene-based nanosheets via chemical reduction of exfoliated graphite oxide," *Carbon*, vol. 45, no. 7, pp. 1558–1565, 2007.

[11] A. Reina, X. Jia, J. Ho et al., "Large area, few-layer graphene films on arbitrary substrates by chemical vapor deposition," *Nano Letters*, vol. 9, no. 1, pp. 30–35, 2009.

[12] P. Ren, D. Yan, X. Ji, T. Chen, and Z. Li, "Temperature dependence of graphene oxide reduced by hydrazine hydrate," *Nanotechnology*, vol. 22, no. 5, pp. 55705–55713, 2011.

[13] H. J. Shin, K. K. Kim, A. Benayad et al., "Efficient reduction of graphite oxide by sodium borohydride and its effect on electrical conductance," *Advanced Functional Materials*, vol. 19, no. 12, pp. 1987–1992, 2009.

[14] B. C. Brodie, "Sur le poids atomique du graphite," *Annales de Chimie et de Physique*, vol. 59, pp. 466–472, 1860.

[15] L. Staudenmaier, "Verfahren zur darstellung der graphitsäure," *European Journal of Inorganic*, vol. 31, pp. 1394–1399, 1898.

[16] W. S. Hummers Jr. and R. E. Offeman, "Preparation of graphitic oxide," *Journal of the American Chemical Society*, vol. 80, no. 6, pp. 1339–1343, 1958.

Hindawi
International Journal of Photoenergy
Volume 2021, Article ID 6639179, 12 pages
https://doi.org/10.1155/2021/6639179

Research Article

Corrosion Reason Analysis of 13Cr110 Tubing in an Injection and Production Well of the Suqiao Gas Storage Group

Rui Cai,[1,2] **Jie Gui**,[3] **Mingxing Li**,[3] **Binbin Zhao**,[3] **Xiaohong Bai**,[3] **and Guangxu Cheng**[1]

[1]*School of Chemical Engineering and Technology, Xi'an Jiaotong University, Xi'an 710049, China*
[2]*State Key Laboratory for Performance and Structure Safety of Petroleum Tubular Goods and Equipment Materials, CNPC Tubular Goods Research Institute, Xi'an 710077, China*
[3]*Oil & Gas Technology Institute of Changqing Oilfield Co. Ltd, Xi'an 710021, China*

Correspondence should be addressed to Rui Cai; cair@cnpc.com.cn

Received 26 November 2020; Revised 21 February 2021; Accepted 3 March 2021; Published 19 April 2021

Academic Editor: Jiangwei LIU

Natural gas as a clean energy, its extensive use can alleviate energy crisis and environmental pollution and other problems. The storage and transportation of natural gas are of great significance to the standard use of natural gas. Suqiao gas storage reservoir is responsible for seasonal peak adjustment and emergency gas supply in the Beijing-Tianjin-Hebei region, and the corrosion of tubular goods is the most important issue. In this paper, the tubing composition analysis, metallographic structure analysis, mechanical property analysis, simulated corrosion test, corrosion morphology, and product analysis were carried out to analyze and study the corrosion behavior under the conditions, and suggestions were put forward to control the corrosion of the outer surface of the tubing.

1. Introduction

According to the 13th Five-Year Plan of Natural Gas, natural gas will account for 10% of China's disposable energy consumption structure in 2020. The construction of Suqiao gas storage is of great significance to maintaining national energy security and reducing air pollution in the Beijing-Tianjin-Hebei region. The "gas storage" usually refers to underground gas storage. Underground gas storage is a kind of artificial gas field or gas reservoir formed by injecting commodity natural gas from oil and gas fields nearby or long-distance pipeline back into underground space. However, when this method is adopted, corrosion of the tubular goods will inevitably occur [1–6]. If a tube corrodes, it will not only hinder the transportation of natural gas but also may cause an explosion in severe cases [7–13]. Therefore, it is very necessary to study the corrosion behavior of natural gas tubular goods.

An injection-production well in the Suqiao Gas Storage Group was completed on October 15, 2013. The completion tubing was 13Cr110 with a wall thickness of 6.88 mm and an outside diameter of 114.3 mm. The schematic diagram of well profile is shown in Figure 1. The well had been in production for 1 year and 6 months, producing 24,521,800 cubic meters of gas. The second operation of the well began on April 30, 2015. A total of 435 gas-sealed tubing were removed from the original well. When the 177th tubing was taken out, rust spots were found on the outer wall of the tubing. After inspection, there were obvious rust blisters on the outer wall of the 200th to 435th tubing, and there were obvious corrosion pits on the surface after removing rust blisters. After the tubing was dissected, it was found that there was no obvious corrosion pit on the internal surface and only different degrees of scaling, which is shown in Figure 2. In order to avoid natural gas leakage and other potential safety hazards, the corrosion causes of tubing were studied.

2. Materials and Methods

The samples used in the test were taken from this well, and 4 typical tubing samples were selected from the top, middle, and bottom positions of the wellbore. According to the

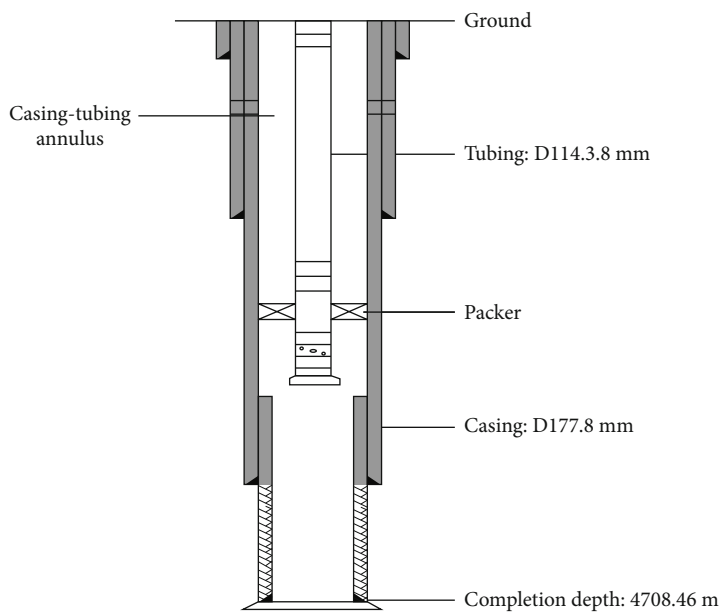

Figure 1: Schematic diagram of well profile.

(a) (b)

Figure 2: Macromorphology of tubing corrosion ((a) external surface; (b) internal surface).

extraction sequence, they were the 84th (84#), the 258th (258#), the 259th (259#), and the 364th (364#), respectively.

The ARL 4460 direct reading spectrometer was used to analyze the chemical compositions of the tubing samples. Metallographic structure, grain size, and inclusions were analyzed by the MeF3A metallographic microscope, MEF4M metallographic microscope, and image analysis system. The tensile properties and Charpy impact properties of the samples were tested, respectively. The high temperature autoclave was used to simulate the working condition on site to evaluate the corrosion resistance of the tubing material. A scanning electron microscope (SEM) was used to analyze the corrosion surface of the tubing. The elements of the corrosion products were analyzed by an energy spectrum analyzer, and the phase of the corrosion products was analyzed by X-ray diffraction.

3. Results and Discussion

3.1. Composition Analysis of Tubing Samples. The chemical compositions of four tubing samples were analyzed by the ARL 4460 direct reading spectrometer. The results are shown in Table 1. The results indicated that there was no significant difference in the chemical composition of the four tubing samples, and all of them met the requirements of the API SPEC 5CT standard.

3.2. Metallographic Analysis of Tubing Samples. According to GB/T 13298-2015, ASTM E45-18a, and ASTM E112-13, the metallographic structure, grain size, and nonmetallic inclusion of the 4 tubing samples were tested, and the test results are shown in Table 2 and Figure 3. It can be seen from the analysis results that there was no abnormal metallographic structure of the four tubing samples, all of which were tempered martensite structures, with a grain size of level 9.0 and no extrasized nonmetallic inclusions.

3.3. Testing of Mechanical Properties of Tubing Samples. The Charpy impact and tensile property test of four tubing samples was carried out according to ASTM E23-12C and ASTM A370-14. The results are shown in Tables 3 and 4. The test results showed that the impact and tensile properties of the four tubing met the requirements of API SPEC 5CT.

3.4. Simulated Working Condition Corrosion Test. A 50 mm × 10 mm × 3 mm hanging piece sample was taken from the four tubing, and a high-temperature autoclave was used for

Table 1: Analysis results of the chemical composition of sample (WT %).

Number Elements	84#	258#	259#	364#
C	0.027	0.023	0.024	0.025
Si	0.14	0.18	0.15	0.17
Mn	0.41	0.38	0.39	0.38
P	0.018	0.018	0.017	0.019
S	0.0008	0.0003	0.0007	0.0006
Cr	12.9	12.9	13.0	13.1
Mo	0.94	0.93	0.90	0.93
Ni	4.4	4.4	4.4	4.4
Nb	<0.001	<0.001	<0.001	<0.001
V	0.0050	0.0040	0.0061	0.0045
Ti	0.0082	0.0069	0.0027	0.0047
Cu	0.026	0.030	0.033	0.030
B	<0.0001	<0.0001	<0.0001	<0.0001
Al	0.036	0.043	0.032	0.044

Table 2: Metallographic analysis results of tubing samples.

Samples	Nonmetallic inclusion								Metallurgical structure	Grain size
	A		B		C		D			
	Thin	Thick	Thin	Thick	Thin	Thick	Thin	Thick		
84#	0.5	0	0.5	0	0	0	0.5	0	Tempered martensite	Level 9.0
258#	0.5	0	0.5	0	0	0	0.5	0	Tempered martensite	Level 9.0
259#	0.5	0	0.5	0	0	0	0.5	0	Tempered martensite	Level 9.0
364#	0.5	0	0.5	0	0	0	0.5	0	Tempered martensite	Level 9.0

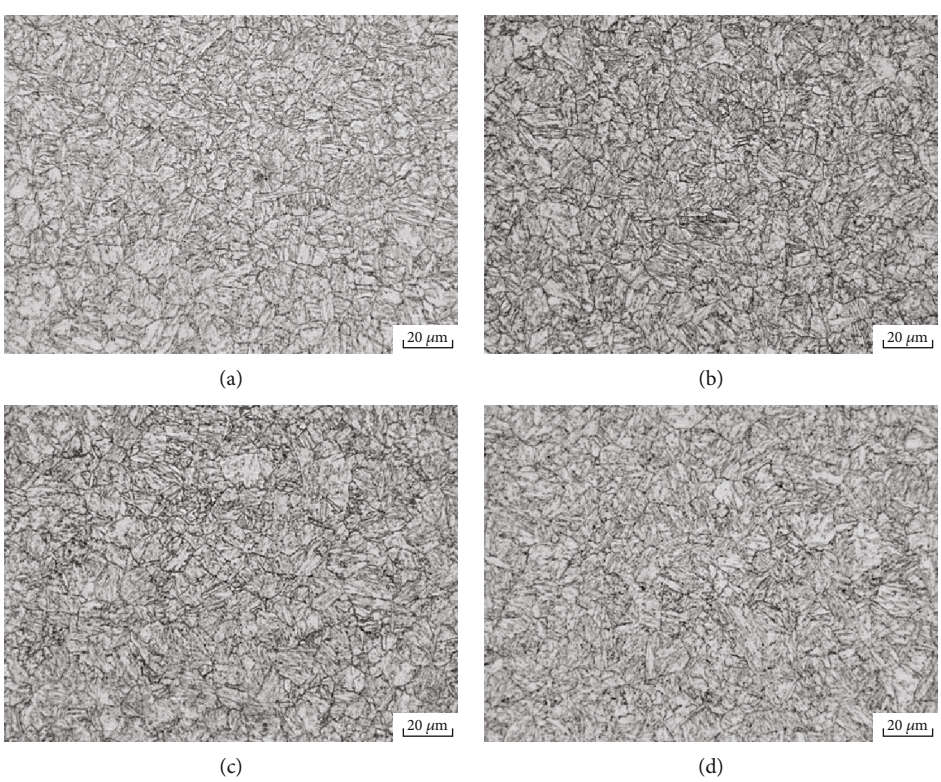

Figure 3: Metallographic diagrams of tubing samples ((a) 84#, (b) 258#, (c) 259#, and (d) 364#).

Table 3: Test results of Charpy impact performance of tubing.

Number	Samples Size (mm)	Notch shape	Temperature (°C)	Absorbed energy (J)			Shear section rate (%)		
84#	5 × 10 × 55	V	0	116	108	107	100	100	100
258#				131	129	128	100	100	100
259#				128	134	121	100	100	100
364#				131	131	121	100	100	100
API SPEC 5CT standard					≥22.55			/	

Table 4: Test results of tubing tensile properties.

Number	Width × gauge length (mm)	Strength of extension R_m (MPa)	Yield strength $R_{t0.5}$ (MPa)	Elongation A (%)
84#	25.4 × 50	905	866	23
		912	868	23
		910	859	22
258#	25.4 × 50	898	835	23
		906	849	24
		904	858	23
259#	25.4 × 50	897	853	23
		904	866	25
		889	847	23
364#	25.4 × 50	884	845	24
		889	848	24
		879	842	24
API SPEC 5CT standard		≥862	758~965	≥12

Table 5: Test conditions.

Condition	Temperature (°C)	Content of CO_2 (%vol)	Gas phase Content of O_2 (%vol)	Total pressure (MPa)	Liquid phase	Test time (h)	Sample location
1	90	2.5	0	20	Shown in Table 6	168	Gas phase, liquid phase
2	90	2.5	0.1	20		168	Gas phase, liquid phase

Table 6: Simulated formation water compositions.

Ion type	HCO_3^-	Cl^-	SO_4^{2-}	Ca^{2+}	Mg^{2+}	Na^++K^+	Water type
Concentration (mg/L)	309.4	5240.9	162.8	634.1	123.6	2632.1	$CaCl_2$

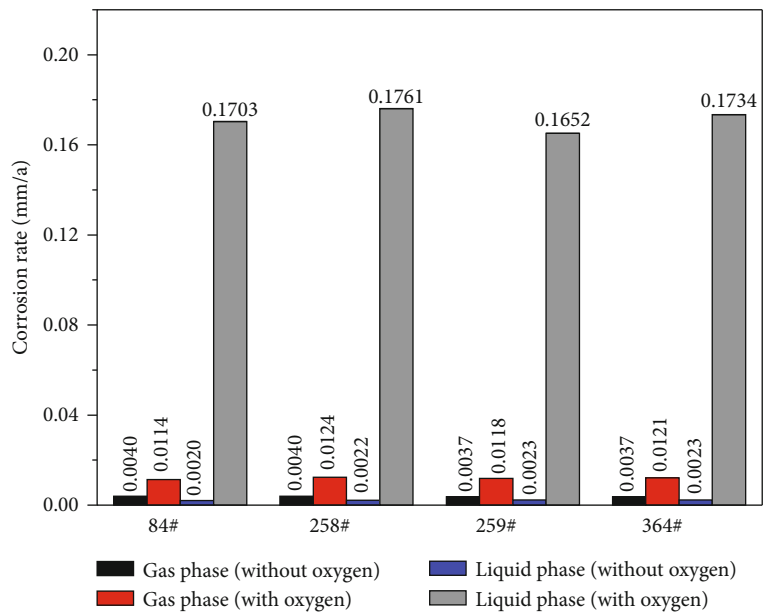

Figure 4: Corrosion rate test results of four tubing samples under different conditions.

the laboratory corrosion test to simulate the on-site working conditions. The test conditions are presented in Table 5, and the compositions of simulated formation water are shown in Table 6.

Figure 4 shows the corrosion rate test results of the four tubing samples under different conditions. It could be seen from the figure that there were no obvious differences for corrosion resistance of the four tubing materials. Compared with the conditions without oxygen, the corrosion rate of the sample in the gas phase increased by 2~3 times and in the liquid phase by 70~80 times. In the absence of dissolved oxygen, the corrosion rate of the sample in the liquid phase was about 2 times that in the gas phase. In the case of dissolved oxygen, the corrosion rate of the sample in the liquid phase was much higher than that in the gas phase, which was about 15 times.

Figure 5 shows the morphologies of the sample surface before and after the test. It could be seen from the figure that the corrosion degree of the samples in the gas phase was light, and the original wear marks could still be observed. The samples showed uniform corrosion in the liquid phase without oxygen, and there was no obvious corrosion pit on the surface. There was obvious local corrosion in the liquid phase in the presence of oxygen, and a large number of corrosion pits could be seen on the surface. It could be concluded that dissolved oxygen is the main factor leading to the corrosion of the tubing outer wall.

3.5. Analysis of Corrosion Products. As the corrosion degree of the outer wall of 84# tubing was relatively light, with only a small amount of floating rust on the surface and no obvious corrosion pits, the research on corrosion products was mainly focused on the corrosion pits of 258#, 259#, and 364# tubing samples. The surface morphology of the corrosion pit was observed by a scanning electron microscope (SEM), and the element composition of the inside and outside surface of the corrosion pit was analyzed by an energy dispersive spectrometer. Figure 6 shows the surface morphologies of the samples at low magnification. It could be seen from the figure that there was a thin layer on the sample surface, and there were obvious corrosion pits locally. The corrosion pits were round in shape, with a diameter of about 2-3 mm, and were all in the positions where the thin-layer broke or bulged.

Figures 7–9 show the surface morphologies of the corrosion pit and the results of energy spectrum analysis of the corrosion products inside and outside the corrosion pit. Tables 7–9 suggest the analysis results of the components of the corrosion products at different parts of the sample surface. The results illustrated that the corrosion pits were round, with a diameter of about 2~3 mm. Also, they were all in the position of surface rupture or uplift caused by a thin layer. The content of Cr and Ni at the bottom of the corrosion pit was significantly higher than that outside the corrosion pit, while the content of Fe in the corrosion pit was significantly lower than that outside the corrosion pit. The content of Ca element in the thin layer substance on the surface of the sample was very high, which was much higher than that in the bottom of the corrosion pit and outside the corrosion pit, and the content of Fe, Cr, and Ni was much lower than that in the corrosion pit and outside the corrosion pit.

X-ray diffraction was used for phase analysis of the surface corrosion products of the samples. Figure 10 shows the results of sample analysis. The results indicated that the sample surface mainly contained Fe_3O_4 and $CaCO_3$. Therefore, it can be concluded that the thin-layered material on the outer surface of the three tubing samples was $CaCO_3$, which was formed by surface scaling. Fe_2O_3 and Fe_3O_4 were the main corrosion products.

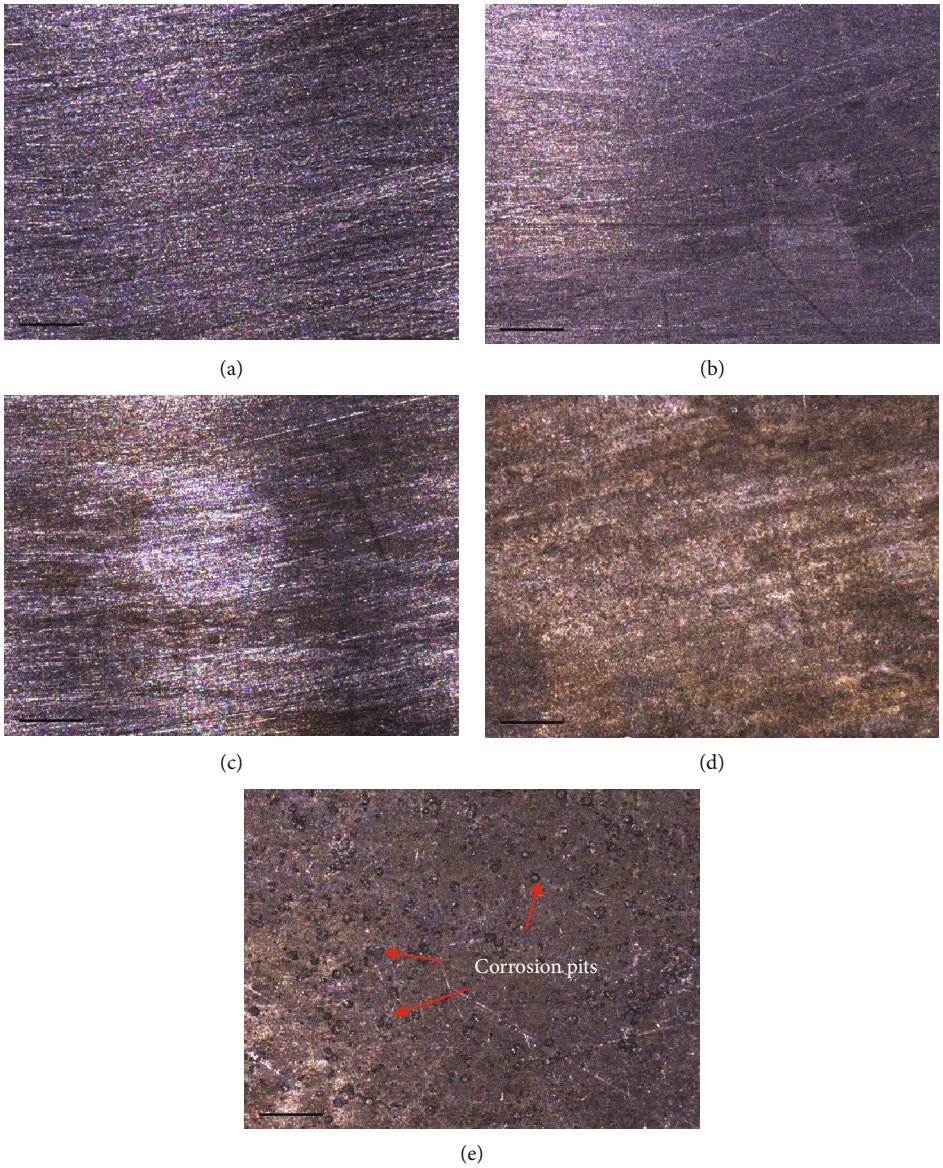

Figure 5: Surface morphologies of samples before and after the test ((a) before test, (b) gas phase without oxygen, (c) gas phase with oxygen, (d) liquid phase without oxygen, and (e) liquid phase with oxygen).

4. Comprehensive Analysis of Corrosion Reason

4.1. Corrosion Characteristics. The corrosion mainly occurred on the outer surface of the tubing, and the seriously corroded samples are located in the middle and lower part of the well. There was a thin layer of material on the outer surface of the tubing. There were obvious corrosion pits on the surface. The corrosion pits were in the position where the thin layer of material on the surface breaks or bulges. The surface of the sample mainly contains Fe_2O_3, Fe_3O_4, and $CaCO_3$. It can be concluded that (1) the thin layer material on the outer surface of the tubing samples is $CaCO_3$, which was formed by surface scaling; (2) Fe_2O_3 and Fe_3O_4 were the main corrosion products.

4.2. Influencing Factors of Corrosion. The field data showed that the packer was not completely sealed after the completion of the well, so the oil (gas) well protection fluid with passivation function was injected immediately. In the process of production, there was leakage of protective solution, so clean water was used to make up the solution, which contains a certain amount of dissolved oxygen. The gas composition analysis results showed that the CO_2 content was 2.37%. Therefore, the corrosion environment of the outer wall of the tubing was as follows:

(1) Below the liquid level: water, dissolved oxygen, dissolved CO_2, etc.

(2) Above the liquid level: water vapor, oxygen, CO_2, etc.

The corrosion test results under simulated conditions showed that the corrosion rate of the sample in the liquid phase was much higher than that in the gas phase, which was about 15 times. This was consistent with the situation

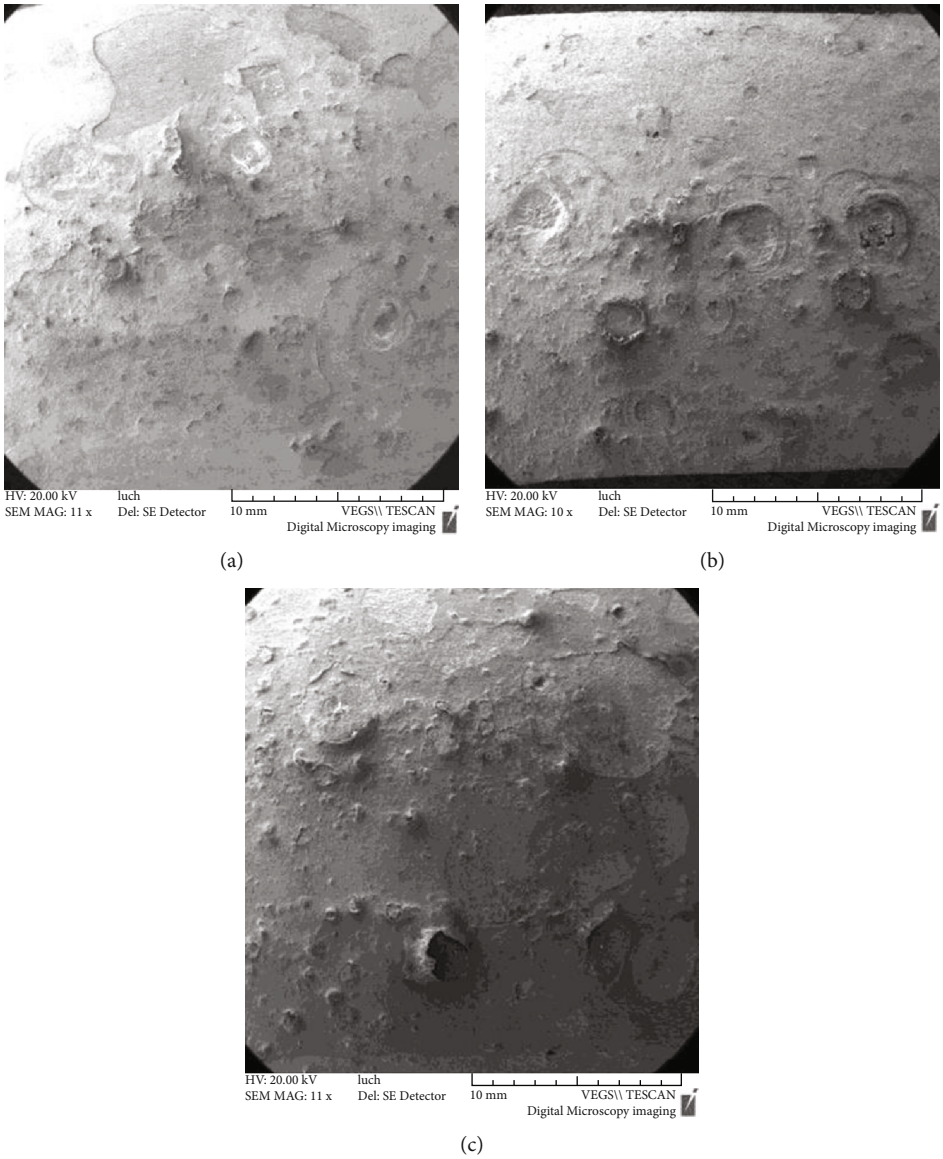

Figure 6: Surface morphologies of samples ((a) 258#, (b) 259#, and (c) 364#).

that the outer wall (containing O_2) of the tubing was more seriously corroded than the inner wall (without O_2) and the middle and lower part (liquid phase) of the outer wall of the tubing was more seriously corroded than the upper part (gas phase).

It could be concluded that dissolved oxygen was the main factor leading to the outer wall corrosion of tubing. The corrosion under scale in dissolved oxygen was the main reason for the formation of local corrosion pits on the outer wall of tubing.

4.3. Corrosion Mechanism Analysis

(1) Dissolved oxygen corrosion

Dissolved oxygen corrosion of tubing outer wall in aqueous solution is an electrochemical corrosion process, and its corrosion mechanism is as follows [14–19]:

Anode reaction: $Fe = Fe^{2+} + 2e$

Cathode reaction: $O_2 + 2H_2O + 4e = 4\,OH^-$

In solution: $Fe^{2+} + 2OH^- = Fe(OH)_2$

$Fe(OH)_2$ can be further oxidized: $4Fe(OH)_2 + O_2 + 2H_2O = 4Fe(OH)_3$

In the case of little oxygen, $Fe(OH)_2$ and $Fe(OH)_3$ can also react as follows:

$2Fe(OH)_3 + Fe(OH)_2 = Fe_3O_4 + 4H_2O$

In a dry environment, $Fe(OH)_3$ dehydrates: $2Fe(OH)_3 = Fe_2O_3 + 3H_2O$

(2) Subscale corrosion

The local corrosion of the tubing wall caused by dissolved oxygen is related to the deposition of corrosion product film and $CaCO_3$ deposit. Due to the influence of scale layer and corrosion product film, the flow of the medium on the surface and the diffusion of the dielectric are limited, resulting in large changes in the composition and pH value of the

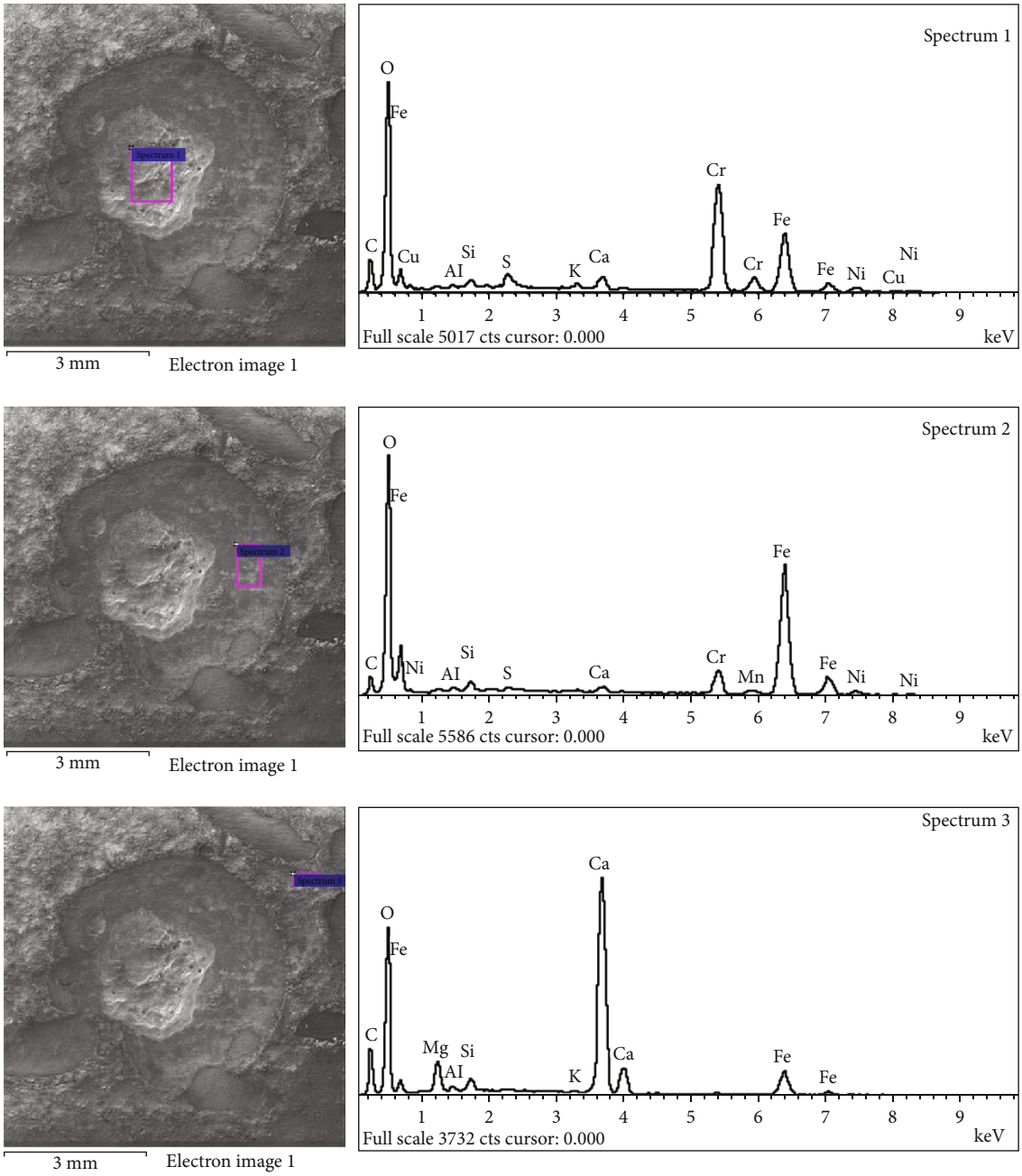

Figure 7: Morphology of corrosion pit and EDS analysis of corrosion products inside and outside pit of 258# sample.

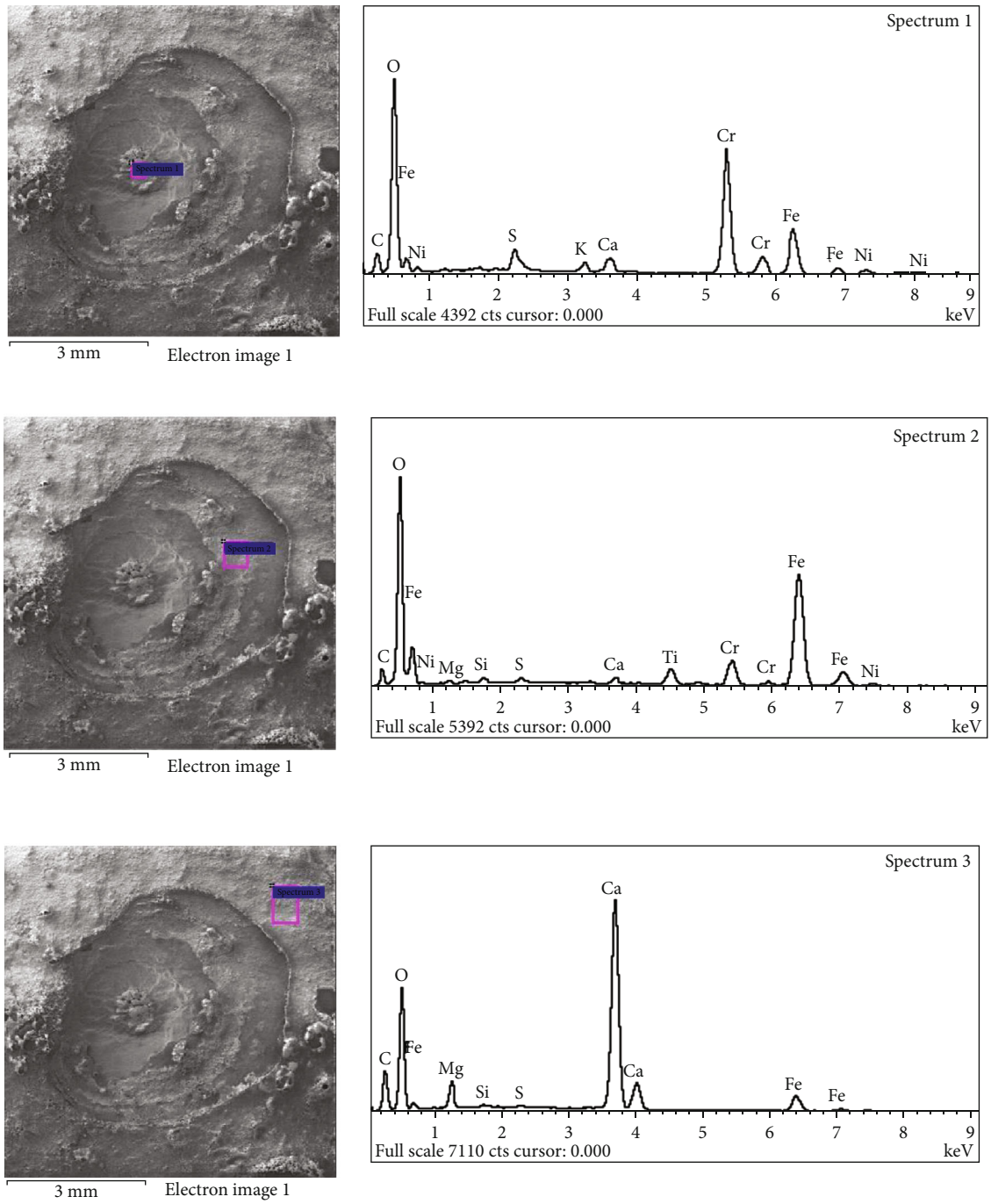

Figure 8: Morphology of corrosion pit and EDS analysis of corrosion products inside and outside pit of 259# sample.

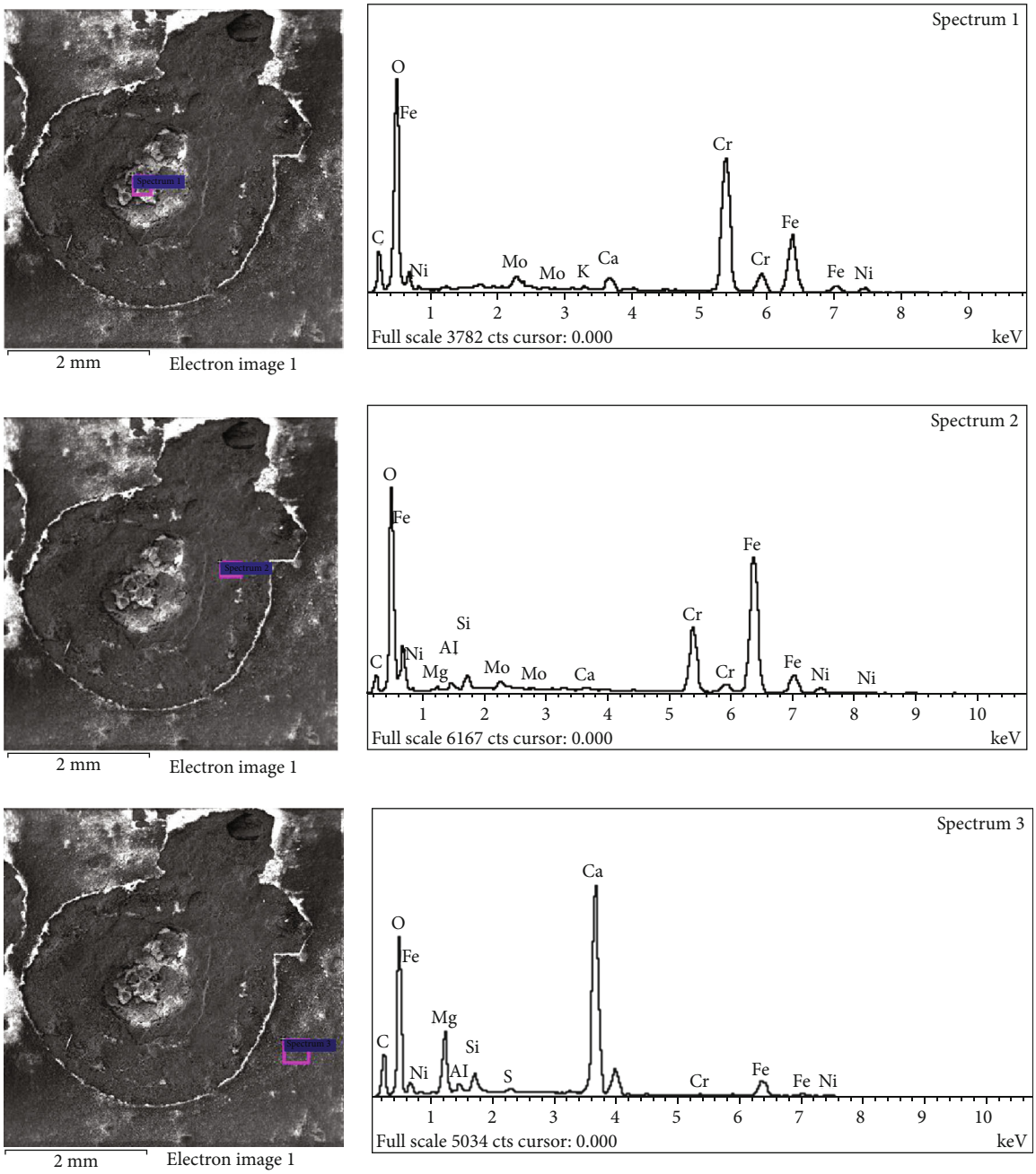

Figure 9: Morphology of corrosion pit and EDS analysis of corrosion products inside and outside pit of 364# sample.

Table 7: Composition analysis results of corrosion products at different positions of 258# sample surface.

Number		C	O	Mg	Al	Si	K	S	Ca	Cr	Mn	Fe	Ni	Cu	Total
1	Weight%	13.48	35.04		0.28	0.51	0.52	0.90	1.35	24.41		20.46	2.35	0.70	100.00
	Atomic%	26.08	50.90		0.24	0.42	0.31	0.66	0.78	10.91		8.51	0.93	0.26	
2	Weight%	8.17	37.58		0.40	0.73		0.34	0.72	4.76	0.48	44.92	1.91		100.00
	Atomic%	16.86	58.20		0.36	0.64		0.26	0.45	2.27	0.21	19.93	0.81		
3	Weight%	12.39	53.57	2.47	0.32	0.73	0.21		22.90			7.41			100.00
	Atomic%	19.72	64.04	1.94	0.23	0.50	0.10		10.93			2.54			

Table 8: Composition analysis results of corrosion products at different positions of 259# sample surface.

Number		C	O	Mg	Al	Si	K	S	Ca	Cr	Ti	Fe	Ni	Total
1	Weight%	9.88	34.54				1.08	1.48	1.78	31.70		17.07	2.46	100.00
	Atomic%	20.28	53.21				0.68	1.14	1.09	15.03		7.54	1.03	
2	Weight%	7.76	39.15	0.43	0.39			0.41	0.72	5.61	2.75	41.30	1.48	100.00
	Atomic%	15.82	59.89	0.43	0.34			0.31	0.44	2.64	1.40	18.10	0.62	
3	Weight%	11.99	52.56	2.60		0.17		0.20	26.82			5.65		100.00
	Atomic%	19.30	63.50	2.07		0.12		0.12	12.93			1.96		

Table 9: Composition analysis results of corrosion products at different positions of 364# sample surface.

Number		C	O	Mg	Al	Si	K	S	Ca	Cr	Fe	Ni	Mo	Total
1	Weight%	14.46	33.68				0.30		1.35	28.43	17.77	2.12	1.88	100.00
	Atomic%	28.19	49.28				0.18		0.79	12.80	7.45	0.85	0.46	
2	Weight%	8.45	30.52	0.37	0.55	1.07			0.28	12.46	42.50	2.24	1.56	100.00
	Atomic%	18.77	50.91	0.40	0.54	1.02			0.18	6.40	20.31	1.02	0.44	
3	Weight%	12.32	52.00	5.09	0.53	1.26		0.22	22.86	0.28	4.97	0.46		100.00
	Atomic%	19.62	62.15	4.01	0.37	0.86		0.13	10.91	0.10	1.70	0.15		

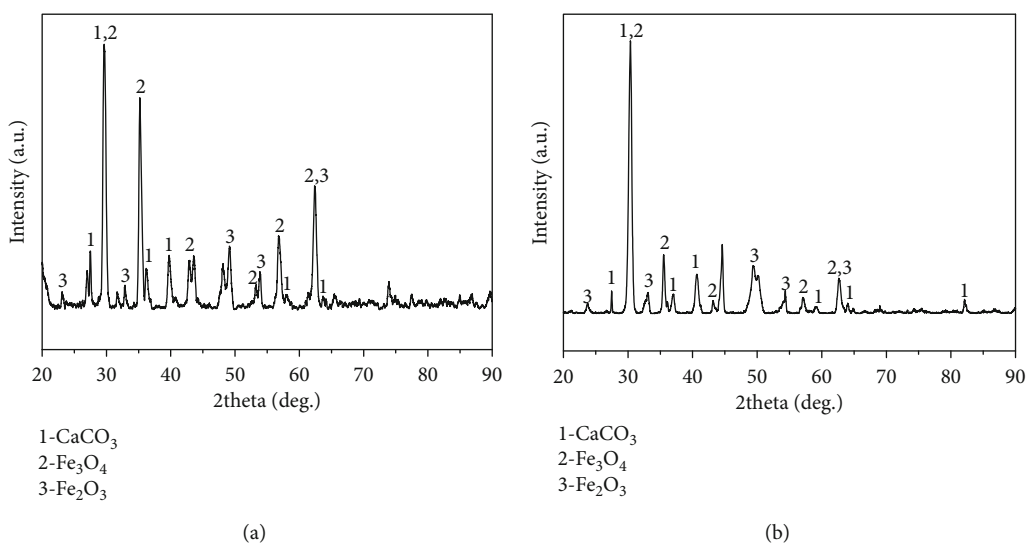

Figure 10: Surface X-ray diffraction analysis results of the sample ((a) blocky; (b) powder).

medium in the blocked corrosion pit, resulting in the blocking battery corrosion [20, 21].

In addition, when an incomplete or partially damaged or detached film layer is formed on the outer surface of the tubing, corrosive electrocution or blocking batteries with a strong autocatalytic effect are formed between different surface coverage areas, which will also accelerate local corrosion.

5. Conclusions and Recommendations

5.1. The Conclusion

(1) The impact property, tensile strength, yield strength, and elongation of the four tubing meet the requirements of API Spec 5CT for P110 tubing; the metallographic structure is normal. All of them are tempered martensite, the grain size is grade 9.0, and there is no oversize nonmetallic inclusion; there is no difference in chemical composition and corrosion resistance

(2) Dissolved oxygen will lead to a significant increase in the corrosion rate of the sample. Compared with the conditions without dissolved oxygen, the corrosion rate of the sample in the gas phase increases by 2 to 3 times, and the corrosion rate in the liquid phase increases by 70 to 80 times

(3) Subscale corrosion under the condition of dissolved oxygen is the main reason for the formation of local corrosion pits on the outer wall of the tubing

5.2. Suggestion. When taking clear water to replenish fluids, avoid direct use. Local corrosion of the tubing surface can be controlled by adding a deoxidizer, a corrosion inhibitor, or a combination of both.

Data Availability

The data used to support the findings of this study are available from the corresponding author upon request.

Conflicts of Interest

The authors declare that they have no conflicts of interest.

References

[1] Z. Y. Liu, X. Z. Wang, R. K. Liu, C. W. Du, and X. G. Li, "Electrochemical and sulfide stress corrosion cracking behaviors of tubing steels in a H_2S/CO_2 annular Environment," *Journal of Materials Engineering and Performance*, vol. 23, no. 4, pp. 1279–1287, 2014.

[2] X. W. Lei, Y. R. Feng, A. Q. Fu et al., "Investigation of stress corrosion cracking behavior of super 13Cr tubing by full-scale tubular goods corrosion test system," *Engineering Failure Analysis*, vol. 50, pp. 62–70, 2015.

[3] S. Nešić, "Key issues related to modelling of internal corrosion of oil and gas pipelines - a review," *Corrosion Science*, vol. 49, no. 12, pp. 4308–4338, 2007.

[4] S. D. Zhu, J. F. Wei, R. Cai, Z. Q. Bai, and G. S. Zhou, "Corrosion failure analysis of high strength grade super 13Cr-110 tubing string," *Engineering Failure Analysis*, vol. 18, no. 8, pp. 2222–2231, 2011.

[5] H. Mansoori, R. Mirzaee, F. Esmaeilzadeh, A. Vojood, and A. S. Dowrani, "Pitting corrosion failure analysis of a wet gas pipeline," *Engineering Failure Analysis*, vol. 82, pp. 16–25, 2017.

[6] P. Li, Y. Zhao, B. Liu et al., "Experimental testing and numerical simulation to analyze the corrosion failures of single well pipelines in Tahe oilfield," *Engineering Failure Analysis*, vol. 80, pp. 112–122, 2017.

[7] H. Wang and I. J. Duncan, "Likelihood, causes, and consequences of focused leakage and rupture of U.S. natural gas transmission pipelines," *Journal of Loss Prevention in the Process Industries*, vol. 30, pp. 177–187, 2014.

[8] A. V. Afanasyev, A. A. Mel'nikov, S. V. Konovalov, and M. I. Vaskov, "The analysis of the influence of various factors on the development of stress corrosion defects in the main gas pipeline walls in the conditions of the European part of the Russian Federation," *International Journal of Corrosion*, vol. 2018, 10 pages, 2018.

[9] D. B. Darmadi, N. A. Sugiarto, and F. Gapsari, "Stress corrosion cracking at ASTM A36 plate with varied grain orientation," *International Review of Mechanical Engineering (IREME)*, vol. 12, no. 12, pp. 987–991, 2018.

[10] M. Chausov, P. Maruschak, A. Pylypenko, and A. Sorochak, "Effect of impact-oscillatory loading on the variation of mechanical properties and crack resistance of pipe steel," in *Degradation Assessment and Failure Prevention of Pipeline Systems Lecture Notes in Civil Engineering*, vol. 102, Springer, Cham, 2021.

[11] D. K. Jana, B. Bej, M. H. A. Wahab, and A. Mukherjee, "Novel type-2 fuzzy logic approach for inference of corrosion failure likelihood of oil and gas pipeline industry," *Engineering Failure Analysis*, vol. 80, pp. 299–311, 2017.

[12] O. Shabarchin and S. Tesfamariam, "Internal corrosion hazard assessment of oil & gas pipelines using Bayesian belief network model," *Journal of Loss Prevention in the Process Industries*, vol. 40, pp. 479–495, 2016.

[13] Y. Zhang and W. G. Weng, "Bayesian network model for buried gas pipeline failure analysis caused by corrosion and external interference," *Reliability Engineering and System Safety*, vol. 203, p. 107089, 2020.

[14] G. Mcintire, J. Lippert, and J. Yudelson, "The effect of dissolved $_{CO2and}$ O2on the corrosion of iron," *Corrosion*, vol. 46, no. 2, pp. 91–95, 1990.

[15] V. D. Makarenko, S. P. Shatilo, K. K. Gumerskii, and V. A. Belyaev, "Effect of oxygen and hydrogen sulfide on carbon dioxide corrosion of welded structures of oil and gas installations," *Chemical and Petroleum Engineering*, vol. 36, no. 2, pp. 125–130, 2000.

[16] N. R. Rosli, Y. S. Choi, and D. Young, *Impact of oxygen ingress in CO_2 corrosion of mild steel*, 2014, NACE-4299.

[17] Y. Li, J. Wu, D. Zhang, Y. Wang, and B. Hou, "The electrochemical reduction reaction of dissolved oxygen on Q235 carbon steel in alkaline solution containing chloride ions," *Journal of Solid State Electrochemistry*, vol. 14, no. 9, pp. 1667–1673, 2010.

[18] X. Lin, W. Liu, F. Wu, C. Xu, J. Dou, and M. Lu, "Effect of O_2 on corrosion of 3Cr steel in high temperature and high pressure CO_2-O_2 environment," *Applied Surface Science*, vol. 329, pp. 104–115, 2015.

[19] P. Sarin, V. L. Snoeyink, J. Bebee et al., "Iron release from corroded iron pipes in drinking water distribution systems: effect of dissolved oxygen," *Water Research*, vol. 38, no. 5, pp. 1259–1269, 2004.

[20] N. M. Alanazi, A. M. El-Sherik, A. H. Rasheed, S. H. Amar, M. R. Dossary, and M. N. Alneemai, "Corrosion of pipeline steel X60 under field-collected sludge deposit in a simulated sour environment," *Corrosion*, vol. 71, no. 3, pp. 305–315, 2015.

[21] G. A. Zhang, N. Yu, L. Y. Yang, and X. P. Guo, "Galvanic corrosion behavior of deposit-covered and uncovered carbon steel," *Corrosion Science*, vol. 86, pp. 202–212, 2014.

Hindawi
International Journal of Photoenergy
Volume 2021, Article ID 6647271, 9 pages
https://doi.org/10.1155/2021/6647271

Research Article

Influence of Retrogression and Reaging Treatment on Microstructure and Microhardness of the 3A21/7075 Aluminum Alloy Cladding Material

Ming Hu,[1,2] **Xiaoxue Ren**,[1] **Jianbo Sun**,[1,2] **and Yunlong Zhang**[1,2]

[1]*College of Materials Science and Engineering, Jiamusi University, Jiamusi, 154007 Heilongjiang, China*
[2]*Department of Education Metal Wear-Resistant Materials and Surface Technology Engineering Research Center, Jiamusi, 154007 Heilongjiang, China*

Correspondence should be addressed to Jianbo Sun; 920340063@qq.com and Yunlong Zhang; ylzhdr@126.com

Received 11 October 2020; Revised 19 January 2021; Accepted 20 February 2021; Published 10 March 2021

Academic Editor: Xuelong Hao

The 7075 aluminum alloy was an important structural material in the field of aeronautics and astronautics. With the development of this field, the requirements for its comprehensive properties were increasing. A novel casting method, the impact jet solid-liquid compound casting, was adopted to fabricate the 3A21/7075 aluminum alloy cladding material. Retrogression and reaging (RRA) treatment was further applied to the 3A21/7075 aluminum alloy cladding material in order to investigate the influence of RRA on microstructure and microhardness of the 3A21/7075 aluminum alloy cladding material. Then, the electron backscattered diffraction (EBSD) technique and the transmission electron microscope (TEM) together with the energy dispersive spectrometer (EDS) and the hardness test were utilized to analyze the influence of RRA treatment on microstructure and hardness of the 3A21/7075 aluminum alloy cladding material. The research results showed the 3A21/7075 aluminum alloy cladding material had better deformability. The amount of fine and dispersed phases precipitated in grains was in favor of improving the comprehensive mechanical properties of the 3A21/7075 aluminum alloy cladding material. This research might provide data and a theoretical approach for the engineering application of the 3A21/7075 aluminum alloy cladding material.

1. Introduction

High-strength aluminum alloy had been exploited as a mold material for prototype, production, and blow molding applications, due to the high thermal conductivity and the convenience of machinability [1]. For example, the 7075 aluminum alloy was a typical representative and Al-Zn-Mg-Cu was the reinforcement. The aluminum alloy contained 1%~8% Zn and a small amount of Mg, Cr, or Cu, which was a heat-treatable strengthened aluminum alloy [2]. After quenching and aging, a large number of dispersive hardening phases were precipitated to strengthen the alloy. In the 1940s, the 7075-T6 alloys with high-strength properties were developed and subsequently used in aerospace fields such as military aircraft. T6 treatment was the most basic heat treatment system and can achieve high strength, but it was more prone to SCC tendencies [3]. At present, the processing technology of rolling aluminum alloy with wide and thick plates was still a bottleneck problem [4]. Currently, materials capable of producing thick aluminum alloy plates include Alcoa, Alcan (Ravenswood rolling Plant in the United States, Isuval rolling Plant in France), the Kaiser aluminum and chemical companies in the United States (Trey wood rolling factory), Alex company (Koblenz rolling factory), and Russian aluminum company in Myanmar (Kamensk Uralsky Metallurgical Plant). The HOKOTOL alloy produced by Corus Aluminum Wlzpodukte was a kind of high-strength aluminum alloy, mainly applied for thick plates of aluminum alloy, and its thickness can reach 700 mm. Mic-6 aluminum alloy belongs to precision casting aluminum heavy plate die alloy, and its typical thickness can reach 6~100 mm. The application of this product can replace the hot-rolled plate of ingot casting, and it can reduce the manufacturing cost of the die. The composition of the alloy was still under wraps. At present, only a

Table 1: Chemical composition of the 7075 and the 3A21 (mass fraction, %).

Material	Si	Fe	Cu	Mn	Mg	Cr	Zn	Ti	Other	Al
7075	0.4	0.5	1.2~2.0	0.3	2.1~2.9	0.18~0.28	5.1~6.1	0.20	0.20	Bal.
3A21	0.6	0.7	0.2	1.0~1.6	0.05	—	0.1	0.15	0.15	Bal.

few companies can produce more than 200 mm thick aluminum alloy die rolling plates. Nowadays, in China it is difficult to produce high-strength aluminum alloy hot-rolled plate with a thickness over 200 mm. However, the thickness of the 7075 hot-rolled aluminum alloy was greatly limited due to the inherent property of the rolling process.

Many mold materials had higher requirements on the material thickness according to the requirements of products. The key problem was how to obtain high thermal conductivity, high strength, and good wear resistance of thick plate aluminum alloy materials, so it can meet the requirement of plastic polymer processing die. It was found that only the parting surface required high strength, while the auxiliary part primarily played a part of supporting. In the meanwhile, the parting surface and the auxiliary part must be an integral material. In consequence, bimetallic cladding materials were considered to fabricate mold material for prototype, production, and blow molding applications. So it was conducive to solve problems of thickness limitation to some extent.

The manufacturing technologies of bimetallic cladding materials included explosive welding [5], roll-bonding [6], and diffusion bonding [7]. However, these technologies had problems such as low bonding strength, high cost, and low efficiency. Solid-liquid compound casting [8–11] was a common compound casting of Al-M (M, metal), but it need to wipe off oxide film on the surface of the matrix, and the production process was relatively complex. Consequently, researchers had developed a novel compound casting, namely, the impact jet solid-liquid compound casting, with no need to process the matrix. During the impact jet solid-liquid compound casting, molten metal was poured on the matrix's surface at a certain angle and speed so that impact convection heat transfer between molten metal and matrix was applied to remove oxidation film on the matrix's surface. Then, it realized metallurgical bonding. Retrogression and reaging (RRA) treatment was commonly employed to improve microstructure, mechanical properties [12–14], resistance to stress corrosion cracking [15–17], and resistance to fatigue crack propagation [18–20] of 7XXX series aluminum alloy.

Based on the above considerations, the authors adopted a novel compound casting, namely, the impact jet solid-liquid compound casting, to fabricate the 3A21/7075 aluminum cladding material. The influence of RRA treatment on the microstructure and hardness of the 3A21/7075 aluminum alloy cladding material was investigated in details. We hope that this research work will provide theoretical and experimental data support for the 7075 aluminum alloy applied as a mold material for prototype, production, and blow molding applications.

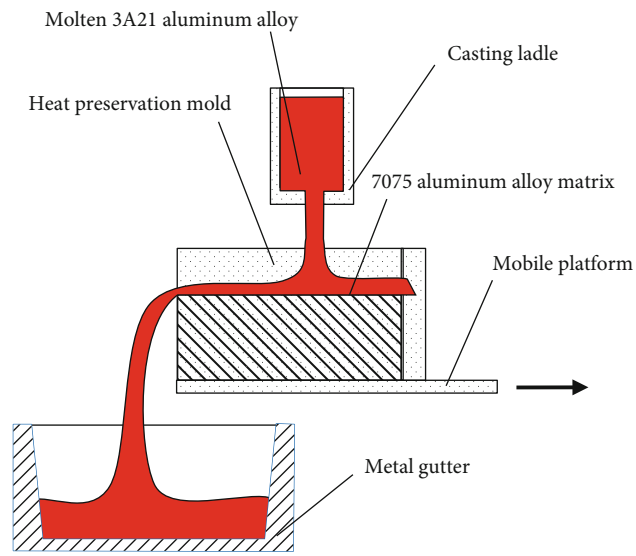

Figure 1: Process diagram of the impact jet solid-liquid compound casting.

Table 2: Process parameters of RRA.

Preaging	Retrogression	Cooling mode	Reaging
120°C × 12 h	350°C × 120 s	Water-cooling	120°C × 12 h

2. Materials and Methods

The commercial 7075-T651 aluminum alloy hot-rolled plates in the T651 condition were utilized as the matrix material (abbreviated as the 7075-T651MM). The molten 3A21 aluminum alloy was chosen as the impact jet solid-liquid compound casting material (abbreviated as the 3A21CCM). The chemical composition was shown in Table 1. The impact jet solid-liquid compound casting technology was chosen to fabricate the 3A21/7075 cladding material. The process diagram of the impact jet solid-liquid compound casting is shown in Figure 1. The experiment was divided into two stages: one was the formation of oxide film breaking and melting layer, and the other was the formation of coating layer. In the first stage, the oxide film on the surface of the substrate was removed by using the enhanced heat transfer effect and impact force of the liquid metal impinging jet. Firstly, the high-temperature cladding liquid metal was poured onto the surface of the metal substrate below. The impinging jet of the liquid metal strengthens the heat transfer and quickly heats and melts the surface of the substrate. The oxide film on the surface

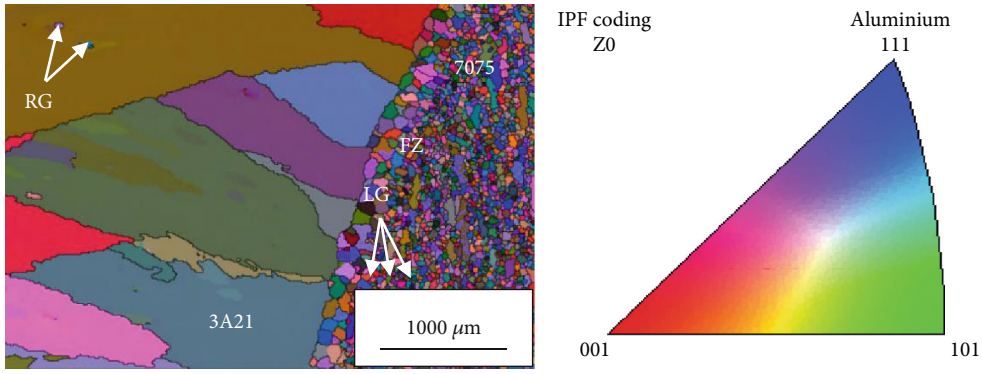

Figure 2: Evolution of grain morphology and size of the 3A21/7075 cladding material.

of the substrate was easily broken and carried away by the impact force of the liquid metal flow due to the loss of solid support. The substrate moves horizontally at a certain speed under the liquid flow, and the oxide film on the surface will be destroyed when removed. In the second stage, a large amount of heat was still transferred to the substrate during the formation of the thicker coating. In order to reduce the heat input during the formation of the coating, another ladle was used to pour the low-temperature molten metal at this stage. The melted base metal was mixed with the molten metal of the coating and finally solidified with the unmelted base metal. The 7075 aluminum matrix was placed on the mobile platform and fixed with a clamping mechanism. The motor was adopted to adjust the mobile speed of the 7075 aluminum matrix and the distance between the casting ladle and the 7075 aluminum matrix. At the initial stage of the impact jet solid-liquid compound casting, the molten 3A21 aluminum alloy was evenly poured from one end of the 7075 matrix to the other end. The movement time of the 7075 aluminum alloy matrix was delayed to achieve the effect of preheating so the 3A21/the 7075 cladding material could be well combined with each other. In the middle stage of the impact jet solid-liquid compound casting, heat and power of the 3A21 aluminum alloy during the casting process were utilized to break through the oxidation film on the surface of the 7075 matrix. When the 7075 matrix moved to the tail end at a speed of 15 mm/s, that is, at the end of the impact jet solid-liquid compound casting, a melting layer was formed on the surface of the 7075 matrix. Finally, a metallurgical bonding between the 3A21 alloy and the 7075 matrix was formed. On the preliminary experiments, the optimized RRA treatment was carried out on the 3A21/7075 cladding material and the process parameters of RRA treatment was shown in Table 2.

The electron backscattered diffraction (EBSD) technique was utilized to analyze the microstructure of the 3A21/7075 cladding material. The Tecnai G2-F30 transmission electron microscope (TEM) with an energy dispersive spectrometer (EDS) was employed to investigate phases of the 3A21/7075 cladding material. A microhardness tester with a load of 0.49 N and holding time of 10 s was applied to examine microhardness distribution of the 3A21/7075 cladding material.

Table 3: Fraction of three kinds of grains (%).

Substructured grains	Recrystallized grains	Lengthened grains
70.83	24.76	4.41

3. Results and Discussion

Figure 2 contains the evolution of morphology and size of grains in the interface area of the 3A21/7075 cladding material. The grain distribution was represented with different colors in Figure 2. The interface in the fusion zone (FZ) between the 7075-T651MM and the 3A21CCM was distinct. On both sides of the fusion zone, that is, in different regions of the matrix and the casting layer, the shape and size of the particles were obviously different. There were a large number of equiaxed grains (grain aspect ratio close to 1 within the visual field) and several lengthened grains (LG) in the 3A21CCM casting zone. It was the reason for the anomalous growth grains of the 3A21 alloy in the casting layer which had a grain boundary movement and grain rearrangement process during the heat treatment process (RRA process). When metal and alloy were heated at high temperatures, they had a spontaneous tendency to move through grain boundary to reduce the total grain boundary area and thus reduced the total grain boundary energy. During the RRA process, some grains usually swallowed up other surrounding grains in appropriate grain boundary orientation through migration of grain boundary to form some different grains from equiaxed grains. There appeared coarsened fibrous grains (grain aspect ratio ranging from 2 to 5 within the visual field), along with some recrystallized grains precipitated in fibrous grains in the 7075-T651MM region. The fraction is given in Table 3. Three different kinds of grains included substructured grains (including equiaxed grains and fibrous grains), recrystallized grains, and lengthened grains, which were detected by statistics of the EBSD system. In general, grain boundaries were divided into three types according to their orientation angles, which were low-angle grain boundaries (LAGBs, $2^\circ \leq \theta \leq 5^\circ$), high-angle grain boundaries (HAGBs, $\theta \geq 15^\circ$), and medium-grain boundaries (MAGBs, $5^\circ < \theta < 15^\circ$) [21, 22]. The fraction of the three kinds of grains was 70.83%, 24.76%, and 4.41%.

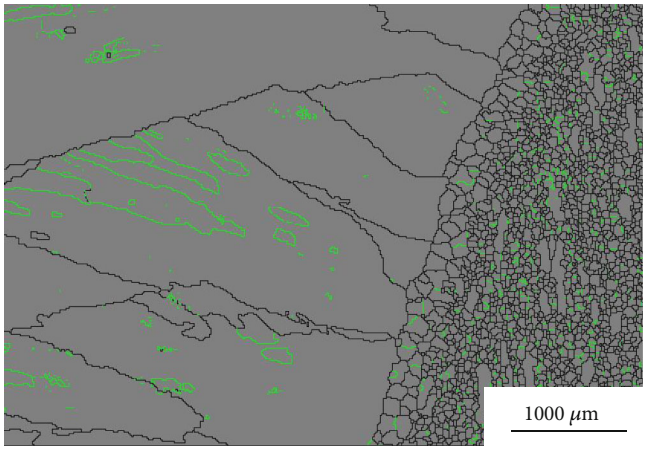

Figure 3: The grain boundary diagram of the 3A21/7075 cladding material.

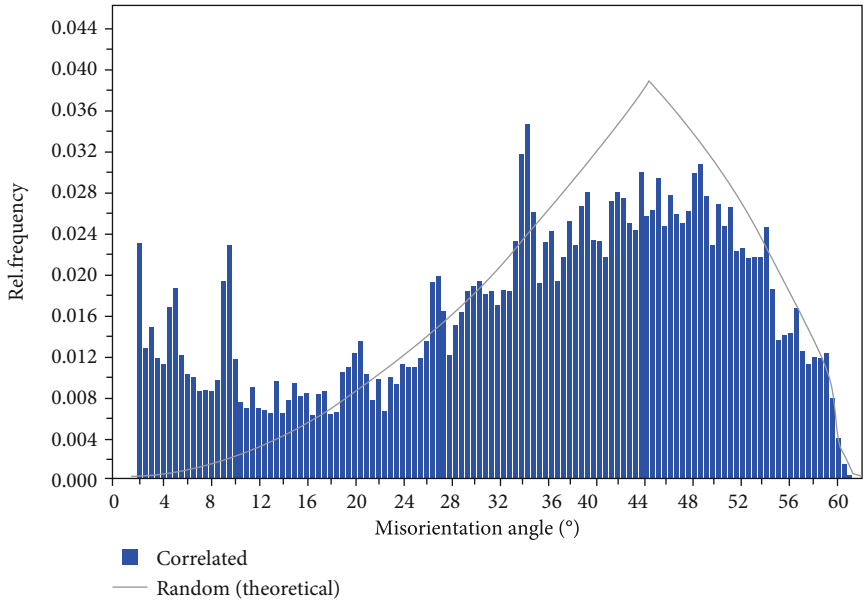

Figure 4: Misorientation angle of grains of the 3A21/7075 cladding material.

For polycrystalline materials, the misorientation angle distribution of grain boundaries had an important influence on the mechanical properties of the materials. Figure 3 presents the grain boundary diagram of the 3A21/7075 cladding material, in which the blue, red, and green lines represented HAGBs, LAGBs, and MAGBs, respectively. However, the magnitude of grain boundary energy was a function of the degree of misorientation, being larger for high-angle boundaries. Grain boundaries had more chemically reactive than the grains as a consequence of this boundary energy. Moreover, impurity atoms are preferentially segregated along the grain boundaries because of their higher energy state. While brittle cracks that expanded along HAGBs need to consume more energy, that is, HAGBs could effectively obstruct the intergranular expansion of cracks. It can be seen from the analysis in Figure 3 that MAGBs with different densities distributed both the internal and boundary of the 7075 matrix grain, so it had relatively lower grain boundary energy. The intergranular crack propagation ability can be reduced by reducing the particle boundary energy to some extent.

Figure 4 displays the misorientation angle distribution of grains of the 3A21/7075 cladding material. "Uncorrelated" meant misorientations calculated from random points in the scan (blue bar). "Random" showed the random distribution of misorientations for a purely random texture (black line). It can be observed from Figure 4 that the misorientation angle distribution of uncorrelated grains was basically consistent with the random curve. Then, it can be observed as a random distribution of grain orientation. However, a little deviation can be found between the uncorrected and the random curve from Figure 4. A conclusion can be drawn that a little rolling deformation texture existed on the side of the 7075 aluminum alloy. For aluminum alloy with a thick plate structure, many factors would affect its properties, including recrystallization structure, residual second phase, aging precipitated phase, and texture. The texture orientation

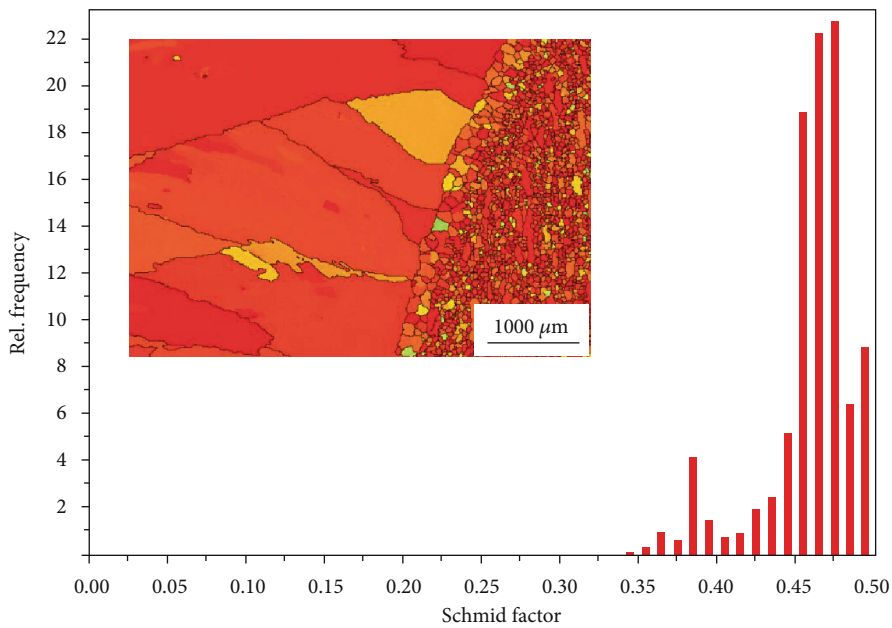

Figure 5: The Schmid factor distribution of grains in each zone of the 3A21/7075 cladding material.

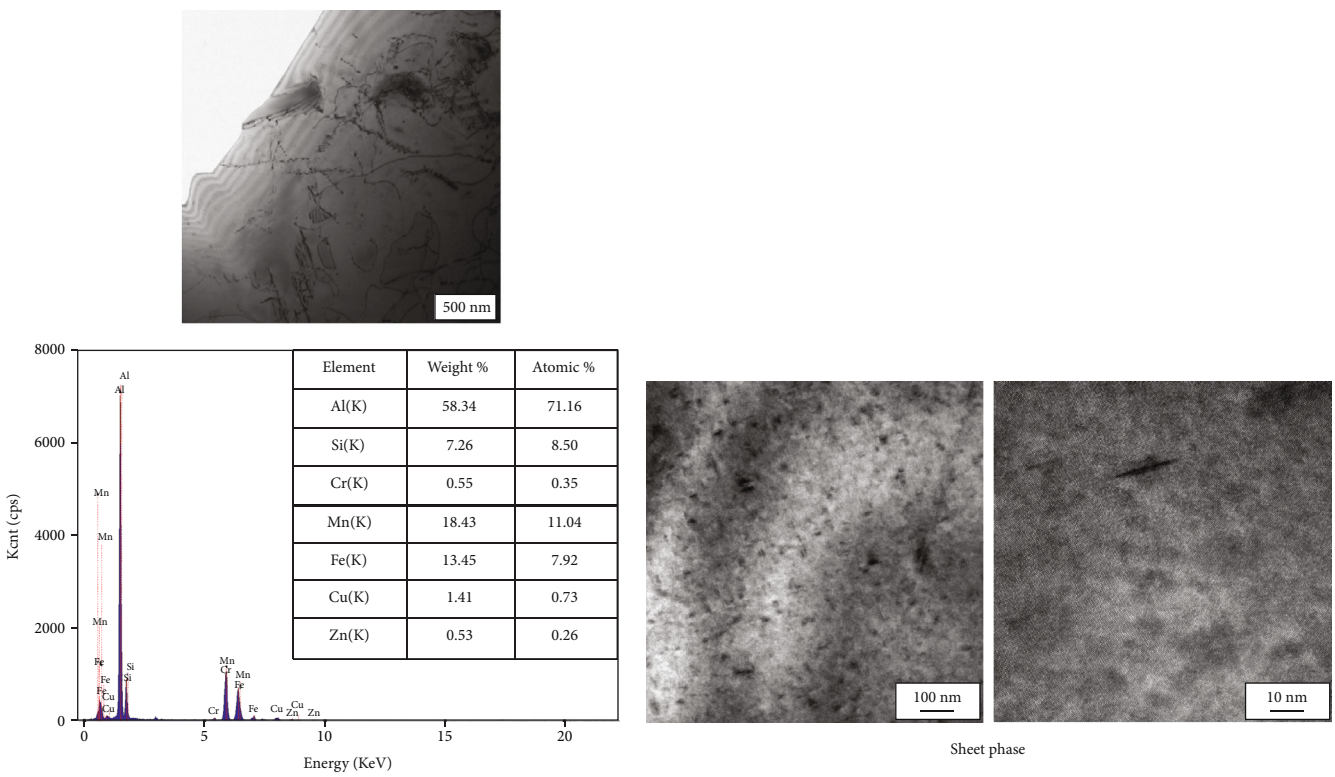

Element	Weight %	Atomic %
Al(K)	58.34	71.16
Si(K)	7.26	8.50
Cr(K)	0.55	0.35
Mn(K)	18.43	11.04
Fe(K)	13.45	7.92
Cu(K)	1.41	0.73
Zn(K)	0.53	0.26

(a) Bulk phase

(b) Sheet phase

Figure 6: TEM photos of the 3A21 cladding layer and EDS result.

of the interfacial layer had an important effect on the grain growth, uniform grain distribution, mechanical properties, and corrosion resistance of the interfacial layer.

Figure 5 describes the grain Schmid factor distribution of the 3A21/7075 cladding material. As being seen from Figure 5, significant differences were displayed between the 3A21 alloy zone and the 7075 matrix zone. The high Schmid factor was located at the 7075 matrix zone. The Schmid factor distribution of the 3A21/7075 cladding material ranged from 0.3 to 0.5. The average value of the Schmid factor was 0.46. The larger value of the Schmid factor was, the larger the resolved shear force was. The high Schmid factor zone of *m*

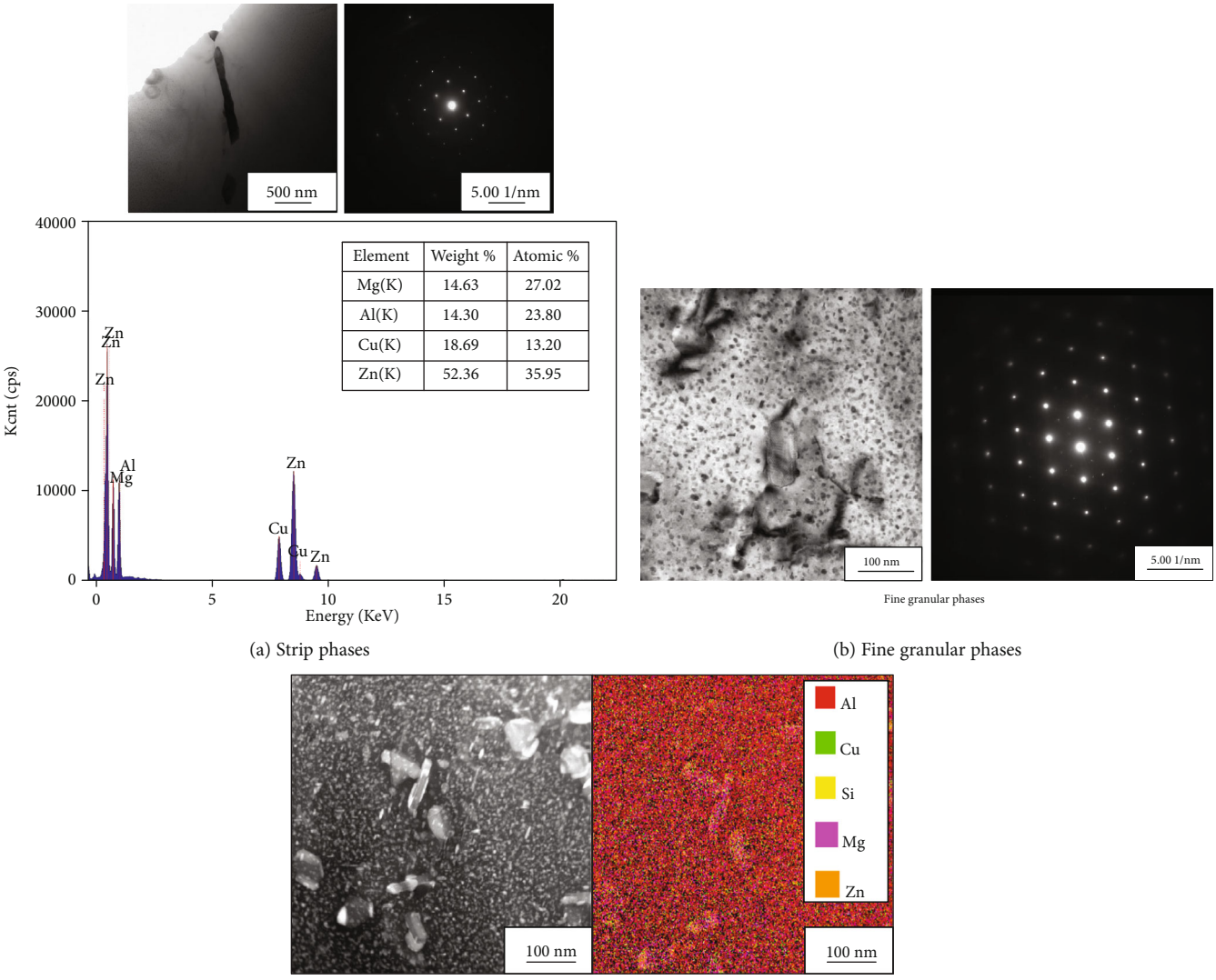

Element	Weight %	Atomic %
Mg(K)	14.63	27.02
Al(K)	14.30	23.80
Cu(K)	18.69	13.20
Zn(K)	52.36	35.95

(a) Strip phases

(b) Fine granular phases

(c) Coarsened granular phases and HAADF

Figure 7: TEM photos of the 7075 matrix.

≥ 0.45 was defined as a "soft" orientation zone in terms of the resolved shear stress, which was higher in "soft" zone than in the rest zones under the same applied stress [23, 24]. It contributed to grain boundary migration and grain rotation under external force [25]. The larger value of the Schmid factor indicated better deformability of the 3A21/7075 cladding material.

Figure 6 indicates a TEM photo of the 3A21 cladding layer. Two different kinds of phases included a bulk phase and some sheet phase. The bulk phase was irregular in shape (Figure 6(a)). It was calculated from EDS result that the ratio of Al : (Fe, Mn) : Si was nearly 9 : 3 : 1. The bulk phase was identified as Al9Fe0.84Mn2.1Si by XRD analysis according to PDF42-1206# card [26]. The 3A21 aluminum alloy belongs to the heat treatment cannot be strengthened aluminum alloy, so a small amount of second phase has little effect on the microstructure and properties of the 3A21 aluminum alloy. Some sheet phases were undetermined and fine with a length of 10 nm and a width of less than 1 nm; then, the tip position tended to cause stress concentration.

Figure 7 provides TEM photos of the 7075 matrix. There appeared three kinds of phases, namely, coarsened strip phase precipitated at the grain boundary, some coarsened granular phases, and amounts of fine granular phases in the internal of the grain. The strip phase was a little coarse and rich in Al, Zn, Mg, and Cu from the result of EDS (Figure 7(a)), which was inferred as T phase (AlCuMgZn). Vast fine granular phases were in the internal of the grain (Figure 7(b)). Fine granular phases were regarded as newly precipitated η' ($MgZn_2$) after RRA treatment, while some coarsened granular phases were judged as unmelted η' ($MgZn_2$) from Figure 7(c). The coarsened granular phases and HAADF image were given. The main elements included Al, Cu, Si, Mg, and Zn. They were consistent with designed material. It is worth noting that these fine and dispersed η' ($MgZn_2$) were beneficial to improve comprehensive

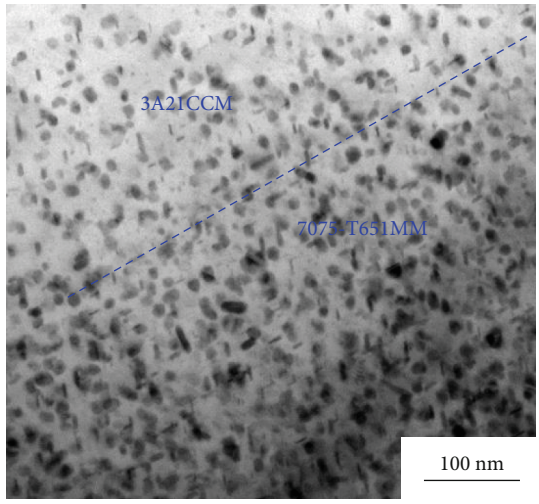

Figure 8: TEM photo of the fusion zone.

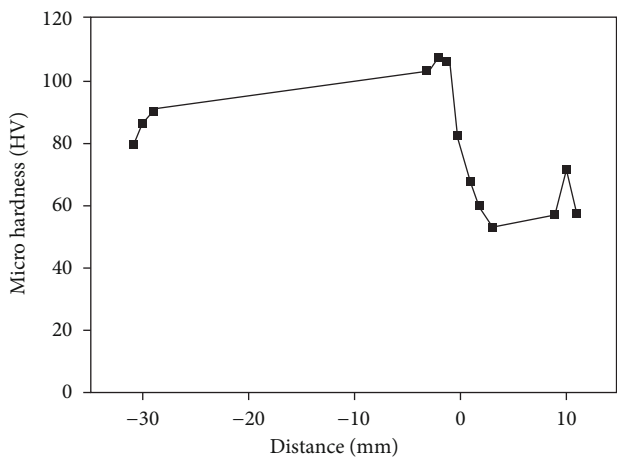

Figure 9: Microhardness test result of the 3A21/7075 aluminum alloy cladding material.

mechanical properties and corrosion resistance of 7055 aluminum alloy. The generally accepted precipitation sequences for 7XXX series alloys were as follows: supersaturated solid solution(SSS)⟶coherent stable GP zones⟶semicoherent intermediate η' ($MgZn_2$)⟶incoherent stable η ($MgZn_2$) or T (AlZnMgCu). The morphology size and the degree of coherence with the matrix would influence the property of aluminum alloy.

Figure 8 illustrates TEM photos of the fusion zone between the matrix and casting materials. They appeared heterogeneous, fine granular phases, and sheet phases in Figure 8. It brought into correspondence with Figures 6(b) and 7(b), respectively. This zone separately and uniquely had two kinds of phases that belonged to the 3A21 cladding layer and the 7075 matrix, so this zone was the fusion zone.

Figure 9 depicts the microhardness test result of the 3A21/7075 cladding material. The 3A21/7075 cladding material showed a degree of softening. It could be found from the EBSD and TEM results that plenty of fine phases precipitated in the inner region of the grains of the 3A21/7075. At the same time, all fine-precipitated phases grew up to some extent. Finally, grain growth was the dominant factor, which was responsible for the softening phenomenon.

4. Conclusion

The 3A21/7075 aluminum alloy cladding material with good quality was successfully prepared by the impact jet solid-liquid compound casting method on self-developed composite equipment. The interface between cladding alloy (the 3A21) and matrix alloy (the 7075) was metallurgical bonding. Three different kinds of grains included substructured grains (including equiaxed grains and fibrous grains), recrystallized grains, and lengthened grains, which were detected by statistics of EBSD system. The fraction of three kinds of grains was 70.83%, 24.76%, and 4.41%. Regression reaging treatment (RRA) has a significant effect on the microstructure and properties of the 3A21/7075 aluminum alloy cladding material. After RRA treatment, the matrix, which was the 7075-T651MM, had better deformability. Both sides of

the 3A21 and the 7075 precipitated amount of fine phases in grains helped to improve comprehensive mechanical properties of the 3A21/7075 aluminum alloy cladding material. The microhardness of the transition region of the 3A21/7075 clad aluminum alloy shows an obvious gradient distribution. However, grains of the 3A21/7075 aluminum alloy cladding material grew up and caused a decrease in hardness. Therefore, the next work was to further optimize RRA treatment in order to obtain fine and dispersed phases with no grain overgrowing.

Data Availability

The data used to support the findings of this study are included within the article.

Conflicts of Interest

The authors declare that there is no conflict of interest.

Acknowledgments

The research was funded by the Natural Science Fund of China (grant number 51671096), Materials Science and Engineering Discipline Team of Jiamusi University (grant number JDXKTD-2019001), Collaborative Innovation Program of Jiamusi University (grant number 2011xtcx2016-03), Natural Science Foundation of Heilongjiang Province (E2015038), and Scientific Research Fund of Heilongjiang Education Department Project (2016-KYYWF-0556, 2017-KYYWF-0582, 2019-KYYWF-1373, 2019-KYYWF-1375).

References

[1] J. Kim, R. Smierciak, Y. S. Shin, and L. Cooper, "Advances in aluminum mold block for plastic injection molding operations," in *Proceedings of the 13th International Conference on Aluminum Alloys*, pp. 1621–1627, Pittsburgh, USA, 2012.

[2] H. Aarabi and M. Alizadeh, "Improvement of microstructure and corrosion properties of AA7075 Al alloy by melt shearing process," *Materials Letters*, vol. 275, article 128085, 2020.

[3] X. Cui, X. Xu, Y. Ning, and Y. Zhao, "Microstructure and Mechanical Properties of 7075 Al Alloy Processed by Combined Cold-rolling and T6 Heat-treatment," *Materials Review*, vol. 31, no. 7, pp. 88–91, 2017.

[4] Z. Tao, W. Yunxin, G. Hai, S. Wenze, J. Fangmin, and J. Shaosong, "Analysis of temperature asymmetry of aluminum alloy thick plate during snake hot rolling," *The International Journal of Advanced Manufacturing Technology*, vol. 87, no. 1-4, pp. 941–948, 2016.

[5] T. Zhang, W. Wang, W. Zhang et al., "Microstructure evolution and mechanical properties of an AA6061/AZ31B alloy plate fabricated by explosive welding," *Journal of Alloys and Compounds*, vol. 735, pp. 1759–1768, 2018.

[6] Z. J. Wang, M. Ma, Z. X. Qiu, J. X. Zhang, and W. C. Liu, "Microstructure, texture and mechanical properties of AA 1060 aluminum alloy processed by cryogenic accumulative roll bonding," *Materials Characterization*, vol. 139, pp. 269–278, 2018.

[7] H. Zhang, J. L. Li, C. S. Wang, J. T. Xiong, and F. S. Zhang, "Equal-strength precision diffusion bonding of AA6063 aluminum alloy with the surface passivated by a self-assembled monolayer," *International Journal of Materials Research*, vol. 108, no. 7, pp. 571–577, 2017.

[8] J. Feng, B. Ye, L. Zuo et al., "Bonding of aluminum alloys in compound casting," *Metallurgical and Materials Transactions A*, vol. 48, no. 10, pp. 4632–4644, 2017.

[9] R. Mola, T. Bucki, and M. Gwoździk, "The effect of a zinc interlayer on the microstructure and mechanical properties of a magnesium alloy (AZ31)-aluminum alloy (6060) joint produced by liquid-solid compound casting," *The Journal of The Minerals, Metals & Materials Society*, vol. 71, no. 6, pp. 2078–2086, 2019.

[10] J. Shin, T. Kim, K. Lim et al., "Effects of steel type and sandblasting pretreatment on the solid-liquid compound casting characteristics of zinc-coated steel/aluminum bimetals," *Journal of Alloys and Compounds*, vol. 778, pp. 170–185, 2019.

[11] G. Y. Li, W. M. Jiang, F. Guan, J. Zhu, H. Jiang, and Z. Fan, "Effect of insert materials on microstructure and mechanical properties of Al/Mg bimetal produced by a novel solid-liquid compound process," *Journal of Manufacturing Processes*, vol. 47, pp. 62–73, 2019.

[12] A. Zieliński, J. Chrzanowski, M. Warmuzek, A. Gazda, and E. Jezierska, "Influence of retrogression and reaging on microstructure, mechanical properties and susceptibility to stress corrosion cracking of an Al-Zn-Mg alloy," *Materials and Corrosion*, vol. 55, no. 2, pp. 77–87, 2004.

[13] H. T. Naeem, K. S. Mohammed, R. A. Khairel, and A. Rahmat, "The role of direct chilling, retrogression and reaging treatment on mechanical properties of high strength aluminum alloy," *Advanced Materials Research*, vol. 795, pp. 211–218, 2013.

[14] G. Ozer and A. Karaaslan, "Properties of AA7075 aluminum alloy in aging and retrogression and reaging process," *Transactions of Nonferrous Metals Society of China*, vol. 27, no. 11, pp. 2357–2362, 2017.

[15] M. Baydogan, H. Cimenoglu, E. Sabri Kayali, and J. Rasty, "Improved resistance to stress-corrosion-cracking failures via optimized retrogression and reaging of 7075-T6 aluminum sheets," *Metallurgical and Materials Transactions A*, vol. 39, no. 10, pp. 2470–2476, 2008.

[16] Y. Reda, R. Abdel-Karim, and I. Elmahallawi, "Improvements in mechanical and stress corrosion cracking properties in Al-alloy 7075 via retrogression and reaging," *Materials Science and Engineering A*, vol. 485, no. 1-2, pp. 468–475, 2008.

[17] Y. P. Xiao, Q. L. Pan, W. B. Li, X. Y. Liu, and Y. B. He, "Influence of retrogression and re-aging treatment on corrosion behaviour of an Al–Zn–Mg–Cu alloy," *Materials and Design*, vol. 32, no. 4, pp. 2149–2156, 2011.

[18] X. Chen, Z. Y. Liu, M. Lin, A. Ning, and S. Zeng, "Enhanced fatigue crack propagation resistance in an Al-Zn-Mg-Cu alloy by retrogression and reaging treatment," *Journal of Materials Engineering and Performance*, vol. 21, no. 11, pp. 2345–2353, 2012.

[19] Y. L. Wang, Q. L. Pan, L. L. Wei, B. Li, and Y. Wang, "Effect of retrogression and reaging treatment on the microstructure and fatigue crack growth behavior of 7050 aluminum alloy thick plate," *Materials and Design*, vol. 55, pp. 857–863, 2014.

[20] Y. Wang, Y. L. Deng, S. D. Liu, Z. Shan, J. Tang, and X. Zhang, "Effect of RRA treatment on the microstructure and fatigue behavior of 7020 aluminum alloy," in *High Performance Structural Materials*, pp. 349–359, 2018.

[21] J. H. Park, K. Hamad, I. P. Widiantara, and Y. G. Ko, "Strain and crystallographic texture evaluation of interstitial free steel cold deformed by differential speed rolling," *Materials Letters*, vol. 147, pp. 38–41, 2015.

[22] Z. F. Yan, D. H. Wang, X. L. He et al., "Deformation behaviors and cyclic strength assessment of AZ31B magnesium alloy based on steady ratcheting effect," *Materials Science & Engineering A*, vol. 723, pp. 212–220, 2018.

[23] C. D. Barrie, A. P. Boyle, S. F. Cox, and D. J. Prior, "Slip systems and critical resolved shear stress in pyrite: an electron backscatter diffraction (EBSD) investigation," *Mineralogical Magazine*, vol. 72, no. 6, pp. 1181–1199, 2008.

[24] X. Chao, S. Qiaoyan, X. Lin, and S. Jun, "Schmid factor maps for predicting slip and twinning behaviors in zirconium," *Rare Metal Materials and Engineering*, vol. 48, no. 8, pp. 2400–2405, 2019.

[25] Z. G. Liu, P. J. Li, L. T. Xiong, T. Liu, and L. He, "High-temperature tensile deformation behavior and microstructure evolution of Ti55 titanium alloy," *Materials Science & Engineering A*, vol. 680, pp. 259–269, 2017.

[26] R. A. Brand, G. Le Caër, J. M. Dubois, F. Hippert, C. Sauer, and J. Pannetier, "The magnetic transition in Fe-substituted hexagonal β-Al9SiMn3," *Journal of Physics: Condensed Matter*, vol. 2, pp. 3855–3866, 1990.

Hindawi
International Journal of Photoenergy
Volume 2021, Article ID 6687288, 7 pages
https://doi.org/10.1155/2021/6687288

Research Article

Study on the Influence of Introducing Al Transition Layer on Deuterium Resistance of Al_2O_3 Coating

Weijing Wang,[1,2,3,4] Qinghe Yu,[1,2,3] Xiaopeng Liu,[2] Lei Hao,[1,2,3] Jing Mi,[1,2] Shijie Li,[1,2] Shuai Li,[1,2] Zheng Lu,[4] Shanshan Li,[1,2] and Hao Liu[1,2]

[1]*National Engineering Research Center of Nonferrous Metals Materials and Products for New Energy, GRINM Group Co., Ltd., Beijing 100088, China*
[2]*GRIMAT Engineering Institute Co., Ltd., Beijing 101407, China*
[3]*General Research Institute for Nonferrous Metals, Beijing 100088, China*
[4]*School of Materials Science and Engineering, Northeastern University, Shenyang 110819, China*

Correspondence should be addressed to Qinghe Yu; yuqh@grinm.com and Xiaopeng Liu; xpgliu@126.com

Received 10 November 2020; Revised 23 December 2020; Accepted 20 January 2021; Published 2 March 2021

Academic Editor: Qiang Fu

The Al/Al_2O_3 composite deuterium barrier was deposited on the polished side of 316 L stainless steel by the method of radio-frequency magnetron sputtering. The influence of the introduction of Al transition layer on the deuterium resistance performance of Al_2O_3 ceramic coating was studied. The field emission scanning electron microscope (SEM), the grazing incident X-ray diffraction technique (GIXRD), and the auger electron spectroscopy (AES) were used to analyze the microscopic morphology, phase, and element distribution in the depth direction of the Al/Al_2O_3 coating, and the gas-driver permeation method was used to measure the deuterium permeation behavior of the coating sample. The results show that Al_2O_3 is amorphous after annealing at 873 K. Due to the oxidation of the Al transition layer, the connection between the coating and the substrate is tightly connected. Under the combined action of permeation temperature and pressure of 873 K and 80 kPa, the deuterium permeability of Al/Al_2O_3 coating is 6.35×10^{-14} mol·m^{-1}·s^{-1}·Pa$^{-0.5}$, which shows that the Al/Al_2O_3 coating has excellent deuterium permeation resistance. Furthermore, deuterium permeability of the Al/Al_2O_3 coating was diminished by about 2 orders of magnitude compared with 316 L stainless steel, and it is reduced 2~3 times compared with the single Al_2O_3 coating sample. The study indicates that the introduction of the Al transition layer can significantly enhance the barrier effect of the Al/Al_2O_3 coating sample.

1. Introduction

Nuclear energy, as a clean energy source, has been received extensive attention in recent decades. For nuclear fusion reactions, deuterium and tritium with tiny atomic radius have the very strong permeability in metallic structure materials, which will lead to hydrogen embrittlement and surface corrosion of the materials. In fusion power plants, tritium with high radioactivity, as a fusion fuel, contacts directly with the inner wall of the vessels and pipes. The high permeation and leakage of tritium not only lead to waste of nuclear fuel but also could cause radioactive contamination to the surroundings. Therefore, the suppression of tritium permeation is required in the operation process. The preparation of tritium permeable barriers (TPBs) on the inner wall of metallic structural materials has been considered a promising solution. A large number of research show that the ceramic coatings, including Al_2O_3 [1–3], Y_2O_3 [4–6], Er_2O_3 [7–9], Cr_2O_3 [10], other metal oxide coatings, AlN [11] and Si_3N_2, other nitride coatings, TiC and SiC [12], and other carbide coatings and their composite coatings, have been demonstrated to be beneficial to reduce tritium permeation flow. Among these TPBs, the Al_2O_3 ceramic coating, as a promising candidate, has been attached much more attention because of its high permeation resistance performance, outstanding compatibility with Pb-Li, good thermal stability with irradiation and corrosion resistance, and excellent comprehensive properties [13–16]. However, the structure of Al_2O_3 ceramic coating is

not compact, there are microcracks being located in it, the internal stress is large, and when the coating is thicker, its bonding with substrate is not firm because of the characteristics of the ceramic material itself, making it unable to withstand the test of high temperature thermal shock cycle. By introducing Al metal transition layer, not only can the bonding force between the coating and substrate be enhanced but also the high temperature stability can be improved.

In this work, the Al/Al_2O_3 composite coating was deposited on the polished side of 316 L stainless steel by physical vapor deposition (PVD) and radio-frequency magnetron sputtering. The microstructure, phase, and element distribution in depth of the coating with before and after deuterium permeation measurement were separately investigated. More importantly, the influence of the introduction of the metal transition layer on the deuterium resistance of the Al_2O_3 ceramic coating and the permeation mechanism of deuterium in the Al/Al_2O_3 composite coating have been studied, which provide experimental support for subsequent coating design.

2. Experimental Details

2.1. Preparation of Samples. The disk-shaped 316 L stainless steel samples were cut from the mechanical polishing 316 L stainless steel plate with mechanical polishing. The samples size specification was $\Phi\, 29 \times 0.5$ mm. Before preparing the coating, the bare samples were orderly washed with acetone, deionized water, and absolute ethanol for 10 min in the ultrasonic cleaner. Then these samples were blown to be dry for use. The method of radio-frequency magnetron sputtering was used to deposit Al/Al_2O_3 composition coatings at room temperature on the one side of the mirror-polished 316 L stainless steel substrates. The Al_2O_3 ceramic target and Al metal target were chosen in this work. The base pressure is about 2×10^{-4} Pa in a magnetron sputtering chamber. When the Al transition coating was deposited, argon with a purity of 99.999% was introduced into the chamber, where the total gas pressure was maintained at the set point, that was ignited to the argon plasma with a power density of 4.98 $W{\cdot}cm^{-2}$ by radio-frequency power. The method of Al_2O_3 coating deposition is similar to the previous research, and the specific preparation process parameters were shown in the previous study [17]. Table 1 shows the specific process parameters by radio-frequency magnetron sputtering, which has a serious impact on the quality of coating. The coated samples were heat treated in vacuum tube furnace for 2 h at 873 K to eliminate inherent stress generated by the coating during the deposition process.

2.2. Permeation Flux Measurement. Tritium has strong radioactivity, and the abundant hydrogen in the atmosphere will affect the measurement results. Thus, deuterium was selected as the permeate gas. The deuterium permeation property was measured by the gas-driven permeation method. An experimental equipment was set up to carry out the permeation measurement in this work. The sample was sealed with two O-ring copper gaskets, whose inside diameter, outside diameter, and thickness were 17 mm, 29 mm, and 0.5 mm, respectively. The effective permeation area was calculated to be $1.43 \times 10^{-3}\, m^2$ by measuring impression of the seal gaskets on the sample after permeation measures. Prior to the measurement, the uncoated side of the samples was polished with an abrasive paper in order to remove the oxide layer, which ensured the accuracy of the experiment. The sample was mounted in a resistance furnace to maintain constant temperature. A thermocouple was inserted through a hole in order to directly contact with the sample room to monitor the sample temperature in real time. The measurement temperature range was between 773 K and 873 K. The specific experimental steps and process parameters were detailed in Ref. [17].

2.3. Characterization Methods. The microtopography of the Al/Al_2O_3 composite coating was observed by the field scanning electron microscope (SEM, Hitachi-S4800). The crystallographic properties of the composite coating were analyzed using Grazing incidence X-ray diffraction (GIXRD, SmartLab 9 kW), and the incidence angle was 3°. The element distribution in depth of the coating was analyzed by the auger electron spectroscopy (AES, PHI-700), and the sputtering rate was 15 nm/min.

3. Results and Discussion

3.1. Microstructure and Phase. Low deuterium permeation requires dense structure and integrity of the coatings [18, 19]. In the previous measurements, it was found that the thickness of the coating was basically similar when the coatings were deposited on the surface of the 316 L stainless steel and Si wafer for the same batch of samples. Therefore, the Si substrate sample was used to characterize the microstructure of the coating. The surface and cross-section morphology of the deposited Al/Al_2O_3 coating are shown in Figure 1. From the surface image (Figure 1(a)), the coating is compact and dense. There are no cracks and voids on the surface of the coatings. The composite layer with a fairly uniform thickness of 542 nm can be observed from Figure 1(b), of which the Al transition layer and Al_2O_3 ceramic coating have the thickness of 135 nm and 407 nm, respectively. The interface of Al/Al_2O_3 composite coating is clear, and the coating has good adhesion with substrate. However, due to different coating preparation methods in applications, there are differences in the optimal thickness range. But it must be ensured that the coating structure is dense and has good adhesion to the substrate.

Figure 2 shows the EDS spectrum of the element distribution along the depth direction and the element weight percent. It can be seen from Figure 2 that the Al element showed an increasing trend. When the scanning distance was 400 nm, reaching the Al metal transition layer, the Al element was basically stable, and the O element content dropped sharply. When scanning to the Si substrate, the content of Si increases, and the content of Al and O decreases. However, it can be seen from the element weight percent located in the lower right corner of Figure 2 that when the EDS was used to analyze the element content, it cannot be accurately detected because it is affected by the carbon

Table 1: The specific process parameters of coating preparation by radio-frequency magnetron sputtering.

Process parameters	Coating	
	Al	Al_2O_3
Target type	Metal	Ceramic
The target diameter (mm)	101.5	101.5
The target-substrate distance (mm)	75	75
The base pressure (Pa)	2×10^{-4}	2×10^{-4}
The sputtering power (W)	250	350
The sputtering power density ($W \cdot cm^{-2}$)	4.98	6.67
Coating deposition pressure (Pa)	0.5	0.5
Sputtering atmosphere and flow (sccm)	Ar (5 N) = 20	Ar (5 N): O_2 = 20 : 1
Coating deposition time (h)	0.5	6

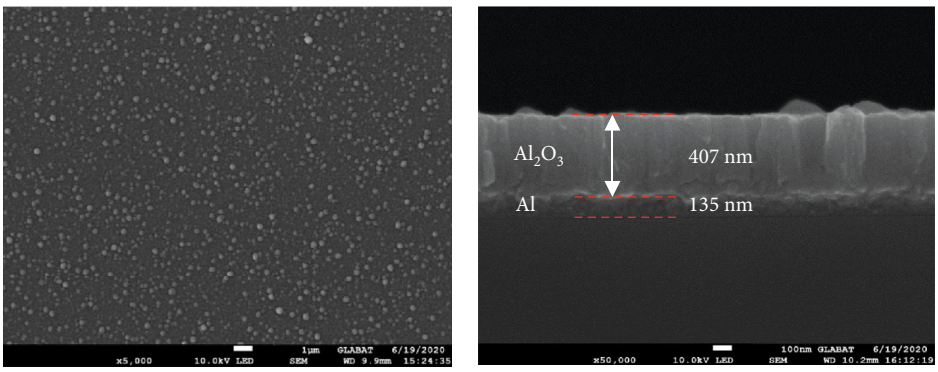

(a) (b)

Figure 1: SEM images of the Al/Al_2O_3 composite coating: (a) surface and (b) cross-sectional.

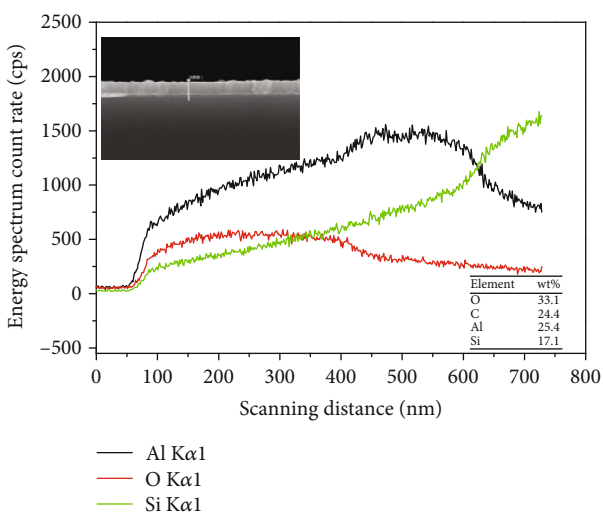

Figure 2: The AES spectrum of Al/Al_2O_3 coating in depth element distribution.

element. The subsequent element content test was carried out by AES.

In addition, the deuterium permeation properties of the coating are influenced on the crystal structure. The GIXRD spectra of Al/Al_2O_3 composite coating are shown in Figure 3, which includes three different state spectra, respectively, the deposited, the annealed, and the deuterium permeation measured. The peaks of the crystalline Al_2O_3 were not observed, which indicated that the coating was still amorphous after the 873 K high temperature measurement. However, compared with the deposited samples, the peaks corresponding to the (111) and (311) orientations of the Al metal transition layer disappeared, indicating that the Al metal transition layer was oxidized during the permeation measurement process. Comparing the annealed and deuterium penetration measured samples, there is no new diffraction peak in the XRD spectrum, which indicates that the coating structure has basically reached a stable state after the high temperature anneal. Besides, the peaks marked with solid circles in the spectra correspond to the diffraction peaks of the 316 L stainless steel substrate.

3.2. Element Distribution. Figure 4 shows the element distribution along the depth direction of the Al/Al_2O_3 in three different states. The coating surface was etched for 5 nm before the measurement in order to avoid surface contamination. For the deposited coating, the atomic ratio of Al : O was about 1.4 in the top Al_2O_3 layer, which was slightly less than the stoichiometric ratio of 1.5. In the bottom metal transition layer, the content of O element became almost zero, and the content of Al element increased significantly. After

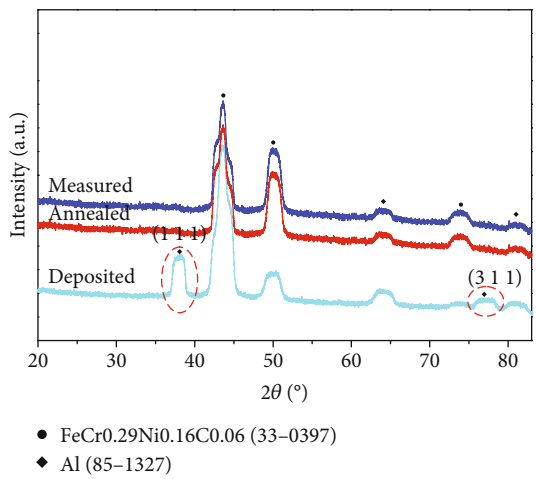

Figure 3: GIXRD spectra of the deposited, annealed and measured Al/Al_2O_3 composite coatings.

873 K anneal treatment, it can be seen from Figure 4(b) that the metal transition layer was completely oxidized to form Al_2O_3 coating. In addition, the atomic ratio of Al : O was 1.5, which met the stoichiometric. It can be seen that the atomic ratio of Al : O remains stable and is fairly constant throughout the coating after deuterium penetration measurement at the 773 K-873 K. Compared with the annealed coating and deuterium permeation measured coating, the atomic ratio of Al and O remained unchanged, so it was considered that the structure of the coating tends to be stable after annealing at 873 K, which is consistent with the analysis result of GIXRD in Figure 3. It is found that the thickness of the measured Al_2O_3 coating sample increases by about 50 nm compared with the annealed. The main reason is that the thickness of the diffusion layer between the coating and the substrate decreases due to the more complete oxidation of the Al element in high temperature, which can be seen from the decreasing slope of the O element.

The comprehensive analysis of the GIXRD and AES test results shows that the deposited coating is composed of an Al metal transition layer and an Al_2O_3 coating, and the coating interface is obvious. After 873 K annealing treatment, the Al metal transition layer was oxidized, but the coating was not completely oxidized because the Al metal phase was present in the coating. After 773 K-873 K high temperature deuterium permeation measurement, the Al metal transition layer disappears, the coating was completely oxidized, and the coating structure tended to be more stable.

3.3. Measurement of Deuterium Permeation. The permeability, as the most important factor in evaluating the quality of permeation barriers, was measured. It is noted that 3 to 5 samples are prepared per batch. To ensure the reliability and repeatability of the experimental data, at least three samples were used to measure deuterium resistance, and the average value was taken as the experimental value of permeability. Figure 5 shows the relationship curve of the deuterium ion flow through the Al/Al_2O_3 composite coating sample with permeation time at 773 K-873 K. It can be seen from the curve in Figure 5 that the deuterium ion flow increased with increasing permeation temperature. The process of deuterium permeation was divided into two states, namely the permeation state and the steady state. For the permeation state, the slope of the curve represents the sensitivity of the coating to deuterium permeation. In terms of the curve of 773 K, its slope was not remarkable and the deuterium ion current changed slightly during the entire process. But the slope increased as the permeation temperature goes up. Because the temperature increases, the movement of deuterium atoms intensifies, which leads to an increase in the permeation ion current and a shorter time to arrive the steady state. The results show that the sensitivity of the coated samples to deuterium is enhanced at high temperatures.

Figure 6 displays the relationship curves between the logarithm of deuterium permeability and the inverse temperature for the Al/Al_2O_3 coating samples and the bare 316 L stainless steel substrate [10], and Al_2O_3 single coating samples are given in order to contrast. The logarithm of deuterium permeability changes linearly with the increase of permeation temperature at 773 K-873 K, which satisfies Arrhenius law. Compared with the bare 316 L stainless steel, the deuterium permeability of the Al/Al_2O_3 coating sample was decreased by about 2 orders, and it is reduced 2~3 times compared with the single Al_2O_3 coating sample. During the high temperature annealing process at 873 K, the metal Al layer was fully oxidized, which improves the tightness of the connection between the coatings, and it is beneficial to the release of high temperature thermal stress. Therefore, the densification of the coating structure can improve the deuterium resistance performance, and the high temperature stability can extend the service life of the coating to a certain extent.

With the permeation of deuterium in materials, it acts as a thermal activation process in a certain temperature range which satisfies the Arrhenius' equation [20].

$$P = P_0 \times e\left(-\frac{E_a}{RT}\right), \tag{1}$$

where P_0 is the permeation frequency factor ($mol \cdot m^{-1} \cdot s^{-1} \cdot Pa^{-n}$); E_a is the permeation activation energy ($J \cdot mol^{-1}$); R is the gas constant, equal to $8.314\, J \cdot mol^{-1} \cdot K^{-1}$; and T is the deuterium permeation temperature (K). Taking the logarithm of both sides of formula (1), formula (2) can be obtained. It can be seen from formula (2) that the logarithm of the permeability has a linear relationship with the reciprocal of the temperature, which verifies the accuracy of the experimental data in Figure 6.

$$\ln P = \ln P_0 - \frac{E_a}{RT}. \tag{2}$$

Levchuk et al. [21] prepared the Al-Cr-O thin coating as a deuterium permeation barrier on Eurofer. The results showed that deuterium permeability of the Al-Cr-O film was 1/3500~1/2000 of the Eurofer at 973 K. It is noted that

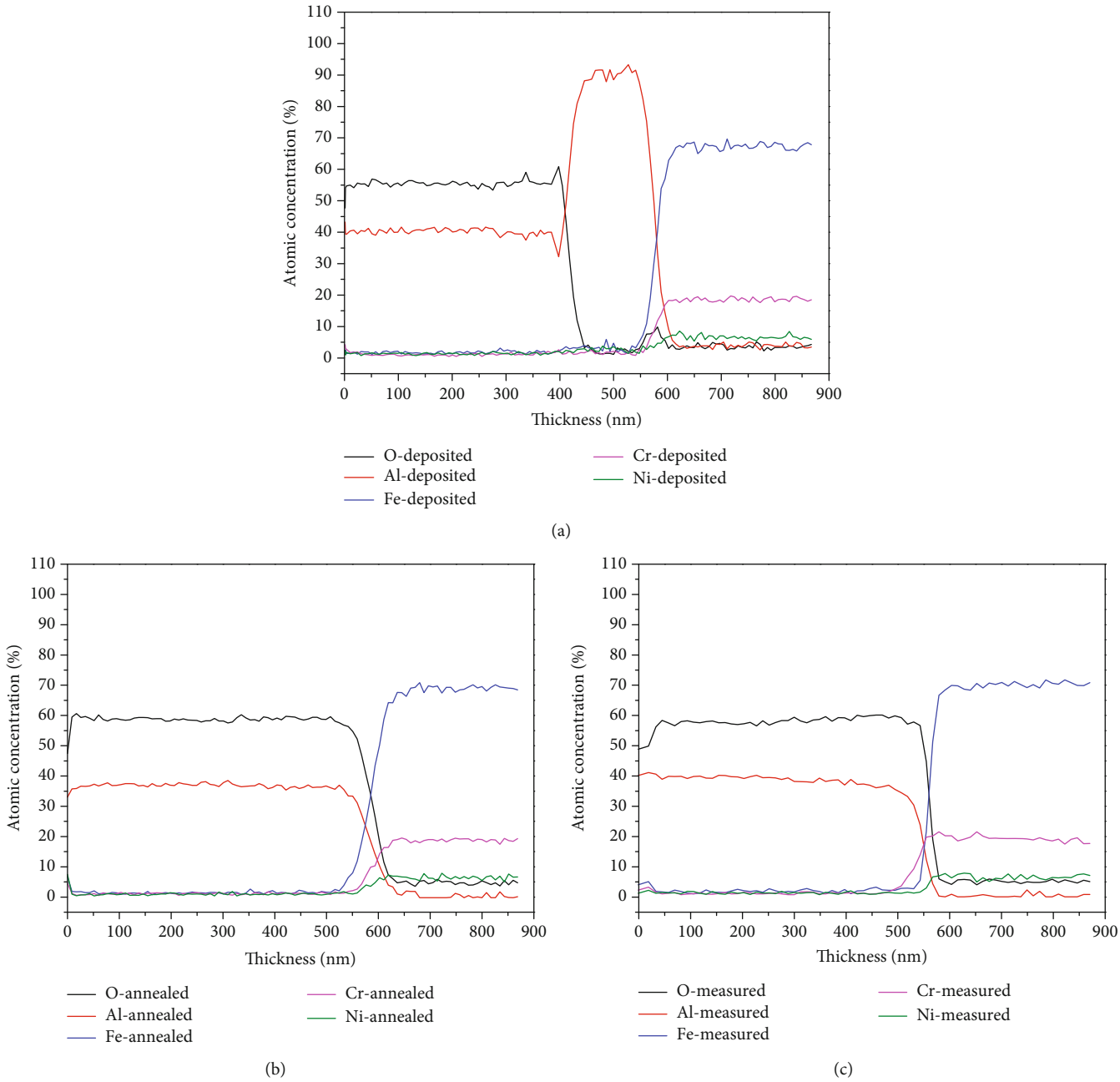

Figure 4: AES depth profile of the Al/Al_2O_3 composite film: (a) the deposited Al/Al_2O_3, (b) the annealed Al/Al_2O_3, and (c) the coating after deuterium permeation measured.

the deuterium permeability of the Al/Al_2O_3 coating in this work is not the best, compared with literature reports [15–21, 22]. The main reason is that the crystalline state of the coating has a certain impact on the deuterium resistance performance [7, 15]. The researches have shown that the coating has a good and stable crystalline state, then its deuterium resistance performance is stronger [15, 23], but the Al_2O_3 layer is amorphous in this work. Therefore, under the premise of ensuring the density and structural integrity of the coating, increasing the coating deposition temperature and subsequent heat treatment is aimed at obtaining crystalline Al_2O_3 coating in the next study.

4. Conclusion

Microstructure analyses and deuterium permeation experiments were carried out for the bare 316 L stainless steel and the Al/Al_2O_3 coating samples prepared by radio-frequency magnetron sputtering. The Al_2O_3 coating of Al/Al_2O_3 composite coating was found to be amorphous by GIXRD. The coating was deposited densely, without cracks, holes, peeling, and other microscopic defects. In the direction perpendicular to the substrate, the interface between the metal transition layer and the Al_2O_3 ceramic layer was clear and tightly connected for the deposited

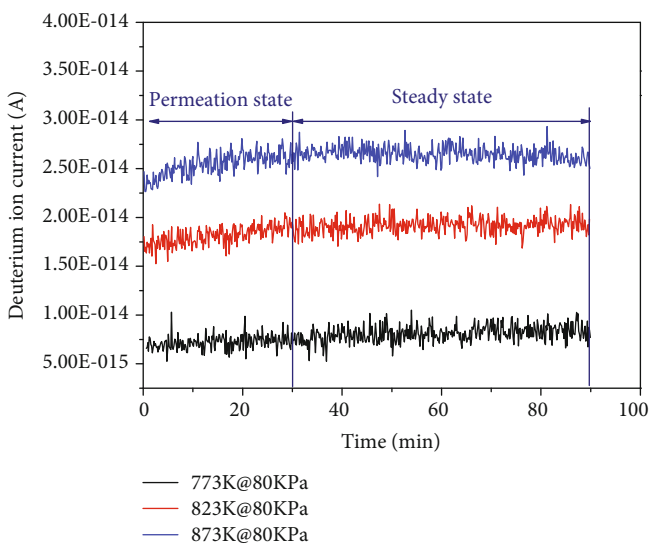

Figure 5: Deuterium ion current of Al/Al_2O_3 samples with different permeation temperature.

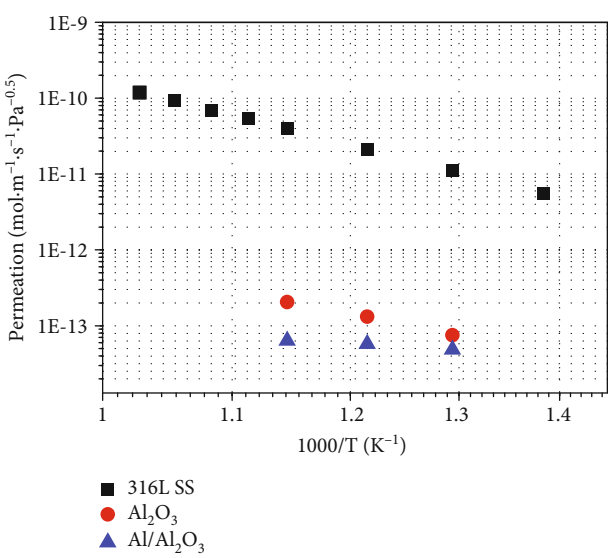

Figure 6: Deuterium permeability through the Al/Al_2O_3 coating and bare 316 L stress steel as a function of the permeation temperature. The test deuterium permeation pressure is 80 kPa.

coating. The total thickness of the coating was 542 nm. After annealing at 873 K, the metal transition layer was oxidized and transformed into Al_2O_3 coating. The chemical composition of the coating remains stable before and after the deuterium penetration measurement. The deuterium permeation experiments of the coating show that the deuterium permeability of the Al/Al_2O_3 coating was decreased by about 2 orders of magnitude compared with 316 L stainless steel, and it is reduced 2~3 times compared with the single Al_2O_3 coating sample. With the stable structure and the low permeability, the Al/Al_2O_3 film could be considered a promising tritium permeation barrier for blanket application in nuclear fusion reactions.

Data Availability

Some of the data used in this study are included within the article, and the rest are derived from the references that have been cited in the article.

Conflicts of Interest

The authors declare that there is no conflict of interest regarding the publication of this paper.

Acknowledgments

This work was supported by the National Natural Science Foundation of China (NSFC, 51671034) and the National Key Research and Development Program of China (grant number 2016YFB0600103 and grant number 2016YFB0600102-5).

References

[1] K. Takahiro, U. Kazuyuki, and O. Atsushi, "Atomic and electronic structures of α -Al_2O_3 surfaces," *Physical review*, vol. 82, pp. 155319.1–155319.14, 2010.

[2] A. B. Belonoshko, A. Rosengren, Q. Dong, G. Hultquist, and C. Leygraf, "First-principles study of hydrogen diffusion inα–Al2O3and liquid alumina," *Physical review B*, vol. 69, no. 2, pp. 204302–1-024302-6, 2004.

[3] S. Li, D. He, X. Liu, S. Wang, and L. Jiang, "Deuterium permeation of amorphous alumina coating on 316L prepared by MOCVD," *Journal of Nuclear Materials*, vol. 420, no. 1-3, pp. 405–408, 2012.

[4] T. Chikada, H. Fujita, J. Engels et al., "Deuterium permeation behavior and its iron-ion irradiation effect in yttrium oxide coating deposited by magnetron sputtering," *Journal of Nuclear Materials*, vol. 511, pp. 560–566, 2018.

[5] T. Chikada, T. Tanaka, K. Yuyama et al., "Crystallization and deuterium permeation behaviors of yttrium oxide coating prepared by metal organic decomposition," *Nuclear Materials and Energy*, vol. 9, pp. 529–534, 2016.

[6] Y. Y. Wu, D. He, S. Li, X. Liu, S. Wang, and L. Jiang, "Microstructure change and deuterium permeation behavior of the yttrium oxide coating prepared by MOCVD," *International Journal of Hydrogen Energy*, vol. 39, no. 35, pp. 20305–20312, 2014.

[7] T. Chikada, A. Suzuki, T. Kobayashi, H. Maier, T. Terai, and T. Muroga, "Microstructure change and deuterium permeation behavior of erbium oxide coating," *Journal of Nuclear Materials*, vol. 417, no. 1-3, pp. 1241–1244, 2011.

[8] S. Horikoshi, J. Mochizuki, Y. Oya, and T. Chikada, "Deuterium permeation and retention behaviors in erbium oxide-iron multilayer coatings," *Fusion Engineering and Design*, vol. 124, pp. 1086–1090, 2017.

[9] T. Chikada, H. Fujita, M. Matsunaga et al., "Deuterium permeation behavior in iron-irradiated erbium oxide coating," *Fusion Engineering and Design*, vol. 124, pp. 915–918, 2017.

[10] D. He, S. Li, X. Liu et al., "Preparation of Cr_2O_3 film by MOCVD as hydrogen permeation barrier," *Fusion Engineering and Design*, vol. 89, no. 1, pp. 35–39, 2014.

[11] J. Wang, Q. Li, Q. Y. Xiang, and J. L. Cao, "Performances of AlN coatings as hydrogen isotopes permeation barriers," *Fusion Engineering and Design*, vol. 102, pp. 94–98, 2016.

[12] T. Chikada, A. Suzuki, and T. Terai, "Deuterium permeation and thermal behaviors of amorphous silicon carbide coatings on steels," *Fusion Engineering and Design*, vol. 86, no. 9-11, pp. 2192–2195, 2011.

[13] W. Krauss, J. Konys, and S. E. Wulf, "Corrosion barriers processed by Al electroplating and their resistance against flowing Pb-15.7Li," *Journal of Nuclear Materials*, vol. 455, no. 1-3, pp. 522–526, 2014.

[14] T. Wang, J. Pu, C. Bo, and L. Jian, "Sol-gel prepared Al_2O_3 coatings for the application as tritium permeation barrier," *Fusion Engineering and Design*, vol. 85, no. 7-9, pp. 1068–1072, 2010.

[15] D. Levchuk, F. Koch, H. Maier, and H. Bolt, "Deuterium permeation through Eurofer and α-alumina coated Eurofer," *Journal of Nuclear Materials*, vol. 328, no. 2-3, pp. 103–106, 2004.

[16] G. W. Hollenberg, E. P. Simonen, G. Kalinin, and A. Terlain, "Tritium/hydrogen barrier development," *Fusion Engineering and Design*, vol. 28, no. 1-2, pp. 190–208, 1995.

[17] W. Wang, Q. Yu, X. Liu, and Z. Lu, "Preparation of Al_2O_3/Y_2O_3 composite coating for deuterium permeation reduction," *Journal of Rare Earths*, vol. 38, no. 11, pp. 1237–1242, 2020.

[18] Z. Bojan, "Hydrogen permeation barrier–recognition of defective barrier film from transient permeation rate," *International Journal of Hydrogen Energy*, vol. 36, pp. 7353–7361, 2011.

[19] A. Pisarev, I. Tsvetkov, and S. Yarko, "Hydrogen permeation through membranes with cracks in protection layer," *Fusion Engineering and Design*, vol. 82, no. 15-24, pp. 2120–2125, 2007.

[20] R. F. Miller, J. B. Hudson, and G. S. Ansell, "Permeation of hydrogen through alpha iron," *Metallurgical Transactions A*, vol. 6, no. 1, pp. 117–121, 1975.

[21] D. Levchuk, H. Bolt, M. Döbeli, S. Eggenberger, B. Widrig, and J. Ramm, "Al-Cr-O thin films as an efficient hydrogen barrier," *Surface and Coatings Technology*, vol. 202, no. 20, pp. 5043–5047, 2008.

[22] P. J. Mcguiness, M. Čekada, V. Nemanič, B. Zajec, and A. Rečnik, "Hydrogen permeation through TiAlN-coated Eurofer '97 steel," *Surface and Coatings Technology*, vol. 205, no. 8-9, pp. 2709–2713, 2011.

[23] D. Levchuk, F. Koch, H. Maier, and H. Bolt, "Gas-driven deuterium permeation through Al_2O_3 coated samples," *Physica Scripta*, vol. T108, pp. 119–123, 2004.

Hindawi
International Journal of Photoenergy
Volume 2021, Article ID 6623776, 8 pages
https://doi.org/10.1155/2021/6623776

Research Article

Fabrication of SiC@Cu/Cu Composites with the Addition of SiC@Cu Powder by Magnetron Sputtering

Zhang Yunlong,[1,2] **Li Wenbo**,[1,2] **Hu Ming**,[1] **Yi Hongyong**,[1] **Zhou Wei**,[2] **Ding Peiling**,[1] **and Tang Lili**[1]

[1]*College of Materials Science & Engineering, Jiamusi University, Jiamusi 154007, China*
[2]*Anyang Institute of Technology, Anyang 455000, China*

Correspondence should be addressed to Hu Ming; huming1962@126.com and Yi Hongyong; yidianskate@163.com

Received 26 October 2020; Revised 24 January 2021; Accepted 17 February 2021; Published 26 February 2021

Academic Editor: Jinlong Liu

In view of the surface engineering application of electrical contact materials, SiC ceramic particles were introduced into copper matrix composites by the hot-press sintering method for the sake of enhancing the service life of copper matrix electrical contact materials. Magnetron sputtering technology was exploited to form the continuous copper film on the β-SiC powders in order to improve interface wettability between SiC powder and copper matrix. The SiC@Cu powders were treated by magnetron sputtering technology. Then, dynamic deposit behavior was described according to SEM results. The phase constitution, fracture morphology, relative density, porosity, Vickers hardness, and coefficient of thermal expansion of SiC@Cu/Cu composites with different SiC@Cu addition were analyzed in detail. The results showed that SiC@Cu powders with higher fraction in the SiC@Cu/Cu composites would decrease relative density and increase porosity, so it resulted in improvement of Vickers hardness. The addition of SiC@Cu decreased CTE values of the SiC@Cu/Cu composite, especially at high-level fraction SiC@Cu powder.

1. Introduction

Electrical contact material was one of the most important materials of the current transmission and conversion process, which was the core component and key surface engineering material. Electrical contact material had wider applications including motor, switches, relays, and connectors. These basic components of electrical contact were extensively applied in the field of information engineering, household electrical appliances, automotive engineering, and so on. The main performance of the above-mentioned electrical contact device would directly affect the reliability, stability, accuracy, and service life. Recently, the tendency of high precision and miniaturization for the various types of electrical contact devices was developed to meet higher performance requirement. Electrical contact devices should possess predominant performance such as better electrical resistivity and contact resistance, low density, high hardness, chemical composition, anticorrosion, connectivity, and structure reliability [1, 2].

The material properties determined the breaking capacity and reliability of an electric contact switch. The electrical contact material was the traditional noble metal (for Ag, Au, and Pt) and their alloys. However, the shortcoming such as high cost and shorter service life limited the wider application for these kinds of electrical contact materials. Compared with Ag system alloys, the copper series alloys had more superior high-temperature performance. In view of the surface engineering application of copper matrix electrical contact materials, SiC ceramic particles were introduced into the copper matrix in order to improve the hardness and friction resistance, whereas it was difficult to resolve the weak wettability between the SiC reinforcement and copper matrix, which limited the wider application scope of copper composites [3, 4]. Recently, the surface modification technologies were developed to improve the interface binding properties,

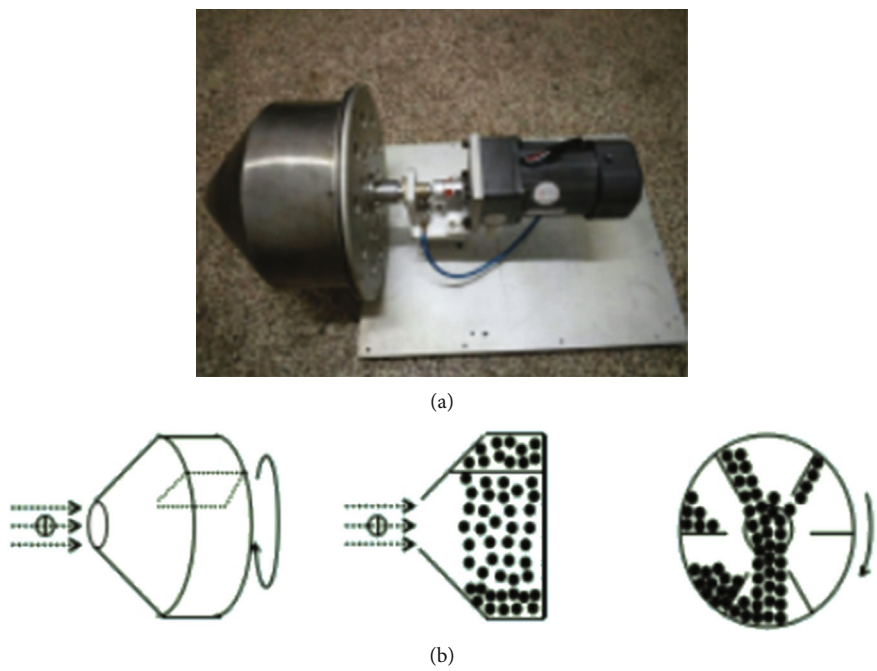

Figure 1: The physical picture self-designed carrier (a) and schematic diagram of the magnetron sputtering process (b).

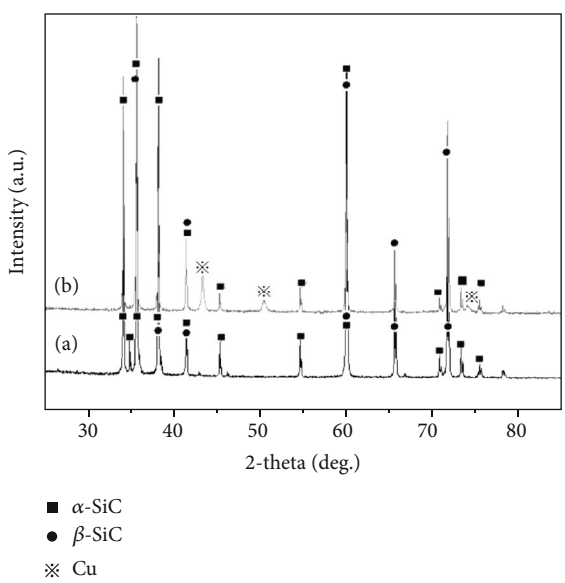

Figure 2: XRD curve of SiC particles and SiC@Cu powder: (a) XRD curve before magnetron sputtering and (b) XRD curve after magnetron sputtering.

for example, electroless plating, sol-gel and plasma modification, and magnetron sputtering [5–9]. At present, the magnetron sputtering deposition method was widely investigated as an important surface modification method. The magnetron sputtering technology was investigated to form the thin coating and/or films on the different substrate materials [10]. However, the reports about magnetron sputtering films on the surface of SiC ceramic particles were scarce. For the sake of enhancing the service life of copper matrix electrical contact materials, we attempt to utilize magnetron sputtering technology to obtain the copper film on the surface of the SiC particle (abbreviation "SiC@Cu"). High-volume fraction SiC@Cu powder in the Cu matrix composites had attracted much attention in thermal management application, which exhibited high thermal conductivity, low thermal expansion, excellent mechanical properties, and better wear resistance [11, 12]. Hot pressing sintering route was a main adopted technique in order to obtain the more dense SiC@Cu/Cu hybrid materials.

In the present investigation, we put focus on the preparation of SiC@Cu powders with copper coating by means of the magnetron sputtering method. The preliminary result was reported by the previous article [13]. Other target was aimed at fabricating SiC@Cu/Cu composites with different SiC@Cu volume fractions. The influence of SiC@Cu fraction on the thermal physical properties of the SiC@Cu/Cu composites was analyzed. The SiC@Cu/Cu composites were fabricated at 750°C for 1 h by the hot-press sintering method. The phase constitution, fracture and surface morphology, relative density, porosity, Vickers hardness, and coefficient of thermal expansion of the SiC@Cu/Cu composites with different SiC@Cu volume fractions were observed and analyzed in detail.

2. Material Fabrication and Characterization

The magnetron sputtering equipment was used to generate copper films on the surface of the SiC particle. The target material used for sputtering was Cu target (purity 99.999%) with a diameter of 100mm and a thickness of 5mm. The target material was placed on the target frame connected with the cooling circulating water device. The self-designed circular carrier was used to load SiC powder and was put on the holder. The physical picture and schematic diagram of the

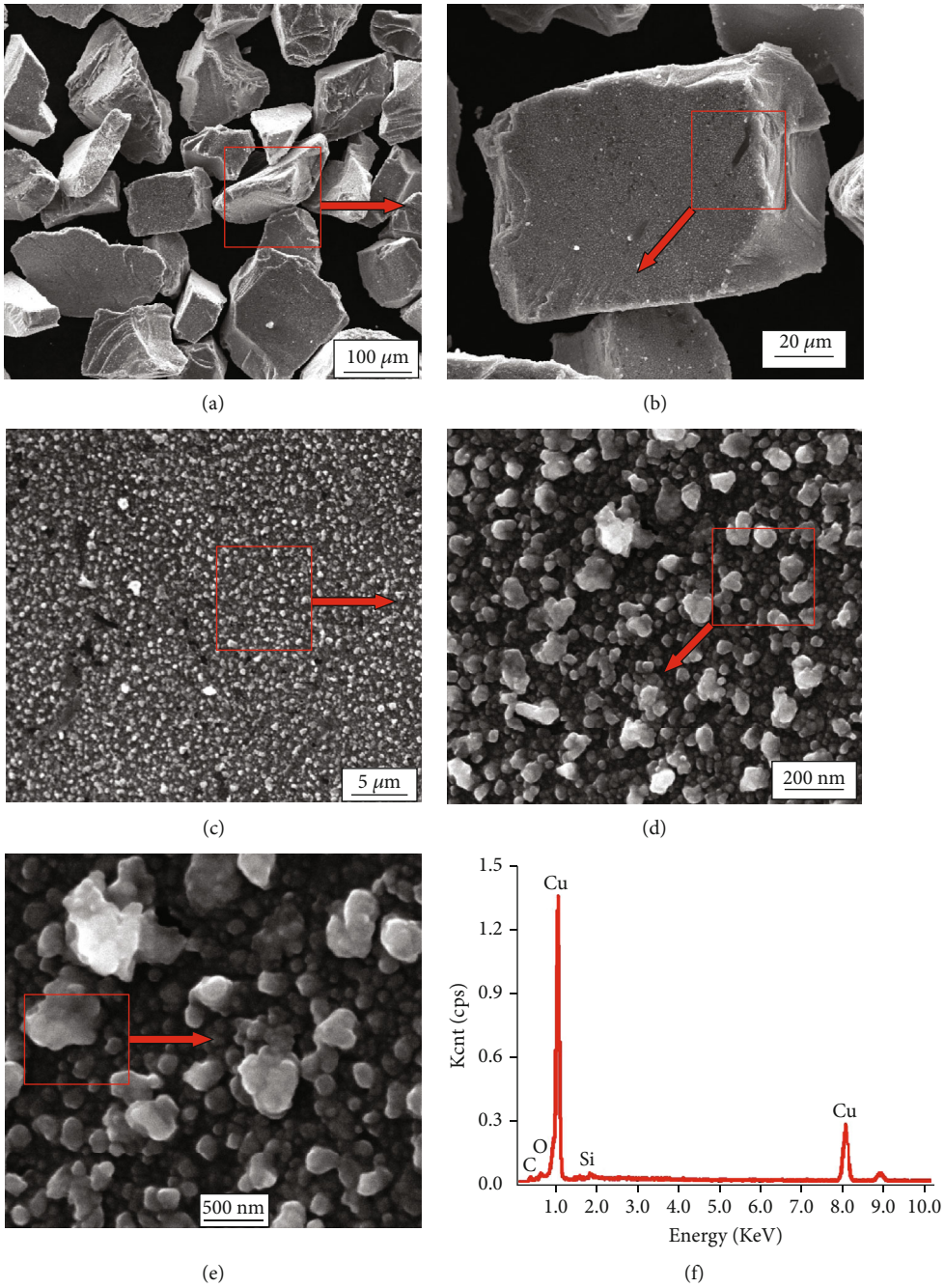

Figure 3: Morphology of the copper film on β-SiCp after magnetron sputtering was formed. β-SiCp with the copper film at low magnification (a) and high magnification (b–e) and energy pattern (f).

self-designed carrier are shown in Figure 1. By adjusting the swing frequency of the specimen holder and the vibration power of the ultrasonic wave, SiC powder can roll horizontally and vibrate vertically to ensure that the surface of each particle can be coated with a copper film evenly. β-SiC powders ($D_{50} = 78\mu$m) were set into the loading powder container, and the target distance was about 150mm. The vacuum pressure was suction filtration to 10^{-3}Pa. The argon gas was introduced into reaction equipment with flow 20 sccm, and puttering pressure was about 1.0Pa. Sputtering power was set as 370W and sputtering time set as 90 min. The temperature was controlled in the scope of 25~150°C. The sample holder with low-frequency swing and ultrasonic wave with high-frequency oscillation were applied to ensure uniform distribution of the copper film on the surface of SiC particles. SiC powders with the Cu film were defined as SiC@Cu powders. The nitric acid impregnation method was applied to calculate the gained copper weight on SiC@Cu powders. After calculation, gained copper weight on the sputtered powders was about 2.2%. SiC@Cu powders and copper powders were mixed by ball milling equipment. The volume ratio of SiC@Cu powders to total mixed powders

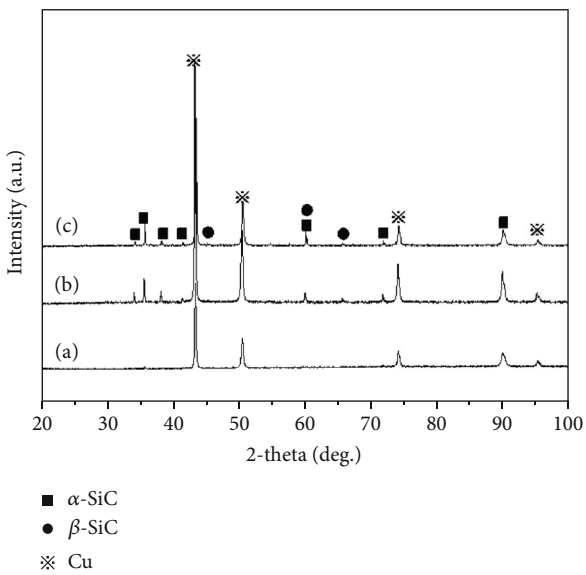

Figure 4: XRD curve of SiC@Cu/Cu composites. (a), (b), and (c) presented the SiC@Cu volume fraction with 10%, 30%, and 50%.

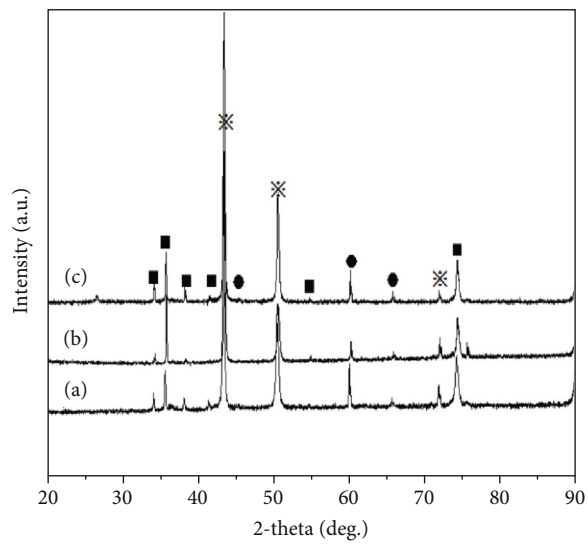

Figure 5: XRD curve of SiC_p/Cu composites with different SiC_p fractions without magnetron sputtering. (a), (b), and (c) presented the SiC_p volume fraction with 10%, 30%, and 50%.

was adjusted as 0%, 10%, 20%, 30%, 40%, and 50%, and the above specimen was named as S0, S10, S20, S30, S40, and S50 ("S" was the abbreviation of "specimen"). The ball milling speed was 300 r/m, and the time was set as 8 h. Prior to the sintering process, the mixture powders was cold-pressed into a cylindrical compact in a metal die of 40 mm in diameter with pressure of 200 MPa. SiC@Cu/Cu composites were sintered at 750°C for 60 min in a multifunctional hot-pressing sintering furnace with argon gas protection, and the heating rate was about 20°C/min. The sintered SiC@Cu/Cu composites were cut into 3 mm × 3 mm × 4 mm for morphology observation. The phase composition of SiC powders and SiC@Cu/Cu composites was identified by X-ray diffraction (D8 Advance, Germany). The scanning speed was 4°/min, and the step length was 0.02°. The morphology of SiC powders with copper films was observed by SEM (Hitachi S4700). Relative densities were calculated according to Archimedes' principle. To determine the microhardness of SiC@Cu/Cu composites, the Vickers indentor was applied with a load of 196 N for 15 s on the polished surface by using a hardness testing machine. The thermal expansion tester (Netzsch-DIL402C) was selected to survey the CTE of SiC@Cu/Cu composites, and the measuring temperature was varied in 25°C~00°C; then, the average value of CTE was obtained. As a comparative test analysis, SiC particles without magnetron sputtering were directly introduced into the copper matrix with volume fractions of 10%, 20%, 30%, 40%, and 50%, respectively, which were named as RS10, RS20, RS30, RS40, and RS50 ("RS" was the abbreviation of "received specimen"). The sintering process and result characterization process were the same as above.

3. Result and Discussion

The XRD curve of SiC powders before magnetron sputtering deposition is shown in Figure 2(a). As seen from original SiC powder, the β-SiC phase can be detected. At the same time, the α-SiC phase can be detected. The possible reason was that the phase of received powder was made up of the β-SiC phase and α-SiC phase. After magnetron sputtering deposition, SiC@Cu powders can be detected in Figure 2(b). The high sputtering yield of copper can be obtained, and the high deposition rate was gained by adjusting sputtering parameters such as temperature, time, and sputtering power. It is worth noting that obvious copper aggregate structure was detected as the sputtering power and/or matrix temperature was too high. So it was beneficial for acquiring uniform and suitable film thickness for copper on the SiC surface by adjusting appropriate magnetron sputtering parameters.

The surface morphology of SiC@Cu powder is illustrated in Figure 3. It needs to be stressed that the growth rate of the copper film on the SiC_p surface in the motion process was similar to that on the flat substrate. The copper film was composed of bigger grains and smaller grains. It was interesting that vast bigger grains were composed of dozens of smaller grains with tens of nanometers, whose shape was the same as an isolated island. The size of "Volmer-Weber" grains was about 200~500 nm. The nucleation rate of copper formation and growth rate of nuclear island enhanced as the sputtering time increased. The higher temperature of SiC powders improved diffusion capacity of copper atoms, and it was beneficial for the formation of the thicker copper film. The process and growth mechanism of magnetron-sputtered copper films had been discussed in reference [14].

The phase constitutions of SiC@Cu/Cu composites with different SiC@Cu fractions after magnetron sputtering are illustrated in Figure 4(a), (b) and (c) in Figure 4 present the volume fraction of SiC@Cu with 10%, 30%, and 50%. The main phase for SiC@Cu/Cu composites was the α-SiC, β-SiC, and Cu phase. The initial pure copper was tested as shown in Figure 4(a). It was seen from Figure 4(b) and (c) that there was no other component except Cu and SiC in the SiC@Cu/Cu composites.

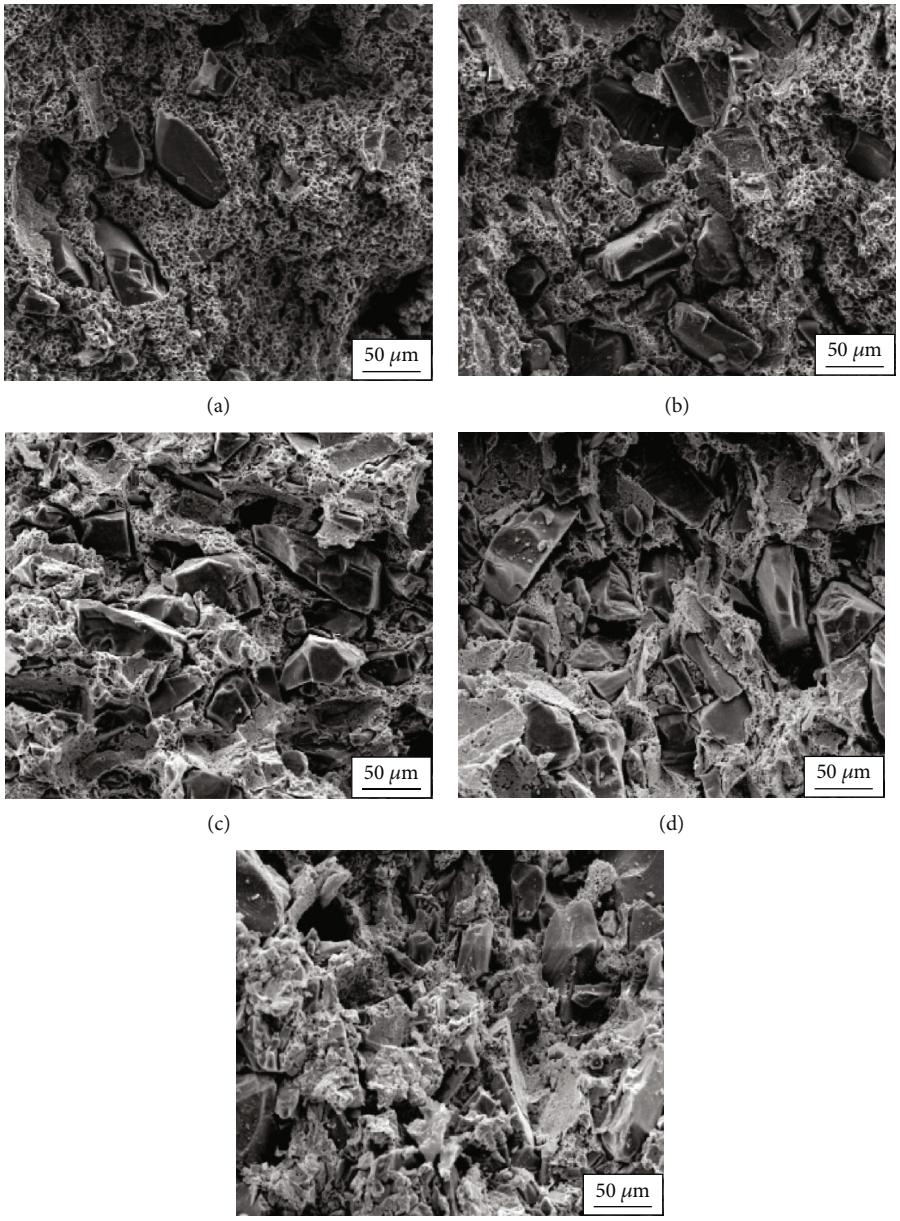

Figure 6: Fracture surface of SiC@Cu/Cu composites with different SiC@Cu fractions: (a–e) SiC@Cu fraction with 10%, 20%, 30%, 40%, and 50%.

Table 1: Vickers hardness and relative density of the SiC@Cu/Cu composite.

Specimen	S0	S10	S20	S30	S40	S50
Relative density	99.6%	98.8%	98.1%	97.7%	97.2%	96.5%
Vickers hardness (kgf/mm^2)	35 ± 2.4	62 ± 2.5	74 ± 2.6	95 ± 2.4	108 ± 3.2	132 ± 2.7

Table 2: Vickers hardness and relative density of the SiC_p/Cu composite.

Specimen	RS10	RS20	RS30	RS40	RS50
Relative density	98.4%	97.8%	97.2%	96.9%	96.3%
Vickers hardness (kgf/mm^2)	56 ± 3.2	70 ± 2.6	92 ± 2.8	101 ± 3.1	125 ± 3.5

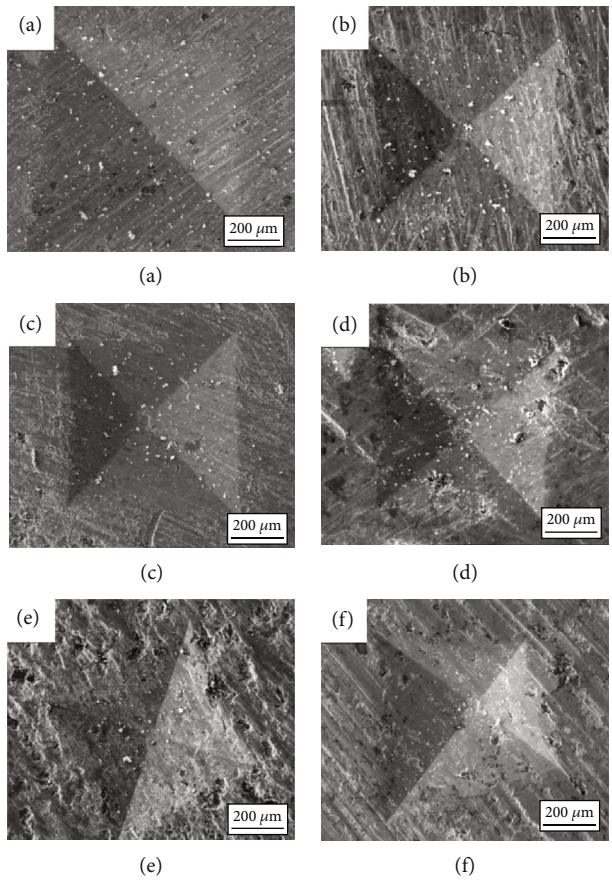

Figure 7: Vickers indentation of the SiC@Cu composites with different SiC@Cu fractions.

Figure 5 displays the XRD curve of SiC_p/Cu composites with different SiC_p fractions. Figure 5(a)–(c) present the SiC_p fraction with 10%, 30%, and 50%. SiC peaks became clear with the increasing SiC_p fraction. As a contrast specimen, XRD results of SiC_p/Cu composites with the same amount of SiC added showed the same phase composition and similar diffraction peaks. Under the same addition amount of SiC, the diffraction peak strength of SiC in the SiC hybrid copper-matrix composites without magnetron sputtering was slightly enhanced. The possible reason was that the copper film effect of the SiC surface was more uniform after magnetron sputtering treatment, so the bonding role between the SiC@Cu powder and copper matrix became stronger in the sintering process. The content of SiC on the exposed surface was relatively low after grinding and polishing before detection. Therefore, the diffraction peak intensity was lower.

The fracture surface of SiC@Cu/Cu composites with different SiC@Cu fractions is shown in Figure 6. As the SiC@Cu fraction was lower than 20%, the ductile rupture at the copper matrix was mainly the fracture mechanism. As the SiC@Cu fraction was higher than 30%, the ductile rupture at the copper matrix and debonding of the SiC/Cu interface were mainly the fracture behaviors. As the SiC@Cu fraction was higher than 30%, more SiC@Cu particles can be seen on the fracture surface. Pulling out of SiC particles and big dimples was clearly found on the fracture surface. Then, SiC@Cu/Cu composites exhibited a brittle fracture mechanism. Some SiC particles gathered with pores were observed. It was revealed that interfacial bond was weak in the near pore region. It can be concluded that weaker bonding strength of the SiC/Cu interface was the primary factor, which was responsible for relatively low flexural strength. Debonding of the SiC/Cu interface was lessened and particle pulling out from copper matrix was not obvious on the fracture surface. Severe ductile deformation in the copper matrix was the main fracture mechanism of SiC@Cu/Cu composites with a lower SiC@Cu fraction.

Test results of relative density and Vickers hardness of SiC@Cu/Cu composites are listed in Table 1. The relative density decreased with the volume fraction of SiC@Cu increasing. For all SiC@Cu composites, relative density was higher than 96%. Even if the SiC@Cu fraction reached 50%, the relative density was about 96.5%. In the SiC@Cu composite with a lower SiC@Cu volume fraction, less interface between Cu and SiC@Cu meant less copper atom diffusion barrier and copper atoms diffused conveniently and filled the interstices between SiC particles; then, it resulted in higher densification. So it can draw to a conclusion that the hot-press sintering method was effective to fabricate compact SiC@Cu/Cu composites. The Vickers hardness of SiC@Cu/Cu composites increased as the volume fraction of SiC@Cu powders increased. The Vickers hardness of sintered pure copper was about 35 kgf/mm^2. When the volume fraction of SiC@Cu reached 50%, the Vickers hardness of

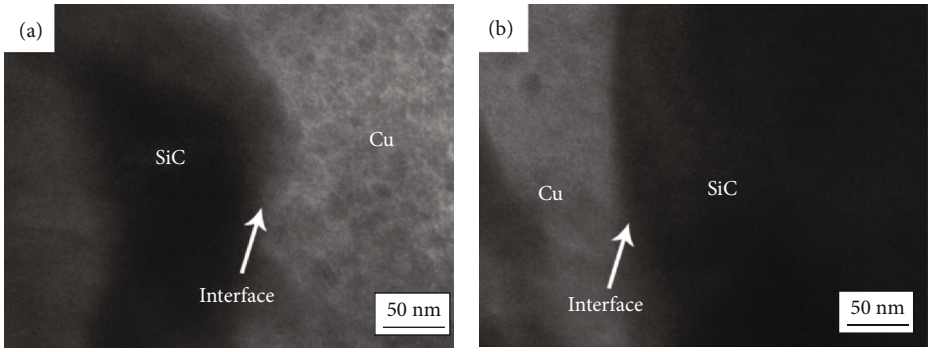

(a) (b)

Figure 8: TEM photo of SiC@Cu/Cu composites: (a) 10% SiC@Cu and (b) 30% SiC@Cu.

SiC@Cu/Cu composites was nearly 132 kgf/mm^2. Therefore, introduction of SiC@Cu improved the Vickers hardness of the SiC@Cu/Cu composite, especially at the high fraction of SiC@Cu powder.

Test results of relative density and Vickers hardness of SiC_p/Cu composites with different fractions of SiC_p are shown in Table 2. The relative density decreased with the volume fraction of SiC_p increasing. The relative density varied in the range of 96.3% and 98.4%. The microhardness corresponding to RS10, RS20, RS30, RS40, and RS50 was 56 kgf/mm^2, 70 kgf/mm^2, 92 kgf/mm^2, 101 kgf/mm^2, and 125 kgf/mm^2, respectively. At the same volume fraction, the relative density of the SiC@Cu/Cu composite was higher than that of the SiC_p/Cu composite. The Vickers hardness of the SiC_p/Cu composite decreased with the increase in the volume fraction of SiC_p powder.

Vickers indentation of SiC@Cu/Cu composites is shown in Figure 7. With the increase in the SiC@Cu fraction, the depth of Vickers indentation for SiC@Cu/Cu composites became shallower. It can be concluded that the second-phase introduction of SiC@Cu powders improved the Vickers hardness of SiC@Cu/Cu composites. It was thought that higher amount of ceramic particles in the copper matrix resulted in more dislocations and the dislocations lead to the increase in hardness of SiC@Cu/Cu composites. The relative density and Vickers hardness of the SiC_p/Cu composite were lower than those of the SiC@Cu/Cu composites, which was related to the bonding degree of the magnetron-sputtered copper film and SiC particles.

TEM photo of SiC@Cu/Cu composites with different SiC@Cu fractions can be seen in Figure 8. Figures 8(a) and 8(b) present the volume fraction of SiC@Cu powder as 10% and 30%. The interdiffuse interface layers were stinct, which was diffused into the interior of the coating. The interdiffuse phenomenon was discovered in the other SiC@Cu/Cu composites. This kind of structure occurred in all SiC@Cu/Cu specimens. As the SiC@Cu fraction was low, the distribution of the structure was obvious. While the SiC@Cu fraction was higher than 40%, the discontinuous interface structure could be detected. It can be concluded that magnetron sputtering technology was an effective way to improve interface interdiffuse behaviors of SiC@Cu/Cu composites.

Figure 9 shows the survey on the relation curve between the SiC@Cu fraction and coefficient of thermal expansion

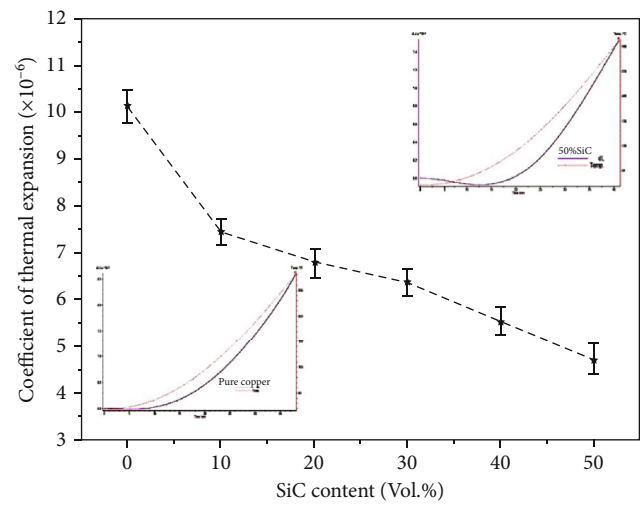

Figure 9: Relation curve between the SiC@Cu fraction and CET of SiC@Cu/Cu composites.

(abbreviation "CET") of the SiC@Cu/Cu composites. It was expected that CTE of SiC@Cu/Cu composites lowered with the introduction of SiC@Cu powders. Figure 9 displays the mean CTE of all specimens in the range of 50°C~300°C. Within the entire investigated temperature range, CTE values decreased apparently with the increasing SiC@Cu fraction. The reduction of CTE was reckoned as the results of mixture rule and the intense restriction effect of SiC@Cu reinforcement on the copper matrix. The relative experiment proved that CTE values of SiC@Cu/Cu composites were lower than those of SiC_p/Cu specimens under the condition of the same doping amount of SiC. CTE values reflected the level of stress mismatched by introducing SiC@Cu reinforcement in the copper matrix.

4. Conclusion

In this thesis, magnetron sputtering technology was applied to obtain a continuous copper film on the SiC grains successfully. The dynamic formation mechanism of the copper film was a mixture model of main island structure growth and secondary layered structure growth as SiC grains moved

during the magnetron sputtering process. The hot-press sintering method was utilized to fabricate SiC@Cu/Cu composites at 750°C for 60 min. The relative density of SiC@Cu/Cu composites decreased as the SiC@Cu fraction increased. For all SiC@Cu/Cu composites, the relative density was higher than 96%. The Vickers hardness of SiC@Cu/Cu composites increased with the volume fraction of SiC@Cu powders increasing. According to TEM result, the interdiffuse phenomenon was discovered in the SiC@Cu/Cu composites. The introduction of SiC@Cu powder improved the Vickers hardness of the SiC@Cu/Cu composite, especially at the high SiC@Cu fraction level. CTE values decreased with the increasing volume fraction of SiC@Cu powders within the range of investigated temperature.

Data Availability

The data used to support the findings of this study are included within the article.

Disclosure

Part of the preliminary research work had been published in the journal "*Advances in Computer Science Research*, volume 71" (4th International Conference on Machinery Materials and Information Technology Applications in 2016).

Conflicts of Interest

The authors declare that they have no conflicts of interest.

Acknowledgments

The authors and collaborators were grateful for the support by the National Science Foundation of China (No. 51671096), Materials Science and Engineering Team Project of Jiamusi University (JDXKTD-2019001), and Scientific Research Project of the Education Department of Heilongjiang Province (2016-KYYWF-0556, 2019-KYYWF-1373). Meanwhile, the thesis was supported by Key Scientific Research Projects of Higher Education Institutions of Henan Province (Project number 18A430006) and Science and Technology Research Projects from Anyang City (Project "thermal conductivity behavior research of copper matrix hybrid materials with wear-resisting/low expansion for aviation electric contact field"). Part of the data in this paper was provided by "Key Laboratory of Aerocraft Simulation Design and Airborne Equipment of Anyang City".

References

[1] J. Zheng, S. Li, F. Dou, and T. Li, "Preparation and microstructure characterization of a nano-sized Ti^{4+}-doped $AgSnO_2$ electrical contact material," *Rare Metals*, vol. 28, no. 1, pp. 19–23, 2009.

[2] T. Varo and A. Canakci, "Effect of the CNT content on microstructure, physical and mechanical properties of Cu-based electrical contact materials produced by flake powder metallurgy," *Arabian Journal for Science and Engineering*, vol. 40, no. 9, pp. 2711–2720, 2015.

[3] R. Zhang, L. Gao, and J. K. Guo, "Preparation and characterization of coated nanoscale Cu/SiC_p composite particles," *Ceramics International*, vol. 30, no. 3, pp. 401–404, 2004.

[4] V. Martínez, S. Ordoñez, F. Castro, L. Olivares, and J. Marín, "Wetting of silicon carbide by copper alloys," *Journal of Materials Science*, vol. 38, no. 19, article 5252263, pp. 4047–4054, 2003.

[5] T. Schubert, A. Brendel, K. Schmid et al., "Interfacial design of Cu/SiC composites prepared by powder metallurgy for heat sink applications," *Composites Part A: Applied Science and Manufacturing*, vol. 38, no. 12, pp. 2398–2403, 2007.

[6] H. Bi, K. C. Kou, A. E. Rider, K. Ostrikov, H. W. Wu, and Z. C. Wang, "Low-phosporous nickel-coated carbon microcoils: Controlling microstructure through an electroless plating process," *Applied Surface Science*, vol. 255, no. 15, pp. 853–858, 2009.

[7] E. Neubauer, G. Kladler, C. Eisenmenger-Sittner et al., "Interface design in copper-diamond composite by using PVD and CVD coated diamonds," *Advanced Materials Research*, vol. 59, pp. 214–219, 2008.

[8] B. Wang, Z. Ji, F. T. Zimone, G. M. Janowski, and J. M. Rigsbee, "A technique for sputter coating of ceramic reinforcement particles," *Surface and Coatings Technology*, vol. 91, no. 1-2, pp. 64–68, 1997.

[9] H. Kersten, P. Schmetz, and G. M. W. Kroesen, "Surface modification of powder particles by plasma deposition of thin metallic films," *Surface and Coating Technology*, vol. 108, pp. 507–512, 1998.

[10] C. M. Fernandes, V. M. Ferreira, A. M. R. Senos, and M. T. Vieira, "Stainless steel coatings sputter-deposited on tungsten carbide powder particles," *Surface and Coating Technology*, vol. 176, no. 1, pp. 103–108, 2003.

[11] K. M. Shu and G. C. Tu, "The microstructure and the thermal expansion characteristics of Cu/SiC_p composites," *Materials Science and Engineering A*, vol. 349, no. 1-2, pp. 236–247, 2003.

[12] P. Yih and L. Chung, "Silicon carbide whisker copper-matrix composites fabricated by hot pressing copper coated whiskers," *Journal of materials science*, vol. 31, no. 2, pp. 399–406, 1996.

[13] D. Peiling, Z. Yunlong, and M. Hu, "Effect of SiC p (Cu) addition on the property of the SiC_p (Cu) /Cu composites," *Advances in Computer Science Research*, vol. 71, pp. 748–751, 2016.

[14] M. Hu, Z. Yunlong, S. Lin et al., "Dynamic Ddeposition of Nnanocopper Ffilm on the β-SiCp Ssurface by Mmagnetron Ssputtering," *Journal of Nanomaterials*, vol. 2015, Article ID 810986, 6 pages, 2015.

Hindawi
International Journal of Photoenergy
Volume 2021, Article ID 6651541, 8 pages
https://doi.org/10.1155/2021/6651541

Research Article

The Effect of Graphite and Fe_2O_3 Addition on Hydrolysis Kinetics of Mg-Based Hydrogen Storage Materials

Kun Yang,[1] Hongyun Qin,[1] Junnan Lv,[1] Rujun Yu,[1] Xia Chen,[1] Zengdian Zhao,[1] Yongjie Li,[1] Fang Zhang,[2] Xianchang Xia,[2] Qiang Fu,[1] and Ming Wang[1]

[1]*School of Chemistry and Chemical Engineering, Shandong University of Technology, Zibo 255049, China*
[2]*Consultant Beijing, 10080, China*

Correspondence should be addressed to Qiang Fu; fuqiang@tju.edu.cn and Ming Wang; wangming@zhongxunhb.com

Received 20 November 2020; Revised 28 December 2020; Accepted 5 February 2021; Published 24 February 2021

Academic Editor: Umapada Pal

In this paper, graphite and Fe_2O_3 are introduced into MgH_2 powder by the method of hydrogenation after magnetic grinding. Hydrogen storage materials which composite of MgH_2–5 wt.% C and MgH_2–5 wt.% C–5 wt.% Fe_2O_3 are successfully prepared. The physical structure of these materials was analyzed and characterized by XRD, SEM, etc. Furthermore, the influence of graphite and Fe_2O_3 on the hydrolysis of MgH_2 was systematically investigated. The results show that MgH_2–C–Fe_2O_3 composite powder has the fastest hydrogen release rate in municipal drinking water and the highest conversion rate. Graphite and Fe_2O_3 can effectively reduce the activation energy of the hydrolysis reaction of MgH_2 and improve the hydrolysis kinetics of MgH_2. The synergistic effect of the coaddition of graphite and Fe_2O_3 can significantly increase the hydrolysis conversion rate of MgH_2 and improve the hydrolysis kinetics.

1. Introduction

Due to the increasing environmental pollution caused by the development and use of fossil fuels such as petroleum, the research and use of green and clean energy has become an increasing focus of the society [1–3]. Hydrogen is an ideal clean energy, whose energy density (142 MJ kg^{-1}) is three times that of gasoline, and the combustion product is only water [4]. In the past few decades, most of the commercial hydrogen was obtained through partial oxidation of natural gas and coal gasification [5], which consumes petrochemical energy to cause certain environmental pollution. Recently, hydrogen production by hydrolysis has become a new focus due to its simple process, mild reaction conditions, safety, clean, and efficiency [6–8]. Researchers have reported several materials for hydrogen production by hydrolysis, such as metals [9], metal hydrides [10, 11], and borohydrides [12–14]. Among all the hydrogen storage materials, MgH_2 has the advantages of large hydrogen storage capacity (7.6 wt.%) and high theoretical hydrolysis hydrogen production (15.2 wt.%). In recent years, it has attracted much attention from scientific researchers. Hydrogen can be obtained by the reaction of MgH_2 with water, and the reaction equation is as follows:

$$MgH_2 + 2H_2O \rightarrow Mg(OH)_2 + 2H_2\uparrow \Delta H = -277\,\text{kJmol}^{-1}. \quad (1)$$

The hydrolysis reaction of MgH_2 is not harsh and can proceed spontaneously in contact with water at room temperature. However, a passivation layer can be formed on the surface of the unreacted MgH_2 during the hydrolysis process, which prevents the water from diffusing into the interior, thus, making the hydrolysis stop rapidly from the high-speed reaction stage. Kojima et al. [15] reported that the hydrogen conversion rate of MgH_2 hydrolysis is less than 30% in municipal drinking water for 1 hour, which hinders the practical application of MgH_2. For improving the low conversion rate of MgH_2 hydrolysis, many studies have been reported, such as reducing the particle size of MgH_2 to nanometer [16, 17] and using other aqueous solutions (such as

acid solution [18] and salt solution [19–21]) to prevent the generation of $Mg(OH)_2$ passivation layer. In addition, adding chloride [22], metal hydride [23, 24], carbon material [25, 26], and metal oxide [27, 28] to MgH_2 by ball grinding and other methods can also significantly improve the hydrolysis kinetic performance of MgH_2. For example, Yang et al. [28] studied the effects of TiO_2, $MgAl_2O_4$, and Fe on the hydrolysis properties of MgH_2. As an amphoteric oxide, TiO_2 can lower the pH value around MgH_2, which can therefore enhance the hydrolysis properties of MgH_2; $MgAl_2O_4$ has a catalytic effect on the hydrolysis of MgH_2; Fe as the cathode of galvanic cell and thereby reduce the activation energy for hydrolysis reaction of MgH_2. Awad et al. [26] studied the effect of adding carbon materials, metals (Ni, Fe, and Al), and metal oxides (Nb_2O_5 and V_2O_5) by using the ball grinding method on the hydrolysis of magnesium-based materials; it was found that the mixture of Mg–5 wt.% C–5 wt.% Ni had the best hydrolysis rate (95% of the theoretical hydrogen production within 2 minutes) and the lowest hydrolysis activation energy (14.34 kJ mol^{-1}). It was proven that the carbon material and the transition metal Ni could promote the hydrolysis of magnesium-based materials. However, the synergistic effect of carbon and metal oxides on magnesium has not been systematically studied, while the mechanism has not been analyzed [25, 26, 28].

Considering the above, in this paper, several MgH_2–C and MgH_2–C–Fe_2O_3 materials were prepared by hydrogenation after magnetic grinding. The synergistic effect of graphite and Fe_2O_3 on the hydrolytic kinetics of magnesium-based hydrogen storage materials was investigated systematically. The hydrolytic conversion rate, hydrolytic reaction rate, and hydrolytic activation energy Ea of pure MgH_2 and composite powders with different additives were obtained.

2. Experimental

2.1. Sample Preparation. Magnesium-based hydride composite materials were prepared by hydrogenation after magnetic grinding. The starting materials are Mg powder (purity ≥ 99%, 200 mesh, Sinopharm Chemical Reagent Co., Ltd), MgH_2, (purity ≥ 99.5%, MG Power Technology Co., Ltd), Fe_2O_3 (average particle size 20 nm, purity ≥ 99.5 %, Shanghai Yaoyi), and graphite (average particle size 80 nm, purity ≥ 99.5%, Shanghai Yaoyi). Place the required raw materials (total weight 3 g, MgH_2–C (Mg : C mass ratio = 0.95 : 0.05), MgH_2–C–Fe_2O_3 (Mg : C : Fe_2O_3 mass ratio = 0.9 : 0.05 : 0.05) into the stainless steel reaction kettle (volume 100 mL, 60 g of steel needle for grinding is installed in the reaction kettle, 0.3 × 5 mm : 1 × 5 mm mass ratio = 1 : 1). In order to prevent Mg oxidation during grinding, high purity Ar gas (99.999%) was used to purge the reactor chamber and pipeline for 20 min before grinding, and a small amount of Ar gas was filled in the chamber and pipeline for protection. Then, the grinding experiment was performed (rotational speed = 2400 rad/min), and the grinding time was 2 h (grinding 30 min + cooling 30 min, repeated four times). Then, the reactor was placed on a constant temperature heating furnace (~ 300°C) and filled with hydrogen gas (~ 2.3 MPa) for 2 h hydrogenation. Then, the furnace was cooling under room temperature and stood for 12 h. The samples were taken out after the reaction kettle which naturally cooled to room temperature. The powder composite of MgH_2–5 wt.% C and MgH_2–5 wt.% Fe_2O_3–5 wt.% C was prepared. The pure MgH_2 powder is also annealed in hydrogen gas.

2.2. Hydrolysis Experiment. The hydrolysis device is shown in Figure 1, which mainly consists of a reaction device and a collection device. The reaction device includes a thermostatic water bath pot, three-necked flask, and condensing tube. The flask's three mouths are, respectively, used for inserting a thermometer, connecting the condensing tube, and adding powder samples. The collecting device consists of a Monteggia washing bottle, beaker, and electronic balance. Adding 100 mL of municipal drinking water into a three-necked flask and using a water bath to control temperature. Then, adding 0.05 g powder into the three-necked flask and recording the time. Through the condenser tube, the condensed hydrogen enters the Monteggia washing bottle. The hydrogen drains the water from the Monteggia washing bottle to the beaker. The hydrogen released is estimated through calculating the weight of the discharged water.

The hydrogen conversion rate is the ratio of the amount of hydrogen produced at time T to the total amount of hydrogen produced by adding excess of 0.1 mol L^{-1} HCl solution [29] (see Table 1).

2.3. Sample Characterization. Components and crystal structures of the samples were examined by powder X–ray diffraction apparatus (XRD, Ultima IV, Rigaku Corporation) equipped with a Cu Kα radiation source. XRD analyses were performed over a range from 10° to 80° at a scanning rate of 10° min^{-1}. Using a scanning electron microscope (SEM, Quanta 250, FEI, equipped with energy dispersive spectroscopy (EDS) system, working voltage 20 kV) to observe the structure and element composition of the composite powder.

3. Results and Discussion

3.1. Composition and Structure of Mg Hydrogen Storage Materials Prepared. XRD patterns of the MgH_2–C and MgH_2–C–Fe_2O_3 powders are shown in Figures 2(a) and 2(b). It can be seen from Figure 2 that the MgH_2–C–Fe_2O_3 powder has diffraction peaks of MgH_2, Mg, MgO, and C, as well as a small diffraction peak of Fe_2O_3. And the MgH_2–C powder only showed diffraction peaks of MgH_2, Mg, MgO, and C. With the exception of MgH_2, neither of the two powders produced any new substances, which proved that no other side reactions during the magnetic grinding and hydrogenation. The appearance of the Mg diffraction peak is due to the fact that part of the Mg particles not sufficiently ground or agglomerated during the magnetic grinding process, resulting in the large particles of Mg not being completely hydrogenated. And the one reason for appearing MgO is that there is an oxide layer on the surface of the raw material Mg particles. The steel needle in the grinding chamber uses mechanical force

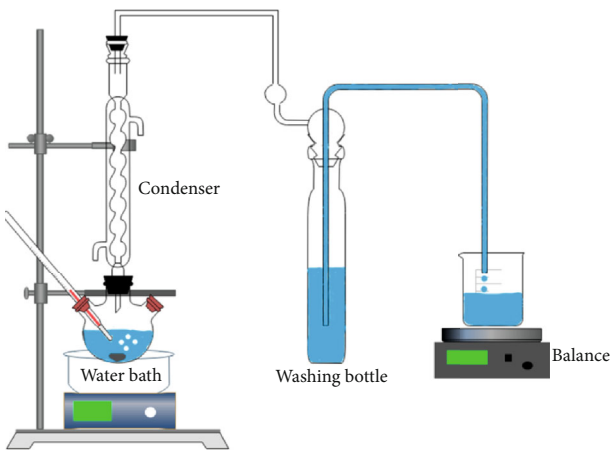

Figure 1: The experimental apparatus used for hydrolyzing hydrogen production.

Table 1: The amount of hydrogen released from each sample after complete hydrolysis.

Samples	Total hydrogen released [mL/g]
Pure MgH_2	1730
MgH_2–C	1602
MgH_2–C–Fe_2O_3	1503

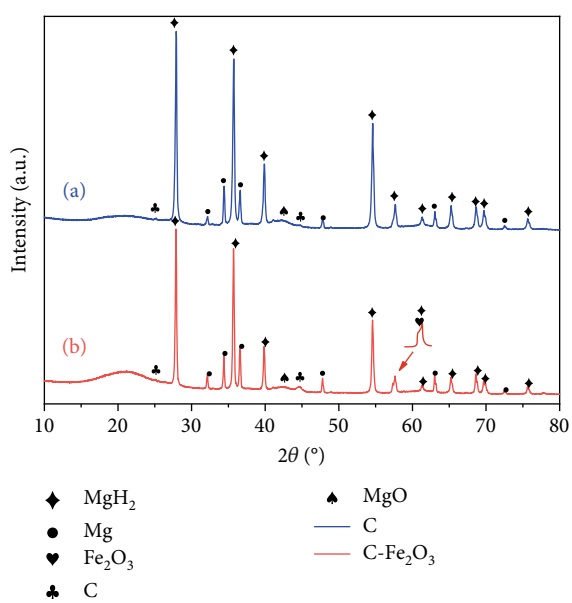

Figure 2: XRD patterns of MgH_2–C (a) and MgH_2–C–Fe_2O_3 (b) powders prepared by magnetic grinding and hydrogenation.

to cut the Mg particles while peeling off the surface MgO layer. MgO is mixed in the hydrogenated MgH_2 powder. Another reason for appearing MgO is the part of Mg that has not been completely hydrogenated quickly producing a dense MgO layer on the surface when it comes in contact with air. In addition, we also found that the diffraction peak strength of C and Fe_2O_3 is relatively low, which may be caused by the low content of these two phases, the excessively small particle size, and the relatively high dispersion.

The SEM measurements were taken out to characterize the structure of the MgH_2–C (Figure 3) and MgH_2–C–Fe_2O_3 (Figure 4). In Figures 3(c) and 3(d) and 4(c) and 4(d), it can be seen that the particle size of MgH_2 is relatively uniform, and the particle size of the two samples is about 300-700 nm. This is because the fine graphite particles are distributed on the surface and gap of the Mg during the magnetic grinding process to play a role of lubrication and dispersion, which reduces the cold welding phenomenon of Mg particles. This effectively prevents the agglomeration of Mg particles, so that the size of the hydrogenated MgH_2 particles is smaller and uniform, which is similar to the research conclusion of the ball milling reaction of C and Mg reported by Awad et al. [26]. Compared with the MgH_2–C powder (Figure 3(c)), the MgH_2–C–Fe_2O_3 powder (Figure 4(c)) has fewer large particles and a more even particle size, which indicates that the addition of Fe_2O_3 can further reduce the size of MgH_2 particles.

The SEM image and EDS spectrum of the MgH_2–C–Fe_2O_3 powder (Figure 4(b)) show that there is a certain amount of Fe on the surface of the particle. Combined with the XRD pattern of the sample (Figure 2(b)), it shows that the Fe element comes from Fe_2O_3, which further proves the presence of Fe_2O_3.

3.2. Kinetics of Hydrolysis. Figure 5 shows the hydrogen release curves of pure MgH_2 (a), MgH_2–C powder (b), and MgH_2–C–Fe_2O_3 powder (c) in municipal drinking water at 353 K. It can be observed that the hydrolysis rate of pure MgH_2 and the hydrogen conversion rate are relatively low. At 353 K, pure MgH_2 produces only 113 mL g^{-1} hydrogen in 2 minutes, 201.9 mL g^{-1} hydrogen in 5 minutes, and the hydrolysis conversion rate in 60 minutes is only 19.3%. It is possible that after the first few minutes of rapid reaction, a dense $Mg(OH)_2$ layer was formed on the surface of MgH_2, which prevented MgH_2 from further reacting with water. In contrast, when the C added sample is at 353 K, the hydrogen production is 268.5 mL g^{-1} in 2 minutes, 416 mL g^{-1} hydrogen is produced in 5 minutes, and the hydrolysis conversion rate is 52.5% in 60 minutes. The sample with C and Fe_2O_3 showed the fastest hydrolysis rate at 353 K, with 280 mL g^{-1} hydrogen produced in 2 minutes, 468 mL g^{-1} hydrogen produced in 5 minutes, and the hydrolysis conversion rate increased to 62.8% in 60 minutes. Compared with pure MgH_2, the two have better hydrolysis kinetics and higher hydrolysis conversion rate, which proves that C and Fe_2O_3 can promote the hydrolysis of MgH_2. This is because, in the magnetic grinding process, C can effectively reduce the agglomeration of magnesium particles, make the particle size of the hydrogenated powder smaller, increase the area in contact with water during hydrolysis, and thus effectively improve the hydrolysis reaction rate. Tayeh et al. [16] also showed a similar effect after ball milling of MgH_2 with C added. Fe_2O_3 can further reduce the particle size of MgH_2 and may have a catalytic effect on the hydrolysis reaction of MgH_2. Furthermore, it can improve the hydrolysis kinetic performance of MgH_2.

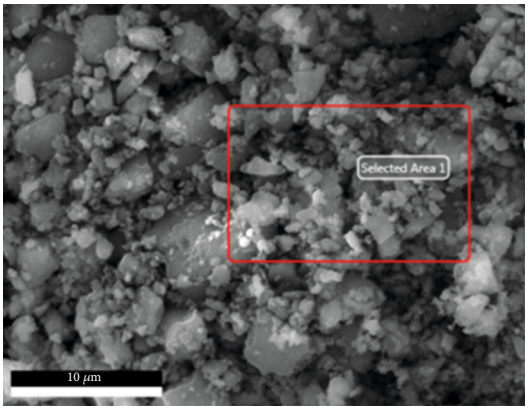

(a)

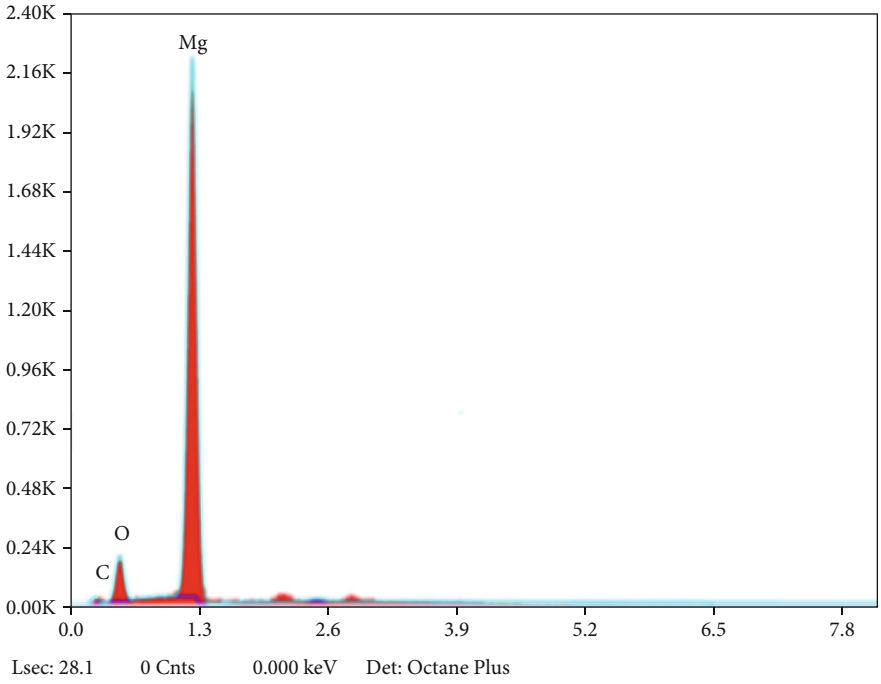

(b)

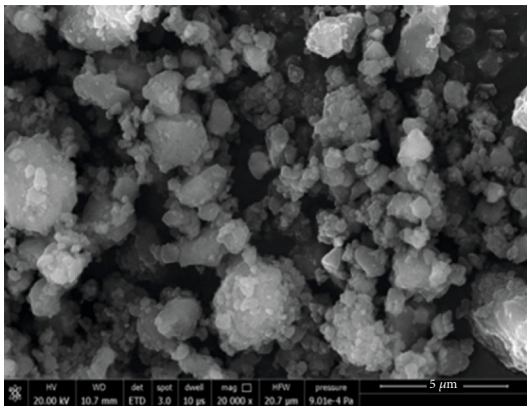

(c)

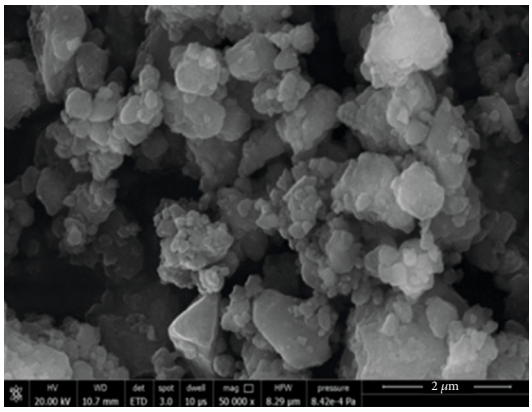

(d)

Figure 3: SEM micrograph of the MgH_2–C (a, c, d) and EDS analysis of (a).

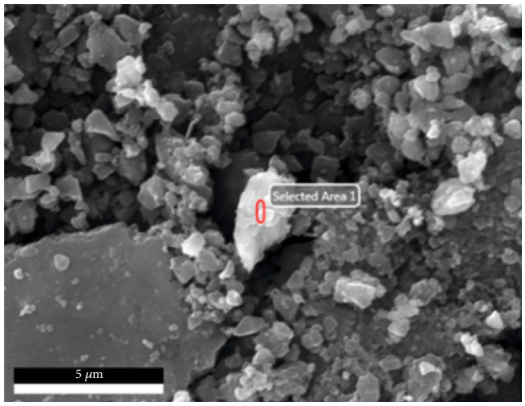

(a)

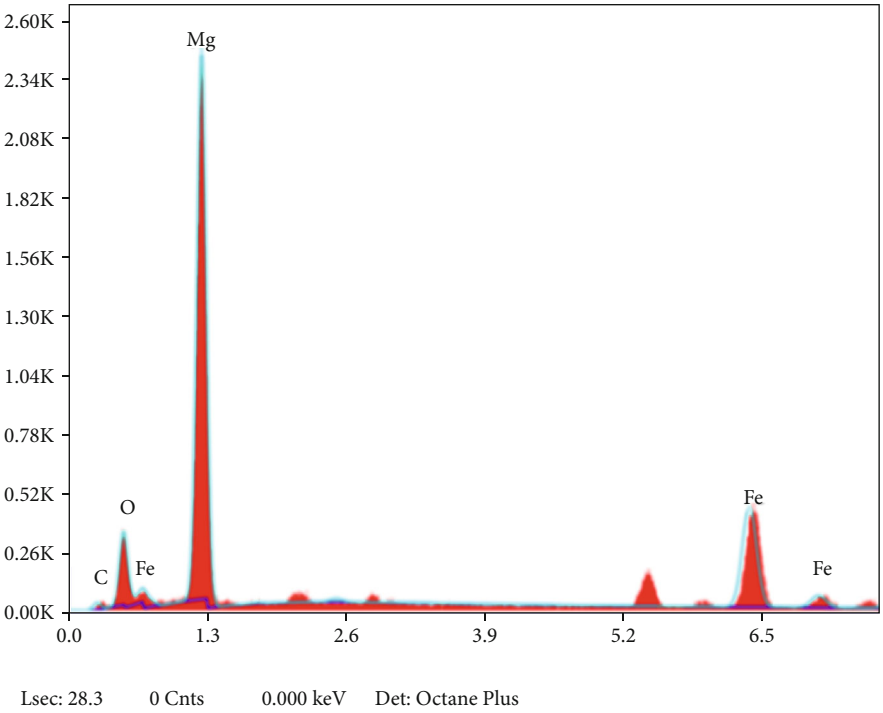

(b)

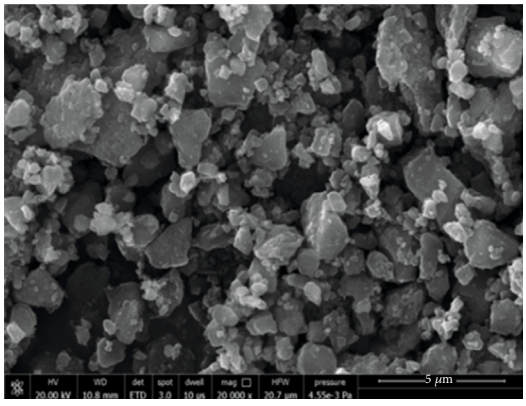

(c)

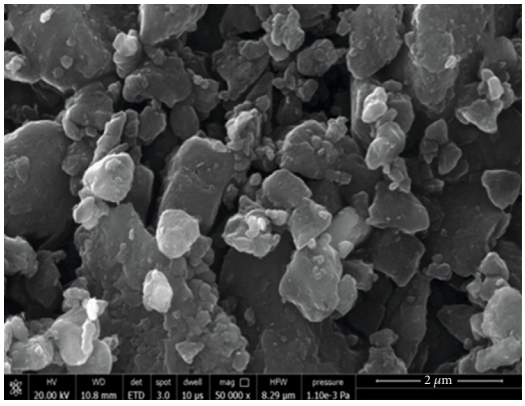

(d)

Figure 4: SEM micrograph of the MgH_2–C–Fe_2O_3 (a, c, d) and EDS analysis of (a).

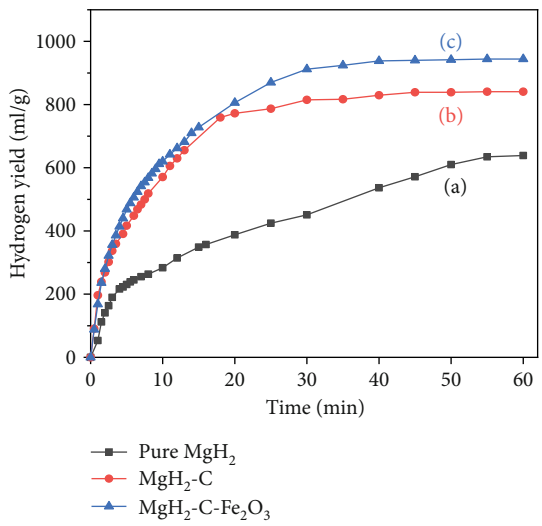

Figure 5: The hydrogen evolution curves for the hydrolysis of pure MgH_2 (a), MgH_2–C (b), and MgH_2–C–Fe_2O_3 (c) at 353 K.

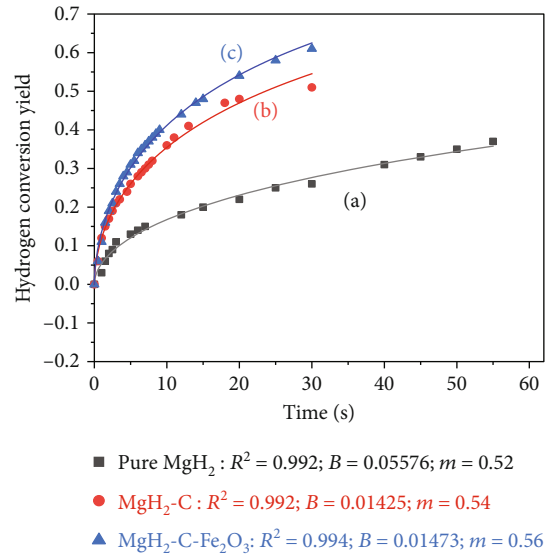

Figure 6: The kinetic curves of hydrogen generation for the hydrolysis of (a) pure MgH_2, (b) MgH_2–C, and (c) MgH_2–C–Fe_2O_3 at 353 K in municipal drinking water.

In order to investigate the synergistic effect of the addition of C and Fe_2O_3 on the hydrolytic hydrogen production performance of MgH_2, we tested the hydrogen liberation performance of pure MgH_2, MgH_2–C powder, and MgH_2–C–Fe_2O_3 powder in municipal drinking water under different temperature conditions. As shown in Figure S1, compared with pure MgH_2 and MgH_2–C powders, the hydrogen production rate and hydrogen conversion rate of MgH_2–C–Fe_2O_3 powder are greatly improved at different temperatures. Figure S1(c) shows that MgH_2–C–Fe_2O_3 powder has the highest hydrogen production rate and hydrogen conversion rate. Compared with MgH_2–C powder, the hydrogen conversion rate increases from 28.6% to 36.4% at 333 K (see Table S1) and from 50.9% to 60.7% in the first 30 min at 353 K (see Table S2), respectively. The results show that the synergistic effect of C and Fe_2O_3 together can significantly improve the hydrolysis kinetics of MgH_2 and increase the hydrogen conversion rate.

Two main models, the diffusion-controlled and the phase-boundary controlled, describe the experimental kinetic curves of MgH_2 hydrolysis [30]. The hydrolysis process of MgH_2 and MgH_2–additives in municipal drinking water can be described by the Avramie–Erofeev equation (Equation (2)) [20]:

$$\alpha(t) = 1 - \exp\left(-Bt^m\right). \tag{2}$$

$\alpha(t)$ is the reaction rate (the ratio of the amount of reacted material to the total amount of material, it can be regarded as hydrogen conversion rate), t is the reaction time, and B and m are constants. Values of B and m obtained by fitting and R^2 (correlation coefficient) are shown in Figure 6. The R^2 values indicate that the fitted results are in good agreement with the experimental data. Different m values represent different nucleation growth rate control steps, and m values for one-dimensional diffusion and for three-dimensional interfacial reaction are 0.62 and 1.07, respectively [20]. According to Figure 6, the m values of MgH_2–C–Fe_2O_3, MgH_2–C, and pure MgH_2 samples are 0.56, 0.54, and 0.52, respectively, which are closer to 0.62. This indicates that the hydrolysis of three samples at 353 K follows a one-dimensional diffusion mechanism.

3.3. Activation Energy of Hydrolysis. The apparent activation energy for hydrolysis of MgH_2 can be determined by the Arrhenius equation (Equation (3)):

$$k = A \cdot \exp\left(-\mathrm{Ea}/RT\right), \tag{3}$$

where k is the reaction rate constant, Ea is the apparent activation energy ($\mathrm{J\,mol^{-1}}$), R is the molar gas constant ($8.314\,\mathrm{J\,mol^{-1}\,K^{-1}}$), and T is the reaction temperature (K). By fitting the lnk–1000/T line, the slope of the line was multiplied by the R value, and the apparent activation energy Ea of different samples was finally obtained. Figure 7 shows the apparent activation energy of three different samples calculated. R^2 values in all cases are >0.98, indicating that the Arrhenius equation is appropriate for describing the hydrolysis of MgH_2. From the slope of the fitted line, Ea of pure MgH_2 was found to be $55.57\,\mathrm{kJ\,mol^{-1}}$. Similarly, Ea values of MgH_2–C and MgH_2–C–Fe_2O_3 samples were 43.40 and $36.92\,\mathrm{kJ\,mol^{-1}}$, respectively, which were lower than the value for pure MgH_2. It can be seen that adding C can reduce the hydrolysis activation energy of MgH_2; adding C and Fe_2O_3 at the same time can further reduce the hydrolysis activation energy of MgH_2. A lower Ea value generally indicates a higher reaction activity. Therefore, the addition of C and Fe_2O_3 simultaneously has a synergistic effect on improving the hydrolysis properties of MgH_2.

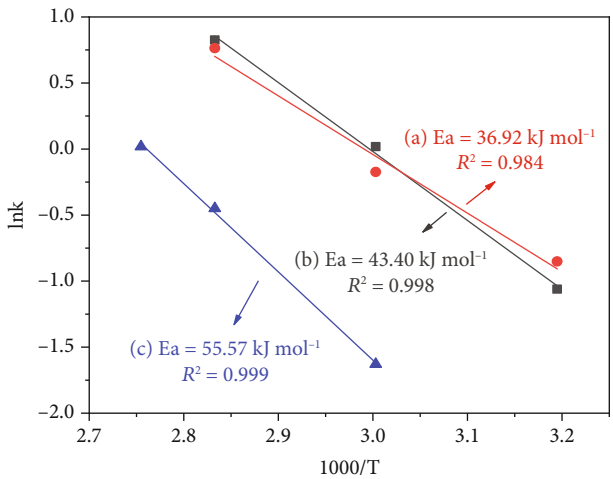

Figure 7: Arrhenius plot for the activation energy calculation hydrolysis of MgH_2–C–Fe_2O_3 (a), MgH_2–C (b), and pure MgH_2 (c) in municipal drinking water.

4. Conclusion

In this work, MgH_2–C and MgH_2–C–Fe_2O_3 composite powders were prepared by the hydrogenation after magnetic grinding. The effects of graphite and Fe_2O_3 on the hydrolysis kinetics of MgH_2 were studied. It was found that both MgH_2–C and MgH_2–C–Fe_2O_3 samples have better performance of hydrolysis reaction rate and hydrogen conversion rate compared with pure MgH_2. Among them, MgH_2–C–Fe_2O_3 sample has the fastest hydrolytic yield rate and the highest conversion rate. The conversion rate of 30 minutes at 353 K is 9.8% higher than that of the MgH_2–C sample, while that is 42.6% higher than that of pure MgH_2. It was also found that the Ea value of hydrolysis activation energy of pure MgH_2 was 55.57 kJ mol^{-1}. The addition of C and Fe_2O_3 could effectively reduce the Ea value of MgH_2–C and MgH_2–C–Fe_2O_3 samples to 43.40 and 36.92 kJ mol^{-1}, respectively. The results show that the addition of graphite and Fe_2O_3 has an obvious synergistic effect on improving the hydrolysis kinetics and hydrogen conversion rate of MgH_2.

Abbreviations

ΔH: Reaction enthalpy
$\alpha(t)$: Hydrogen conversion rate
B: Constant
t: Reaction time
m: Constant
k: Reaction rate constant
Ea: Hydrolysis activation energy
A: Preexponential factor
R: Molar gas constant
T: Reaction temperature.

Data Availability

All data used to support the this study are available from the corresponding author upon request.

Conflicts of Interest

The authors declare no conflict of interest.

Authors' Contributions

Kun Yang and Hongyun Qin contributed equally to this work.

Acknowledgments

This work is financially supported by the National Natural Science Foundation of China (No. 51976112).

Supplementary Materials

Figure S1: the hydrogen evolution curves for the hydrolysis of (a) pure MgH_2, (b) MgH_2–C, and (c) MgH_2–C–Fe_2O_3 in municipal drinking water at different temperatures. Table S1: hydrogen conversion rate at 333 K. Table S2: hydrogen conversion rate at 353 K. *(Supplementary Materials)*

References

[1] Q. Lai, M. Paskevicius, D. A. Sheppard et al., "Hydrogen storage materials for mobile and stationary applications: current state of the art," *Chensuschem*, vol. 8, no. 17, pp. 2789–2825, 2015.

[2] M. Rueda, L. M. Sanz-Moral, and Á. Martín, "Innovative methods to enhance the properties of solid hydrogen storage materials based on hydrides through nanoconfifinement: a review," *The Journal of Supercritical Fluids*, vol. 141, pp. 196–217, 2018.

[3] L. Ouyang, M. Ma, M. Huang et al., "Enhanced hydrogen generation properties of MgH_2-based hydrides by breaking the magnesium hydroxide passivation layer," *Energies*, vol. 8, no. 5, pp. 4237–4252, 2015.

[4] M. Huang, L. Ouyang, Z. Chen, C. Peng, X. Zhu, and M. Zhu, "Hydrogen production via hydrolysis of Mg-oxide composites," *International Journal of Hydrogen Energy*, vol. 42, no. 35, pp. 22305–22311, 2017.

[5] M. Ni, M. K. H. Leung, D. Y. C. Leung, and K. Sumathy, "A review and recent developments in photocatalytic water-splitting using TiO_2 for hydrogen production," *Renewable & Sustainable Energy Reviews*, vol. 11, no. 3, pp. 401–425, 2007.

[6] L. Ouyang, J. Huang, H. Wang et al., "Excellent hydrolysis performances of Mg_3RE hydrides," *International Journal of Hydrogen Energy*, vol. 38, no. 7, pp. 2973–2978, 2013.

[7] L. Ouyang, Y. Xu, H. Dong, L. X. Sun, and M. Zhu, "Production of hydrogen via hydrolysis of hydrides in Mg-La system," *International Journal of Hydrogen Energy*, vol. 34, no. 24, pp. 9671–9676, 2009.

[8] L. Ouyang, H. Zhong, Z. Li et al., "Low-cost method for sodium borohydride regeneration and the energy efficiency of its hydrolysis and regeneration process," *Journal of Power Sources*, vol. 269, pp. 768–772, 2014.

[9] M. Fan, F. Xu, and L. Sun, "Studies on hydrogen generation characteristics of hydrolysis of the ball milling Al-based materials in pure water," *International Journal of Hydrogen Energy*, vol. 32, no. 14, pp. 2809–2815, 2007.

[10] C. Haertling, R. J. Hanrahan, and R. Smith, "A literature review of reactions and kinetics of lithium hydride hydrolysis," *Journal of Nuclear Materials*, vol. 349, no. 1-2, pp. 195–233, 2006.

[11] C. Ward, D. Stanga, L. Pataki, and R. D. Venter, "Design for the cold start-up of a man-portable fuel cell and hydrogen storage system," *Journal of Power Sources*, vol. 41, no. 3, pp. 335–352, 1993.

[12] W. Chen, L. Ouyang, J. Liu et al., "Hydrolysis and regeneration of sodium borohydride ($NaBH_4$) - A combination of hydrogen production and storage," *Journal of Power Sources*, vol. 359, pp. 400–407, 2017.

[13] Z. Xiong, L. Cao, J. Wang, and J. Mao, "Hydrolysis behavior of $LiBH_4$ films," *Journal of Alloys and Compounds*, vol. 698, pp. 495–500, 2017.

[14] Y. Zhu, L. Ouyang, H. Zhong et al., "Closing the loop for hydrogen storage: facile regeneration of NaBH4from its hydrolytic product," *Angewandte Chemie, International Edition*, vol. 59, no. 22, pp. 8623–8629, 2020.

[15] Y. Kojima, K. I. Suzuki, and Y. Kawai, "Hydrogen generation by hydrolysis reaction of magnesium hydride," *Journal of Materials Science*, vol. 39, no. 6, pp. 2227–2229, 2004.

[16] T. Tayeh, A. S. Awad, M. Nakhl, M. Zakhour, J. F. Silvain, and J. L. Bobet, "Production of hydrogen from magnesium hydrides hydrolysis," *International Journal of Hydrogen Energy*, vol. 39, no. 7, pp. 3109–3117, 2014.

[17] J. Huot, G. Liang, and R. Schulz, "Magnesium-based nanocomposites chemical hydrides," *Journal of Alloys and Compounds*, vol. 353, no. 1–2, pp. L12–L15, 2003.

[18] Ç. Öz, B. Coşkuner Filiz, and A. Kantürk Figen, "The effect of vinegar-acetic acid solution on the hydrogen generation performance of mechanochemically modified magnesium (Mg) granules," *Energy*, vol. 127, pp. 328–334, 2017.

[19] J. Chen, H. Fu, Y. Xiong, J. Xu, J. Zheng, and X. Li, "$MgCl_2$ promoted hydrolysis of MgH_2 nanoparticles for highly efficient H_2 generation," *Nano Energy*, vol. 10, pp. 337–343, 2014.

[20] M. Huang, L. Ouyang, H. Wang, J. Liu, and M. Zhu, "Hydrogen generation by hydrolysis of MgH_2 and enhanced kinetics performance of ammonium chloride introducing," *International Journal of Hydrogen Energy*, vol. 40, no. 18, pp. 6145–6150, 2015.

[21] D. Gan, Y. Liu, J. Zhang et al., "Kinetic performance of hydrogen generation enhanced by $AlCl_3$ via hydrolysis of MgH_2 prepared by hydriding combustion synthesis," *International Journal of Hydrogen Energy*, vol. 43, no. 22, pp. 10232–10239, 2018.

[22] S. Wang, L. Sun, F. Xu et al., "Hydrolysis reaction of ball-milled Mg-metal chlorides composite for hydrogen generation for fuel cells," *International Journal of Hydrogen Energy*, vol. 37, no. 8, pp. 6771–6775, 2012.

[23] H. Wang, J. Zhang, J. Liu, L. Z. Ouyang, and M. Zhu, "Catalysis and hydrolysis properties of perovskite hydride $NaMgH_3$," *Journal of Alloys and Compounds*, vol. 580, pp. S197–S201, 2013.

[24] J. P. Tessier, P. Palau, J. Huot, R. Schulz, and D. Guay, "Hydrogen production and crystal structure of ball-milled MgH_2-Ca and MgH_2-CaH_2 mixtures," *Journal of Alloys and Compounds*, vol. 376, no. 1-2, pp. 180–185, 2004.

[25] M. Ma, L. Yang, L. Ouyang, H. Shao, and M. Zhu, "Promoting hydrogen generation from the hydrolysis of Mg-graphite composites by plasma-assisted milling," *Energy*, vol. 167, pp. 1205–1211, 2019.

[26] A. S. Awad, E. El-Asmar, T. Tayeh et al., "Effect of carbons (G and CFs), TM (Ni, Fe and Al) and oxides (Nb_2O_5 and V_2O_5) on hydrogen generation from ball milled Mg-based hydrolysis reaction for fuel cell," *Energy*, vol. 95, pp. 175–186, 2016.

[27] S. Hong, H. Kim, and M. Y. Song, "Rate enhancement of hydrogen generation through the reaction of magnesium hydride with water by MgO addition and ball milling," *Journal of Industrial and Engineering Chemistry*, vol. 18, no. 1, pp. 405–408, 2012.

[28] B. Yang, J. Zou, T. Huang, J. Mao, X. Zeng, and W. Ding, "Enhanced hydrogenation and hydrolysis properties of core-shell structured Mg–MOx (M = Al, Ti and Fe) nanocomposites prepared by arc plasma method," *Chemical Engineering Journal*, vol. 371, pp. 233–243, 2019.

[29] R. V. Lukashev, N. A. Yakovleva, S. N. Klyamkin, and B. P. Tarasov, "Effect of mechanical activation on the reaction of magnesium hydride with water," *Russian Journal of Inorganic Chemistry*, vol. 53, no. 3, pp. 389–396, 2008.

[30] N. Senes, L. Fernández Albanesi, S. Garroni et al., "Kinetics and hydrogen storage performance of Li-Mg-N-H systems doped with Al and $AlCl_3$," *Journal of Alloys and Compounds*, vol. 765, pp. 635–643, 2018.

Hindawi
International Journal of Photoenergy
Volume 2021, Article ID 6684802, 12 pages
https://doi.org/10.1155/2021/6684802

Research Article

Simulation of the Residual Stress of the Y_2O_3/Al_2O_3 Composite Deuterium Permeation Barrier under Thermal Shock

Kezhi Huang,[1,2,3] Weijing Wang,[1,2,3,4] Qinghe Yu,[1,2,3] Lei Hao,[1,2,3] Jing Mi,[1,2] Shijie Li,[1,2] Hao Liu,[1,2] Shanshan Li,[1,2] Juan Liu,[5] and Jianwei Wang[2]

[1]*National Engineering Research Center of Nonferrous Metals Materials and Products for New Energy, GRINM Group Co., Ltd., Beijing 100088, China*
[2]*GRIMAT Engineering Institute Co., Ltd., Beijing 101407, China*
[3]*General Research Institute for Nonferrous Metals, Beijing 100088, China*
[4]*School of Materials Science and Engineering, Northeastern University, Shenyang 110819, China*
[5]*Beijing Academy of Science and Technology, Beijing 100089, China*

Correspondence should be addressed to Qinghe Yu; yuqh@grinm.com

Received 10 November 2020; Revised 15 January 2021; Accepted 10 February 2021; Published 23 February 2021

Academic Editor: Jiangwei Liu

A deuterium permeation barrier is an essential part in the core component of nuclear reactors. It can protect the structure made of steel from being penetrated by deuterium in a fusion reactor. However, residual stress induced in the operation would dramatically influence the mechanical endurance of the coating, threatening the safety of the facilities. In this paper, finite element analysis was conducted to investigate the residual stress in nanoscale Al_2O_3 and Y_2O_3 coatings and their composites under thermal shock, from 700°C to 25°C. The max principal stress is assumed as the cause of crack initiation in the coating, because ceramics are brittle and fragile under tensile stress. Max shear stress and max Mises stress in the systems are also analyzed, and the effect of thickness in the range 100 nm to 1000 nm was investigated. The max principal stress in Al_2O_3 coating reaches its maximum value, 1.33 GPa, when the thickness of coating reaches 450 nm. And the max principal stress decreases at a very low rate as the thickness increases exceeding 450 nm. The max principal stress in Y_2O_3 coating increases rapidly as the thickness increases when the thickness of the coating is below 250 nm, and the max principal stress is at about 0.9 GPa when the thickness exceeds 500 nm. The max principal stress in the Y_2O_3/Al_2O_3 (150 nm) composite coating occurs in the Al_2O_3 layer and shows no difference from the single layer of 150 nm thick Al_2O_3 coating. The max principal stress site of all three kinds of coating is located at the edge of the coating 25 nm away from the interface. The result shows that residual thermal stress in the coating increases as the thickness increases when the thickness of the coating is below 200 nm due to the stress singularity of the interface. And as the thickness exceeds 500 nm, the increase in thickness has little impact on the residual thermal stress in the coating. Coating an Y_2O_3 top layer will not introduce any more residual thermal stress under the thermal shock condition. The Y_2O_3 coating causes much less residual stress under thermal shock compared with Al_2O_3 owing to its much lower Young's modulus. The max principal stress in the 300 nm thick Y_2O_3 coating is 0.85 GPa while that of the Al_2O_3 coating is 1.16 GPa. The max residual stress of the composite Y_2O_3/Al_2O_3 (150 nm) coating is determined by the Al_2O_3 layer.

1. Introduction

Deuterium permeation is one of the most critical threats to the safety of fusion reactors. Deuterium has strong reducibility and ability to be dispersed in other materials for most structural materials. When deuterium is dispersed into the structural material, it can cause nuclear fuel leakage, contamination, and material embrittlement which can lead to structure failure [1–3]. In order to solve this critical problem, ceramic coatings, including the oxides (Al_2O_3, Cr_2O_3, Y_2O_3, and Er_2O_3), the nitrides (Fe_2N, TiN), the carbides (SiC, TiC), and their composites, are applied to act as a deuterium permeation barrier [4–7]. Among all kinds of ceramic coatings, oxide ones are the most common choice because of their

high deuterium permeation resistance and low cost. Al_2O_3 has been proven to be ideal coating to prevent deuterium gas-driven permeation. This coating could significantly reduce deuterium penetration into the substrate. The combination of Al_2O_3 coating and 316L stainless steel substrate, with high strength, high deuterium permeation resistance, strong thermodynamic stability, and relatively low cost, is the ideal candidate to construct fusion reactors [8–11]. However, Al_2O_3 coating has a huge thermal mismatch with the substrate, 316L stainless steel, because their coefficient of thermal expansions differs widely, causing tremendous residual thermal stress after the system endures thermal shock during processing and serving, such as the operation of the fusion reactor, thus threatening the bond between the coating and the substrate, causing cracks initiating and propagating near the interface [12]. Many efforts have been made to analyze the residual thermal stress in the coating/substrate system in search of the failure mechanism and the optimization methods, most of which are on the micron dimension [13–19]. This paper advances further into nanodimension, because nanothick coatings show better mechanical performance [20, 21], investigating the effect of thickness on the residual stress of nanoscale composite Al_2O_3/Y_2O_3 coating under thermal shock via finite element analysis (FEA), as previous study reveals that Al_2O_3/Y_2O_3 composite coating has better deuterium permeation resistance than the single-layer Al_2O_3 coating due to the interface between the layers [21]. And the thermal residual stress distribution of the coatings was also analyzed to determine the most likely crack initiation site in the coatings. The research is the preliminary work for understanding the crack initiation and propagation mechanism of the nanoscale deuterium permeation barrier and the optimization of nanoscale permeation barrier preparation.

2. Material and Methods

ANSYS 19 is employed to simulate the stress field of the coatings under thermal shock. All models are considered stress-free under 700°C. Because specimens were annealed in a vacuum tube furnace for 2 h at 700°C, the residual stress produced during the deposition process should be eliminated [21]. Max principal stress and max shear stress and max Mises stress are analyzed. Max principal stress is the major criterion of the coating because oxide ceramics are considered brittle material and fragile under tensile stress.

2.1. Analytic Model. In the finite element analysis, displacements are the solution factors that are stored in nodal positions. Loads are defined as prescribed forces and displacements. Thus, the strain and stress increments at any point in the element can be calculated with the interpolation functions. ANSYS transforms those mechanical equilibrium equations into simultaneous equations. And the displacements and forces can be calculated via figuring out elemental stiffness matrixes.

The total strain vector, $\{\Delta\varepsilon\}$, can be expressed as

$$\{\Delta\varepsilon\} = \left\{\Delta\varepsilon^{\mathrm{el}}\right\} + \left\{\Delta\varepsilon^{\mathrm{th}}\right\}, \tag{1}$$

where $\{\Delta\varepsilon^{\mathrm{el}}\}$ is the elastic strain increment vector and $\{\Delta\varepsilon^{\mathrm{th}}\}$ is the thermal strain increment vector.

Within each element, the relation between $\{\Delta\varepsilon\}$ and the strain matrix, $\{B\}$, fulfill the following equation:

$$\{\Delta\varepsilon\} = \{B\}\{\delta\}^e, \tag{2}$$

where $\{\delta\}$ is the displacement vector for any given element (e).

The elastic stress increment vector, $\{\Delta\sigma^{\mathrm{el}}\}$, can be calculated with Hooke's law:

$$\left\{\Delta\sigma^{\mathrm{el}}\right\} = \{D\}\left\{\Delta\varepsilon^{\mathrm{el}}\right\}, \tag{3}$$

where $\{D\}$ is the elastic matrix related to the elastic modulus, E, and Poisson's ratio, ν, for the given material at given temperature.

The thermal stress increment vector, $\{\Delta\varepsilon^{\mathrm{th}}\}$, can be calculated as follows:

$$\left\{\Delta\varepsilon^{\mathrm{th}}\right\} = \{\alpha\}\Delta T, \tag{4}$$

where α is the thermal expansion coefficient and ΔT is the temperature increment.

Stresses are calculated by applying the principle of virtual work.

$$\{\delta\}^T\{\Delta F\}^e = \iiint \{\varepsilon\}^T\{\sigma\}dxdydz. \tag{5}$$

Substitution of equations (3) and (4) into (5) gives

$$\{\Delta F\}^e = \iiint \{B\}^T\{D\}\{\Delta\varepsilon^e\}dxdydz. \tag{6}$$

The element stiffness matrix $\{K\}$ fulfills the equilibrium equation:

$$\{K\}\{\delta\} = \{F\}. \tag{7}$$

In the thermal shock condition, the load vector $\{\Delta F\}$ only includes the thermal force. And the thermal stress can be derived as follows:

$$\{\Delta F\}_T^e = \iiint \{B\}^T\{D\}\{B\}\{\alpha\}dxdydz. \tag{8}$$

2.2. Model Geometry and Material Properties. The models simulate coatings prepared on the 316L stainless steel by radio-frequency magnetron sputtering. The morphologies of the systems in SEM (Hitachi-S4800) are shown in Figure 1. The nanoscale coatings were dense and homogeneous according to the pictures. And the interface between layers and the surface of the top coating was rather smooth, and no obvious defects were observed before the thermal shock test. More detailed information about the preparation and the characterization of the coatings can be checked in [21] and are shown in Figure 2.

The model used in the analysis is made up of 2 parts. One is a cylinder-shape 316L stainless steel substrate with 1 mm in diameter and 0.5 mm in thickness. The other is a coating with

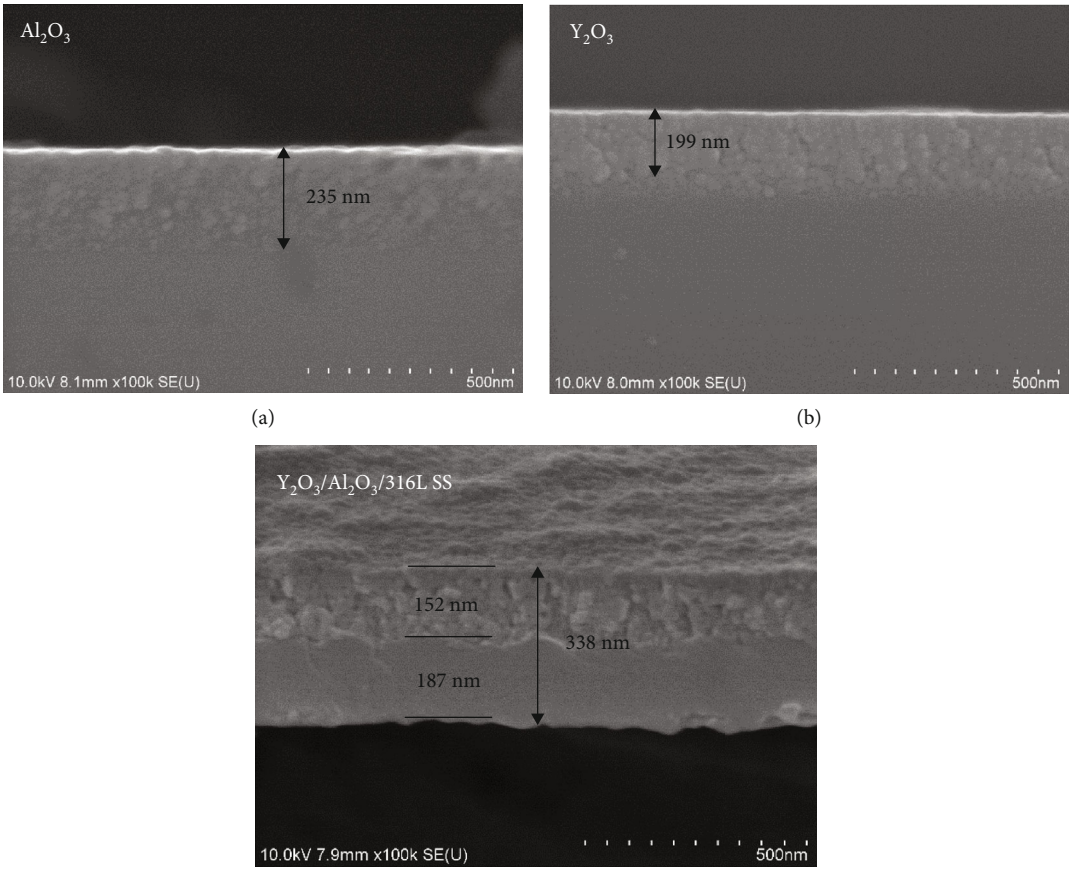

Figure 1: SEM images of the nanoscale coatings [21]: (a) Al_2O_3; (b) Y_2O_3; (c) Y_2O_3/Al_2O_3/316L SS.

thickness, t, deposited on the top surface of the 316L SS substrate. Each part is assumed to be uniform and homogenous. Thus, 2-dimensional axisymmetric models are applied to simplify the analysis. The properties of the materials are shown in Table 1.

2.3. Meshing. In order to construct a nanoscale model with an adequate space for meshing, the standard unit of length in all models is set to micron. Thus, all parameters that involve length are converted to match the change (e.g., Young's modulus of the 316L stainless steel is set to 0.2 N/μm^3). Through this process, it is possible to build a model with adequate numerical size to properly mesh the nanoscale coatings with fine enough elements. The element edge length of the coating is 25 nm while the element edge length of the substrate varied from 25 nm to 50 μm. The total number of the elements for all models is approximately 400,000.

2.4. Boundary Condition and Load. The left edge of the model cannot translate horizontally, and the bottom edge of the model cannot translate vertically. The contacting surfaces are bonded, and no relative tangential translation would occur on the interface between them. In other words, all nodes of the neighbor surfaces on the interface that are at the same point at the initial stage will always stick together. Further experiments can be taken to analyze the actual behavior of the interface for more accurate simulation. The whole section is linearly cooling down from 700°C to room temperature, 25°C, during the static structure simulation. Because the max temperature of the ITER enhanced flux first wall is about 800°C [22], the coatings analyzed in the previous study were annealed at 700°C for stress relief [21]. The mesh and boundary conditions of the finite element model are shown in Figure 3.

3. Result and Discussion

3.1. Al_2O_3 Coating and Y_2O_3 Coating. Stress fields of single-layer nanothick coatings with different thickness cooling from 700°C to 25°C are analyzed. As shown in Figure 4, the max principal stress in both Al_2O_3 and Y_2O_3 coating increases as the thickness increases when the thickness is below 500 nm. Moreover, as the thickness exceeds 500 nm, the max principal stress levels, showing little relevance to the thickness. The max shear stress in both coatings and the max Mises stress in Y_2O_3 show the same trend. And the max stress site of all these kinds of stress is located near the edge of the interface. The only exception is the max Mises stress in the Al_2O_3 coating where the max stress site is located in the center of the interface and the max value shows no relevance to the thickness.

The result reveals that there exists a critical thickness for a single-layer coating in which the exceeding values

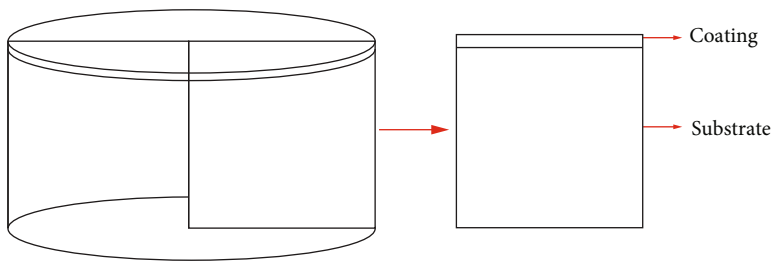

Figure 2: The geometry of the model.

Table 1: Properties of the coating and substrate (25°C).

Materials	Density (kg/m^3)	Young's modulus (GPa)	Poisson's ratio	Coefficient of thermal expansion ($10^{-6}\,K^{-1}$)	Thermal conductivity ($W{\cdot}m^{-1}{\cdot}K^{-1}$)	Specific heat ($J{\cdot}kg^{-1}{\cdot}K^{-1}$)
316L	8000 [19]	200 [19]	0.25 [27]	17.3 [19]	20 [19]	535 [19]
α-Al_2O_3	3980 [19]	370 [19]	0.22 [19]	8.8 [19]	30 [19]	800 [19]
Y_2O_3	5000 [28]	120 [28]	0.26 [28]	8 [28]	2.3 [24]	400 [28]

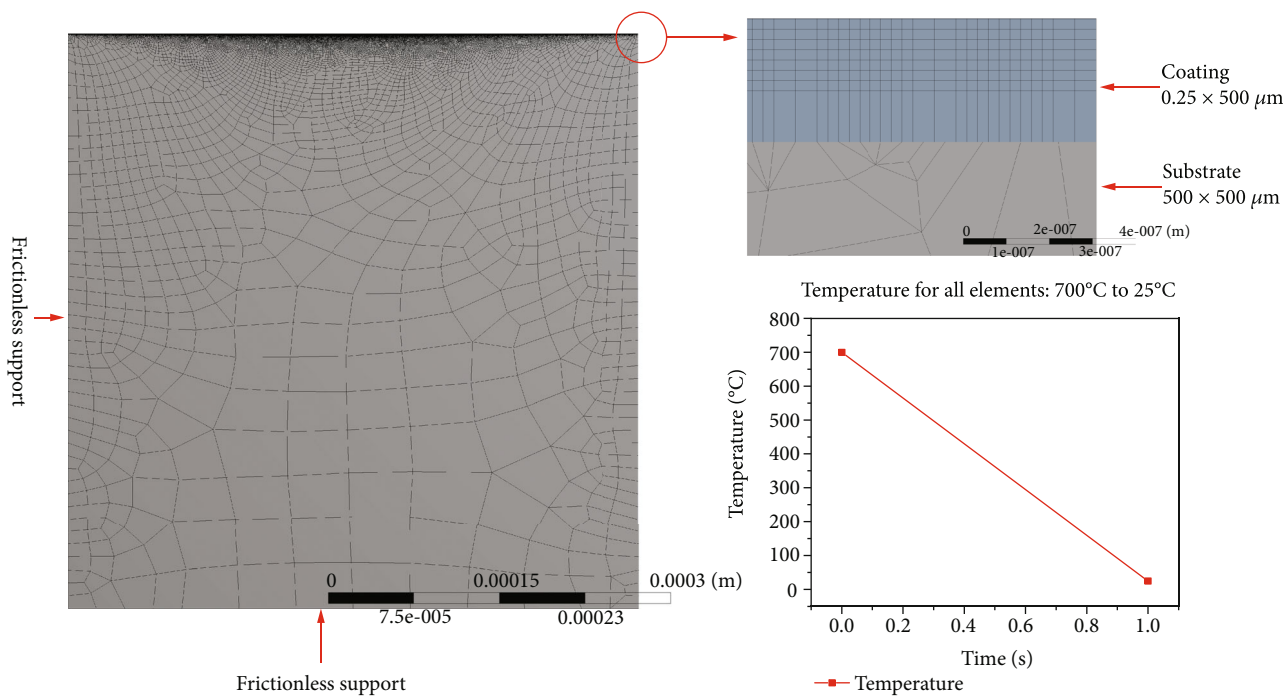

Figure 3: Mesh and boundary condition of the finite element ($t = 250$ nm).

contribute little to the residual stress. The edge of the interface can be considered a stress singular point because of the sudden change of the stiffness. When the stress singular region is small, the thermal residual stress at the edge, σ_p, can be expressed as follows:

$$\sigma_p = \frac{K}{r^{\lambda}}, \quad r < r_0, \tag{9}$$

where r_0 is the vicinity zone of the stress singularity and K is the stress intensity factor. Both K and λ are functions of Poisson's ratio and Young's modulus and the contact angles of the two layers. When the thickness of the coating is small, with the thickness, t, increasing, the λ decreases, meaning that the stress singularity zone becomes wider and the σ_p at the edge increases [23]. When the thickness increases to a point, the bending effect which is negligible for a very thin film due to its very low stiffness plays a more dominant role. And the stress concentrated at the stress singularity will be relieved. According to Stoney's [24] equation, for the coating with enough thickness, the thermal stress in thin coating can be derived as follows:

$$\sigma_f = \frac{E_{ef}\int_{T_f}^{T_i}(\alpha_s - \alpha_f)dT}{1 + 4(E_{ef}/E_{es})(h/H)}, \tag{10}$$

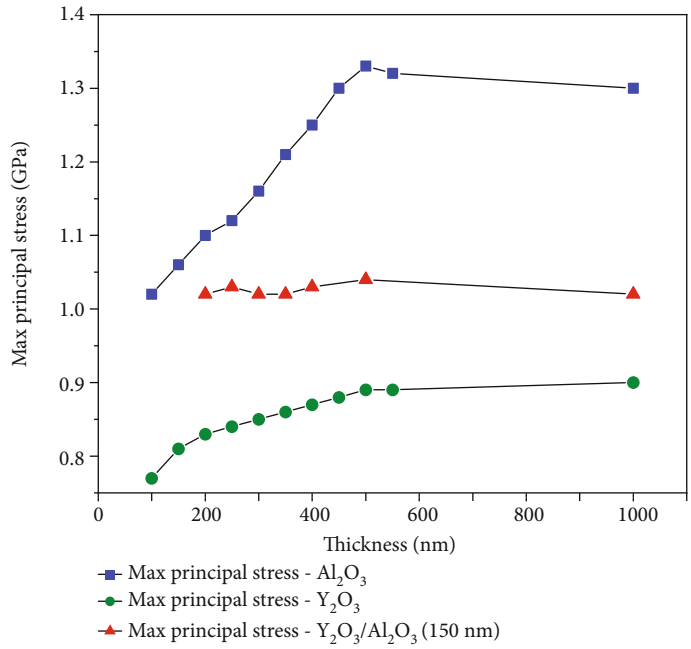

(a) Effect of the thickness on the max principal stress

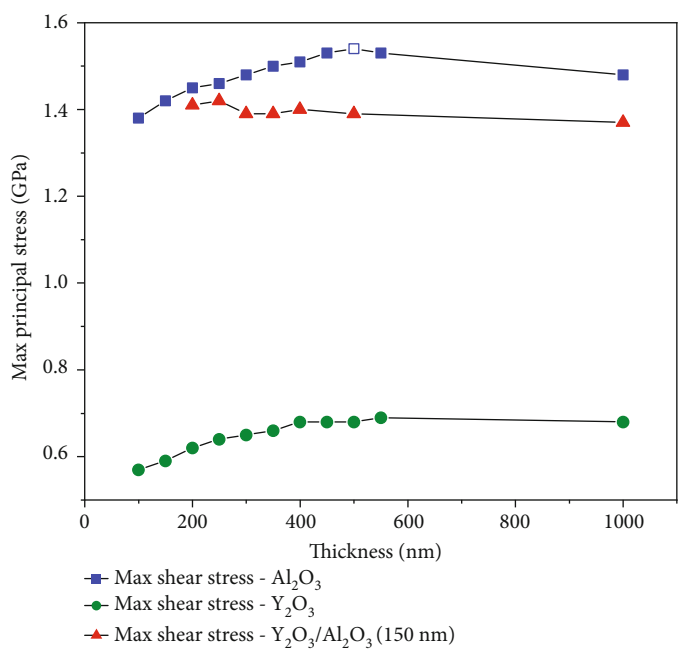

(b) Effect of the thickness on the max shear stress

Figure 4: Continued.

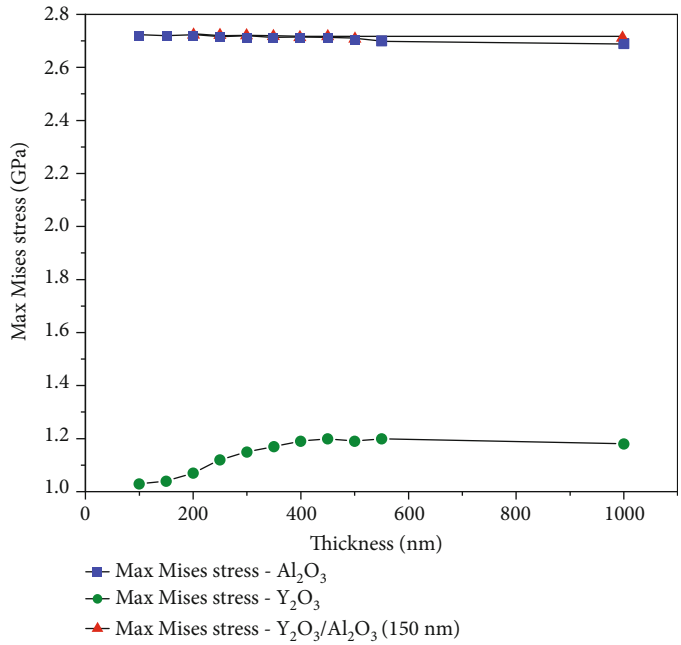

(c) Effect of the thickness on the max Mises stress

Figure 4: Effect of thickness on different kinds of stress in the system: (a) effect of the thickness on the max principal stress, (b) effect of the thickness on the max shear stress, and (c) effect of the thickness on the max Mises stress.

where $E_{ef} = E_f/(1-\nu_f)$ and $E_{es} = E_s/(1-\nu_s)$ are effective Young's modulus of the coating and the substrate, respectively. ν_f and ν_s are Poisson's ratio of the coating and substrate, respectively. h and H are coating thickness and substrate thickness, respectively. T_i and T_t are the initial temperature and terminal temperature. α_f and α_s are the thermal expansion coefficients of the coating and substrate, respectively. When the thickness of the coating is big enough, with the thickness increasing, the thermal stress decreases, because when the coating-substrate system is bent, bending-induced stress relaxation occurs. The thicker the coating, the more the stress reduction [25].

However, under the given condition in this simulation, the thickness-induced stress relief effect is still negligible even the thickness of the coating is 1000 nm. Meanwhile, 500 nm is the critical thickness for both Y_2O_3 coating and Al_2O_3 coating where the stress singularity effect on the increase in stress with the increasing thickness becomes negligible and the stress is almost not relevant to the thickness. It indicates that preparing coatings with more than 500 nm thickness will get consistent thermal shock endurance. It can make the quality control and the life span evaluation easier when the coatings are mass manufactured. But when the thickness of coating is below 500 nm, thinner coatings will have less residual stress and thus better thermal shock endurance.

On the other hand, all 3 kinds of stress in the Y_2O_3 coating are smaller compared with the Al_2O_3 coating at the same thickness because Young's modulus of Y_2O_3 is much smaller than that of the Al_2O_3, as their coefficients of thermal expansion are almost even. Y_2O_3 coating is more deformable thus resulting in less residual stress in the system during thermal shock. Deformable material is favored when fabricating a deuterium permeation barrier exposed to thermal shock.

It should be noted that except the max Mises stress in the Al_2O_3 coating, the max stress site of all 3 kinds of stress of all models with varied thickness is located near the edge of the interface, as shown in Figure 5. The max Mises stress in the Al_2O_3 coating is located at the center of the interface. However, the local stress near the edge also concentrates near the interface. It reveals that the edge near the interface is the most likely crack initiation site with the most severe stress concentration in the system. It also shows that the stress distribution is more a geometry-relevant issue than a material property-relevant one.

3.2. Composite Coating. Previous work shows that the Y_2O_3/Al_2O_3 composite coating has excellent deuterium permeation resistance because the interface between layers contains defects that would trap deuterium and the lattice mismatch of 2 layers would cause the transmission mechanism of the deuterium to change [21]. In order to test the thermal shock endurance of this deuterium permeation barrier, the Y_2O_3/Al_2O_3/316L SS system was simulated using finite element analysis. The thickness of the Al_2O_3 layer is 150 nm which is close to that of the specimen as shown in Figure 1. The thickness of the Y_2O_3 top coating varies from 50 nm to 850 nm. As shown in Figure 4, the max stress in the Y_2O_3/Al_2O_3 coating was determined by the Al_2O_3 coating under these specific conditions. The max value of all 3 kinds

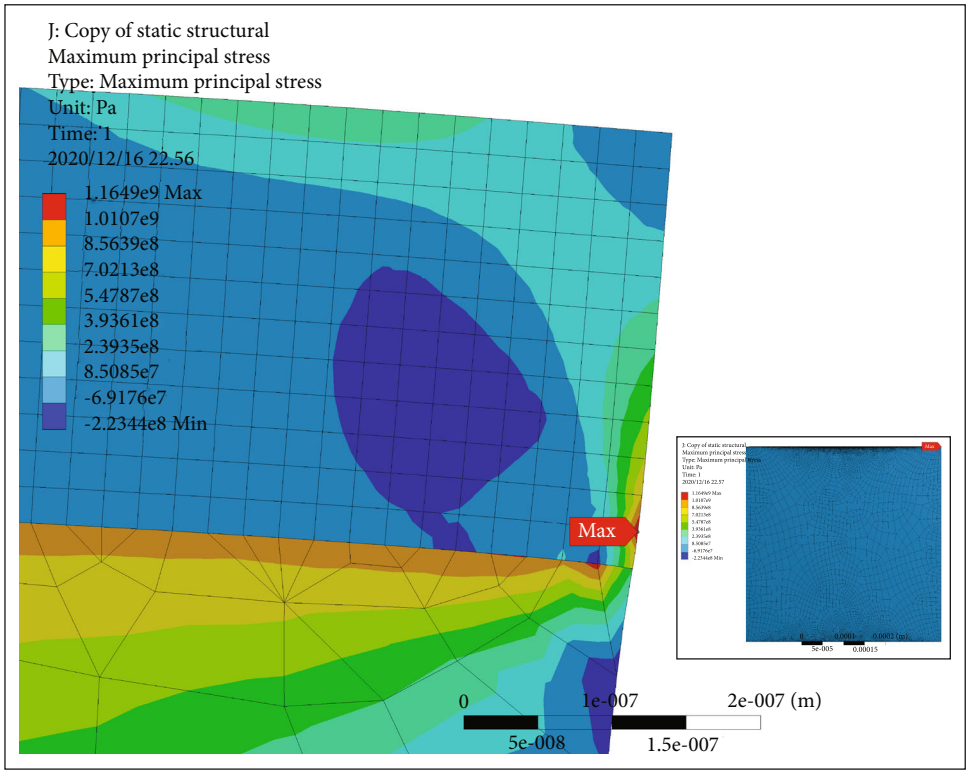

(a)

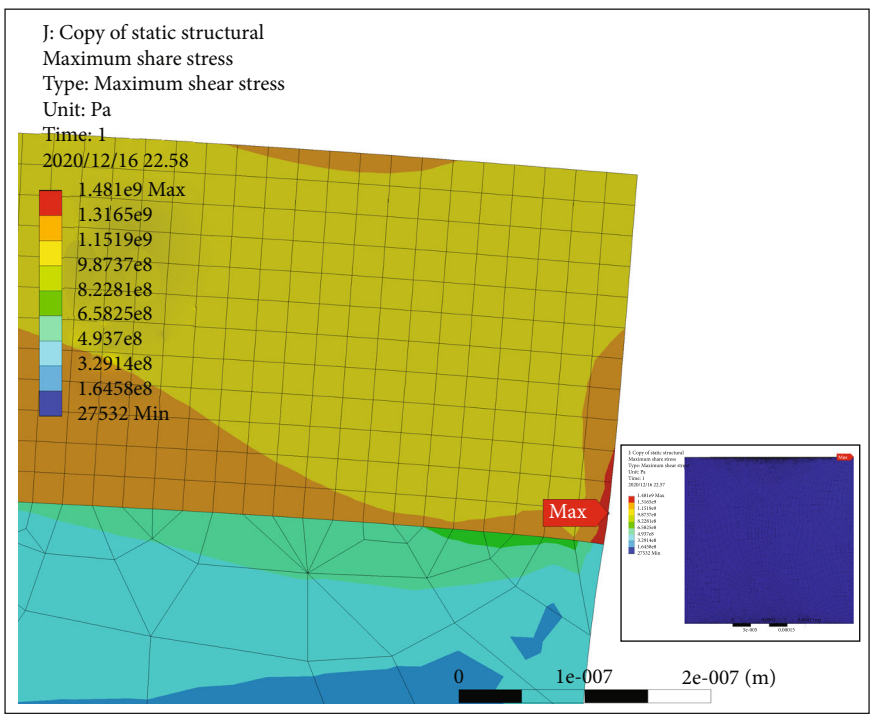

(b)

Figure 5: Continued.

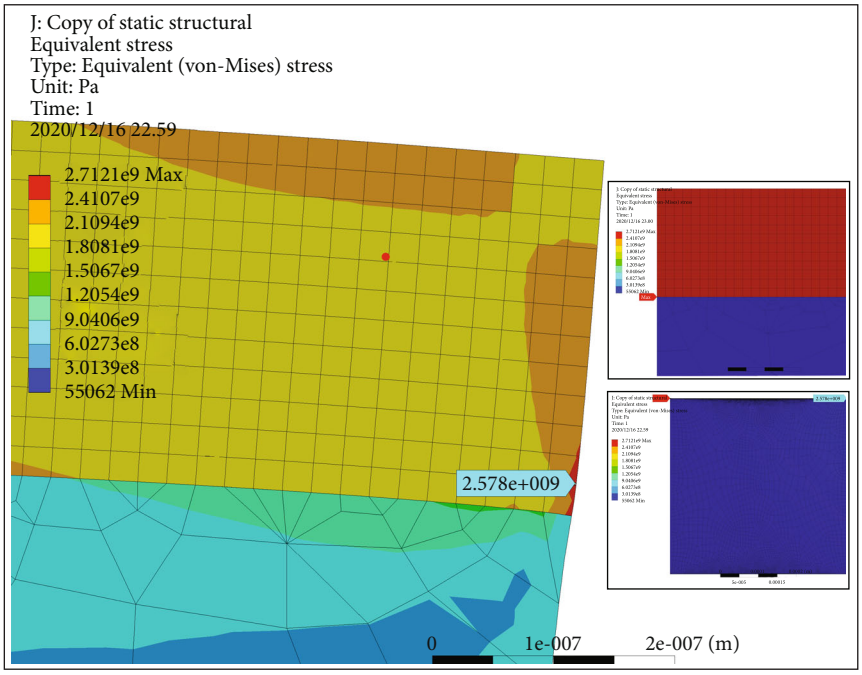

(c)

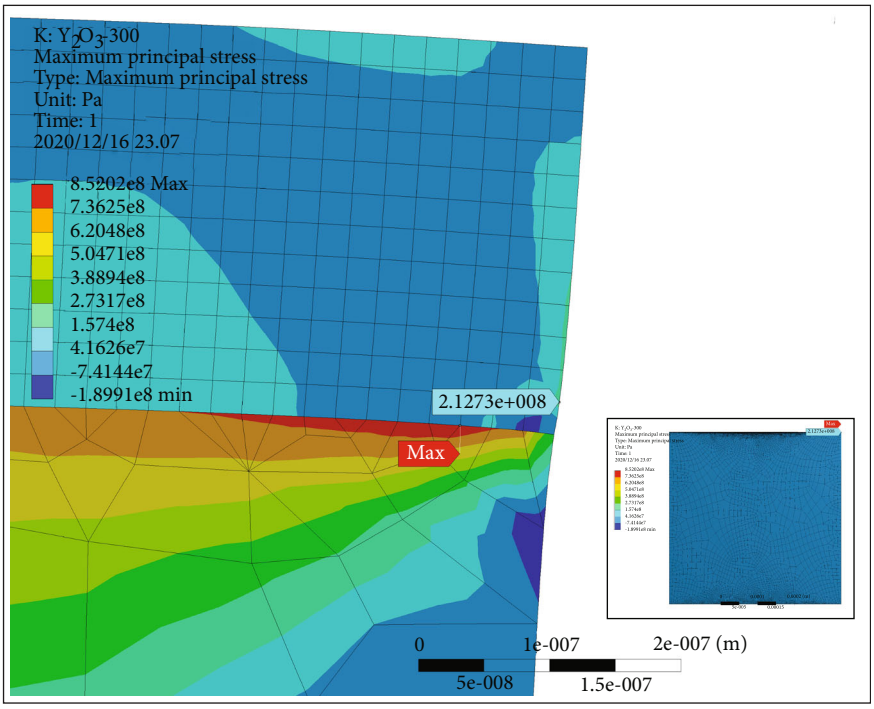

(d)

Figure 5: Continued.

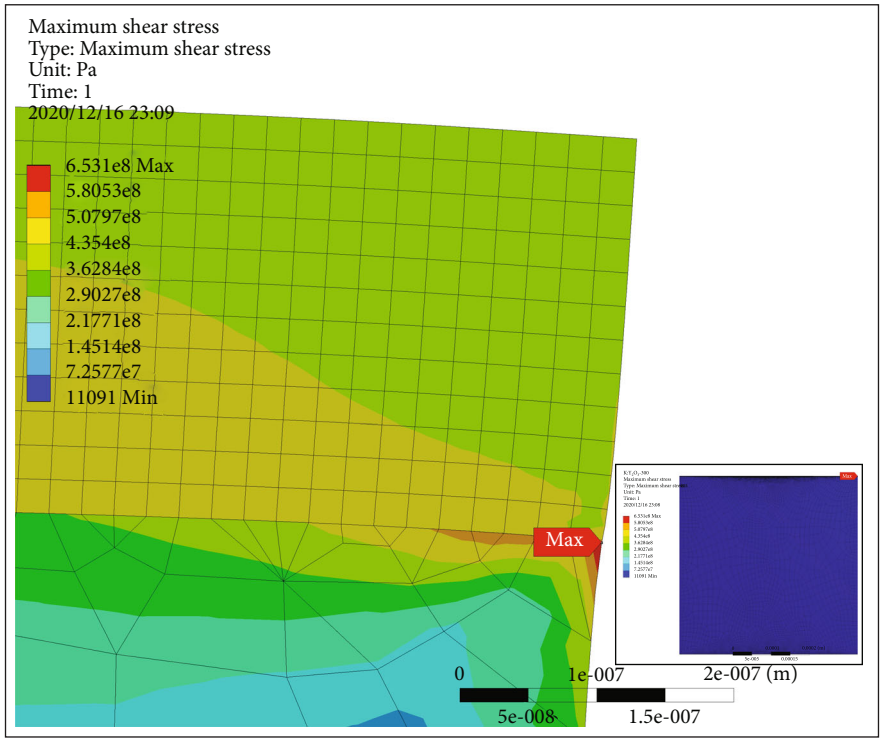

(e)

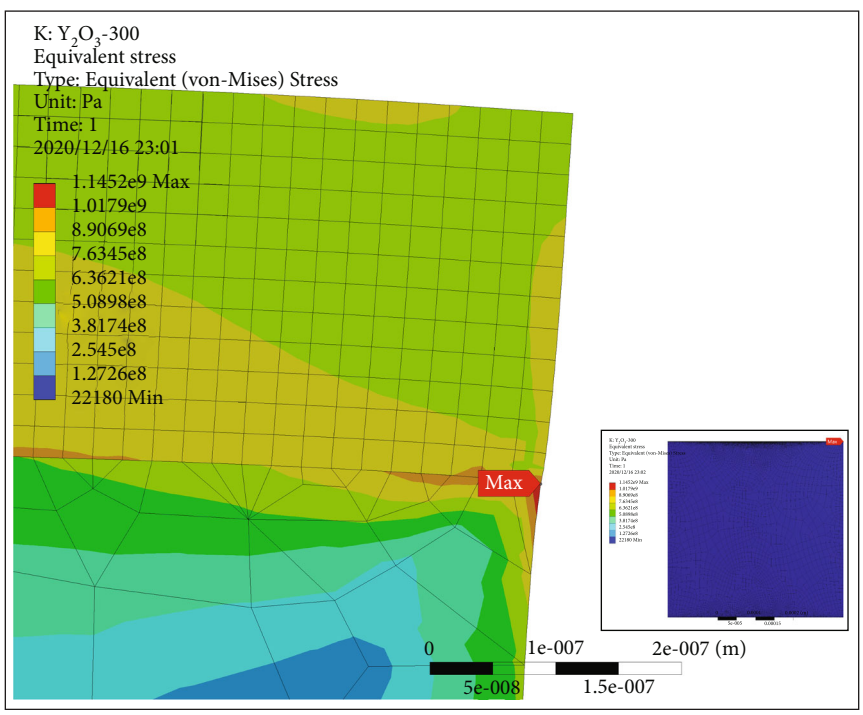

(f)

Figure 5: Comparison of 3 kinds of stress distribution: (a) max principal stress (Al_2O_3, $t = 300$ nm); (b) max shear stress (Al_2O_3, $t = 300$ nm); (c) max Mises stress (Al_2O_3, $t = 300$ nm); (d) max principal stress (Y_2O_3, $t = 300$ nm); (e) max shear stress (Y_2O_3, $t = 300$ nm); (f) max Mises stress (Y_2O_3, $t = 300$ nm).

of stress is almost equal to that of the 150 nm thick Al_2O_3 coating.

As shown in Figure 6, the max stress in the Y_2O_3/Al_2O_3 coating occurs in the Al_2O_3 layer and about an order higher than that in the Y_2O_3 coating. Though the tensile stress of Y_2O_3 is not included in the CRC handbook, all tensile stresses of oxide ceramics listed in the CRC handbook are of the same order [26]. Thus, under the assumption that the tensile

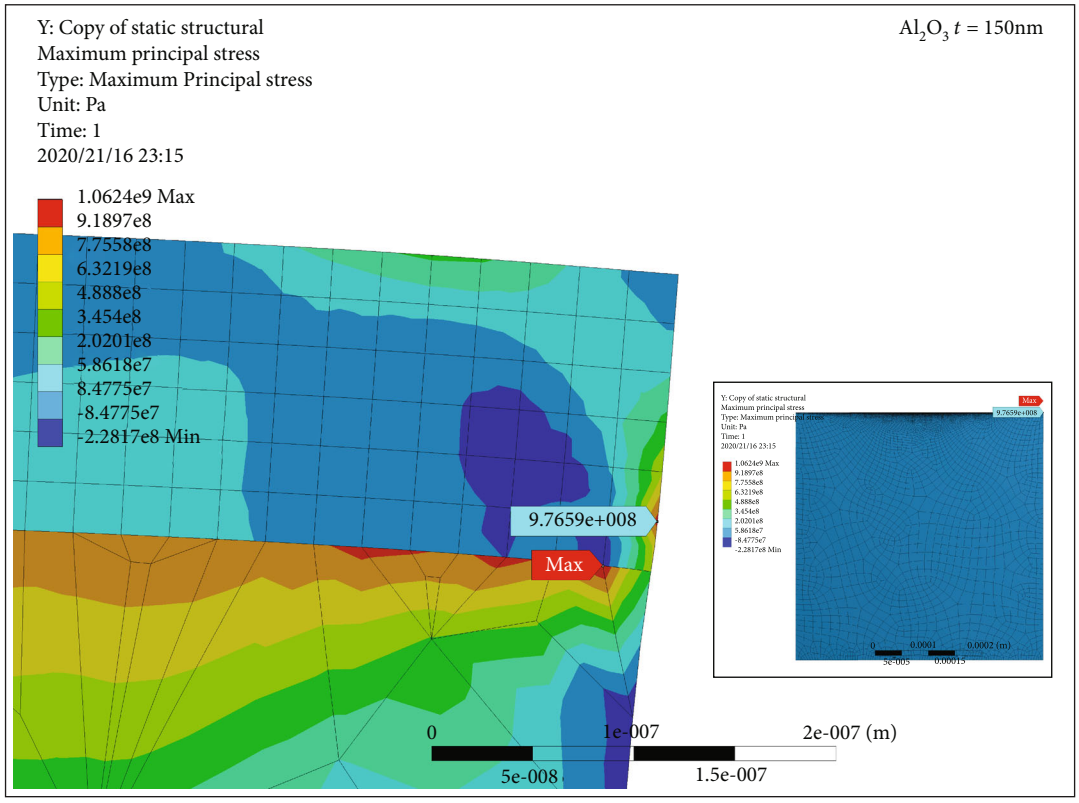

(a) Al_2O_3, t = 150 nm

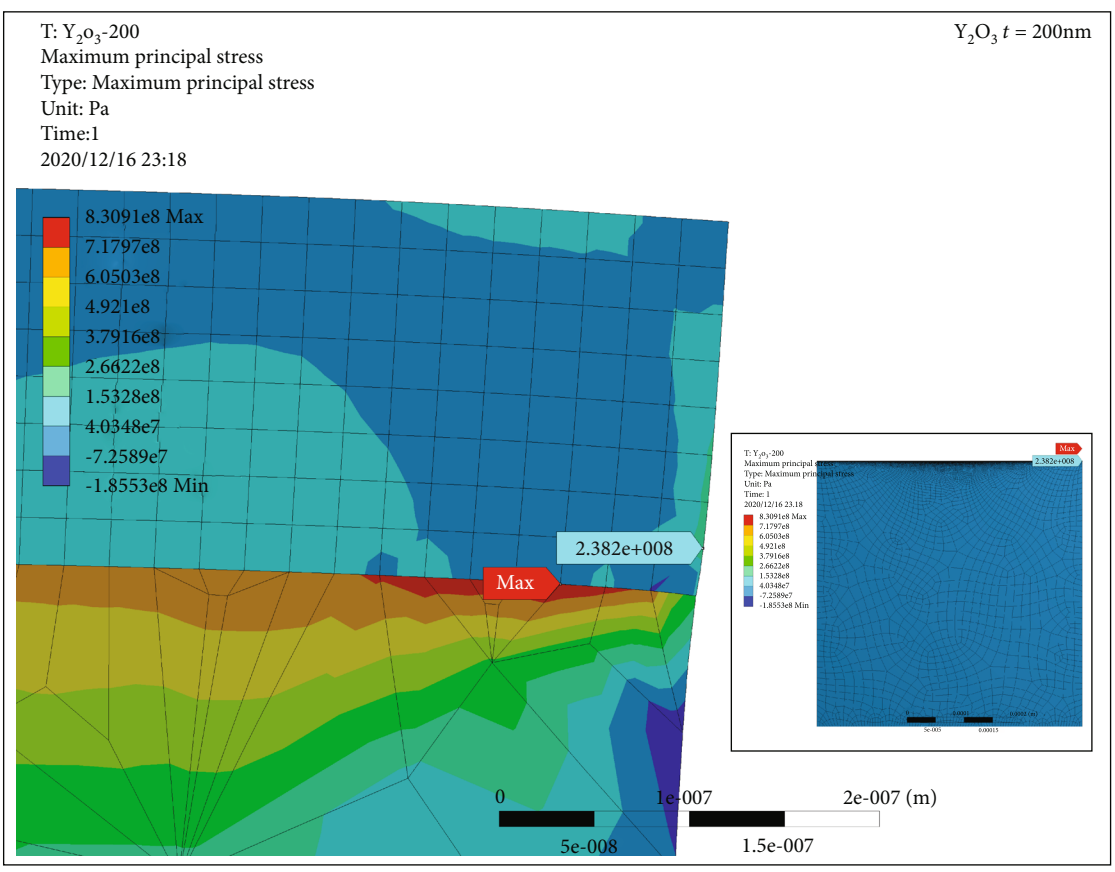

(b) Y_2O_3, t = 200 nm

Figure 6: Continued.

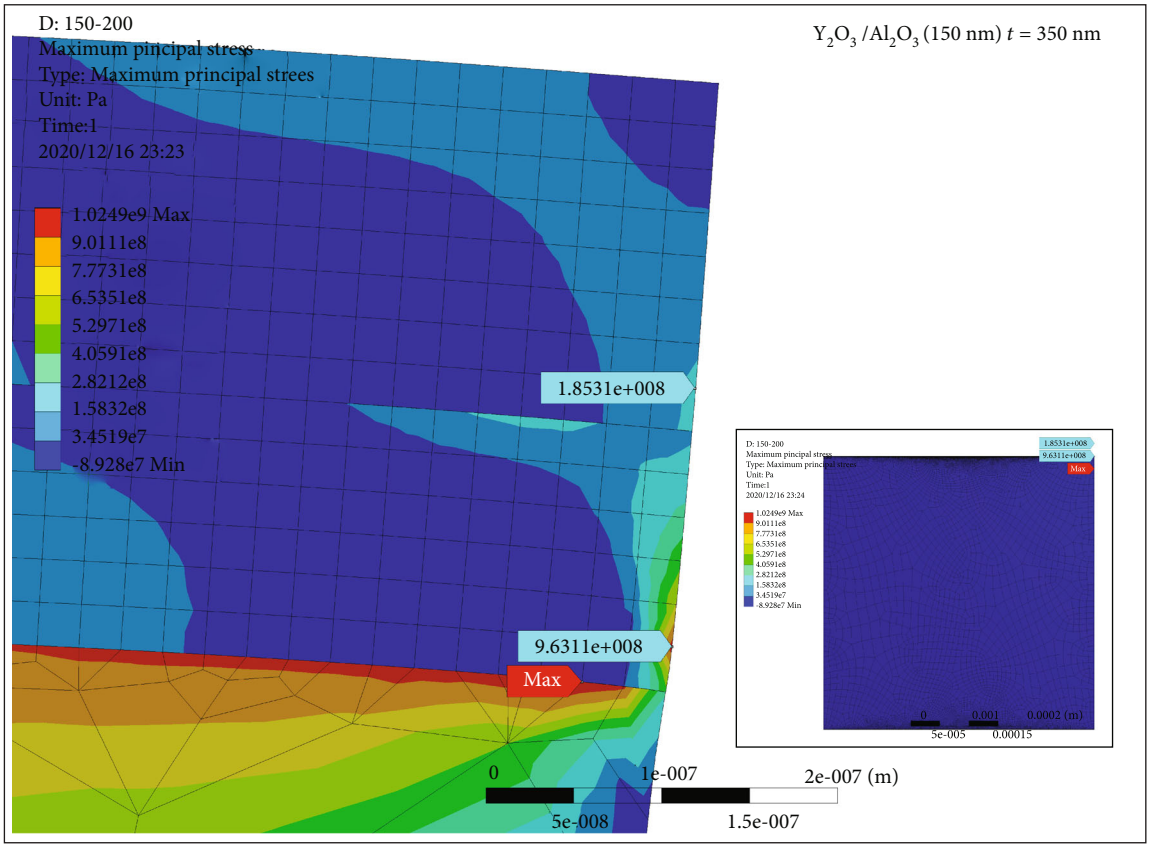

(c) Y_2O_3/Al_2O_3 (150 nm), t = 350 nm

Figure 6: Comparison of the max principal stress in 3 systems of the same individual thickness: (a) max principal stress in Al_2O_3 coating (t = 150 nm); (b) max principal stress in Y_2O_3 coating (t = 200 nm); (c) max principal stress in Y_2O_3/Al_2O_3 (150 nm) coating (t = 350 nm).

stresses of Y_2O_3 and Al_2O_3 are of the same order, the crack will originate from the boundary of the Al_2O_3 layer. Moreover, according to the result, stress distribution in each layer of the composite coating is similar to that of the monolayer coating of the same individual thickness. And coating an Y_2O_3 top coat over the Al_2O_3 layer have a little effect on the stress in the Al_2O_3 layer. And the max stress in the Y_2O_3 top coat is about 20% lower than that of the monolayer coating. The adjacent material, Al_2O_3, has a more similar CTE to the Y_2O_3 than the 316L SS and causes less stress concentration at the edge. However, the Al_2O_3 is too thin to make such a big effect. The mesh quality of the adjacent layer also contributes to the decline of the max stress as the mesh of Al_2O_3 is much finer and regular than that of the 316L SS.

Adding an Y_2O_3 top coat have a little effect on the thermal stress in the Al_2O_3. And the thermal shock behavior of the Al_2O_3 layer in the bilayer Y_2O_3/Al_2O_3 coating should be similar to that of the single-layer Al_2O_3 coating at the same thickness.

4. Conclusion

(1) Y_2O_3 coating will introduce less residual stress under thermal shock compared with Al_2O_3 coating due to its smaller Young's modulus

(2) The edge of the interface between the coating and the substrate is the most severe stress concentration site and thus the most likely crack initiation site in Al_2O_3, Y_2O_3, and Y_2O_3/Al_2O_3 coatings. And the max stress site and stress distribution pattern are more a geometry-dependent issue than a material property-relevant one

(3) The residual thermal stress increases as the thickness of the coating increases, and the rate of the increase declines as the thickness increases due to the stress singularity effect. When the thickness of the coating reaches 500 nm, the residual thermal stress becomes less dependent on thickness

(4) Adding an Y_2O_3 layer over the Al_2O_3 coating would not significantly affect the residual thermal stress in the Al_2O_3 coating. The thermal shock behavior of the Al_2O_3 layer in the Y_2O_3/Al_2O_3 composite deuterium permeation barrier could be evaluated as that of the single-layer Al_2O_3 coating of the same thickness of Al_2O_3

Data Availability

The data used to support the findings of this study are included within the article.

Conflicts of Interest

The authors declare that there is no conflict of interest regarding the publication of this paper.

Acknowledgments

Thanks are due to the support of the team in the National Engineering Research Center of Nonferrous Metals Materials and Products for New Energy, GRINM Group Co., Ltd. This work is funded by the National Key Research and Development Program of China (2016YFB0600102, 2016YFB0600103) and the National Natural Science Foundation of China (NSFC, 51671034).

References

[1] S. Fukada, Y. Oya, and Y. Hatano, "Review of recent Japanese activities on tritium accountability in fusion reactors," *Fusion Engineering and Design*, vol. 113, pp. 231–235, 2016.

[2] J. Konys, D. L. Smith, T. Muroga, and V. Evitkhin, "Development of coatings for fusion power applications," *Journal of Nuclear Materials*, vol. 307-311, pp. 1314–1322, 2002.

[3] T. Otsuka, K. Goto, A. Yamamoto, and K. Hashizume, "Effects of shot-peening on permeation and retention behaviors of hydrogen in alpha iron," *Fusion Engineering and Design*, vol. 136, pp. 509–512, 2018.

[4] Y. Wu et al., "The adhesion strength and deuterium permeation property of SiC films synthesized by magnetron sputtering," *International Journal of Hydrogen Energy*, vol. 41, pp. 10837–10839, 2016.

[5] T. V. Kulsartov, K. Hayashi, M. Nakamichi et al., "Investigation of hydrogen isotope permeation through F82H steel with and without a ceramic coating of Cr_2O_3-SiO_2 including $CrPO_4$ (out-of-pile tests)," *Fusion Engineering and Design*, vol. 81, no. 1-7, pp. 701–705, 2006.

[6] S. Liu, X. Ju, J. Qiu et al., "Tritium-permeation-barrier properties of erbium oxide (TPB) coating on CLAM steel," *Fusion Engineering and Design*, vol. 138, pp. 347–351, 2019.

[7] A. Houben, M. Rasiński, L. Gao, and C. Linsmeier, "Tungsten nitride as tritium permeation barrier," *Nuclear Materials and Energy.*, vol. 24, p. 100752, 2020.

[8] Y.-P. Xu, F. Liu, S.-X. Zhao et al., "Deuterium permeation behavior of HTUPS4 steel with thermal oxidation layer," *Fusion Engineering and Design*, vol. 113, pp. 201–204, 2016.

[9] Q. Han, Y. Geng, R. Setchi, F. Lacan, D. Gu, and S. L. Evans, "Macro and nanoscale wear behaviour of Al- Al_2O_3 nanocomposites fabricated by selective laser melting," *Composites Part B Engineering*, vol. 127, pp. 26–35, 2017.

[10] H. Liu, J. Tao, J. Xu, Z. Chen, and X. Luo, "Microstructure and mechanical properties of alumina coatings prepared by double glow plasma technique," *Applied Surface Science*, vol. 256, no. 20, pp. 5939–5945, 2010.

[11] L. Wang, J. J. Yang, Y. J. Feng et al., "Preparation and characterization of Al_2O_3 coating by MOD method on CLF-1 RAFM steel," *Journal of Nuclear Materials*, vol. 487, pp. 280–287, 2017.

[12] L. Xu, S. Liu, M. Wang, and S. Zhou, "Crack initiation and propagation mechanism of Al_2O_3-DBC substrate during thermal cycling test," *Engineering Failure Analysis*, vol. 116, p. 104720, 2020.

[13] F. Yang, X. Xiang, G. Lu et al., "Tritium permeation characterization of Al_2O_3/FeAl coatings as tritium permeation barriers on 321 type stainless steel containers," *Journal of Nuclear Materials*, vol. 478, pp. 144–148, 2016.

[14] H. Liu, J. Tao, Y. Gautreau, P. Zhang, and J. Xu, "Simulation of thermal stresses in SiC-Al_2O_3 composite tritium penetration barrier by finite-element analysis," *Materials and Design*, vol. 30, no. 8, pp. 2785–2790, 2009.

[15] J. Huang, H. Xie, L.–. M. Luo, X. Zan, D.–. G. Liu, and Y.–. C. Wu, "Preparation and properties of FeAl/Al_2O_3 composite tritium permeation barrier coating on surface of 316L stainless steel," *Surface and Coating Technology*, vol. 383, p. 125282, 2020.

[16] H. Yang, Z. Shao, W. Wang, X. Ji, and C. Li, "A composite coating of GO-Al_2O_3 for tritium permeation barrier," *Fusion Engineering and Design*, vol. 156, p. 111689, 2020.

[17] Y. Wu, D. He, S. Li, X. Liu, S. Wang, and L. Jiang, "Deuterium permeation properties of Y_2O_3/Cr_2O_3 composite coating prepared by MOCVD on 316L stainless steel," *International Journal of Hydrogen Energy*, vol. 41, pp. 7425–7430, 2016.

[18] Z. Liu, F. Meng, and L. B. Yi, "Simulation of the effects of different substrates, temperature, and substrate roughness on the mechanical properties of Al_2O_3 coating as tritium penetration barrier," *Nuclear Science and Techniques*, vol. 30, no. 4, 2019.

[19] H. Liu, J. Tao, P. Zhang, and J. Xu, "Modeling of residual stresses in functionally gradient Al_2O_3 coating on 316L substrate," *Journal of Computational and Theoretical Nanoscience*, vol. 5, no. 8, pp. 1677–1680, 2008.

[20] C. Zhou, N. Wang, and H. Xu, "Comparison of thermal cycling behavior of plasma-sprayed nanostructured and traditional thermal barrier coatings," *Materials Science and Engineering A*, vol. 452-453, pp. 569–574, 2007.

[21] W. Wang, Q. Yu, X. Liu, and Z. Lu, "Preparation of Al_2O_3/Y_2O_3 composite coating for deuterium permeation reduction," *Journal of Rare Earths*, vol. 38, no. 11, pp. 1237–1242.

[22] G. le Marois, E. Rigal, and P. Bucci, "Fusion reactor first wall fabrication techniques," *Fusion Engineering and Design*, vol. 61-62, pp. 103–110, 2002.

[23] B. Gu and P. E. Phelan, "Thermal peeling stress analysis of thin-film high- _TC_ superconductors," *Applied Superconductivity*, vol. 6, no. 1, pp. 19–29, 1998.

[24] G. G. Stoney, "The tension of metallic films deposited by electrolysis," *Proceedings of the Royal Society of London A*, vol. 82, pp. 172–175, 1909.

[25] J. Haider, M. Rahman, B. Corcoran, and M. S. J. Hashmi, "Simulation of thermal stress in magnetron sputtered thin coating by finite element analysis," *Journal of Materials Processing Technology*, vol. 168, no. 1, pp. 36–41, 2005.

[26] J. F. Shackelford, Y- H. Han, S. Kim, and S-H. Kwon, *CRC Materials Science and Engineering Handbook*, CRC Press, Boca Raton, 4th edition, 2015.

[27] R. A. Van Konynenburg, R. D. McCright, A. K. Roy, and D. A. Jones, *Engineered Materials Characterization Report for the Yucca Mountain Site Characterization Project Volume 2: Design Data*, Lawrence Livermore National Lab, CA (United States), 1995.

[28] W. Martienssen and H. Warlimont, *Springer Handbook of Condensed Matter and Materials Data*, Springer, Berlin, Heidelberg, 2005.

Hindawi
International Journal of Photoenergy
Volume 2021, Article ID 8839411, 12 pages
https://doi.org/10.1155/2021/8839411

Research Article

Investigation on Mechanical Properties of GH4720Li at High Strain Rates at Wider Temperature Range

Jie Chen, Haifeng Zhang, Yunlong Zhang, Hongtao Zhang, Qingxiang Yang, and Longhai Ye

Anyang Institute of Technology, Anyang 455000, China

Correspondence should be addressed to Yunlong Zhang; hnagzyl@126.com

Received 28 September 2020; Revised 16 December 2020; Accepted 7 January 2021; Published 15 January 2021

Academic Editor: Xuelong Hao

In this paper, the dynamic mechanical properties of GH4720Li nickel-base alloy under a large temperature range and high and low strain rates were studied by the hot compression test. The difference of mechanical properties of GH4720Li alloy under high and low strain rates was analyzed from the perspective of microstructure. The hot compression test experimental results showed that the true stress of GH4720Li alloy decreased at a low strain rate as the trial temperature elevated. Nevertheless, it was abnormal that the true stress increased at high strain rate condition as temperature elevated. By comparing the microstructure under high and low strain rates, it was found that the precipitates under low strain conditions contained a large amount of Cr (Mo). However, the content of Cr (Mo) in the precipitates at a high strain rate decreased, while the content of Fe increased. It would be concluded that Cr (Mo) would reduce the compressive strength and plasticity of GH4720Li alloy, while Fe would increase the compressive strength and plasticity of GH4720Li alloy. In addition, under the condition of a low strain rate, the shape of Cr (Mo) precipitates obtained at 20°C was lamellar, but it was spherical at 800°C. The compressive strength of GH4720Li composites with lamellar precipitates was higher than that of spherical precipitates.

1. Introduction

GH4720Li was a kind of advanced high-strength wrought Ni-matrix superalloy, which was developed for application in high-integrity rotating components of gas turbine engines such as discs and turbine blades [1–3]. Over the past few years, a great deal of efforts had been made with regard to GH4720Li alloys [4–9]. Wan et al. had investigated the high-temperature deformation behavior of an U720ULi alloy by the hot compression test at a temperature of 1060°C~1080°C and strain rates of 0.001~10 s^{-1}. It demonstrated that high activation energy for $\gamma + \gamma'$ dual-phase microstructures was mainly attributed to the precipitation hardening effect of γ' (Ni_3 (Al, Ti)) particles [4]. Zhao et al. have studied fine-grain ingot casting technology of a Ni-base superalloy 720Li by the hot compression test at a temperature of 1110°C~1150°C and strain rates of 0.001-0.1 s^{-1}, and they found that a hot die forged pancake was produced with an ASTM 7 fine grain structure, which demonstrated the potential of GH720Li alloy disk to meet the component technical requirement [5]. Liu et al. had inspected the hot deformation behavior of U720Li alloy with fine, coarse, and mixed grains by the hot compression test in the range of 1040°C~1190°C and strain rates of 0.01~0.5 s^{-1}. In the single-phase region, dynamic recrystallization (DRX) mainly occurred along the boundaries, while a decrease in the grain size accelerated DRX kinetics. In the two-phase region, DRX on grain boundaries of coarse grain was limited [6]. Yu et al. had identified a relationship between the dynamic recrystallization (DRX) and presence of γ' precipitates for Udimet720Li by the hot compression test at a temperature of 1070°C~1190°C and strain rates of 0.01~0.5 s^{-1}. For coarse grain, the nucleation of DRX grains was influenced by the γ' interparticle spacing [7]. Qu et al. had established a constitutive equation and processing map of GH4720Li alloy based on the flow stress

during the hot compression test at a temperature of 1100°C~1170°C and strain rates of 0.01~1 s^{-1} [8]. Monajati et al. had investigated the hot temperature deformation behavior of nickel-base superalloy UDIMET720 by the hot compression test at 1000°C~1175°C at strain rates of 10^{-3}~1 s^{-1}, and it applied the power-law, the Sellars-Tegart, and an empirical equation to thermomechanical behavior [9]. The mechanical properties of GH4720Li alloy were mainly concentrated in a low strain rate and high-temperature section, but few studies on the mechanical properties of high strain and medium-low-temperature section. It was also of great practical significance to study the mechanical properties of GH4720Li alloy in the medium- and low-temperature section and high strain rate.

In general, turbine blades were small components, which were wholly exposed to a narrow range of high temperatures. But the turbine discs were relatively larger components. Hence, in the process of actuation, there existed a wide range of temperature gradient conditions on the surface of the turbine disk. In other words, there existed a wide range of temperature difference between different parts such as the interior and edges of a turbine disc. For example, the service temperature of the inner diameter part was relatively low, while the temperature of the web part was relatively medium. At the same time, the temperature of the rim part was the highest.

Therefore, in addition to high-temperature mechanical properties of GH4720Li alloy, it was necessary to investigate the mechanical properties at low and intermediate temperatures. Besides, the turbine discs suffered the scour by high-temperature and high-pressure gas and may be impact by a foreign object; in other words, the turbine discs got damaged not only by creep and fatigue but also impact, which would lead to the failure of an engine [10]. Thus, it was important to research mechanical properties of GH4720Li alloy at the high strain rate. In the open literature, there were few reports on the high strain rate dynamic mechanical properties of GH4720Li alloy at a wide range of temperatures. Therefore, the high strain rate mechanical properties of GH4720Li alloy were investigated under a wide range of temperature changes. In the same temperature range, the mechanical properties of GH4720Li alloys with high strain rate and low strain rate showed different trends. The differentiation of mechanical properties between high strain rate and low strain rate was explained in detail.

2. Experimental Details

The chemical compositions of GH4720Li superalloys were measured as C, Cr, Al, Mo, B, Ti, Mn, Si, Nb, Ni, and Fe. The size of specimen at a strain rate of 10 s^{-1} is ∅6 mm × 9 mm, and the size of specimen at a strain rate of 1000 s^{-1} and 5000 s^{-1} is ∅5 mm × 5 mm. Hot compression tests were conducted at a temperature of 20°C, 200°C, 400°C, 800°C, and 1000°C, and the strain rates were set to be 10 s^{-1}, 1000 s^{-1}, and 5000 s^{-1}, respectively. Uniaxial compression tests of the nickel-base superalloy GH4720Li were conducted, and three duplicate tests were carried out at each temperature and strain rate. Low strain rate isothermal compression experiments were carried out on a Gleeble-3500 mechanical simulator. The simulator was equipped with a control system to impose exponential decay of the actuator speed to obtain a constant strain rate. The deformation temperature was measured by thermocouples that were welded to the center region of the specimen surface. The strain, deformation temperature, and strain rate were automatically controlled and recorded. However, high strain rate compression experiments were carried out on an enhanced split Hopkinson bar system. The enhanced split Hopkinson bar technique was originally developed by Wang et al. for the experiments at elevated temperatures [10]. When the specimen was sandwiched between the bars in the traditional way, a temperature gradient developed in the elastic bars during the specimen preheating. Such a temperature gradient could cause an unwanted change in the elastic constants, and thus the mechanical impedance of the bars. As a result, the state of the stress wave propagation in the elastic bars could be affected. To avoid such influence, the incident and transmit bars of the split Hopkinson bar system were left outside the furnace with an environment temperature. A synchronous bar-moving system was utilized to make sure that the incident and transmitted bars were in full contact with the specimen microseconds before the stress wave arrived at the far end of the incident bar. To reduce the end friction during compression tests, the specimen ends were first polished by waterproof SiC paper and then greased in the tests. Prior to the hot compression, the specimens were heated to deformation temperature at a rate of 10°C/s and hold for 5 min to eliminate thermal gradients as well as to ensure uniform temperature of the specimens. Then, the specimens were compressed with a specified strain rate and quenched in water immediately to retain the microstructures at elevated temperature. Finally, the specimens were after polished and etched in the corrosive solution. The microstructure and chemical composition of the phases were observed by a Scanning Electron Microscope (SEM) with energy dispersive spectrometry (EDS). X-ray diffraction meter (XRD) was applied to determine the phase composition.

3. Result and Discussions

3.1. The True Stress-Strain Curves. The true stress-strain curves of hot compression of GH4720Li alloys under different conditions are shown in Figure 1. It can be seen from Figure 1(a) that the flow stress decreased gradually as the temperature increased at the low strain rate (10 s^{-1}). However, the abnormal mechanical properties of GH4720Li alloy appeared at a high strain rate (1000 s^{-1}/5000 s^{-1}). When the strain rate was 1000 s^{-1}/5000 s^{-1}, the flow stress did not decrease with an increase of deformation temperatures; on the contrary, when the temperature reached 200°C, the true stress value of GH4720Li alloy reached the maximum, followed by the stress value at 800°C. Under the condition of a high strain rate, the stress values of GH4720Li alloy from large to small were 200°C, 800°C, 400°C, 20°C, and 1000°C, as shown in Figures 1(b) and 1(c). Therefore, GH4720Li exhibited completely different mechanical properties at high and low strain rates. To further understand the anomalous phenomenon about flow stress of GH4720Li alloy at high strain rates (1000 $s^{-1}$and 5000 s^{-1}), the flow stress-deformation temperature relationship is plotted in Figure 2.

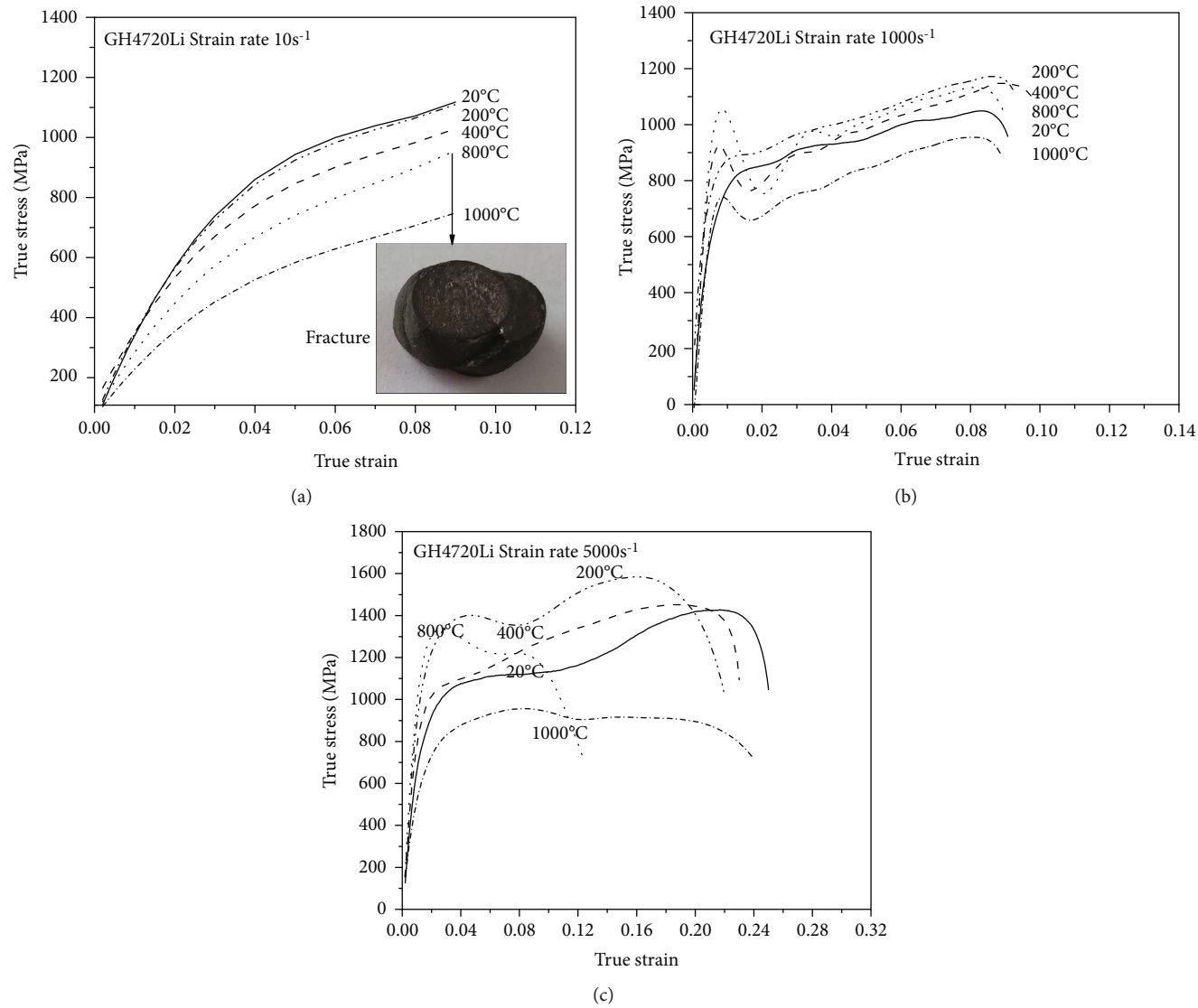

Figure 1: The true stress-strain curve of GH4720Li alloy under the different conditions (a) 10 s^{-1}, (b) 1000 s^{-1}, and (c) 5000 s^{-1}.

Figure 2 showed the flow stress vs. deformation temperature with various strain rates and strains. Generally, plastic deformation produced a lot of heat. For the loading at a high strain rate, there was no sufficient time for this heat to dissipate into the surroundings. The actual temperature in consideration of a significant increase in temperature with a specimen would be estimated by [10, 11]

$$T = T_0 + \Delta T = T_0 + \int_0^{\varepsilon} \frac{\eta}{\rho C_v} \sigma d\varepsilon, \quad (1)$$

where T_0 is the initial temperature in compressive experiments, ΔT is the increasement in temperature within specimen caused by the adiabatic process under high-rate loading, C_v is the heat capacity, ρ is the density of the material, ε is the plastic strain, σ is the flow stress, and η is the fraction of the heat generated by the plastic work that applies to the sample.

As seen in Figures 2(a)–2(c), for the studied range of temperatures (20°C~1000°C) and the selected strain rates (10, 1000, and 5000/s), when the strain rate was 10 s^{-1}, the true stress decreased with the increase of temperature; when the strain rate increased to 1000 s^{-1}/5000 s^{-1}, the true stress increased with the increase of temperature (20°C~200°C); when the temperature continued to increase to 400°C, the stress decreased gradually; when the temperature reached 800°C, the stress began to increase with the increase of temperature; when the temperature increased to 1000°C, the stress was to weaken.

3.2. Microstructures of Deformed Specimens. There was no precipitate in the microstructure of GH4720Li alloy before the hot compression test, as shown in Figure 3. However, during the low strain rate test (10 s^{-1}), a large number of precipitates were produced in the microstructure of GH4720Li alloy, as shown in Figures 4(a) and 4(b), and the precipitates produced contained a large amount of Cr (Mo) elements, as

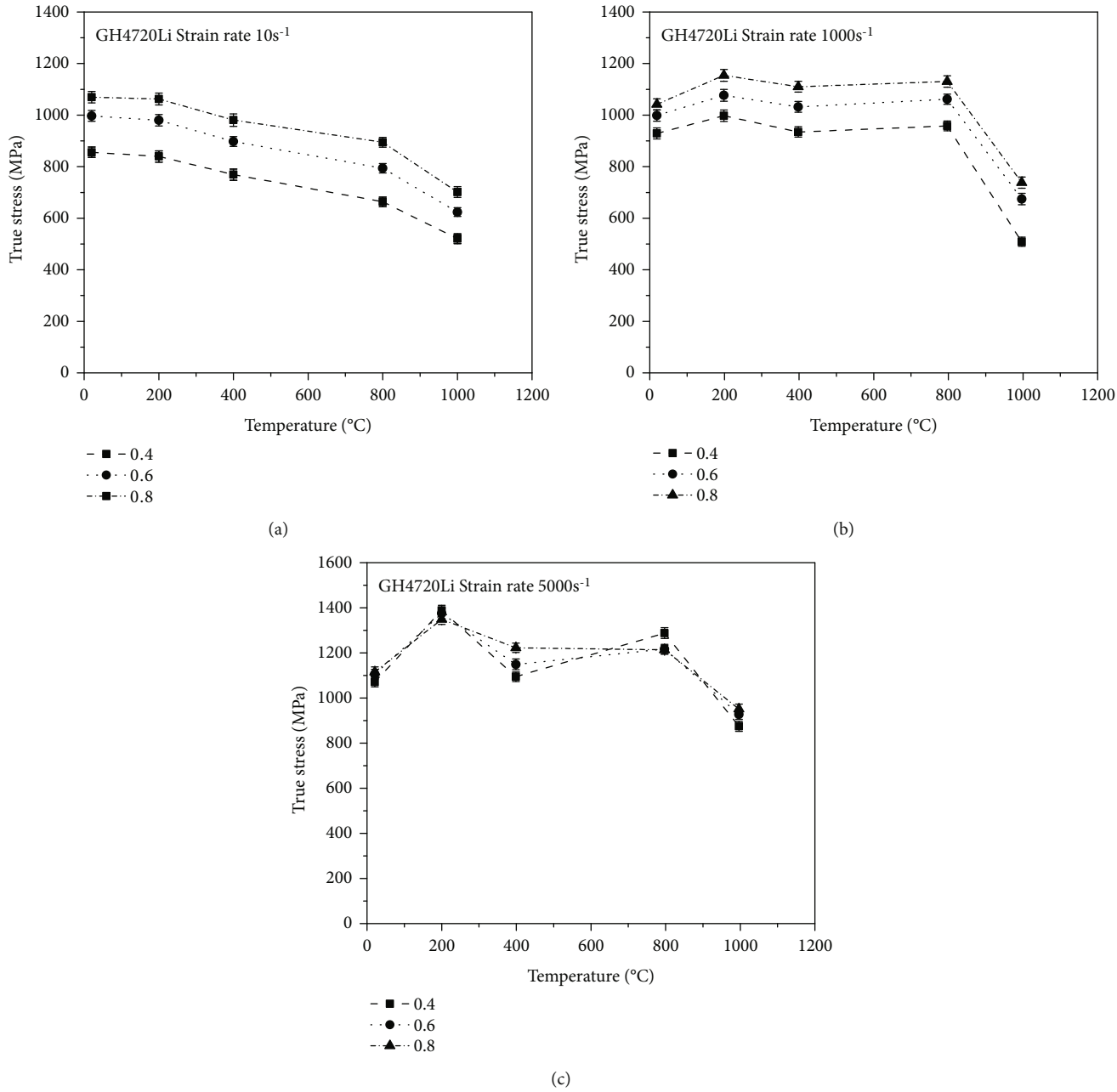

Figure 2: The flow stress VS. Temperature relations with strain rate of (a) 10/s, (b) 1000/s, and (c) 5000/s.

shown in Figures 5(a) and 5(b). The toughness of precipitates could effectively inhibit the crack growth [12]. When the toughness strength of precipitates exceeded the limit value of local stress, the precipitates could prevent the crack from expanding [13, 14]. For the precipitates with a layered structure, the crack front could not surround the tough precipitates and could renucleate in the adjacent material. Therefore, the crack may also be blunted or deflected by the ductile phase [15–17]. Once a crack had initiated, the plastic work expended upon stretching these second-phase particles during crack propagation provided a resistance to crack growth and was referred to as crack bridging [18]. The amount of toughening provided by crack bridging depended upon the toughness of precipitates [12]. However, a large amount of Cr (Mo)-rich precipitates made the matrix brittle [19], which reduces the mechanical properties of GH4720Li alloy. In addition, because the cracks were easy to occur in Cr (Mo) precipitates and the fracture surface of Cr (Mo) precipitates was flat and intact, it showed that the Cr (Mo) precipitates absorbed less energy in the fracture process [19–21]. Therefore, Cr (Mo) precipitates would reduce the compressive strength of GH4720Li alloy. In addition, secondary cracks usually occurred at the edge of Cr (Mo) precipitates [19, 21], which further reduced the mechanical properties of GH4720Li alloy. Figure 6 was an enlarged view of the rectangular area in Figures 7(a) and 7(b). It can be seen

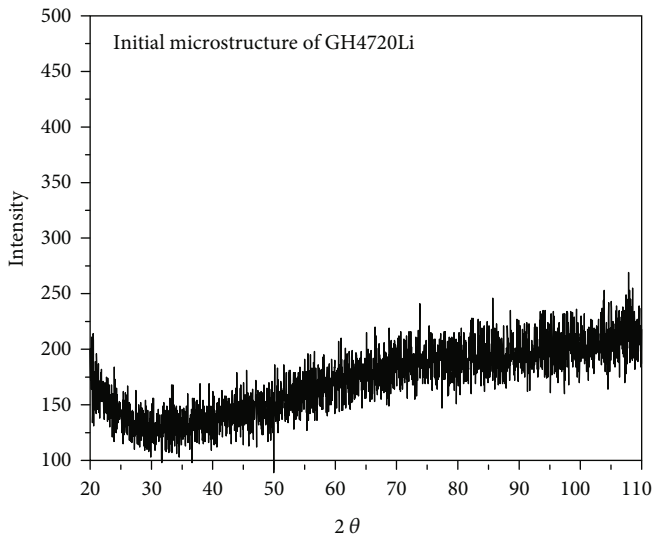

(a) Microstructure

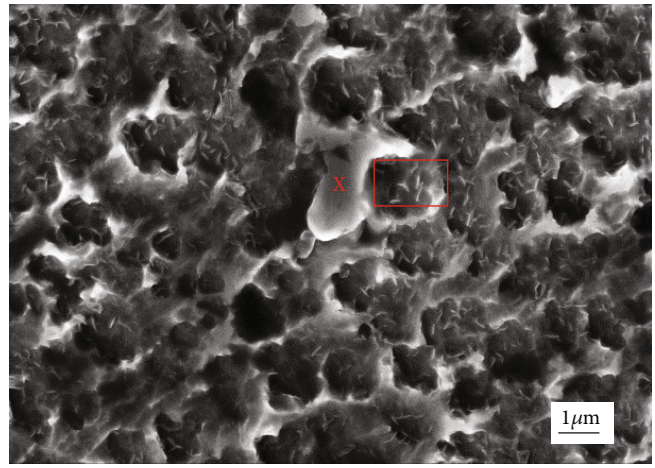

(b) XRD pattern

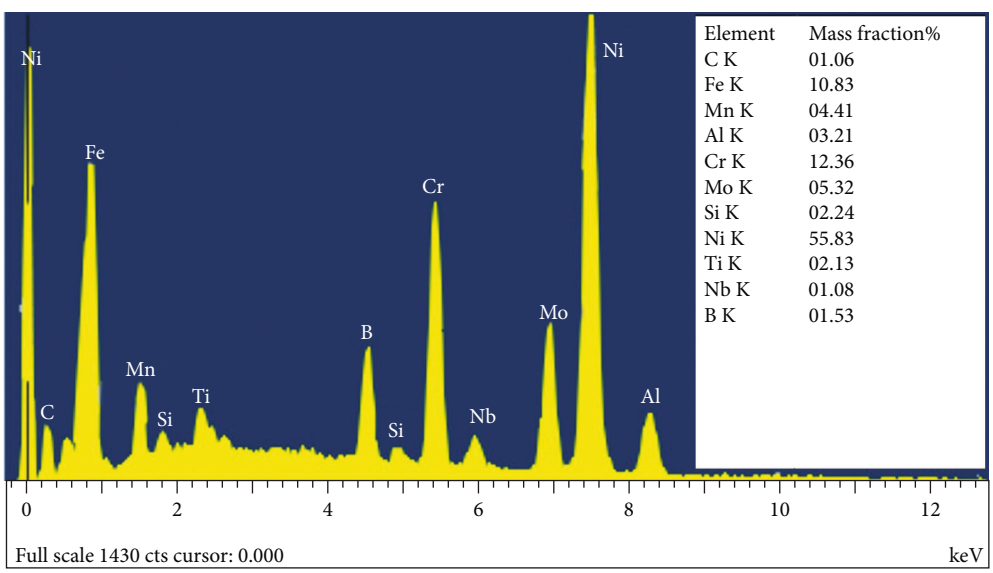

(c) EDS spectra

Figure 3: The microstructure and XRD pattern and EDS spectra of GH4720Li alloy.

from Figures 6(a) and 6(b) that under the condition of low strain rate ($10\,s^{-1}$), Cr (Mo) precipitation was similar to lamellar when the temperature was 20°C, while the shape of Cr (Mo) precipitation was approximately spherical when the temperature was 800°C. During the dynamic compression test, the lamellar Cr (Mo) precipitates were not completely pinched off [22]; only a part of the layered structure was destroyed [22], which showed high compressive strength. In addition, the density defect of Cr (Mo) lamellar precipitate was smaller [12], so it would improve the mechanical properties of the material. Moreover, due to the different morphology of the two Cr (Mo) precipitates, different lattice defects were caused, which made the dislocation spacing of Cr (Mo) lamellar precipitates smaller than that of spherical precipitates, so the Cr (Mo) lamellar precipitates displayed a slightly greater strength over the low strain rates tested [12]. Besides, the presence of shear ribs demonstrated that Cr (Mo) lamella phase could absorb more fracture energy in comparison to spherical precipitates. Therefore, compared with spherical precipitates, the dynamic mechanical properties of layered precipitates are better [21].

It would be concluded that under the low strain rate ($10\,s^{-1}$) experimental conditions, the true stress of GH4720Li alloy was smaller than that under high strain rate conditions due to the presence of a large amount of Cr (Mo) precipitates in the test piece; moreover, the strength of lamellar Cr (Mo) precipitates was greater than that of spherical Cr (Mo) precipitates [19, 23], resulting in a stress of 20°C greater than that of 800°C.

Under the condition of high strain rate ($1000/5000\,s^{-1}$), precipitates appeared in GH4720Li alloy test pieces, as shown in Figures 4(c)–4(f) and Figures 7(c)–7(f). Compared with the low strain rate ($10\,s^{-1}$), the content of Fe in the precipitate

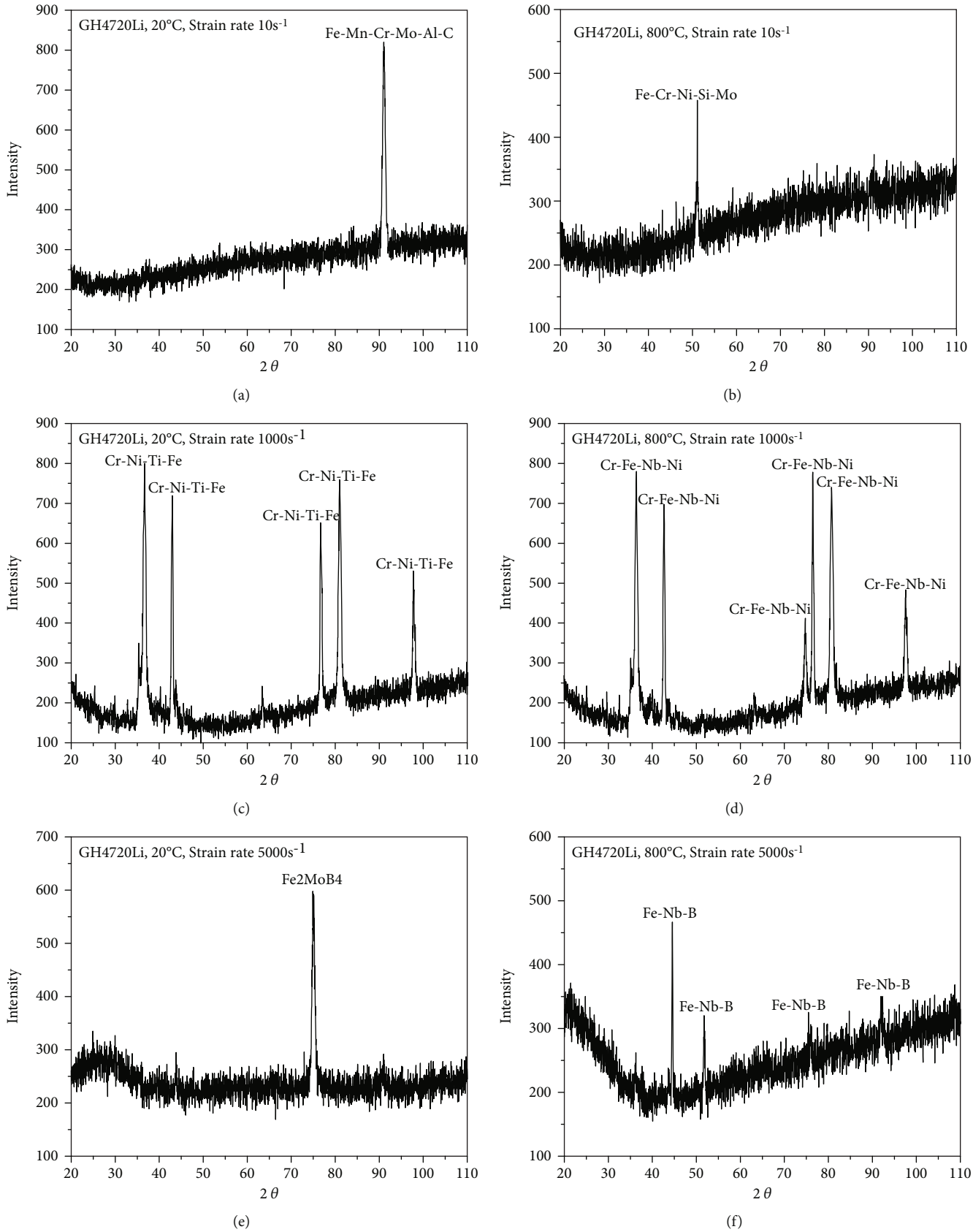

Figure 4: XRD patterns of GH4720Li superalloy under different conditions: (a) 10 s^{-1}, 20°C; (b) 10 s^{-1}, 800°C; (c) 1000 s^{-1}, 20°C; (d) 1000 s^{-1}, 800°C; (e) 5000 s^{-1}, 20°C; (f) 5000 s^{-1}, 800°C.

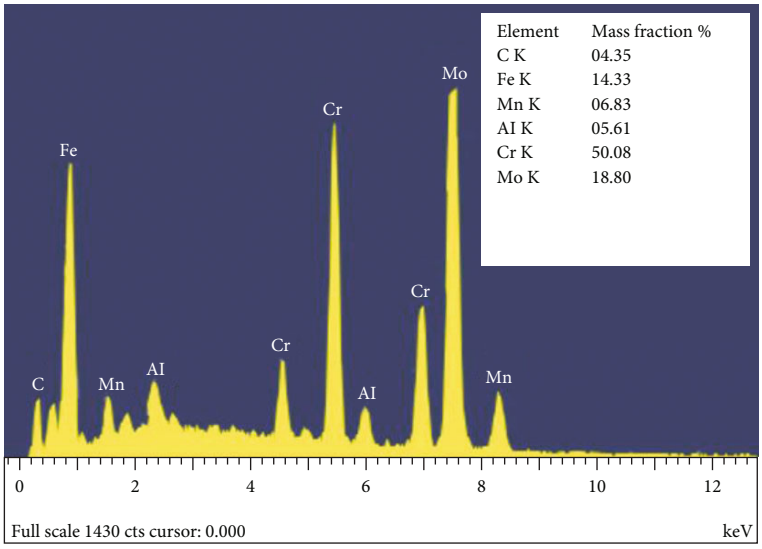

(a)

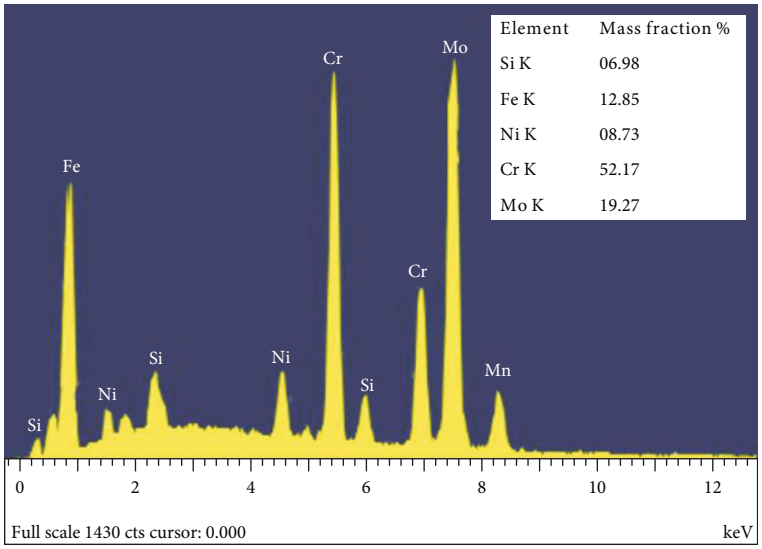

(b)

Figure 5: Continued.

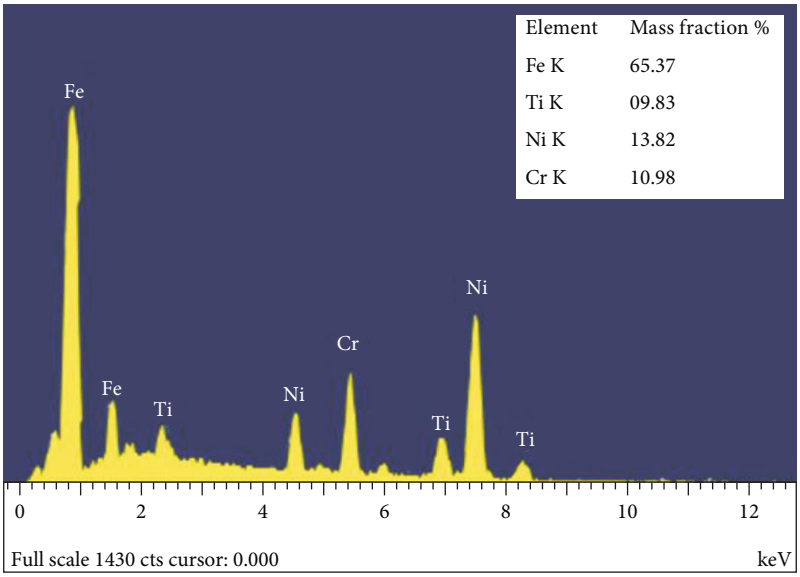

(c)

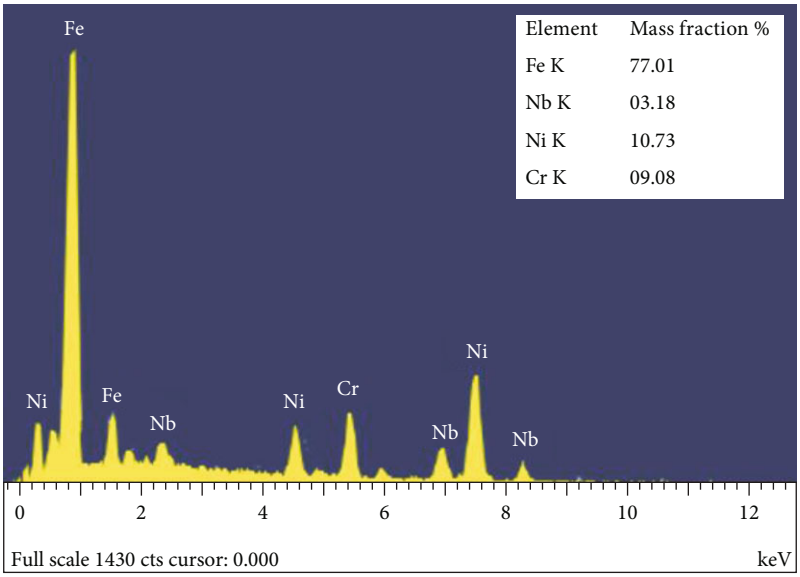

(d)

Figure 5: Continued.

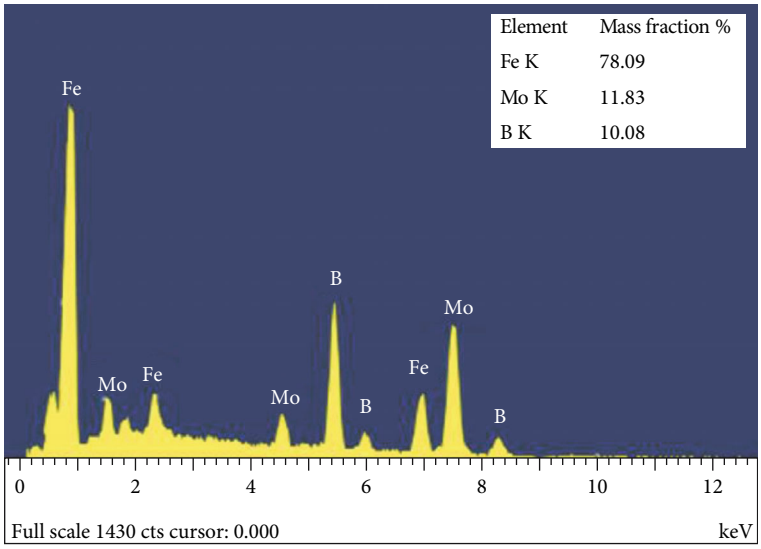

(e)

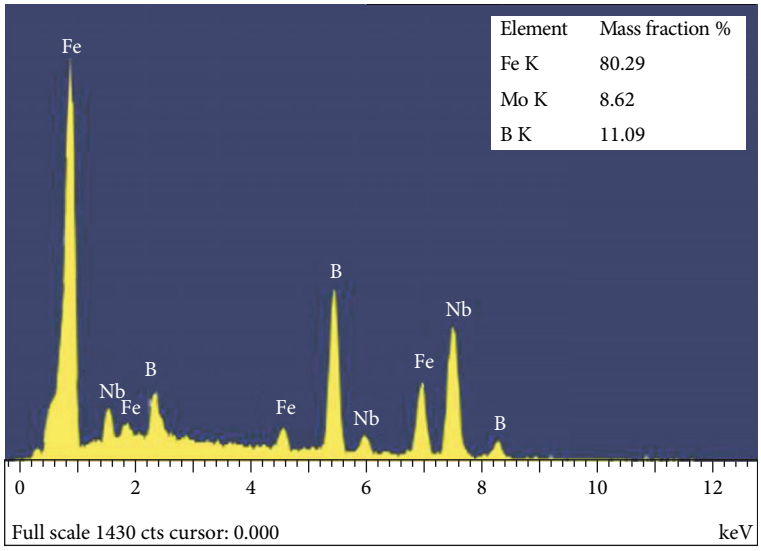

(f)

Figure 5: EDS spectra of GH4720Li alloy under different deformation conditions: (a) 10 s^{-1}, 20°C; (b) 10 s^{-1}, 800°C; (c) 1000 s^{-1}, 20°C; (d) 1000 s^{-1}, 800°C; (e) 5000 s^{-1}, 20°C; (f) 5000 s^{-1}, 800°C.

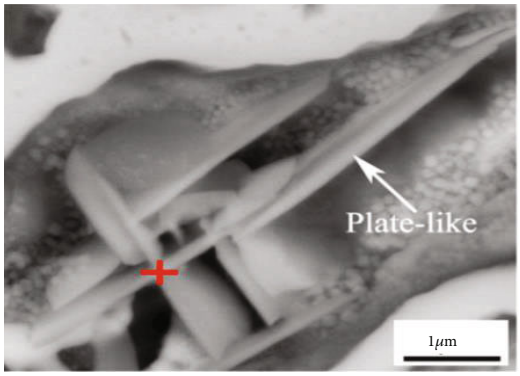

(a)

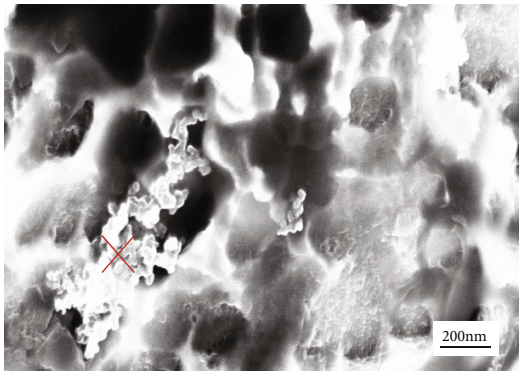

(b)

Figure 6: The magnified microstructures of GH4720Li alloy corresponding to the closed rectangle area in Figure 7(a) [12] and Figure 7(b).

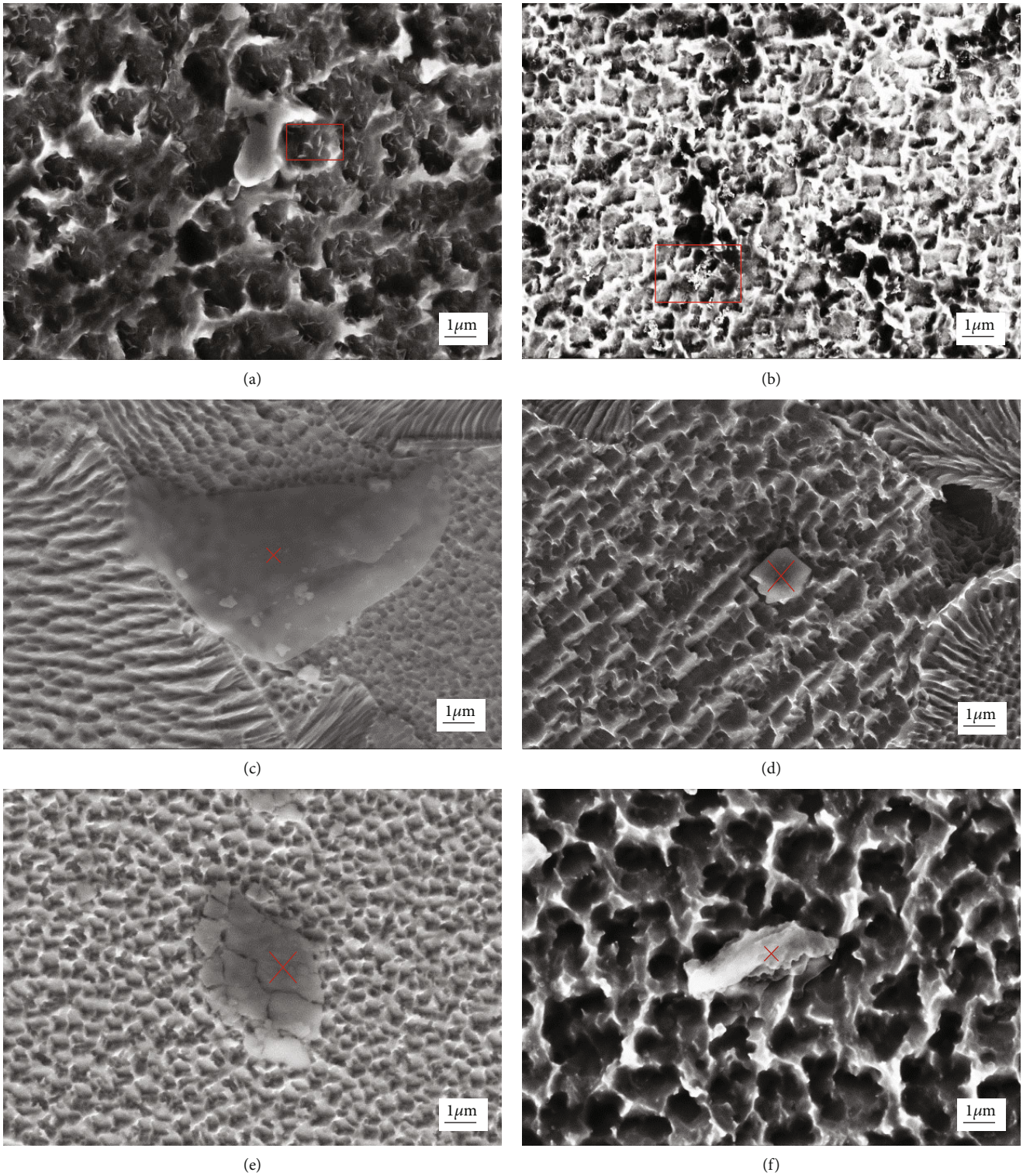

Figure 7: Microstructure of the GH4720Li alloy under different test conditions: (a) 10 s^{-1}, 20°C; (b) 10 s^{-1}, 800°C; (c) 1000 s^{-1}, 20°C; (d) 1000 s^{-1}, 800°C; (e) 5000 s^{-1}, 20°C; (f) 5000 s^{-1}, 800°C.

at a high strain rate (1000/5000 s^{-1}) was significantly increased, and the content of Cr was significantly reduced or even disappeared, as shown in Figure 5. In addition, when the strain rate is 1000 s^{-1} or 5000 s^{-1}, the Fe content in the precipitate at 800°C was higher than that in the precipitate at 20°C. In addition, compared with the initial microstructure of GH4720Li alloy, the content of Fe in the precipitate at a high strain rate (1000/5000 s^{-1}) increased, but the content of Ni decreased. This indicated that Fe and Ni atoms transferred between the precipitate and the surrounding phase. The precipitates absorbed Fe atoms from the surrounding phase and released their own Ni atoms [24]. In this case, the Fe atoms in

the precipitates occupied the position originally belonging to Ni atoms, which led to the increase of vacancy concentration. Furthermore, with the increase of Fe content, the lattice parameters of GH4720Li alloy decreased slightly, which promoted the increase of vacancy concentration [17]. The compressive strength of GH4720Li alloy was improved with the increase of vacancy concentration. Besides, the increase of Fe content resulted in the increasement of metallic bond and the decreasement of covalent bond [19, 25]; the increasement of metallic bond would improve the ductility for mental materials [12]. Therefore, the true stress value of GH4720Li alloy at a high strain rate (1000/5000 s^{-1}) was larger than that at low strain rate, and at a high strain rate (1000/5000 s^{-1}), the true stress at 800°C was greater than that at 20°C. This was the reason why the true stress of GH4720Li alloy appeared abnormal characteristics at a high strain rate (1000/5000 s^{-1}).

4. Conclusion

In this paper, the hot compression tests were conducted over a wide range of temperature (20~1000°C) and strain rate (10~5000 s^{-1}) to obtain further understandings of the deformation behavior of GH4720Li alloy. It was found that the mechanical properties of GH4720Li alloy showed different trends under high and low strain rates. The reasons for the difference were analyzed from the perspective of microstructure. The following conclusions were drawn:

(1) Under the condition of a high strain rate (1000/5000 s^{-1}), the mechanical properties of GH4720Li did not decrease with the increase of temperature; on the contrary, the abnormal phenomenon that the stress increased with the increase of temperature appeared. This anomalous phenomenon was different from our common sense, which the flow stress decreased successively with increasing temperature

(2) In the low strain rate (10 s^{-1}), a large number of precipitates containing Cr (Mo) elements appeared in the GH4720Li alloy specimens. The precipitation containing Cr (Mo) elements reduced the compressive strength of GH4720Li alloy. In addition, compared with the precipitates of spherical Cr (Mo), the precipitates of lamellar Cr (Mo) elements would improve the mechanical properties of GH4720Li alloy better

(3) Under the condition of a high strain rate (1000/5000 s^{-1}), precipitates containing a large amount of Fe element appeared in the test piece. The mechanical properties of GH4720Li alloy would be improved with the increase of Fe content and the decrease of Cr content

Data Availability

The data used to support the findings of this study are included within the article.

Conflicts of Interest

The authors declare that they have no conflicts of interest.

Acknowledgments

The authors were grateful for fund support by the Science and Technology Research Projects from Anyang City (project " thermal conductivity behavior research of copper matrix hybrid materials with wear-resisting/low expansion for aviation electric contact field"), the scientific research projects in the Education Department of Henan Province (No. 18A430006), and the university level training project of Anyang Institute of Technology (No. YPY2019001). Meanwhile, part of the data in this paper was provided by the "Key laboratory of Aerocraft Simulation Design and Airborne Equipment of Anyang City" and "Key disciplines of human and environmental engineering". This work is also supported by the R&D and Promotion Key Program of Henan Province in 2021 (Soft Science Research), the R&D and Promotion Key Program of Anyang in 2020 (grant number 2020-14-256), and the Development Program for University Key Teacher of Henan Province (grant number 2020GGJS233).

References

[1] F. E. Sczerzenie and G. E. Maurer, "Development of Udimet 720 for high strength disk applications," in *Superalloys 1984 (Fifth International Symposium)*, pp. 573–582, Champion, Pennsylvania, USA, 1984.

[2] M. Fahrmann and A. Suzuki, "Effect of cooling rate on Gleeble hot ductility of Udimet alloy 720 billet," in *Superalloys 2008 (Eleventh International Symposium)*, pp. 311–316, Champion, Pennsylvania, USA, 2008.

[3] A. A. N. Nemeth, D. J. Crudden, D. E. J. Armstrong et al., "Environmentally-assisted grain boundary attack as a mechanism of embrittlement in a nickel-based superalloy," *Acta Materialia*, vol. 126, pp. 361–371, 2017.

[4] K. Gopinath, A. K. Gogia, S. V. Kamat, and U. Ramamurty, "Dynamic strain ageing in Ni-base superalloy 720Li," *Acta Materialia*, vol. 57, no. 4, pp. 1243–1253, 2009.

[5] Y. X. Zhao, S. H. Fu, S. W. Zhang, X. Tang, N. Liu, and G. Q. Zhang, "An advanced cast/wrought technology for GH720Li alloy disk from fine grain ingot," in *7th International Symposium on Superalloy 718 and Derivatives*, pp. 271–280, The Minerals, Metals & Materials Society, 2010.

[6] F. F. Liu, J. Y. Chen, J. X. Dong, M. Zhang, and Z. Yao, "The hot deformation behaviors of coarse, fine and mixed grain for Udimet 720Li superalloy," *Materials Science and Engineering A*, vol. 651, pp. 102–115, 2016.

[7] Q. Y. Yu, Z. H. Yao, and J. X. Dong, "Deformation and recrystallization behavior of a coarse-grain, nickel-base superalloy Udimet720Li ingot material," *Materials Characterization*, vol. 107, pp. 398–410, 2015.

[8] J. L. Qu, Z. N. Bi, J. H. Du, M. Q. Wang, Q. Z. Wang, and J. Zhang, "Hot deformation behavior of nickel-based superalloy GH4720Li," *Journal of Iron and Steel Research International*, vol. 18, pp. 59–65, 2011.

[9] H. Monajati, M. Jahazi, S. Yue, and A. K. Taheri, "Deformation characteristics of isothermally forged udimet 720 nickel-base

superalloy," *Metallurgical and Materials Transactions A*, vol. 36, no. 4, pp. 895–905, 2005.

[10] J. J. Wang, W. G. Guo, P. H. Li, and P. Zhou, "Modified Johnson-Cook description of wide temperature and strain rate measurements made on a nickel-base superalloy," *Materials at High Temperatures*, vol. 34, pp. 157–165, 2017.

[11] Y. Zhang, X. Li, and X. Lin, "Thermomechanical behavior of laser metal deposited Inconel 718 superalloy over a wide range of temperature and strain rate: testing and constitutive modeling," *Mechanics of Materials*, vol. 135, pp. 13–25, 2019.

[12] D. R. Johson, X. F. Chen, B. F. Oliver, R. D. Noebe, and J. D. Whittenberger, "Processing and mechanical properties of in-situ composites from the NiAl-Cr and the NiAl-(Cr, Mo) eutectic systems," *Intermetallice*, vol. 3, no. 2, pp. 99–113, 1995.

[13] N. Fares and V. Lv, "General image method in a plane-layered elastostatic medium," *Journal of Applied Mechanics*, vol. 55, 1989.

[14] H. Gao and J. R. Rice, "A first-order perturbation analysis of crack trapping by arrays of obstacles," *Journal of Applied Mechanics*, vol. 56, no. 4, pp. 828–836, 1989.

[15] M. Y. He, F. E. Heredia, G. E. Lugas et al., "The mechanics of crack growth in layered materials," *Acta Metallurgica et Materialia*, vol. 41, pp. 1223–1228, 1989.

[16] K. S. Chan, "Understanding fracture toughness in gamma TiAl," *JOM*, vol. 5, pp. 30–38, 1992.

[17] K. S. Chan, "Influence of microstructure on intrinsic and extrinsic toughening in an alpha-two titanium aluminide alloy," *Metallurgical Transactions A*, vol. 23, no. 1, pp. 183–199, 1992.

[18] B. D. Flinn, M. Rühle, and A. G. Evans, "Toughening in composites of Al_2O_3 reinforced with Al," *Acta Metallurgica*, vol. 37, no. 11, pp. 3001–3006, 1989.

[19] L. Wang, C. L. Yao, J. Shen et al., "Microstructures and compressive properties of NiAl-Cr(Mo) and NiAl-Cr eutectic alloys with different Fe contents," *Materials Science and Engineering: A*, vol. 744, pp. 593–603, 2019.

[20] J. T. Guo, C. Y. Cui, Y. X. Chen, D. X. Li, and H. Q. Ye, "Microstructure, interface and mechanical property of the DS NiAl/Cr(Mo,Hf) composite," *Intermetallics*, vol. 9, no. 4, pp. 287–297, 2001.

[21] L. Wang, J. Shen, Y. P. Zhang, and H. Z. Fu, "Microstructure, fracture toughness and compressive property of as-cast and directionally solidified NiAl-based eutectic composite," *Materials Science and Engineering A*, vol. 664, pp. 188–194, 2016.

[22] L. Wang, J. Shen, Z. Shang, and H. Z. Fu, "Microstructure evolution and enhancement of fracture toughness of NiAl–Cr(Mo)–(Hf,Dy) alloy with a small addition of Fe during heat treatment," *Scripta Materialia*, vol. 89, pp. 1–4, 2014.

[23] L. Wang, J. Shen, Y. P. Zhang, L. L. Guo, H. X. Xu, and H. Z. Fu, "Microstructure evolution and room temperature fracture toughness of as-cast and directionally solidified novel NiAl-Cr(Fe) alloy," *Intermetallics*, vol. 84, pp. 11–19, 2017.

[24] L. M. Pike, Y. A. Chang, and C. T. Liu, "Solid-solution hardening and softening by Fe additions to NiAl," *Intermetallics*, vol. 5, pp. 601–608, 1997.

[25] A. I. Kovalev, R. A. Barskaya, and D. L. Wainstein, "Effect of alloying on electronic structure, strength and ductility characteristics of nickel aluminide," *Surface Science*, vol. 532-535, pp. 35–40, 2003.

Hindawi
International Journal of Photoenergy
Volume 2020, Article ID 8891541, 7 pages
https://doi.org/10.1155/2020/8891541

Research Article

Prototype of an Expert System for the Selection of Aircraft Structural Materials

Xuelong Hao,[1,2] Chen Wen,[3] Ning Zhao,[4] Lu Lu,[1,2] Kai Zhang,[5] and Donghui Zhang[1,2]

[1]*National Center of Analysis and Testing for Nonferrous Metals and Electronic Materials, Guobiao (Beijing) Testing & Certification Co., Ltd., Beijing 101407, China*
[2]*China United Testing & Certification Co., Ltd., Beijing 101407, China*
[3]*Beijing Spacecrafts, Beijing 100094, China*
[4]*Youke Publishing Co., Ltd., Grinm Group Co., Ltd., Beijing 100088, China*
[5]*Guangdong Provincial Academy of Building Research Group Co., Ltd., Guangzhou, 510500, China*

Correspondence should be addressed to Xuelong Hao; xlhaogrinm@126.com

Received 4 August 2020; Revised 16 November 2020; Accepted 7 December 2020; Published 21 December 2020

Academic Editor: Alberto Álvarez-Gallegos

Expert systems (ES) are widely used for engineering and manufacturing applications nowadays. In order to solve the problems in material selection in the aviation field, an aircraft material expert system (AMES) was developed. This expert system is based on the knowledge of multiple experts and aviation data. A decision support system (DSS) was designed for selecting the materials used in aviation fields. The flows of material selection were designed, and the models of AMES were established. A data base system was also designed to implement AMES.

1. Introduction

Aviation engineering application fields are developing towards intelligence, digitalization, and integration [1]. It is complicated to select an appropriate material for aircraft design [2]. In order to meet the demands of the aviation development, expert systems (ES) have been used in aerospace and have solved a lot of problems successfully [3–5].

Expert systems were developed by the AI (artificial intelligence) community in the mid-1960s [6]. With the development of science and technology, ES was successfully used for engineering and manufacturing applications and dealing with complicated problems in aviation fields [7–14]. Liu et al. [15] studied the optimization of short-haul aircraft schedule recovery problems by using a hybrid multiobjective genetic algorithm. Li et al. obtained a semantic-based approach for collaborative aircraft tooling design [16]. Athanasopoulos [17] developed an ES for coating selection based on fuzzy and multicriterion decision-making. Grainer and Blunt [18] presented a thorough analysis of the properties and the applications of using a simpler material for the substrate; the engineers can diminish the cost of purchase. Mao-Jiun and Wang [19] designed an ES for tool steel material selection under fuzzy environment. Kim et al. [20] developed an expert system for fatigue life prediction under variable loadings.

However, all these expert systems were developed to solve problems without considering the whole capabilities of aircrafts. In this paper, an aircraft material expert system (AMES) on the capability and layout of aircraft was developed based on the knowledge of multiple experts and aviation data. A decision support system (DSS) was designed, and the flows were modeled by ES for aircraft material selection.

This paper is organized as follows: Sections 2–4 present the design of AMES and the model of selection flows of core functions. Sections 5 and 6 present the data base system of AMES and the data frame. An example of ES solution is given in Section 7. Section 8 contains brief conclusions.

2. Design of AMES

The frame of AMES was designed as shown in Figure 1.

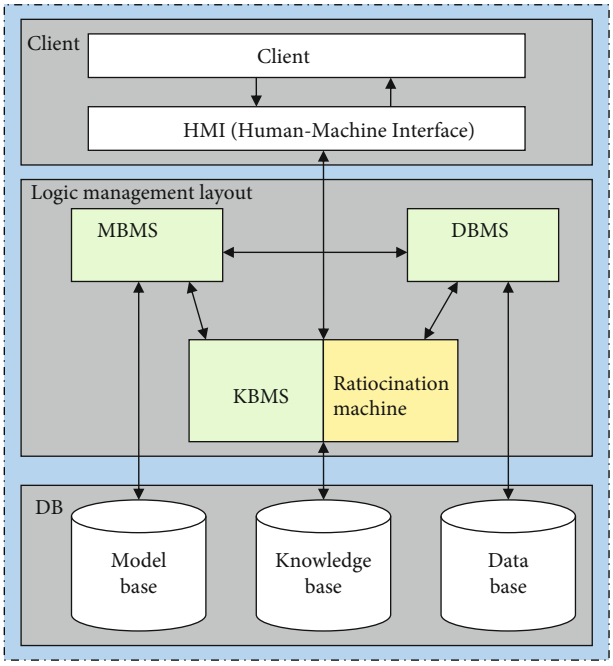

Figure 1: Frame of AMES.

The flow of AMES is as follows: clients visit the system via the HMI (human machine interface), and then the system transfers the request of clients to DB and returns the results to the clients.

The system contains three parts: client, logic management layout, and DB.

The core function logic of AMES is discussed in the second part. It contains the ratiocination and calculation of ES: ratiocination machine and the flow of material selection: MBMS (model base management system), DBMS (data base management system), and KBMS (knowledge base management system). The details will be given in Sections 3 and 4.

The core business logic of AMES is designed in Part 3: DB. It contains MB (model base), KB (knowledge base), and DB (data base). MB contains the methods of material selection which are formed from the experience of the experts. KB contains the knowledge of aircrafts and materials and the experts' knowledge. DB contains the data which is used to assist clients to make decisions of material selection. The data base management system and the data frame are designed and given in Sections 5 and 6.

3. Selection Methods of AMES

The ratiocination and calculation methods are designed by ES.

Qualitative and quantitative properties are needed to be considered to select an appropriate material for aircraft use. So the DSS of AMES is based on fuzzy logic and multicriterion decision-making theories. As the decision is made by multiexpert and fuzzy multiattribution, a prototype of the multicriterion neural network (NN) system is applied to prototype system functionality approach.

The prototype is established and operated as follows:

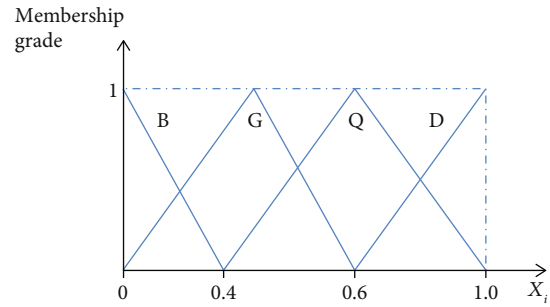

Figure 2: Membership functions for linguistic rating values.

The membership functions for linguistic ratings can be defined by the functions in Figure 2 [21].

It is assumed that the system has r input variables x_i $(i = 1, 2, \cdots, r)$ and y_j $(j = 1, 2, \cdots q)$.

The fuzzy membership function is defined as

$$R_t = \frac{1}{n}(X_{it1} \oplus X_{it2} \oplus X_{it3} \cdots \oplus X_{it1}), \tag{1}$$

where $i = 1, 2, \cdots m$, $t = 1, 2, \cdots k$, R_t is the aggregate ratings of alternative I under criterion t, and X_{itn} are the assigned ratings of alternative I under criterion t by decision-maker n. The symbol "$\oplus$" is a proposed calculation method.

Similarly, if G_t is the aggregated weighting for criterion t, and k is the number of criteria. Then, their opinions can be aggregated by

$$G_t = \frac{1}{n}(G_{it1} \oplus G_{it2} \oplus G_{it3} \cdots \oplus G_{it1}). \tag{2}$$

U_i is defined as the approximated fuzzy number of the fuzzy suitability index. And $f(x)$ is defined as M with the membership function. The symbol "$\oplus$" is a proposed calculation

If the rule amount X is given, the prototype of the system is established as

$$U_i = \left(\frac{1}{k}\right) \otimes [(R_{t1} \otimes G_{t1}) \oplus (R_{t2} \otimes G_{t2}) \oplus \cdots \oplus (R_{tk} \otimes G_{tk})]. \tag{3}$$

If $x_1 \le x \le x_2$, $f(x) = |(x - x_1)(x_1 - x_2)|$; otherwise, $f(x) = 0$. Then, we can get the following result:

$$M(U_i) = \frac{[M_M(U_I) + 1 - M_G(U_i)]}{2}, \tag{4}$$

where $M_M(U)$ and $M_G(U)$ are the maximizing set and the minimizing set, respectively, according to the input data. Equation (4) is the arithmetic of AMES.

4. Core Function Models of AMES

Equations (1)–(4) are the methods of material selection. It gives the flows of these methods. Four methods are designed

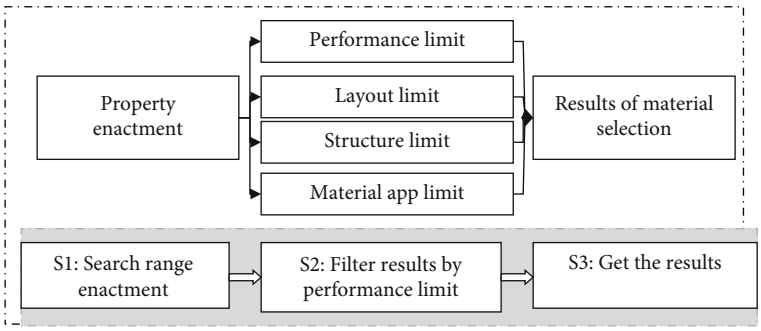

Figure 3: Methods of material selection: filter.

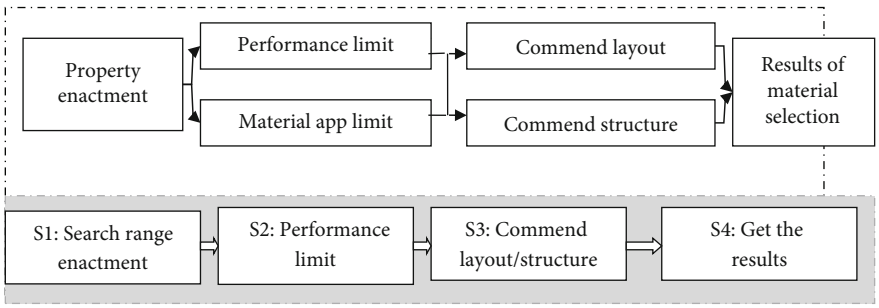

Figure 4: Methods of material selection: performance limit.

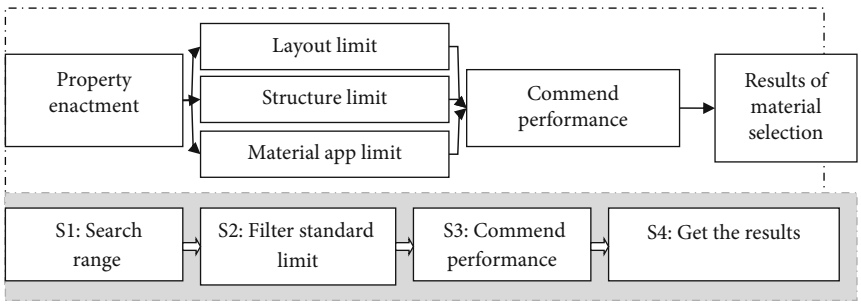

Figure 5: Methods of material selection: layout design.

to select materials for aircraft design: "filter," "performance limit", "layout design", and "experience." And the core function models are designed in Figures 2–5. The top of the figure gives the disposal flow of AMES. And the bottom gives the computer instruction of the flow.

The flow of "filter" is designed in Figure 3. Clients set the property conditions and the goals of material selection. The system filters the results by limiting the material performance. Then, the clients deal with the results returned by the system and choose the rights.

The flow of "performance limit" is described in Figure 4. After the properties were restricted, clients set the performance and the application of materials. Then, the system deals with the requests and commends the layout or structure of the aircraft. Clients could select the rights from the results returned by the system.

The flow of "layout design" is designed in Figure 5. This method commends the aircraft's performance through limiting the layout and structure of the aircraft. The method is often used by engineers to manufacture parts and so on.

The flow of "experience" is designed in Figure 6. This method depends on the experience of experts. It selects materials or parts based on the isometric spectrum. A lot of work is needed to ensure the validity of this method. But this method of material selection is the most useful way for aircraft designers.

5. Actualization Technique of AMES

After determining the frame and the core function, the actualization technique of AMES is designed.

As described in Figure 7, the frame of the DBMS (data base management system) is contrived by JCDF (Java Common Development Frame). It contains four lays: client layer, view layer, business layer, and resource layer. The differences of this frame from usual frames

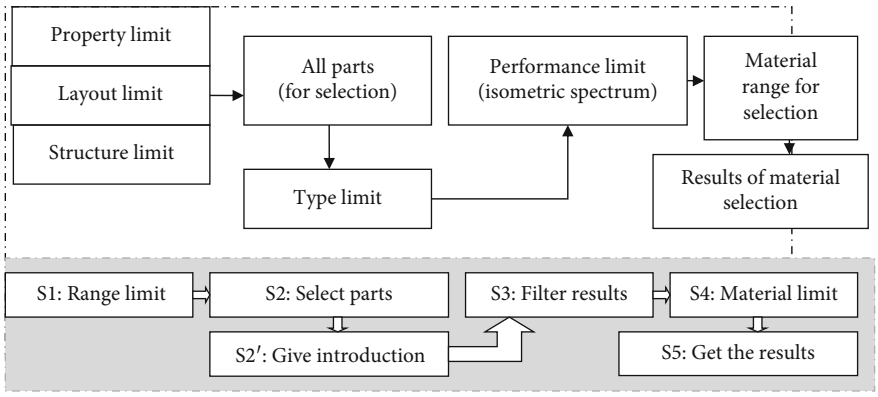

Figure 6: Methods of material selection: experience.

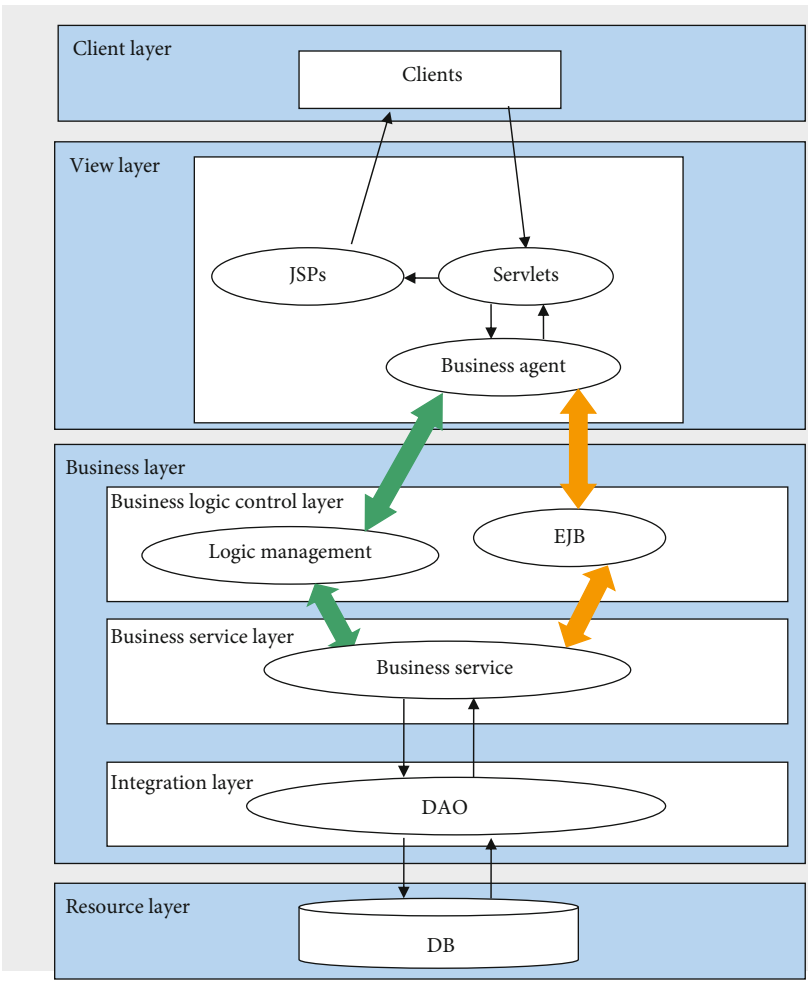

Figure 7: DBMS of AMES.

are as follows: the Servlets separate the view layer from the business layer, and the logic management is done by EJB. These sets promote the system to run fast and efficiently. JCDF can choose different flows to deal with different requests. It visits the data base via DAO and saves a lot of space.

6. BL (Business Logic) of AMES

In order to realize the transfer of the data successfully and make sure the system is easy to use, the design of the data base is important. The BL of AMES contains the model base, knowledge base, and data base. The model base and the knowledge

Table 1: Frame of data base.

AMES (BL) DB	Aircraft information module	Aircraft property
		Aircraft performance
		Aircraft layout
		Aircraft structure
		Aircraft material app
	Component information module	Component property
		Component performance
		Component layout
		Component structure
		Component material app
	Part information module	Part property
		Part performance
		Part structure
		Part material app
	Material information module	Material property
		Material component
		Material performance
		Material application

base contain expert experience and aircraft knowledge. But the data base should be arranged reasonably, or the system could run with a lot of problems. The data base of AMES contains aircraft information, component information, part information, and material information. These are outlined in Table 1. Every module has its own values, but they are related. The parameters of the whole aircraft and parts are based on the material.

7. Example

In this section, we use a new method based on equation (6) and give an example to illustrate the proposed method.

Firstly, let us consider the linguistic terms: disqualification (D), qualified (Q), good (G), and best (B). The fuzzy numbers corresponding to the terms are given in Table 2. The values present the limits of the selection.

$$\begin{aligned} \text{D is equal to } \frac{1+1+0.6+0.6}{4} &= 0.8, \\ \text{Q is equal to } \frac{0.6+0.6+0.4+0.4}{4} &= 0.5, \\ \text{G is equal to } \frac{0.4+0.4+0+0}{4} &= 0.2, \\ \text{B is equal to } \frac{0+0.4+0+0}{4} &= 0.1. \end{aligned} \tag{5}$$

We choose four X_i variables X_1 (performance limit), X_2 (layout limit), X_3 (structure limit), and X_4 (material app limit) as given in Section 2, which are given in the method "filter." Then, we get the defuzzified values. Assume that the ratings of the program under four criteria decided by decision-makers are as shown in Table 3.

Table 2: Linguistic terms and corresponding fuzzy numbers.

Linguistic terms	Fuzzy numbers
Disqualification (D)	1, 1, 0.6, 0.6
Qualified (Q)	0.6, 0.4, 0.4, 0
Good (G)	0.4, 0.4, 0, 0
Best (B)	0, 0.4, 0, 0

Table 3: Ratings of design plan of ES under the four criteria.

Plan	X_1	X_2	X_3	X_4
I	Q	G	G	B
II	G	B	B	Q
III	B	B	G	G
IV	B	G	G	Q

Table 4: The importance weights of the four criteria.

Criteria	Decision				IW
	A	B	C	D	
X_1	Q	B	G	G	0.25
X_2	G	Q	B	Q	0.325
X_3	Q	G	B	B	0.225
X_4	G	B	B	G	0.15

A committee of four decision-makers conducts this task and gives the decision also based on Table 2. The important weights of the four criteria are shown in Table 4.

Based on the equations, the ranking values can be evaluated as follows:

$$\begin{aligned} M(\mathrm{I}) &= 0.5 \times 0.25 + 0.2 \times 0.325 + 0.2 \\ &\quad \times 0.225 + 0.1 \times 0.15 = 0.25, \\ M(\mathrm{II}) &= 0.2 \times 0.2815 + 0.1 \times 0.34375 + 0.1 \\ &\quad \times 0.25 + 0.5 \times 0.1875 = 0.18, \\ M(\mathrm{III}) &= 0.1 \times 0.2815 + 0.1 \times 0.34375 + 0.2 \\ &\quad \times 0.25 + 0.2 \times 0.1875 = 0.1325, \\ M(\mathrm{IV}) &= 0.1 \times 0.2815 + 0.2 \times 0.34375 + 0.5 \\ &\quad \times 0.25 + 0.5 \times 0.1875 = 0.21. \end{aligned} \tag{6}$$

From the above calculations, the best selection is program III.

8. Conclusions

This paper developed an aircraft material expert system (AMES) to solve the problems of material selection in the aviation field. It provides a way of material selection by considering the whole performance of aircrafts by ES.

A selection method of fuzzy logic and multicriterion decision-making theories is designed by multiexpert and fuzzy multiattribution. And the prototype of the multicriterion neural network (NN) system is applied to the prototype system functionality approach. The computerized flows of selecting materials are also designed.

A DBMS is designed for realizing the core functions of AMES. A data base system is also designed for carrying out AMES.

Based on the knowledge of multiple experts and aviation data, the decision support system (DDS) could be used for selecting the materials used in aviation fields.

Data Availability

The data used to support the findings of this study are available from the corresponding author upon request.

Conflicts of Interest

The authors declare that they have no conflicts of interest.

Authors' Contributions

Xuelong Hao and Chen Wen contributed equally to this work.

Acknowledgments

(1) This study was financially supported by the National New Material Testing and Evaluation Platform construction project–nonferrous metal material industry (bidding no.: TC190H3ZW/2). (2) This study was financially supported by the National New Material Testing and Evaluation Platform main center project (bidding no.: TC170A5SU-1).

References

[1] Z. Y. Shen Jun, "Progress and layout for the database domain of aeronautical material," *Aeronautical material transaction*, vol. 23, p. 291, 2003.

[2] A. Jahan, M. Y. Ismail, S. M. Sapuan, and F. Mustapha, "Material screening and choosing methods - A review," *Mater Des*, vol. 31, no. 2, pp. 696–705, 2010.

[3] B. S. Adamczyk, A. L. Szejka, and O. Canciglieri Júnior, "Knowledge-based expert system to support the semantic interoperability in smart manufacturing," *Computers in Industry*, vol. 115, p. 103161, 2020.

[4] J. Liebowitz, "Expert systems: a short introduction," *Engineering Fracture Mechanics*, vol. 50, no. 5-6, pp. 601–607, 1995.

[5] M. D. Hassan, "An evaluation of input and output of expert systems for selection of material handling equipment," *Journal of Manufacturing Technology Management*, vol. 25, no. 7, pp. 1049–1067, 2014.

[6] S.-H. Liao, "Expert system methodologies and applications–a decade review from 1995 to 2004," *Expert Systems with Applications*, vol. 28, no. 1, pp. 93–103, 2005.

[7] H.-S. Shih, H.-J. Shyur, and E. S. Lee, "An extension of TOPSIS for group decision making," *Mathematical and Computer Modelling*, vol. 45, no. 7-8, pp. 801–813, 2007.

[8] V. Goel and J. Chen, "Application of expert network for material selection in engineering design," *Computers in Industry*, vol. 30, no. 2, pp. 87–101, 1996.

[9] A. Loganathan and I. Mani, "A fuzzy based hybrid multi criteria decision making methodology for phase change material selection in electronics cooling system," *Ain Shams Engineering Journal*, vol. 9, no. 4, pp. 2943–2950, 2018.

[10] A. Giorgetti, C. Cavallini, G. Arcidiacono, and P. Citti, "A mixed C-VIKOR fuzzy approach for material selection during design phase: a case study in valve seats for high performance engine," *International Journal of Applied Engineering Research*, vol. 12, no. 12, pp. 3117–3129, 2017.

[11] S.-K. Kim, M.-I. Roh, and K.-S. Kim, "Evaluation of feasibility index in the arrangement design of an offshore topside based on the automatic transformation of experts' knowledge and the fuzzy logic," *Ocean Engineering*, vol. 130, pp. 284–299, 2017.

[12] R. Nourian, S. M. Mousavi, and S. Raissi, "A fuzzy expert system for mitigation of risks and effective control of gas pressure reduction stations with a real application," *Journal of Loss Prevention in the Process Industries*, vol. 59, pp. 77–90, 2019.

[13] D. İçen and S. Günay, "Design and implementation of the fuzzy expert system in Monte Carlo methods for fuzzy linear regression," *Applied Soft Computing*, vol. 77, pp. 399–411, 2019.

[14] C. Urrea, G. Henríquez, and M. Jamett, "Development of an expert system to select materials for the main structure of a transfer crane designed for disabled people," *Expert Systems with Applications*, vol. 42, no. 1, pp. 691–697, 2015.

[15] T.-K. Liu, C.-H. Chen, and J.-H. Chou, "Optimization of short-haul aircraft schedule recovery problems using a hybrid multi-objective genetic algorithm," *Expert Systems with Applications*, vol. 37, no. 3, pp. 2307–2315, 2010.

[16] Y. Li, R. Yan, and J. Jian, "A semantics-based approach for collaborative aircraft tooling design," *Advanced Engineering Informatics*, vol. 24, no. 2, pp. 149–158, 2010.

[17] G. Athanasopoulos, C. R. Riba, C. A. G. Athanasopoulos, C. R. Riba, and C. Athanasopoulou, "A decision support system for coating selection based on fuzzy logic and multi-criteria decision making," *Expert Systems with Applications*, vol. 36, no. 8, pp. 10848–10853, 2009.

[18] S. B. Grainer, "Engineering coatings," *Design and applications. Cambridge: Abington Publishing*, pp. 445-446, 1998.

[19] M.-J. J. Wang, T.-C. C. M.-J. J. Wang, and T.-C. Chang, "Tool steel materials selection under fuzzy environment," *Fuzzy Sets and Systems*, vol. 72, no. 3, pp. 263–270, 1995.

[20] Y.-H. Kim, J.-H. Song, and J.-H. Park, "An expert system for fatigue life prediction under variable loading," *Expert Systems with Applications*, vol. 36, no. 3, pp. 4996–5008, 2009.

[21] S.-M. Chen, "A new method for tool steel materials selection under fuzzy environment," *Fuzzy Sets and Systems*, vol. 92, no. 3, pp. 265–274, 1997.

Hindawi
International Journal of Photoenergy
Volume 2020, Article ID 8859770, 8 pages
https://doi.org/10.1155/2020/8859770

Research Article

Study on Hydrolysis of Magnesium Hydride by Interface Control

Yanyan Chen, Ming Wang, Fenggang Guan, Rujun Yu, Yuying Zhang, Hongyun Qin, Xia Chen, Qiang Fu, and Zeyao Wang

School of Chemistry and Chemical Engineering, Shandong University of Technology, Zibo 255049, China

Correspondence should be addressed to Qiang Fu; fuqiang@tju.edu.cn

Received 13 August 2020; Revised 11 November 2020; Accepted 24 November 2020; Published 17 December 2020

Academic Editor: K. R. Justin Thomas

Magnesium hydride (MgH_2) is one of the competitive hydrogen storage materials on account of abundant reserves and high hydrogen content. The hydrolysis of MgH_2 is an ideal and controllable chemical hydrogen generation process. However, the hydrolyzed product of MgH_2 is a passivation layer on the surface of the magnesium hydride, which will make the reaction continuity worse and reduce the rate of hydrogen release. In this work, hydrogen generation is controllably achieved by regulating the change of the surface tension value in the hydrolysis, a variety of surfactants were systematically investigated for the effect of the hydrolysis of MgH_2 In the meantime, the passivation layer of MgH_2 was observed by scanning electron microscope (SEM), and the surface tension value of the solution with different surfactants were monitored, investing the mechanism of hydrolysis adding different surfactants. Results show that different surfactants have different effects on hydrogen generation. The hydrogen generation capacity from high to low is as follows: tetrapropylammonium bromide (TPABr), sodium dodecyl benzene sulfonate (SDBS), Ecosol 507, octadecyl trimethyl ammonium chloride (OTAC), sodium alcohol ether sulfate (AES), and fatty methyl ester sulfonate (FMES-70). When the ratio of MgH_2 to TPABr was 5 : 1, the hydrogen generation was increased by 52% and 28.3%, respectively, at the time of 100 s and 300 s. When hydrolysis time exceeds 80 s, the hydrogen generation with AES and FMES-70 began to decrease; it was reduced by more than 20% at the time of 300 s. SEM reveals that surfactants can affect the crystalline arrangement of $Mg(OH)_2$ and make the passivation layer three-dimensionally layered providing channels for H_2O molecules to react with MgH_2.

1. Introduction

With the rapid development of industrial technology, the global demand for energy is growing exponentially. Fossil fuels, as the most widely used energy materials, are not renewable, environmental pollution, and other defects; therefore, it is an urgent problem to find new clean and efficient energy sources at the present stage. Hydrogen has the characteristics of environmental protection, renewable, and high heat energy. Since the 1970s, it has been widely concerned by researchers. Hydrogen storage and release technology limits the development and application of hydrogen energy [1–4]. Among many hydrogen storage materials, the hydrogen content of MgH_2 reaches 7.69% (wt. %), and its theoretical hydrolysis hydrogen yield is 15.3% (wt. %) [5, 6]. Magnesium hydride is considered one of the best choices for portable hydrogen fuel cells due to stable storage and mild hydrolysis [7–19]. The chemical equation of the reaction between MgH_2 and H_2O is as following:

$$MgH_2 + 2H_2O \longrightarrow Mg(OH)_2\downarrow + 2H_2\uparrow \cdots \Delta H = -277 KJ\,mol^{-1}. \quad (1)$$

The magnesium hydroxide is difficult to dissolve in water whose solubility product is $5.6 \times 10^{-12}\,mol^3 \cdot L^{-3}$. It easily forms the passivation layer during the hydrolysis process, prevents the diffusion of water molecules toward the surface of magnesium hydride, reduces the rate, and shortens the duration of hydrolysis reaction [20–22]. Eliminating the cladding effect of magnesium hydroxide passivation layer on MgH_2 has become an urgent problem to be solved in the hydrogen yield of hydrolysis [23].

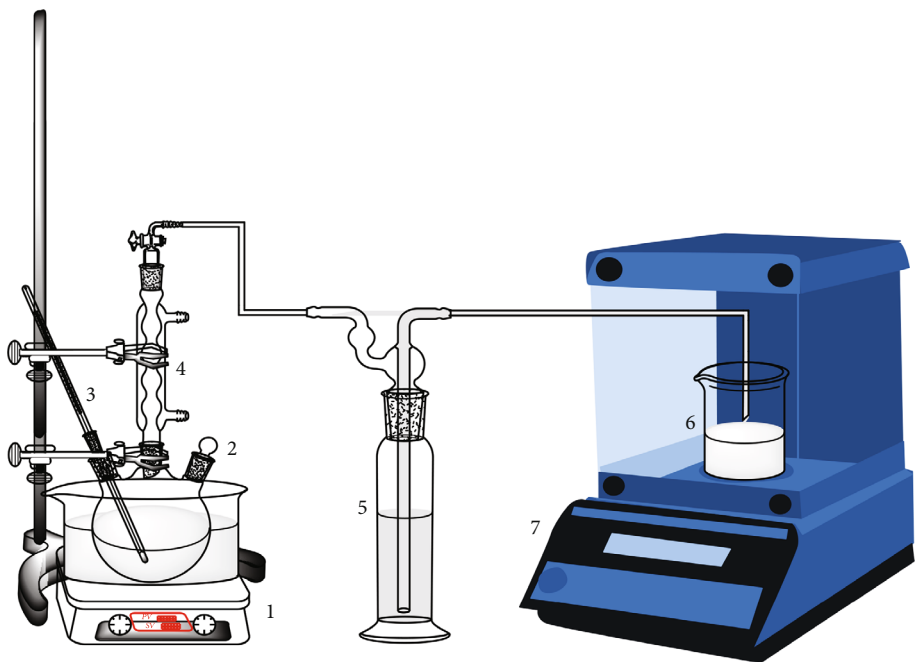

Figure 1: Hydrolysis unit. ((1) water bath, (2) three-necked flask, (3) thermometer, (4) condenser, (5) gas washing bottle, (6) beaker, and (7) analytical balance).

As we all know, surfactants can change the surface tension of the solution by means of forming an adsorbed layer with a certain orientation at the solid-liquid interface [24–27]. Based on the above principles, this study selected several typical surfactants to study the influence on the quantity of hydrogen generation and the rate of hydrogen generation. These data were combined with the surface tension value of the aqueous solution and the scanning electron micrograph of the product to analyze the corresponding mechanism. The study of interface control in this work provides the theoretical basis for the future researches of H_2 generation by hydrolysis of MgH_2.

2. Experimental

2.1. Experimental Materials. H_2 is generated from the reaction of MgH_2 (purity ≥99.5%, MG Power Technology Co., Ltd) and H_2O (deionized water). To investigate the effects of surfactants on the generation of H_2, different series of surfactants were added into deionized water: sodium dodecyl benzene sulfonate (SDBS, purity ≥90.0%, Shandong Yousuo Chemical Technology Co., Ltd), fatty methyl ester sulfonate (FMES-70, purity ≥70.0%, Shandong Yousuo Chemical Technology Co., Ltd), sodium alcohol ether sulfate (AES, purity ≥70%, Shandong Yousuo Chemical Technology Co., Ltd), tetrapropylammonium bromide (TPABr, purity ≥99.0%, Sinopharm Chemical Reagent Co., Ltd), octadecyl trimethyl ammonium chloride (OTAC, purity ≥99.5%, Shandong Yousuo Chemical Technology Co., Ltd), and Ecosol 507 (purity ≥90.0%, Shandong Yousuo Chemical Technology Co., Ltd).

2.2. Experimental Device and Process. The experimental device (Figure 1) is composed of the reaction system and the metering system. The reaction system is composed of a 250 mL three-necked flask, a condenser, a thermometer, and a water bath; the metering system is composed of a gas washing bottle, a beaker, and an analytical balance. The two systems are connected with silicone tubes.

Firstly, add 200 mL of water to a 250 mL three-necked flask. After the temperature of the water bath reaches 70°C, surfactant and stir were added. Then, the magnesium hydride was put to the three-necked flask. The hydrogen produced by hydrolysis is condensed by the condenser. An equal volume of water of gas washing bottle was discharge. Finally, the volume of hydrogen generated was calculated as follows:

$$V_{H_2} = \frac{m_{H_2O}}{\rho_{H_2O}} \tag{2}$$

2.3. Analytical Method. The surface morphology and dispersion state of magnesium hydride and hydrolyzed products are tested by SEM (Quanta 250, FEI); the surface tension (ST) of aqueous solutions with different surfactants is tested by surface tension meter K100C-MK2.

3. Results and Discussion

Surfactants with different groups, structures, and dosages have different impacts on the surface energy and the wetting effect between solid and liquid.

3.1. Effect of Anionic Surfactant. According to the structure of hydrophilic groups, anionic surfactants mainly include sulfonate and sulfate ester salts. Typical anionic surfactants were used in this study: SDBS, AES, and FMES-70.

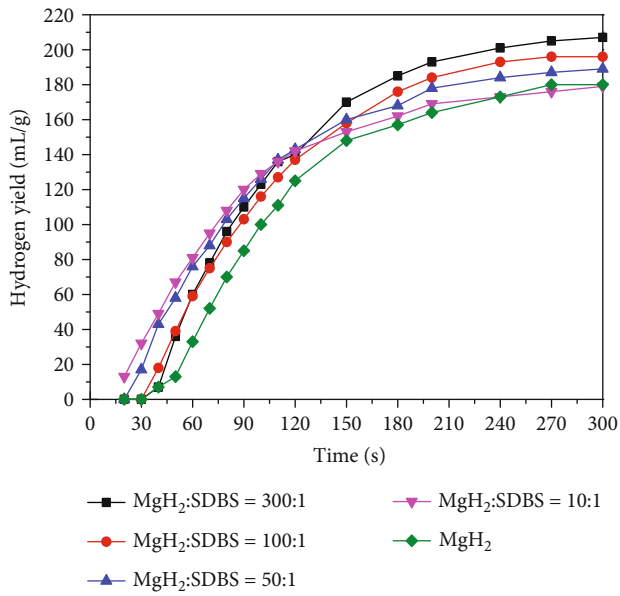

Figure 2: The effect of different SDBS dosages on hydrogen generation.

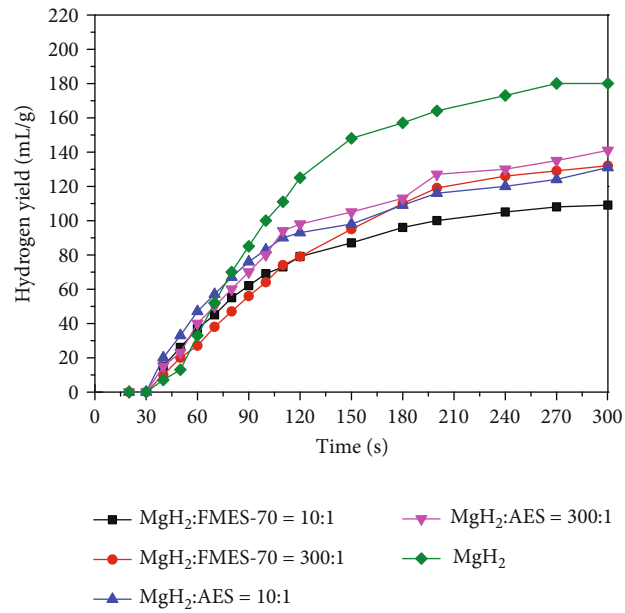

Figure 3: The effect of different FMES-70, AES dosages on hydrogen generation.

Table 1: Surface tension values of aqueous solutions with different SDBS dosages.

Ratio*	ST (mN/m)
Water	71.57
$MgH_2 : SDBS = 300 : 1$	70.51
$MgH_2 : SDBS = 100 : 1$	59.00
$MgH_2 : SDBS = 50 : 1$	47.80
$MgH_2 : SDBS = 10 : 1$	38.48

*: the ratio represents dosages of surfactants in experiments without MgH_2.

Table 2: Surface tension values of aqueous solutions with different FMES-70, AES dosages.

Ratio	ST (mN/m)
Water	71.57
$MgH_2 : FMES\text{-}70 = 300 : 1$	45.25
$MgH_2 : FMES\text{-}70 = 10 : 1$	39.74
$MgH_2 : AES = 300 : 1$	30.05
$MgH_2 : AES = 10 : 1$	37.86

Under the same condition, the volume of the water, the temperature of the water bath, and the mass of MgH_2, surfactants with different dosages were added, time (seconds) is the x-coordinate, and hydrogen yield (mL/g) is the y-coordinate.

It is shown in Figure 2 that the hydrogen generation rate are approximately the same at 110 s when $MgH_2 : SDBS = 300 : 1$, $MgH_2 : SDBS = 50 : 1$, and $MgH_2 : SDBS = 10 : 1$. While the hydrogen generation rate is slightly lower when $MgH_2 : SDBS = 100 : 1$ at 110 s. When the hydrolysis time is 120 s, the hydrogen generation rate of $MgH_2 : SDBS = 300 : 1$ is greater than the other. When the hydrolysis time is 155 s, the hydrogen generation rate of $MgH_2 : SDBS = 100 : 1$ is higher than $MgH_2 : SDBS = 10 : 1$ and $MgH_2 : SDBS = 50 : 1$. All the hydrogen generation rate reduces gradually over 200 s. The final hydrogen yield are ranked as follows: $MgH_2 : SDBS = 300 : 1 > MgH_2 : SDBS = 100 : 1 > MgH_2 : SDBS = 50 : 1 > MgH_2 : SDBS = 10 : 1 = MgH_2$.

The hydrogen generation rate will improve with the increase of SDBS dosages (time ≤100 s). It is possible that the surface tension of water becomes lower as surfactants increase (it is presented in Table 1). However, the lower the surface tension, the easier bubbles will foam. These bubbles gather into a foam layer, which binds H_2. It is difficult for H_2 escape from the reaction system (e.g., the curve of $MgH_2 : SDBS = 10{:}1$ in the Figure 2). Besides, the SDBS concentration is bigger than the critical micelle concentration ($CMC = 1.47 \times 10^{-3} - 1.60 \times 10^{-3}$ mol/L) when $MgH_2 : SDBS = 10 : 1$. Self-polymerization process of SDBS molecules possibly employed, which inhibits the detachment of $Mg(OH)_2$ from the surface of MgH_2 and the dispersion of $Mg(OH)_2$ in the water.

From Figure 3, the hydrogen generation of two experiments ($MgH_2 : FMES = 10 : 1$, $MgH_2 : AES = 10 : 1$) are 100% and 153.8% at the hydrolysis time of 50 s, which is higher than that without surfactant. When the hydrolysis time is over 75 s, the generation rate of four experiments ($MgH_2 : FMES\text{-}70 = 300 : 1$, $MgH_2 : FMES\text{-}70 = 10 : 1$, $MgH_2 : AES = 300 : 1$, and $MgH_2 : AES = 10 : 1$) are lower than that without surfactants.

It is observed from Table 2 that surface tension of solutions becomes lower as the ratio of MgH_2 to surfactants increases. On one hand, the system foams more easily [28, 29], and the foam layer weakens the diffusion of H_2. On the other hand, the hydrolysis reaction is essentially a

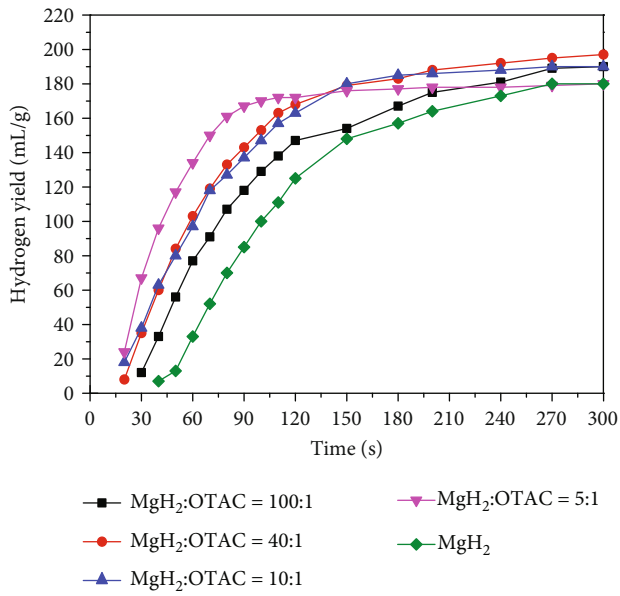

Figure 4: The effect of different OTAC dosages on hydrogen generation.

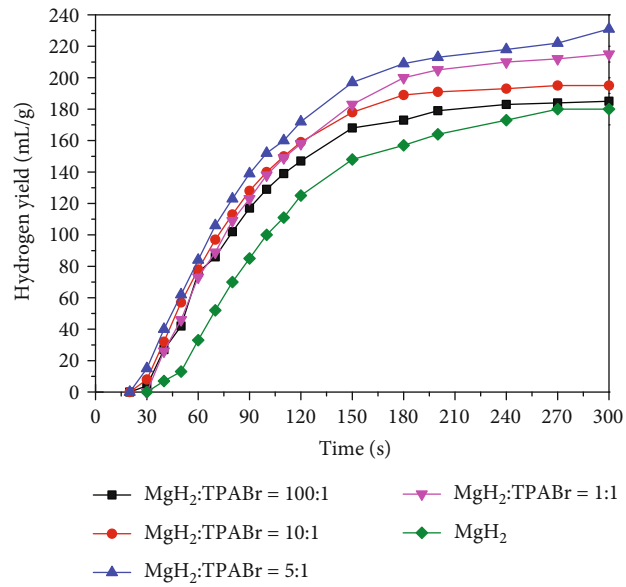

Figure 5: The effect of different TPABr dosages on hydrogen generation.

Table 3: Surface tension values of aqueous solutions with different OTAC dosages.

Ratio	ST (mN/m)
Water	71.57
$MgH_2:OTAC = 100:1$	36.87
$MgH_2:OTAC = 40:1$	35.79
$MgH_2:OTAC = 10:1$	34.24
$MgH_2:OTAC = 5:1$	32.99

Table 4: Surface tension values of aqueous solutions with different TPABr dosages.

Ratio	ST (mN/m)
Water	71.57
$MgH_2:TPABr = 100:1$	61.54
$MgH_2:TPABr = 10:1$	65.39
$MgH_2:TPABr = 5:1$	68.67
$MgH_2:TPABr = 1:1$	69.23

reaction with H^+, while the negatively charged groups of FMES-70 and AES may combine with H^+ decreasing the hydrogen generation.

3.2. Effect of Cationic Surfactant. Cationic surfactants are mainly nitrogen-containing organic amine derivatives, composed of a long-chain hydrophobic group and a positive charged hydrophilic group. With good emulsification, wetting effect, and other properties, it is easier to absorb on the solid surface and improves the solid-liquid interface effect.

It is shown in Figure 4 that the hydrogen generation of $MgH_2:OTAC = 5:1$ and $MgH_2:OTAC = 100:1$ are 70% and 29% higher than that without surfactants at time of 100 s. When the hydrolysis time is over 100 s, the hydrogen generation curves gradually become smooth. At the time of 300 s, the hydrogen generation of $MgH_2:OTAC = 40:1$ reaches the maximum which is 11.0% higher than that without surfactants.

Within 120 s of the hydrolysis, the hydrogen generation and the hydrogen generation rate improve as the ratio of MgH_2 to OTAC. After 120 s, the foam layer hinders the continuation of the hydrolysis. It can be seen from Table 3 that the surface tension of $MgH_2:OTAC = 100:1$ decrease to 36.87 mN/m. When $MgH_2:OTAC = 5:1$, the surface tension decreases to 32.99 mN/m slightly. Therefore, OTAC reduces the surface energy of solution preventing the agglomeration of $Mg(OH)_2$ between crystals.

It is also possible that the positively charged groups of the cationic surfactants may combine with OH^- inhibiting the combination of OH^- and Mg^{2+} and delay the formation of the passivation layer in the surface of MgH_2. Zheng et al. [30] studied the hydrolysis of Mg in different solutions ($MgCl_2$, $MnCl_2$, $NiCl_2$, $AlCl_3$, NH_4Cl, and HCl). They found that there was a significant improvement in NH_4Cl and HCl solution, the conversion efficiency increased by more than 60%. Researchers believe that the higher the affinity between the cations and OH^- in the solution, the more effective it is to inhibit the formation of the passivation layer.

In addition, the groups of the cationic surfactants can absorb on $Mg(OH)_2$ along the direction of growth and prevent its growth [31].

Figure 5 reveals the effect of TPABr on hydrogen generation. When the time is 100 s, the hydrogen generation of $MgH_2:TPABr = 5:1$ and $MgH_2:TPABr = 100:1$ increases by 52% and 29% compared with that without surfactants, respectively. At the time of 300 s, the hydrogen generation of $MgH_2:TPABr = 5:1$ and $MgH_2:TPABr = 100:1$ increases by 28.3% and 3%.

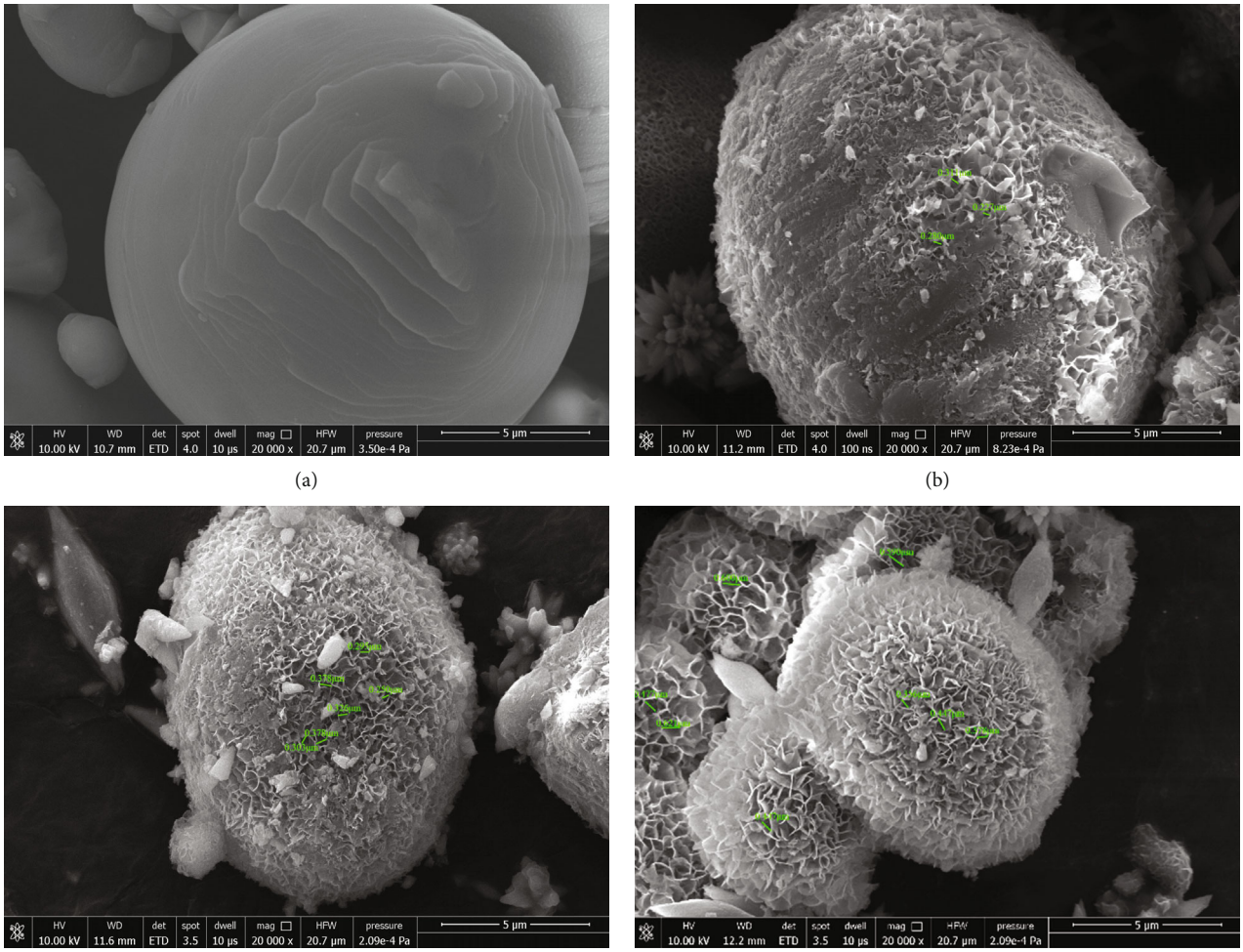

Figure 6: (a) Magnesium hydride. (b) Hydrolyzed product without surfactants. (c) MgH_2 : SDBS = 300 : 1, hydrolyzed product. (d) MgH_2 : TPABr = 1 : 1, hydrolyzed product (×20000).

According to the previous results in this work, the surface tension of solution decreases with the increase of the ratio of MgH_2 to surfactants. At the initial stage of the reaction, the lower the surface tension, the more hydrogen generation. And at the middle and late stages, the foam layer caused by the low surface tension impedes the hydrogen generation. However, there are some differences when TPABr added to the solution. As shown in Table 4, the surface tension decreases from 71.57 mN/m to 61.54 mN/m and then increases to 69.23 mN/m with increase of the ratio of MgH_2 to TPABr. And the hydrogen generation has the same trend, the final hydrogen yield are ranked as follows: MgH_2 : TPABr = 5 : 1 > MgH_2 : TPABr = 1 : 1 > MgH_2 : TPABr = 10 : 1 > MgH_2 : TPABr = 100 : 1 > MgH_2.

Figure 6(d) illustrates that $Mg(OH)_2$ grows evenly around the surface of MgH_2, like a blooming flower. The "petals"-$Mg(OH)_2$ form uniform channels instead of coating MgH_2 in the form of flakes. Because of the better passability, H_2O molecules can contact MgH_2 through these channels. Contrarily, the high concentration of TPABr may cause $Mg(OH)_2$ to grow as many points as possible on the surface of MgH_2 forming narrow and long channels. As a result, it is difficult for H_2O molecules to reach the surface of MgH_2 through the channels.

When the surface tension decreases to 61.54 mN/m, there is no obvious foam layer. Thus, H_2 can easily escape from the solution. In addition, TPABr inhibits the formation of passivation layer and prolongs the time for $Mg(OH)_2$ to reach the critical volume. It may also because of the adsorptive effect of TPABr. When TPABr absorbs on the surface of $Mg(OH)_2$ newly formed and the adsorption layer cannot only inhibit the growth of the $Mg(OH)_2$ [31, 32], it also reduces the surface energy. Therefore, the interaction among the particles is weakened, and it prevents the agglomeration among the particles [33–35].

3.3. Effect of Nonionic Surfactant. Nonionic surfactants are different in structure from other ionic surfactants. The main hydrophilic group is an ether group that does not dissociate in aqueous solution. It has an excellent wetting effect and superior antideposition ability for particles.

As shown in Figure 7, when the time is 100 s, the hydrogen generation of MgH_2 : Ecosol 507 = 100 : 1 is 50% higher

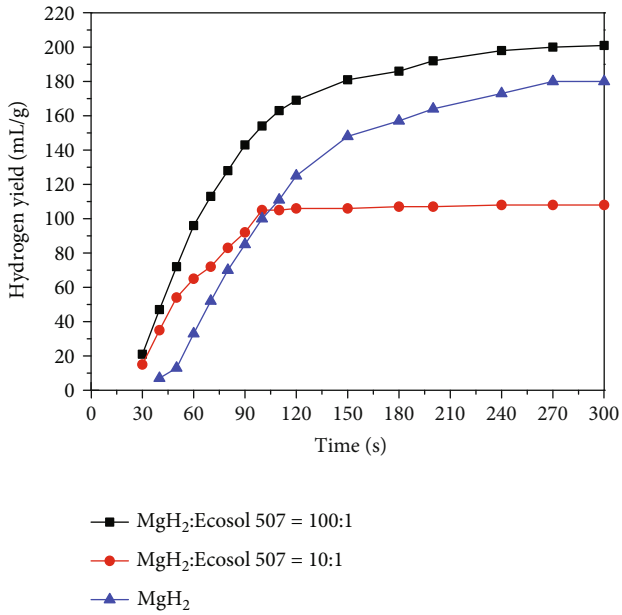

Figure 7: The effect of different Ecosol 507 dosages on hydrogen generation.

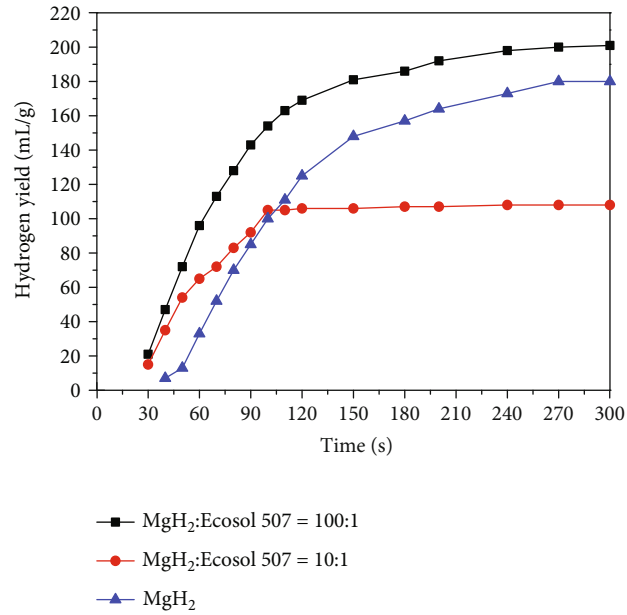

Figure 8: Comparison of hydrogen generation curves of MgH_2.

Table 5: Surface tension values of aqueous solutions with different Ecosol 507 dosages.

Ratio	ST (mN/m)
Water	71.57
MgH_2 : Ecosol 507 = 100 : 1	28.38
MgH_2 : Ecosol 507 = 10 : 1	20.49

than that without surfactants. When the time is 300 s, the hydrogen generation of MgH_2 : Ecosol 507 = 10 : 1 is 40% lower than that without surfactants, but the hydrogen generation of MgH_2 : Ecosol 507 = 100 : 1 is 11.7% higher than it.

It can be seen from Table 5 that Ecosol 507 significantly reduces the surface tension. In this experiment, we observed the volume of the foam was far much larger than the other surfactants. When the reaction time is over 100 s, the foam of MgH_2 : Ecosol 507 = 10 : 1 fills the whole three-necked flask and seriously weakens diffusion of H_2.

3.4. Comparison of Maximum Hydrogen Generation. Sort by maximum hydrogen generation (Figure 8): TPABr > SDBS > Ecosol 507 > OTAC > no surfactants > AES ≈ FMES − 70.

3.5. Analysis of SEM. In order to further explore the influence of surfactants on the hydrogen generation and the hydrogen generation rate, samples are observed and analyzed by SEM.

Figure 6 shows the scanning electron microscope pictures of the products of four illustrative experiments. The surface of MgH_2 particles used in the experiments can be observed in Figure 6(a) with a smooth surface and localized layered deposition. Figure 6(b) shows the morphology of MgH_2 after the hydrolysis reaction without surfactants. The smooth surface is pitted by H_2O molecules. There are two forms of $Mg(OH)_2$ on the surface of MgH_2. One forms a dense passivation layer that prevents H_2O molecules from contacting with MgH_2, and the other forms a discontinuous layered structure in the form of three-dimensional stacking that provides channels for H_2O molecules.

Surfactants can improve the morphology of the hydrolysate through interface control. After adding SDBS (MgH_2 : SDBS = 300 : 1), it is observed that the area of the coating layer in Figure 6(c) is significantly smaller than that in Figure 6(b), the relative stratigraphic structure becomes more and more evenly distributed on the hydrogenated, and the number and diameter of the channels have also increased. Therefore, the addition of SDBS increases the hydrogen generation and the hydrogen generation rate of the reaction system compared without surfactants. On one hand, adding TPABr increases the growth sites of $Mg(OH)_2$ to make the distribution of $Mg(OH)_2$ more uniform; on the other hand, it makes the directional growth of $Mg(OH)_2$, which further changes the morphology. Compared with Figure 6(b), the hydrolyzed product in Figure 6(d), there is no cladding layer; instead, a layered structure is formed by three-dimensional accumulation. Compared with Figure 6(c), the layered structure in Figure 6(d) is more uniform and stable (i.e., the distribution and the diameter of channels is more uniform and larger), and it allows more H_2O molecules to reach the surface of MgH_2 improving the hydrogen generation rate. At the same time, $Mg(OH)_2$ crystals formed by the reaction grow in the form of three-dimensional accumulation instead of encapsulating MgH_2, so that H_2O can react with MgH_2 constantly.

4. Conclusion

(1) The addition of surfactants reduces the surface tension of the liquid, improves the wetting effect of the liquid on the MgH_2, and increases the hydrogen

generation and the hydrogen generation rate at the initial stage of the hydrolysis

(2) With the addition of surfactants, the reaction system is more prone to foam. When these foams gather to form a foam layer, it hinders the escape of hydrogen and reduces the hydrogen generation and the hydrogen generation rate

(3) Surfactants can change the morphology of $Mg(OH)_2$. $Mg(OH)_2$ stake in three-dimensions to form a discontinuous layered structure improving the continuity of the hydrolysis reaction

(4) When the surfactant concentration reaches CMC, the self-polymerization of surfactants inhibits the separation of $Mg(OH)_2$ and affects the dispersion effect

(5) On one hand, the negatively charged groups of surfactants may combine with H^+ in the water, which reduces the concentration of H^+ affecting the hydrogen generation; on the other hand, the positively charged groups may combine with OH^- inhibiting the nucleated growth of $Mg(OH)_2$

Data Availability

The experimental data used to support the findings of this study are included within the article.

Conflicts of Interest

The authors declare no conflict of interest.

Acknowledgments

This work is financially supported by National Natural Science Foundation of China (No.51976112).

References

[1] D. J. C. Mackay and D. Hafemeister, "Sustainable energy-without the hot air," *American Journal of Physics*, vol. 78, no. 2, pp. 222-223, 2010.

[2] R. B. Gupta, *Hydrogen Fuel: Production, Transport, and Storage*, CRC Press, 2009.

[3] J. E. Mason, "World energy analysis: H2 now or later?," *Energy Policy*, vol. 35, no. 2, pp. 1315–1329, 2007.

[4] A. C. D. Chaklader, "Hydrogen generation from water split reaction," US Patent 6440385, 2002.

[5] S. I. Orimo, Y. Nakamori, J. R. Eliseo, A. Züttel, and C. M. Jensen, "Complex hydrides for hydrogen storage," *Chemical Reviews*, vol. 107, no. 10, pp. 4111–4132, 2007.

[6] W. Grochala and P. P. Edwards, "Thermal decomposition of the non-interstitial hydrides for the storage and production of hydrogen," *Chemical Reviews*, vol. 104, no. 3, pp. 1283–1316, 2004.

[7] H. Kato and A. Kudo, "New tantalate photocatalysts for water decomposition into H2 and O2," *Chemical Physics Letters*, vol. 295, no. 5-6, pp. 487–492, 1998.

[8] M. A. Rosen, "Advances in hydrogen production by thermochemical water decomposition: a review," *Energy*, vol. 35, no. 2, pp. 1068–1076, 2010.

[9] A. C. Dillon and M. J. Heben, "Hydrogen storage using carbon adsorbents: past, present and future," *Applied Physics A Materials Science & Processing*, vol. 72, no. 2, pp. 133–142, 2001.

[10] S. Satyapal, J. Petrovic, C. Read, G. Thomas, and G. Ordaz, "The U.S. Department of Energy's National Hydrogen Storage Project: progress towards meeting hydrogen-powered vehicle requirements," *Catalysis Today*, vol. 120, no. 3-4, pp. 246–256, 2007.

[11] Y. Wang, Z. Ding, X. Li et al., "Improved hydrogen storage properties of MgH2 by nickel@nitrogen-doped carbon spheres," *Dalton Transactions*, vol. 49, no. 11, pp. 3495–3502, 2020.

[12] M. Ismail, M. S. Yahya, N. A. Sazelee, N. A. Ali, and N. S. Mustafa, "The effect of K_2SiF_6 on the MgH_2 hydrogen storage properties," *Journal of Magnesium and Alloys*, vol. 8, no. 3, pp. 832–840, 2020.

[13] T. Biasetti Andrés, L. Mendoza Zélis, and M. Marcos, "Differences in the heterogeneous nature of hydriding/dehydriding kinetics of MgH_2-TiH_2 nanocomposites," *International Journal of Hydrogen Energy*, vol. 45, no. 51, pp. 27421–27433, 2020.

[14] N. A. Ali, N. H. Idris, M. F. M. Din, M. S. Yahya, and M. Ismail, "Nanoflakes $MgNiO_2$ synthesised via a simple hydrothermal method and its catalytic roles on the hydrogen sorption performance of MgH_2," *Journal of Alloys and Compounds*, vol. 796, pp. 279–286, 2019.

[15] J. Zhang, L. He, Y. Yao et al., "Catalytic effect and mechanism of NiCu solid solutions on hydrogen storage properties of MgH2," *Renewable Energy*, vol. 154, pp. 1229–1239, 2020.

[16] F. A. Halim Yap, N. N. Sulaiman, and M. Ismail, "Understanding the dehydrogenation properties of MgH2 catalysed by Na3AlF6," *International Journal of Hydrogen Energy*, vol. 44, no. 58, pp. 30583–30590, 2019.

[17] N. A. Sazeleea, N. H. Idrisa, M. F. M. Din, M. S. Yahya, N. A. Ali, and M. Ismail, "$LaFeO_3$ synthesised by solid-state method for enhanced sorption properties of MgH2," *Results in Physics*, vol. 16, pp. 102844–102850, 2020.

[18] N. H. Idris, N. S. Mustafa, and M. Ismail, "MnFe2O4 nanopowder synthesised via a simple hydrothermal method for promoting hydrogen sorption from MgH2," *International Journal of Hydrogen Energy*, vol. 42, no. 33, pp. 21114–21120, 2017.

[19] N. A. Ali, N. H. Idris, M. F. M. Din et al., "Nanolayer-like-shaped $MgFe_2O_4$ synthesised *via* a simple hydrothermal method and its catalytic effect on the hydrogen storage properties of MgH_2," *RSC Advances*, vol. 8, no. 28, pp. 15667–15674, 2018.

[20] V. C. Y. Kong, F. R. Foulkes, D. W. Kirk, and J. T. Hinatsu, "Development of hydrogen storage for fuel cellgenerators. i: Hydrogen generation using hydrolysishydrides," *International Journal of Hydrogen Energy*, vol. 24, no. 7, pp. 665–675, 1999.

[21] C. Wu, Y. Bai, and F. Wu, "Fast hydrogen generation from NaBH4 solution accelerated by ferric catalysts," *Materials Letters*, vol. 62, no. 27, pp. 4242–4244, 2008.

[22] C. Cento, P. Gislon, and P. P. Prosini, "Hydrogen generation by hydrolysis of NaBH4," *International Journal of Hydrogen Energy*, vol. 34, no. 10, pp. 4551–4554, 2009.

[23] M. S. Zou, R. J. Yang, X. Y. Guo, H. T. Huang, J. Y. He, and P. Zhang, "The preparation of Mg-based hydro-reactive

materials and their reactive properties in seawater," *International Journal of Hydrogen Energy*, vol. 36, no. 11, pp. 6478–6483, 2011.

[24] K. Azzaoui, E. Mejdoubi, S. Jodeh et al., "Eco friendly green inhibitor Gum Arabic (GA) for the corrosion control of mild steel in hydrochloric acid medium," *Corrosion Science*, vol. 129, pp. 70–81, 2017.

[25] T. Arslan, F. Kandemirli, E. E. Ebenso, I. Love, and H. Alemu, "Quantum chemical studies on the corrosion inhibition of some sulphonamides on mild steel in acidic medium," *Corrosion Science*, vol. 51, no. 1, pp. 35–47, 2009.

[26] M. Drach, A. Andrzejewska, J. Narkiewicz-Michałek, W. Rudziński, and L. K. Koopal, "Theoretical modeling of cationic surfactants aggregation at the silica/aqueous solution interface: effects of pH and ionic strength," *Physical Chemistry Chemical Physics*, vol. 4, no. 23, pp. 5846–5855, 2002.

[27] I. A. Khan, A. J. Khanam, M. S. Sheikh, and Kabir-ud-Din, "Influence of ionic and nonionic hydrotropes on micellar behavior of a cationic gemini surfactant butanediyl-1,4-bis(dimethylcetylammonium bromide)," *Journal of Colloid and Interface Science*, vol. 359, no. 2, pp. 467–473, 2011.

[28] M. Qiao, J. Chen, C. Yu, S. Wu, N. Gao, and Q. Ran, "Gemini surfactants as novel air entraining agents for concrete," *Cement and Concrete Research*, vol. 100, pp. 40–46, 2017.

[29] A. Bureiko, A. Trybala, N. Kovalchuk, and V. Starov, "Current applications of foams formed from mixed surfactant-polymer solutions," *Advances in Colloid and Interface Science*, vol. 222, pp. 670–677, 2015.

[30] J. Zheng, D. C. Yang, W. Li, H. Fu, and X. Li, "Promoting H2 generation from the reaction of Mg nanoparticles and water using cations," *Chemical Communications*, vol. 49, no. 82, pp. 9437–9439, 2013.

[31] H. Dhaouadi, H. Chaabane, and F. Touati, "Mg(OH)2 nanorods synthesized by a facile hydrothermal method in the presence of CTAB," *Nano-Micro Letters*, vol. 3, no. 3, pp. 153–159, 2011.

[32] Z. Hu, Y. Ji, S. Hou, and X. Wu, "Minimizing the effect of near-distance dielectric sensitivity on retrieving average aspect ratio of gold nanorod by optical extinction spectroscopy: in the case of CTAB adsorption," *Chinese Science Bulletin*, vol. 59, no. 16, pp. 1822–1831, 2014.

[33] J. P. Zheng and T. R. Jow, "A new charge storage mechanism for electrochemical capacitors and charge storage density vs. crystalline structure of metal oxides," *MRS Proceedings*, vol. 393, no. 1, pp. 439–444, 1995.

[34] M. G. Sullivan, R. Kötz, and O. Haas, "Thick active layers of electrochemically modified glassy carbon. Electrochemical impedance studies," *Journal of the Electrochemical Society*, vol. 147, no. 1, pp. 308–317, 2000.

[35] H. Y. Lee and J. B. Goodenough, "Supercapacitor behavior with KCl electrolyte," *Journal of Solid State Chemistry*, vol. 144, no. 1, pp. 220–223, 1999.

Hindawi
International Journal of Photoenergy
Volume 2020, Article ID 8844874, 5 pages
https://doi.org/10.1155/2020/8844874

Research Article

Effect of Stress on Creep Behavior of Single Crystal Alloy IC6SX at 980°C

Liwu Jiang,[1,2] **Xuezheng Dou**,[1] **and Meiling Wu**[3]

[1]*National Center for Materials Service Safety, University of Science and Technology Beijing, Beijing 100083, China*
[2]*NCS Testing Technology Co., Ltd., Beijing 100081, China*
[3]*Beijing Institute of Aeronautical Materials, Beijing 100095, China*

Correspondence should be addressed to Liwu Jiang; lwjiang@ustb.edu.cn

Received 21 September 2020; Revised 6 November 2020; Accepted 27 November 2020; Published 14 December 2020

Academic Editor: Qiang Fu

Ni_3Al-based single crystal alloy IC6SX was prepared by seed crystal method. The effect of different stress conditions on creep behavior of this alloy at 980°C was investigated. The results showed that the creep life of this alloy at 980°C decreased significantly with the increase of stress. When the stress increased from 180 MPa to 230 MPa, the creep life dropped from 245.5 h to 69.3 h, and the steady-state creep rate increased slightly but not significantly. Meanwhile, the morphology of γ' phase and dislocation after creep were studied. The results showed that with the increase of stress, the density of dislocations in the γ' phase increased gradually, the strength of this alloy decreased gradually, so the creep life decreased significantly. The Y-NiMo phase resolved from the γ phase decreased gradually as the creep life decreased. The creep experiment of the alloy was carried out at 980°C. Due to the higher temperature, the diffusion of atoms in this alloy became faster. Deformation was not only caused by the slippage of dislocations in the crystal but also by the diffusion of atoms. Therefore, the creep mechanism of single crystal alloy IC6SX at this temperature is a mixed mechanism of dislocation glide and diffusion.

1. Introduction

With the rapid development of modern aviation technology, the requirements for the turbine inlet temperature and thrust-to-weight ratio of gas turbine engines are improved constantly, so the properties of the alloys used in aeroengines should also be improved [1]. Compared with nickel-based single crystal alloy, Ni_3Al-based single crystal alloy has the advantages of low density, high melting point, large specific strength, high plasticity, low cost, long service life, good mechanical properties at high temperature, and strong oxidation resistance. Therefore, the research and development on Ni_3Al-based single crystal alloys have been becoming a research hotspot in the field of high-temperature structural materials [2–5].

American scientists have developed many Ni_3Al-based superalloys such as IC50, IC218, and IC221M [6]. The researches in the field of materials have achieved certain results on Ni_3Al-based materials during the last decades, and several Ni_3Al-based superalloys with excellent properties have been developed for turbine blades and vanes of aeroengines, such as IC6, IC6A, IC10, and IC6SX [7–9]. And the single crystal Ni_3Al-based superalloy IC6SX has been developed on the basis of DS IC6 which is the directionally solidified alloy with similar contents for further increasing mechanical properties [10]. IC6SX has low density, high initial melting point, high-temperature durable strength, low cost, and good comprehensive properties [11, 12]. The result of Kong and Li [13] showed that the dislocation configuration and movement pattern of Ni_3Al-based single crystal alloy IC6SX are different under the different temperature and stress conditions. The result of Zhang et al. [14] showed that the creep mechanisms are dislocation glide at lower testing temperatures in higher stress levels and dislocation climb at higher temperatures in lower stress levels.

It can be seen that material workers have carried out a lot of research on the creep behavior of nickel-based single crystal alloys, and many new developments have been made.

Table 1: Creep properties of single crystal alloy IC6SX at 980°C.

Creep stress Creep properties	180 MPa	205 MPa	230 MPa
Instantaneous elastic strain (%)	0.206	0.223	0.252
Plastic strain during deceleration creep stage (%)	0.089	0.131	0.14
Deceleration creep stage time (h)	0.95	0.84	0.56
Plastic strain during steady-state creep stage (%)	0.776	0.549	0.518
Steady-state creep stage time (h)	129.53	41.81	14.61
Steady-state creep rate (%/S)	1.66×10^{-6}	3.65×10^{-6}	9.85×10^{-6}
Plastic strain during accelerated creep stage (%)	35.035	22.637	38.386
Accelerated creep phase time (h)	115.02	78.82	54.13
Creep life (h)	245.5	121.47	69.3

However, the scientific problem of how different stress conditions affect the creep behavior of Ni_3Al-based single crystal alloy IC6SX remains unsolved.

In this paper, Ni_3Al-based single crystal alloy IC6SX specimens were prepared by seed crystal method [15]. And the effect of different stress conditions on creep behavior of this alloy at 980°C was explored. This experiment has never been studied before, and it is also the innovative point of this work. The creep mechanism of IC6SX at 980°C was found out by comparing the changes in properties, microstructures, and dislocations of single crystal alloys during creep process under different stress conditions, providing a theoretical basis for the application of Ni_3Al-based single crystal alloy.

2. Experimental Procedure

The material used for the present study was a Ni_3Al-based alloy IC6SX, with a nominal composition of Ni-7.4~8.0Al-13.5~14.3Mo-0.02~0.03B (wt%). The raw materials used were all high-purity elements, including Ni (99.9%), Al (99.9%), and Mo (99.9%). Firstly, the master alloy ingot with a size of $\varphi 75 \times 500$ mm was prepared by vacuum induction melting method in the GVR-100 vacuum induction furnace. Then, the single crystal alloy test bars with different crystal orientations were prepared by seed crystal method in the DZG-0.025 directional solidification furnace, and the size of the test bars was $\varphi 15 \times 160$ mm. All the test bars were calibrated for crystal orientation by X-ray backscattering Laue method. The test bars with orientation deviation less than 5° and without defects were selected for this study.

The heat treatment conditions of IC6SX test bars were 1260°C/10 h air cooling solution treatment +870°C/32 h air cooling aging treatment. Then, they were machined into creep specimens and placed in the GWT504 high-temperature endurance creep testing machine, maintaining a temperature environment of 980°C, and uniaxial constant-load tensile creep tests were performed under 180 MPa, 205 MPa, and 230 MPa stress conditions, and the creep data were obtained.

The microstructure of the specimens was analyzed by an optical microscope (OM) and a scanning electron microscope (SEM). The morphology and evolution of dislocation were observed by the Tecnai F30 field emission transmission electron microscope.

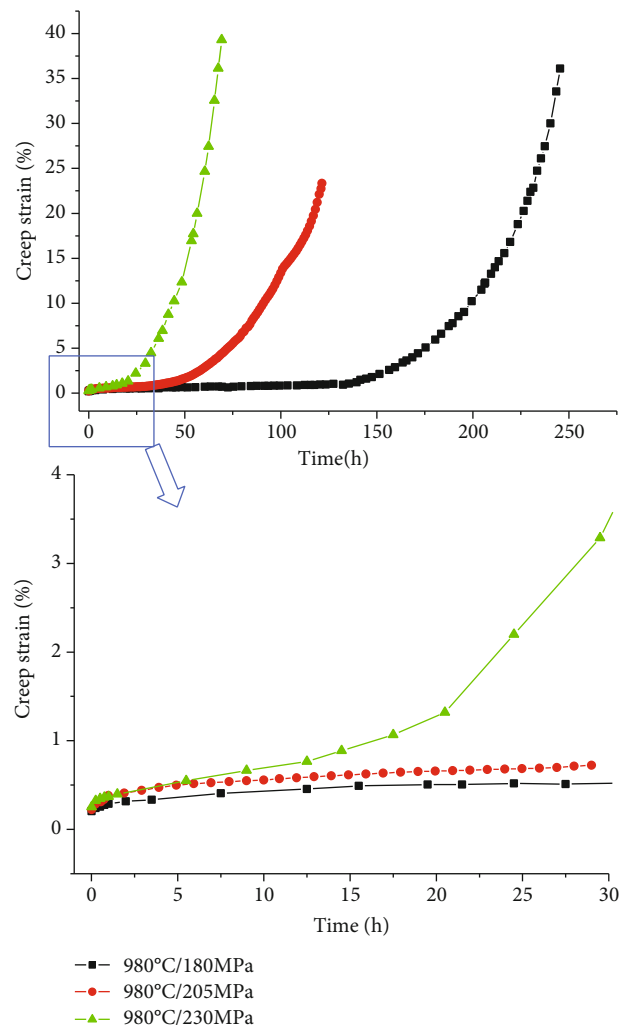

Figure 1: Creep curve of single crystal alloy IC6SX at 980°C.

3. Results and Discussion

3.1. Creep Properties of Single Crystal Alloy IC6SX at 980°C. All the creep property parameters of single crystal alloy IC6SX under the three stress conditions of 180 MPa, 205 MPa, and 230 MPa at 980°C are shown in Table 1.

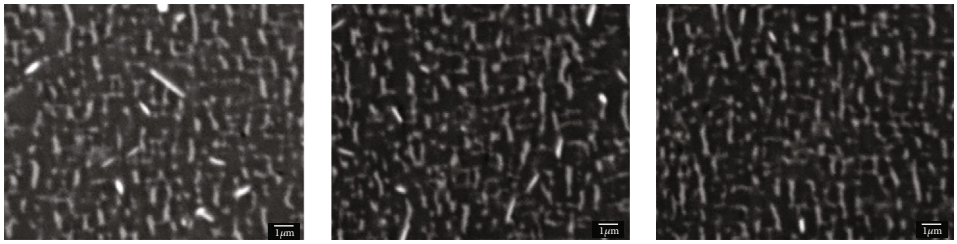

(a) (b) (c)

Figure 2: Microstructure of single crystal alloy IC6SX after creep at 980°C: (a) 180 MPa, 245.5 h; (b) 205 MPa, 121.47 h; (c) 230 MPa, 69.3 h.

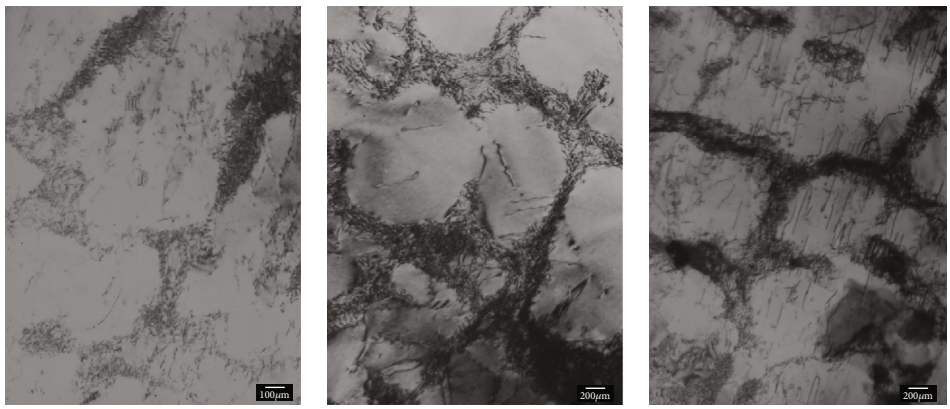

(a) (b) (c)

Figure 3: Dislocation structure morphology of single crystal alloy IC6SX after creep at 980°C: (a) 180 MPa, 245.5 h; (b) 205 MPa, 121.47 h; (c) 230 MPa, 69.3 h.

Figure 1 shows the creep curves of single crystal alloy IC6SX under three different stress conditions at 980°C. From Figure 1, it can be identified that the creep curves of this alloy under three stress conditions can be divided into deceleration creep stage, steady-state creep stage, and accelerated creep stage. All the deceleration creep stage times of this alloy under three stress conditions were short and still less than 1 h to the end. As the stress increased from 180 MPa to 230 MPa, the duration of the steady-state creep stage decreased from 129.53 h to 14.61 h. When the stress was 180 MPa, the alloy entered the steady-state creep stage of 129.53 h after the deceleration creep stage of 0.95 h, the creep strain was 0.776%, and the steady-state creep rate was 1.66×10^{-6} (%/S). Then, it entered the accelerated creep stage of 115.02 h, and the final creep life was 245.5 h. When the creep stress increased to 205 MPa, the steady-state creep stage duration of the alloy decreased rapidly to 41.81 h, the creep strain was 0.549%, and the steady-state creep rate increased to 3.65×10^{-6} (%/S), increased by more than 1 time. Then, the alloy entered the accelerated creep stage of 78.82 h; the creep life of the alloy under this stress was 121.47 h. When the creep stress continued to increase to 230 MPa, the steady-state creep stage duration of the alloy decreased to 14.61 h, the creep strain was 0.518%, and the steady-state creep rate continued to increase to 9.85×10^{-6} (%/S), the creep life was only 69.3 h.

The results showed that the creep life and steady-state creep stage duration of single crystal alloy IC6SX at 980°C decreased significantly with the increase of stress. When the stress increased from 180 MPa to 230 MPa, the creep life decreased from 245.5 h to 69.3 h. The duration of the creep stage dropped from 129.53 h to 14.61 h. But with the increase of stress, the change of creep strain was not significant, and the steady-state creep rate increased slightly but not significantly. To analyze the reasons for these results, it is necessary to further study the structure and dislocation morphology of the alloy after creep.

3.2. Creep Structure Evolution of Single Crystal Alloy IC6SX at 980°C

3.2.1. Morphology of γ' Phase after Creep at 980°C. Figure 2 shows the microstructure of single crystal alloy IC6SX after creep under different stress conditions at 980°C. It can be identified that the degree of cubicization of the γ' phase reduced significantly under the three stress conditions. Due to the diffusion of atoms in the single crystal alloy, a typical directional coarsening of the γ' phase was formed. The network structure was damaged severely and disconnected by the γ' phase; most of the γ' phase had been connected. The creep life decreased with the increase of stress, and the Y-NiMo phase precipitated from the γ phase decreased gradually.

3.2.2. Morphology of Dislocation after Creep at 980°C. Figure 3 shows the morphology of dislocation after creep under different stress conditions at 980°C. When the stress was 180 MPa, since the creep life was as high as 245.5 h, both γ and γ' phases underwent severe directional coarsening.

There was a high-density dislocation network in the γ phase, some dislocations cut into the γ' phase, but the dislocation density in the γ' phase was not high. When the stress increased to 205 MPa, the high-density dislocation network in the γ phase was still there, and some dislocation pairs cut into the γ' phase. As the stress increased to 230 MPa, a large number of dislocation pairs cut into the γ' phase and crossed each other, and the density of dislocations increased. As a result, the strength of this alloy decreased, so the creep life was only 69.3 h.

3.3. Analysis and Discussion. Meanwhile, the morphology of the γ' phase and dislocation after creep were studied. The results showed that with the increase of stress, the dislocations cut from the γ phase into the γ' phase increased gradually, so the dislocation network density in the γ phase decreased gradually. The density of dislocations in the γ' phase increased gradually, and the dislocations crossed each other. As a result, the strength of this alloy decreased gradually, so the creep life decreased significantly.

The creep experiment of the alloy was carried out at 980°C. Due to the higher temperature, the diffusion of atoms in this alloy became faster. A typical directional coarsening of the γ' phase was formed, the dislocation network in the γ phase was destroyed by the γ' phase, and the organizational evolution had occurred. So the deformation was not only caused by the slippage of dislocations in the crystal but also by the diffusion of atoms. Therefore, the creep mechanism of single crystal alloy IC6SX at this temperature is a mixed mechanism of dislocation glide and diffusion.

4. Conclusions

In this paper, Ni_3Al-based single crystal alloy IC6SX was taken as the research object. The effect of different stress conditions on creep behavior of this alloy at 980°C was explored. The creep mechanism of IC6SX at 980°C was found out by comparing the changes in properties, microstructures, and dislocations of single crystal alloys during creep process under different stress conditions, providing a theoretical basis for the application of Ni_3Al-based single crystal alloy. The main conclusions are as follows:

(1) The creep life of single crystal alloy IC6SX at 980°C decreased significantly with the increase of stress

(2) When the stress increased from 180 MPa to 230 MPa, the steady-state creep rate increased slightly but not significantly

(3) The creep experiment of the alloy was carried out at 980°C. Due to the higher temperature, the diffusion of atoms in this alloy became faster. Deformation was not only caused by the slippage of dislocations in the crystal but also by the diffusion of atoms. Therefore, the creep mechanism of single crystal alloy IC6SX at this temperature is a mixed mechanism of dislocation glide and diffusion

Data Availability

The research data used to support the findings of this study are included within the article.

Conflicts of Interest

The authors declare that they have no conflicts of interest.

Acknowledgments

This research was financially supported by the National Science and Technology Major Project (Grant Nos. 2017-VI-0012-0084 and 2017-VI-0011-0083), the Fundamental Research Funds for the Central Universities (Grant No. FRF-GF-19-029B), and the National Natural Science Foundation of China (Grant No. 51471022).

References

[1] L. Wei, Z. G. Zhang, H. Zhang, S. S. Li, and S. K. Gong, "Influence of aging heat treatment on microstructure and hardness of single crystal Ni_3Al-base superalloy IC21," *Procedia Engineering*, vol. 27, no. 1, pp. 1081–1088, 2012.

[2] L. Pichon, J. B. Dubois, S. Chollet, F. Larek, J. Cormier, and C. Templier, "Low temperature nitriding behaviour of Ni_3Al-like γ' precipitates in nickel-based superalloys," *Journal of Alloys and Compounds*, vol. 771, no. 8, pp. 176–186, 2019.

[3] A. Mohammadnejada, A. Bahramia, M. Sajadia, P. Karimia, H. R. Fozveha, and M. Y. Mehr, "Microstructure and mechanical properties of spark plasma sintered nanocrystalline Ni_3Al-xB ($0.0 < x < 1.5$ at%) alloy," *Materials Today Communications*, vol. 17, no. 9, pp. 161–168, 2018.

[4] D. Kotoban, A. Nazarov, and I. Shishkovsky, "Comparative study of selective laser melting and direct laser metal deposition of Ni_3Al intermetallic alloy," *Procedia IUTAM*, vol. 23, no. 6, pp. 138–146, 2017.

[5] C. B. Xiao, Y. F. Han, K. Q. Yin, and X. H. Zhao, "High temperature creep behaviour of a directionally solidified Ni_3Al based alloy IC6," *Journal of Materials Engineering*, vol. 1, no. 3, pp. 6–8, 1996.

[6] L. Wei, H. Zhang, S. S. Li, Y. Ma, and S. K. Gong, "Influence of heat treatments on microstructure of single crystal Ni_3Al-base superalloy," *Chinese Journal of Rare Metals*, vol. 36, no. 2, pp. 178–183, 2012.

[7] Y. F. Han and S. H. Li, "A directionally solidified Ni_3Al based alloy IC6- high-performance gas turbine guide blade material," *Gas Turbine Experiment and Research*, vol. 1, no. 1, pp. 48–51, 1994.

[8] C. B. Xiao, Y. F. Han, and X. A. Zhang, "Study on directionally solidified Ni_3Al based high temperature structural material IC6A alloy," *Journal of Materials Engineering*, vol. 1, no. 6, pp. 3–6, 2001.

[9] X. H. Zhao, C. H. Huang, Y. N. Tan, Q. Zhang, Q. Yu, and H. B. Xu, "New Ni_3Al-based directionally-solidified superalloy IC10," *Journal of Aeronautical Materials*, vol. 26, no. 3, pp. 20–24, 2006.

[10] P. Cao, B. Huang, Y. He, Y. Zhang, J. Yu, and W. Fang, "Influence of hot corrosion on high temperature creep rupture for single crystal superalloy DD3," *Rare Metals*, vol. 14, no. 4, pp. 290–295, 1995.

[11] X. Liu, J. X. Song, S. S. Li, and Y. F. Han, "Effect of NiCoCrAlY(Si) gradient coatings on oxidation resistances of Ni_3Al based single crystal alloy IC6SX," *Journal of Materials Engineering*, vol. 5, no. 5, pp. 52–56, 2008.

[12] P. Li, S. S. Li, and Y. F. Han, "Effect of heat treatment on microstructure and stress rupture properties of a Ni_3Al base single crystal alloy IC6SX," *Journal of Materials Engineering*, vol. 5, Supplement 1, pp. 131–135, 2009.

[13] Z. G. Kong and S. S. Li, "Effects of temperature and stress on the creep behavior of a Ni_3Al base single crystal alloy," *Progress in Natural Science: Materials International*, vol. 23, no. 2, pp. 205–210, 2013.

[14] G. Y. Zhang, H. Zhang, X. M. Wu, and J. T. Guo, "Creep behavior for NiAl-28Cr-5.5Mo-0.5Hf-0.012P alloy at high temperature," *Chinese Journal of Rare Metals*, vol. 30, no. 3, pp. 305–309, 2006.

[15] J. Zhang, L. Wang, D. Wang et al., "Recent progress in research and development of nickel-based single crystal superalloys," *Acta Metallurgica Sinica*, vol. 55, no. 9, pp. 1077–1094, 2019.

Hindawi
International Journal of Photoenergy
Volume 2020, Article ID 8885737, 7 pages
https://doi.org/10.1155/2020/8885737

Research Article

Experimental Study on the Distribution Trends of Fouling on a Compressor Blade

Jie Tang,[1,2] **Dianrong Gao**,[1] **Liwen Wang**,[2] **and Jinjian Huo**[2]

[1]*Institute of Mechanical Engineering, Yanshan University, Qinhuangdao, China*
[2]*Aviation Engineering Institute, Civil Aviation University of China, Tianjin, China*

Correspondence should be addressed to Jie Tang; tangjie_cauc@163.com

Received 14 August 2020; Revised 19 October 2020; Accepted 16 November 2020; Published 28 November 2020

Academic Editor: Qiang Fu

The formation of a scale on a compressor blade surface is inevitable, and the study of the distribution of the scale can provide effective guidance for the cleaning of a wing engine. Using the waste liquid collected from the engine during the wing water washing process as a data sample, the main components of compressor blade surface fouling were analysed, which included 49.9% SiO_2, 14.5% FeO, 11.5% Al_2O_3, 9.4% CaO, etc. Based on JKR contact theory, a model for calculating the total thickness of the fouling layer on the blade surface was established. Through a simulation experiment on the fouling of a blade surface, the number of particulates deposited on the pressure surface was lower than the amount of the secondary deposition mass on the suction surface. From contrastive analysis of the results of perforation, the fouling is divided into three types: loose, dense, and transitional. The surface of a single blade can be divided into four different fouling areas. The parameters of the engine cleaning process can be designed according to the characteristics of the fourth area.

1. Introduction

An aero engine needs to continuously pull in air while functioning, and the suspended particulate pollutants in the air are inevitably be drawn into the engine and gradually adhere to the blade surface or edge to form fouling. The fouling on a blade surface has an important effect on the engine performance. Fouling results in surges in severe cases and poses hidden dangers to flight safety, which has aroused widespread concern.

Kurz et al. [1, 2] conducted an experimental study of fouling adhesion on the blade surface, quantitatively analysed the amount of fouling formed on blade surfaces under different conditions, and believed that the retention mode of particulate matter was related to the boundary layer shear stress. Osvaldo and Zuniga [3] found that oil residues caused by seals, steel, and aluminium particles generated by the wear of seal brushes and bearing parts and internal wear all contribute to fouling inside the compressor source. Tarabrin et al. [4] believed that due to the structural differences between the pressure surface and suction surface of the blades and the complex structure of the inner wall of the engine, the flow direction of the airflow changes, resulting in the accumulation of particulates trapped in the airflow. Song et al. [5] believed that the particles were mainly transported to the pressure surface of the blade under the action of inertial force, so the fouling on the pressure surface was mainly caused by larger particles. Yang and Xu [6] found in their research that the fouling of the leading edge of a blade is mainly affected by large particles, the mechanism of which is inertial impact, and the formation of a scale on the pressure area of the blade is mainly due to the impact of large particles after the deviation of the adjacent suction surface. Mathioudakis and Tsalavoutas [7] believed that the greater the relative humidity of the air is, the easier it is for water vapor to condense into a thick liquid film on the surface of the compressor blade, causing the dissolved particles to adhere to the blade

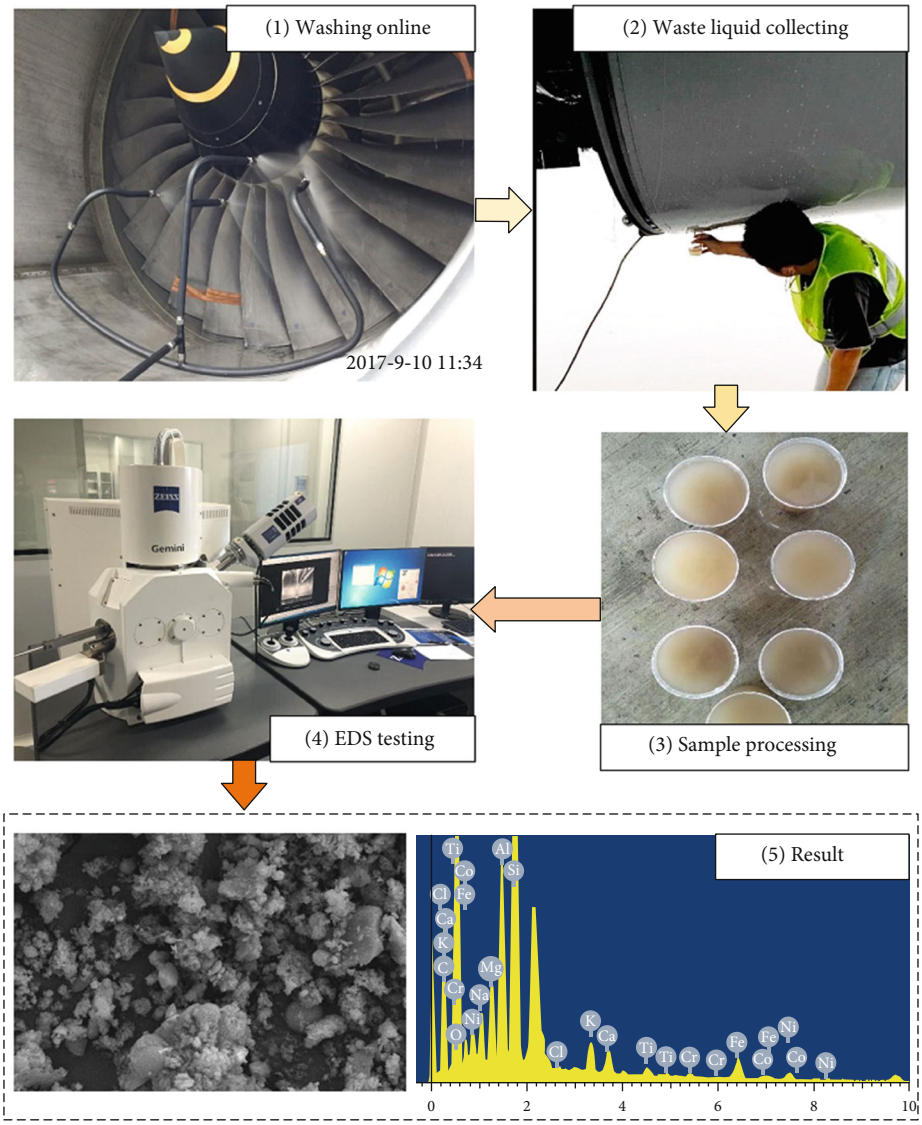

Figure 1: Collection and treatment of scale.

surface. Fielder [8] pointed out that natural environmental factors such as dense fog, rain, and snow and excessive humidity accelerate the adhesion process of particles. The size of the particles determines the movement trajectory of the particles and the influence of turbulent diffusion.

However, research on the distribution of scale on the blade surface still needs to be improved. First, the calculation model for the thickness of the scale deposited on the surface of a compressor blade has not been accurately judged. Additionally, the distribution of scale on the blade surface has not been quantified. Therefore, in this paper, research is carried out on the distribution trends of fouling mass and thickness calculation models for the surface of an engine compressor blade. The zoning method is used to analyse the changes in fouling mass and fouling characteristics, which provides guidance for the optimization of the parameters of the engine wing water washing process.

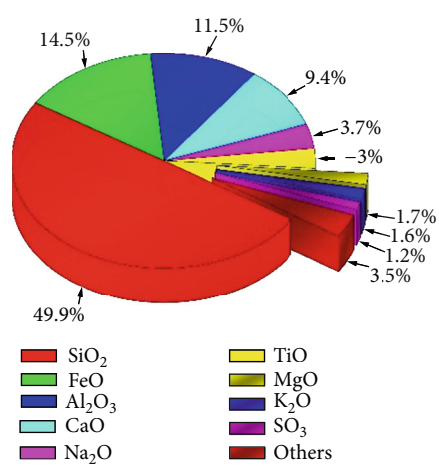

Figure 2: Compressor blade fouling.

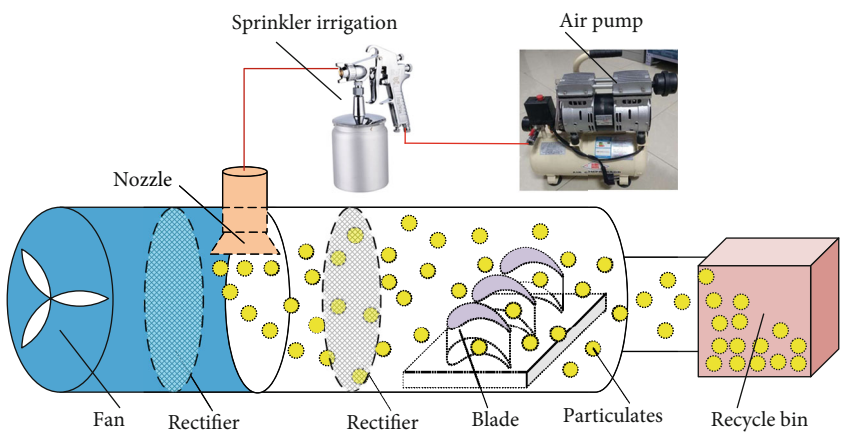

Figure 3: Schematic diagram of the experimental system.

2. Collection and Analysis of Scale Samples on the Blade Surface

The composition of the fouling on the blade surface has an important influence on the fouling rule. It is necessary to develop the sampling and analysis of the fouling on the blade surface to obtain the composition of the fouling. The cleaning of a wing engine provides a good opportunity to obtain scale samples from the surfaces of blades. A measuring cup is used to collect the cleaning waste liquid flowing out of the residual water hole of the engine. The sampling and analysis process of the waste liquid sample is shown in Figure 1. First, the sample is heated and dried to evaporate the water in the waste liquid, and finally, a scale sample of solid particles is obtained. Second, the glass sample is ground using a glass grinding rod and a grinding bowl to make the scale particles discrete, and finally, an energy dispersive spectrometer is used to measure and analyse the sample.

Through analysis of the scale samples, the scale components are obtained. The main elemental composition of scale includes C, N, O, Na, Mg, Al, Si, and other components. According to the atomic mass fraction, the sample contains CaO, SiO_2, MgO, Al_2O_3, etc., where SiO_2 comprises 49.9%, FeO comprises 14.5%, Al_2O_3 comprises 11.5%, CaO comprises 9.4%, Na_2O comprises 3.7%, and TiO comprises 3%. The remaining impurities account for 8%, as shown by the detailed mass scores in Figure 2.

3. Experiment on Fouling of Compressor Blade Surface

3.1. Experimental System Construction. Figure 3 is a schematic diagram of a simulation experiment platform system for fouling on a compressor blade surface. The test system is composed of a fan, a rectifier net, an air pump, a pneumatic sprayer, a nozzle, a blade under testing, a particulate recovery box, and its culvert. The maximum air volume of the fan is 13980 m^3/h, and the speed is controlled by the inverter. During the experiment, the pneumatic sprayer sends the particulate matter into the experimental cavity through the nozzle.

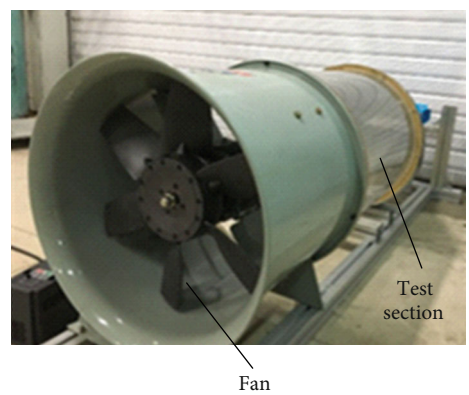

Figure 4: Experimental system physical map.

Under the action of the fan, the air velocity in the cavity is approximately 20 m/s. After passing through the rectifying mesh, the particulate matter enters the area of the tested blade and gradually forms a scale on the surface of the blade. After passing through the blades, the particulate matter enters the recovery box for collection. The undeposited particles are collected by the bag filter in the recovery box, and the airflow without particulate matter is discharged into the atmosphere.

The actual experimental system is shown in Figure 4.

3.2. Particulate Matter Ratio. The scaling of solid particles is completed in a gas-solid two-phase flow field. This system uses the blower process to simulate the gas-solid two-phase flow field. The experimental gas medium is air (20°C) at normal temperature, its density is 1.293 kg/m^3, and its dynamic viscosity is 1.8×10^{-5} Pa · s.

According to the research results of the relevant literature [9], the size of the scale particles is 16 μm. The proportions of scale particles are 49.9% SiO_2, 14.5% FeO, 11.5% Al_2O_3, and 9.4% CaO. The remaining scale components are replaced by water-insoluble SiC particles, so 14.7% SiC particles are added. The composition ratio of particles in the scale simulation experiment is shown in Table 1.

Table 1: Composition ratio of particles in the experiment.

Composition	SiO_2	FeO	Al_2O_3	CaO	SiC
Ratio (%)	49.9	14.5	11.5	9.4	14.7

4. Theoretical Analysis of the Thickness of the Fouling Layer on the Blade Surface

Solid particles are coupled with a variety of forces inside an engine and gradually deposit to form fouling. The deposition process can be divided into three stages: (1) The particles move with the air flow due to rotation. At this time, the particles are subject to drag forces and electrostatic forces, and thermophoretic forces, inertial centrifugal forces, and van der Waals forces change the speed of the particles. (2) The particles collide with the blade wall surface; some particles are gradually deposited to form a loosely deposited adhesion layer, and the others rebound from the surface, returning to the flow field at a certain speed. (3) During the accumulation stage of the scale layer, the loosely deposited adhesion layer continues to accumulate under the impact of temperature, pressure, and other solid particles, and phase change adhesion even occurs, forming a relatively dense dirt layer, as shown in Figure 5.

The movement of solid particles in the inner tract is a typical gas-solid two-phase flow. When the particles touch the surface of the blade, the particles themselves are deformed. The profile of the blade surface affects adhesion and binding. This belongs to the category of contact theory. Typical contact theories include Hertz contact theory, JKR theory, DMT theory, M-D theory, GW theory, and Persson theory [10].

The fouling process of the low-pressure compressor blade surface conforms to JKR contact theory. Combined with the research results of the literature [11], the thickness H of the scale deposit on the blade surface follows the following relationship:

$$H = f(T, F, t, C, \sigma_s, \alpha). \tag{1}$$

In the formula, T is the engine working time, s; F is the compressor air flow rate, m^3/s; t is the compressor working temperature, K; C is the particulate concentration, kg/m^3; σ_s is the solid particle scaling stress, Pa; and α is the contact angle between the solid particles and the blade surface and is dimensionless.

Let d_1 be the contact radius without considering the adhesion force, d_2 is the contact radius with the adhesion force considered, and the contact surface is equivalent to a circle with radius d, as shown in Figure 6. The solid particles in contact with the blade surface have a total energy of U satisfying $U = f(A)$, where A is the contact area and $A = \pi d^2$.

According to the contact area, the contact stress between the solid particles and the blade surface σ_{jc} can be obtained:

$$\sigma_{jc} = k\frac{P}{A}. \tag{2}$$

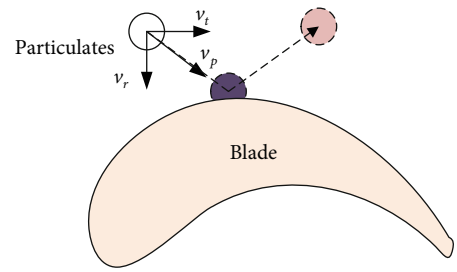

Figure 5: Particulate matter and blade surface contact process.

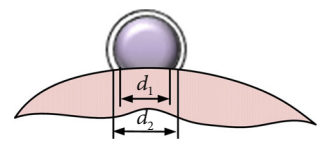

Figure 6: Schematic diagram of contact between particle and blade based on JKR contact theory.

Table 2: The mass of particles deposited on the blades.

No.	Pressure surface deposition mass (g)	Suction surface deposition mass (g)
1	0.05304	0.06749
2	0.05122	0.06607
3	0.05200	0.06830
4	0.05616	0.06983
5	0.05685	0.07026

In the formula, P is the impact force between the particle and the blade, N; k is the correction coefficient, $k = 0.01$; σ_{jc} is the contact stress between the particle and the blade, Pa; and A is the equivalent contact area between the particle and the blade surface, m^2.

Under the condition of a certain temperature, the solid particles collide with the blade to produce contact stress. When the contact stress σ_{jc} reaches or exceeds a certain critical value, the particles undergo plastic deformation, and the particles change from an ideal elastomer to an ideal plastic body. When the physical and mechanical properties of the particles are consistent with an ideal plastic body, the critical value is defined as the scaling stress σ_s of the particles. After the particulate matter is combined with the blade to form fouling, the contact area is A_1, and then the single solid particulate and the blade surface form a fouling thickness of height h.

$$h = \frac{V}{A_1}. \tag{3}$$

The total thickness of the scale layer on the blade surface can be expressed as

$$H = \sum_{i=1}^{N} h_i. \tag{4}$$

In the formula, A_1 is the contact area of single particles to form the scale, m^2; V is the volume of solid particles, m^3; h is the thickness of the sscale layer formed by single particles, m; h_i is the thickness of the scale layer formed by different particles, m; N is the number of particles deposited in the same area of the blade; and H is the total height of the scale layer formed by N particles deposited in the same area on the surface of the blade, m.

5. Analysis of Results

There are a total of three blades in the experimental system. Considering the influence of the boundary layer in the simulation process of scaling, only the intermediate blades are selected for the analysis of the experimental results to ensure the rationality of the experimental results. In this experiment, a total of 5 full-scale simulation experiments are carried out. After each experiment, the sediment on the surface of the middle blade is measured and analysed, and the blade is cleaned again and then dried for the next experiment.

5.1. Deposition Mass Measurements. The deposition mass is an important indicator for measuring particle deposition. The deposition mass of the scale on the surface of a single blade is very small, generally on the order of 10^{-2} g. In the experiment, a 0.00001 electronic balance is used to measure the deposition mass to ensure the accuracy of the experiment.

In the experiment, the air volume of the fan is set to 800 m^3/h, the particle concentration is adjusted to 50 g/m^3 through a powder feed sprayer, and the results of the five experiments are weighed. The deposition amount on the blade surface is shown in Table 2. The standard deviation of the mass of the deposition on the surface of the blades is small, below 10^{-3}.

It can be seen from the measurement results that the number of particulates deposited on the pressure surface is lower than the secondary deposition mass of the suction surface; the average value of the particulate deposition on the pressure surface is 0.05385 g, the average value of the deposition mass of the suction surface is 0.06839 g, and the difference between the scale accumulation on each side of the blade is 0.01454 g. Figure 7 shows a comparison of the amounts of scale deposits on the blade surface.

5.2. Observation of Sediment Distribution Patterns. The distribution of solid particles on the compressor blades is an important part of the study of particle deposition. Using a camera to photograph the scaled blades, the distribution of sediment particles on the blade surface, as shown in Figure 8, is obtained. Comparing the images of the five experiments, it can be found that the particle deposition morphology on the blade surface is very similar, so the difference between the blades can be ignored, and a morphological analysis is performed based on the results of a single experiment.

5.3. Contrastive Analysis of Penetration Testing. Penetration is an important means of nondestructive testing of the engine state in the wing. A flexible probe with an optical lens is sent into a borehole, and an internal image of the engine is obtained using optical imaging principles, which is then analysed and evaluated regarding the status of the engine. This provides a decision-making basis for fault diagnosis and maintenance plan formulation.

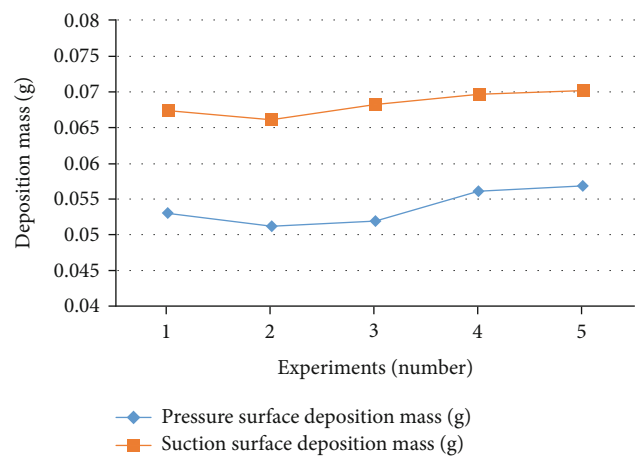

Figure 7: Comparison of the scale qualities of the blade surface areas.

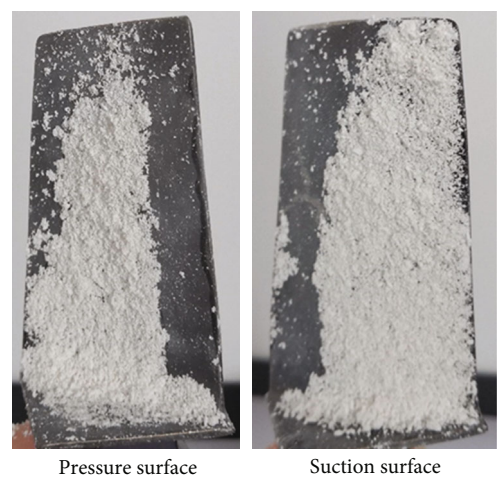

Figure 8: Observation of the surface morphology of the compressor blade surface area.

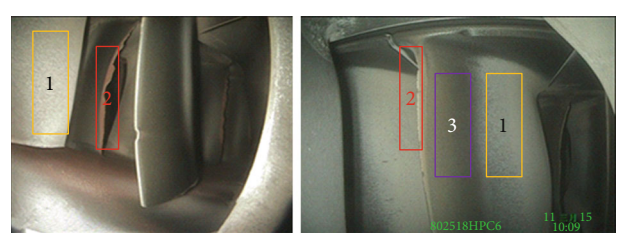

Figure 9: Dirt classifications.

Figure 9 shows the results of compressor blade borehole inspection. It can be seen from the figure that the fouling is mainly concentrated on the trailing edge of the blade and the root area of the blade. A large amount of accumulated fouling occurs on the trailing edge of the blade, and the fouling layer of the blade is relatively thin. Analysis shows that

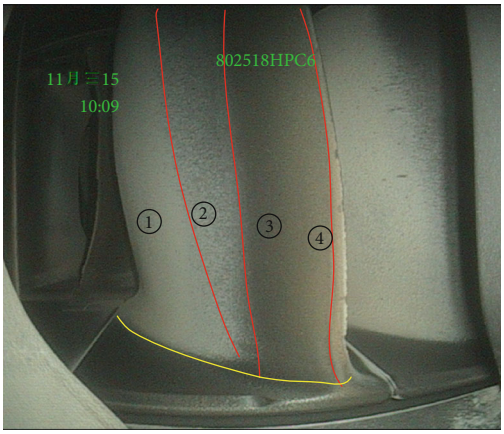

Figure 10: Pressure surface dirt zones.

the scale is divided into three types: loose type, dense type, and transitional type. As shown in Figure 9, No. 1 is the loose type, No. 2 is the dense type, and No. 3 is the transitional type.

The scaling of a single blade can be divided into four different fouling areas through analysis, as shown in Figure 10. Area 1 is the leading edge fouling layer, and the main feature of this area is that the fouling layer is thin and dense. Area 2 is the transitional scale layer in the middle of the blade, which is characterized by a sparse and discontinuous scale. Area 3 is a trailing edge scale layer, which is characterized by a firm but sparse scale. The trailing edge scale area is the 4th area, and the scale layer is thick, with massive amounts of accumulation and high hardness.

To achieve complete cleaning, the energy of the cleaning fluid must exceed the dirt binding energy. According to the dirt distribution characteristics on the surface of the blade, the dirt binding energy in the 4th zone is the highest. This area is cleaned, so in the design process of the scale cleaning process parameters, the design calculations are mainly carried out for the scale 4 area to ensure the complete removal of all the scales on the surface of the compressor blade.

6. Conclusion

In this paper, in accordance with the design requirements of the on-wing engine cleaning process parameters, the trends of surface area fouling of compressor blades were studied:

(1) Using a surface sample from the compressor blade surface, the composition of the fouling on the aero engine compressor blade surface was obtained, which included SiO_2 49.9%, FeO 14.5%, Al_2O_3 11.5%, CaO 9.4%, Na_2O 3.7%, TiO 3%, and remaining impurities 8%

(2) A theoretical analysis was carried out for the thickness of the fouling layer on the surface of a compressor blade. Based on JKR contact theory, the factors affecting the fouling thickness on a blade surface were analysed

(3) Through a simulation experiment of particulate fouling on the surface of compressor blades, it was found that the number of particulates deposited on the pressure surface was lower than the secondary deposition mass of the suction surface, and the difference between the fouling deposition on each side of the blade was 0.01454 g. Compared with the results of engine drilling, the dirt was divided into three types: loose type, dense type, and transitional type. The surface of a single blade can be divided into four different fouling areas. The parameters of the engine cleaning process can be based on the characteristics of the fourth area

Data Availability

The data used to support the findings of this study are available from the corresponding author upon request.

Conflicts of Interest

The authors declare that they have no conflicts of interest.

Acknowledgments

The authors are thankful for the teacher's guidance and modifications to make this paper more perfect. This thesis was supported by the National Natural Science Foundation of China (U1733201, 51705518).

References

[1] R. Kurz, G. Musgrove, and K. Brun, "Experimental evaluation of compressor blade fouling," in *Volume 9: Oil and Gas Applications; Supercritical CO2 Power Cycles; Wind Energy*, Seoul, South Korea, 2016.

[2] R. Kurz and K. Brun, "Fouling mechanisms in axial compressors," *Journal of Engineering for Gas Turbines and Power*, vol. 134, no. 3, article 032401, 2012.

[3] M. Osvaldo and V. Zuniga, *Intake Systems for Industrial Gas Turbines*, Cranfield University, 2002, 2003.

[4] A. P. Tarabrin, V. A. Schurovsky, A. I. Bodrov, and J. P. Stalder, "An analysis of axial compressor fouling and a blade cleaning method," *Journal of Turbomachinery*, vol. 120, no. 2, pp. 256–261, 1998.

[5] T. W. Song, J. L. Sohn, T. S. Kim, J. H. Kim, and S. T. Ro, "An analytical approach to predicting particle deposit by fouling in the axial compressor of the industrial gas turbine," *Proceedings of the Institution of Mechanical Engineers, Part A: Journal of Power and Energy*, vol. 219, no. 3, pp. 203–212, 2005.

[6] H. Yang and H. Xu, "The sensitive parameter study of axial flow compressor fouling," *Research Journal of Applied Sciences Engineering and Technology*, vol. 5, no. 10, pp. 3057–3062, 2013.

[7] K. Mathioudakis and A. Tsalavoutas, "Uncertainty reduction in gas turbine performance diagnostics by accounting for humidity effects," *Journal of Engineering for Gas Turbines and Power*, vol. 124, no. 4, pp. 801–808, 2002.

[8] J. Fielder, "Evaluation of zero compressor wash routine in RN service," in *ASME Turbo Expo 2003, collocated with the 2003*

International Joint Power Generation Conference, pp. 543–547, Atlanta, Georgia, USA, 2003.

[9] Y. Xiaojun and Z. Jiaxiong, "Numerical simulation of particle deposition process inside turbine cascade," *Acta Aeronautica et Astronautica Sinica*, vol. 38, no. 5, pp. 120–130, 2017.

[10] S. F. Chen, J. J. Wang, and Y. H. Jin, "Model of particle deposition and adhesion on blade surface of flue gas turbine (in Chinese)," *The Chinese Journal of Process Engineering*, vol. 18, no. 3, pp. 447–453, 2018.

Hindawi
International Journal of Photoenergy
Volume 2020, Article ID 8893816, 9 pages
https://doi.org/10.1155/2020/8893816

Research Article

Effects of Initial Nitrate Concentrations and Photocatalyst Dosages on Ammonium Ion in Synthetic Wastewater Treated by Photocatalytic Reduction

Orawan Rojviroon,[1] **Sanya Sirivithayapakorn**,[1] **Thammasak Rojviroon**,[2] **and Chalermraj Wantawin**[1]

[1]*Department of Environmental Engineering, Faculty of Engineering, Kasetsart University, Bangkok 10900, Thailand*
[2]*Division of Environmental Engineering, Faculty of Engineering, Rajamangala University of Technology Thanyaburi, Pathum Thani 12110, Thailand*

Correspondence should be addressed to Sanya Sirivithayapakorn; fengsys@ku.ac.th

Received 6 August 2020; Revised 16 October 2020; Accepted 24 October 2020; Published 16 November 2020

Academic Editor: Jiangwei LIU

Ammonium (NH_4^+) is an undesirable by-product of photocatalytic nitrate (NO_3^-) reduction since it is harmful to aquatic life once it converts into ammonia (NH_3). This research investigated the removal efficiency of NO_3^- and for the first time quantified the relationships of initial nitrate concentrations ($[NO_3^-]_0$) and photocatalyst dosages on the remaining ammonium (NH_4^+) in synthetic wastewater using photocatalytic reduction process with either nanoparticle titanium dioxide (TiO_2) or 1.0%Ag-TiO_2 under Ultraviolet A (UVA). The experiments were systematically carried out under various combinations of $[NO_3^-]_0$ (10, 25, 50, 80, and 100 mg-N/L) and photocatalyst dosages (0.1, 0.5, 1.0, and 2.0 g). The NO_3^- removal efficiency of both photocatalysts was 98.96-99.98%, and the catalytic selectivity products were nitrogen gas (N_2), nitrite (NO_2^-), and NH_4^+. Of the two photocatalysts under comparable experimental conditions, 1.0%Ag-TiO_2 provided better NO_3^- removal efficiency. For both photocatalysts, the remaining NH_4^+ was predominantly determined by $[NO_3^-]_0$; higher $[NO_3^-]_0$ led to higher NH_4^+. Multiple linear regression analysis confirmed the dominant role of $[NO_3^-]_0$ in the remaining NH_4^+. The photocatalyst dosage could play an essential role in limiting NH_4^+ in the treated wastewater, with large variation in $[NO_3^-]_0$ from different sources.

1. Introduction

Photocatalytic reduction is an effective technology for removal of nitrate (NO_3^-) in wastewater. The major disadvantage of this process is the ammonium (NH_4^+), an undesirable by-product, remaining at the end. Many researchers studied NO_3^- removal efficiency and the NO_3^- conversion selectivity [1–3]. There are also studies on the influencing factors on the remaining NH_4^+, which investigated the relationships between remaining NH_4^+ and those influencing factors in the process.

Previous studies demonstrated that high efficiency nitrate removal by photocatalytic reduction with low remaining $[NH_4^+]$ could be achieved by silver- (Ag-) doped TiO_2 nanoparticles under high-performance light sources (i.e., high-pressure Hg lamps and xenon lamps) [4–6]. However, those light sources have disadvantages that include high energy consumption, potential human health hazard, and generating high heat [7, 8]. For those reasons, the UVA light bulb is chosen for this process because it overcomes those disadvantages and is powerful enough for this process [9–11].

The influencing factors of the photocatalytic selectivity of NO_3^- conversion include initial nitrate concentration ($[NO_3^-]_0$), light source intensity, type of photocatalyst, type of dopant, and quantity of photocatalyst dosage [4, 12, 13]. Evidence shows that manipulating the photocatalytic selectivity of photocatalytic reduction helps limit environmentally harmful compounds, particularly NH_4^+ [14, 15]. NH_4^+ is

harmful to aquatic life once in the natural waterways where it converts into ammonia (NH_3). According to the United States Environmental Protection Agency (US EPA), the upper safety limit of total ammonia nitrogen (NH_3-N) is 17 mg-N/L (1-hour average) and 1.9 mg-N/L (30-day rolling average) at pH 7.0 and 20°C for acute and chronic criteria, respectively [16]. The reported total ammonia concentrations in treated wastewater from photocatalytic reduction vary between 0.07 and 57.8 mg-N/L [4, 17–22].

Doping of silver (Ag^+) on photocatalysts, especially TiO_2, to improve the photocatalytic performance was a common practice. Previous studies applied 0.1%-7.0% Ag^+ loading on TiO_2 photocatalysts and found that 1% Ag^+ was the most optimum dose to enhance the photocatalytic NO_3^- reduction activity [23–25].

This research investigated the effects of initial nitrate concentrations ($[NO_3^-]_0$) and photocatalyst dosages on NO_3^- removal efficiency in synthetic wastewater using photocatalytic reduction. The experiments were carried out under various $[NO_3^-]_0$ (10, 25, 50, 80, and 100 mg-N/L) and photocatalyst dosages (0.1, 0.5, 1.0, and 2.0 g) under UVA irradiation as light source for photocatalytic nitrate reduction. The experimental photocatalysts were TiO_2 and 1.0%Ag-TiO_2 nanoparticle as photocatalysts [21]. The catalytic selectivity of NO_3^- conversion was also determined, and the actual concentrations of NH_4^+ under different experimental NO_3^- removal conditions were compared. Multiple linear regression was performed to characterize the relationship between the remaining NH_4^+ and $[NO_3^-]_0$ and photocatalyst dosages. Essentially, the novelty of this research lies in the use of TiO_2 nanopowder as photocatalyst, as opposed to commercial-grade TiO_2. By comparison, TiO_2 nanopowder possesses larger surface area for adsorption and reaction. Another research novelty is the systematical use of various $[NO_3^-]_0$ and photocatalyst dosages, unlike previous researches which experimented with specific $[NO_3^-]_0$ and photocatalyst dosages.

2. Materials and Methodology

2.1. Ag-TiO_2 Photocatalyst Preparation and Characteristics. In this research, 1.0%Ag-TiO_2 photocatalyst was prepared by composite colloid deposition under alkaline condition, following Doudrick et al. [4, 9] with minor modifications. In the experiment, 12 g of TiO_2 nanopowder was dispersed in 500 mL deionized water and purged with nitrogen gas (N_2) for 30 min to remove O_2. After degassing, 8 mL of methanol was added and stirred prior to adding NaOH to adjust pH of the mixture to 12-13. Afterward, 1.0%$AgNO_3$ (w/v; Fluka) was added and stirred in the dark for 30 min before irradiation with UVA (800 μW/cm^2) for 1 h at room temperature.

The mixture was then centrifuged at 200 rpm for 2 min to settle the powder, and the supernatant was discarded. Deionized water was added to wash the powder. It was then stirred and centrifuged. The process was repeated until the mixture pH was 7. The washed powder was oven dried at 103°C for 24 h and calcined at 450°C for 1 h for Ag-TiO_2 photocatalyst in the form of dried light purple powder.

The experimental TiO_2 nanopowder was of 15 nm in particle size and 99.5% anatase crystalline phase (US Research Nanomaterials, Inc., USA). The composition and specific surface area of dose photocatalysts were characterized by transmission electron microscopy (TEM, JEM-1400 TEM instrument) and X-ray fluorescence spectrometer (XRF; Bruker model S8 Tiger), Brunauer, Emmett and Teller (BET) analyzer (BELSORP-max Bel Japan Inc.).

2.2. Photocatalytic Reduction for NO_3^- Removal. The photocatalytic reduction to remove nitrate (NO_3^-) was carried out using TiO_2 and Ag-TiO_2 photocatalysts in 125 mL cylindrical borosilicate glass photoreactor. Figure 1 illustrates the schematic of experimental photocatalytic reduction for NO_3^- removal. Synthetic NO_3^- wastewater of variable initial nitrate concentrations was prepared by dissolving potassium nitrate (KNO_3 > 99%, Fluka) in deionized water. The initial nitrate concentration ($[NO_3^-]_0$) varied between 10, 25, 50, 80, and 100 mg-N/L.

The photoreactor was filled with 100 mL synthetic wastewater of varying $[NO_3^-]_0$ and 58 mM of formic acid (FA) as hole scavenger, with the mixture pH ranging from 2.28 to 2.42. TiO_2 and Ag-TiO_2 photocatalysts of varying dosages were independently added into the photoreactor. The photocatalyst dosage was varied from 0.1, 0.5, 1.0, and 2.0 g. The photoreactor condition was anaerobic by purging with N_2 for 30 min to remove dissolved oxygen (DO) in the synthetic wastewater.

Prior to UVA irradiation, samples were drawn for initial measurement of pH, DO, $[NH_4^+]$, $[NO_2^-]$, and $[NO_3^-]$. The samples were subsequently irradiated with two UVA light bulbs (300 W, Osram) for 6 h. The UVA light bulbs were located on either side of the photoreactor vessel at a distance of 20 cm. The UVA intensity in the photoreactor vessel was 800 μW/cm^2 on average. The concentrations of NO_3^- and by-products ($[NO_2^-]$ and $[NH_4^+]$) relative to reaction time were periodically measured throughout the experiment, while pH and DO were measured at the beginning and at termination (at 360 min). The concentrations of NO_3^-, NO_2^-, and NH_4^+ in the synthesis wastewater were determined using ion chromatography instrument with chemical suppression (Metrohm 882 Compact IC Plus). Nitrogen gas (N_2) was calculated by the mass balance of nitrogen of the photocatalytic reduction process.

To verify the experiment, photocatalytic reduction was also carried out under three control conditions: (1) in the absence of photocatalyst but with UVA irradiation; (2) with Ag-TiO_2 photocatalyst of varying dosages but without UVA irradiation; and (3) with TiO_2 photocatalysts of varying dosages but without UVA irradiation. The measured $[NO_3^-]$, $[NO_2^-]$, and $[NH_4^+]$ of photocatalytic reduction using Ag-TiO_2 and TiO_2 photocatalysts irradiated with UVA were subsequently compared against the controls.

2.3. Selectivity of Photocatalytic Reduction for NO_3^- Removal. The NO_3^- removal efficiency of photocatalytic reduction (η) and the catalytic selectivity (S) of NO_3^- into NH_4^+, NO_2^-, and N_2 (denoted by $S_{NH_4^+}$, $S_{NO_2^-}$, and S_{N_2}) [21, 26] are

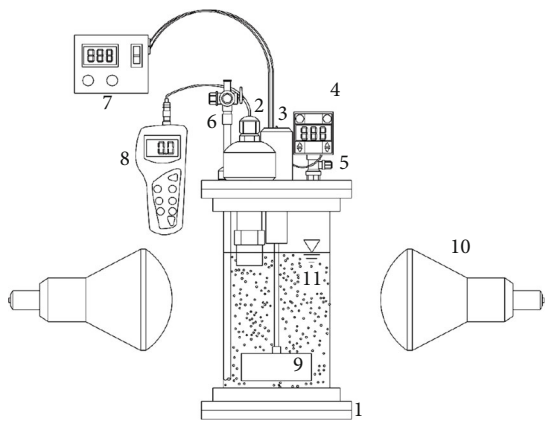

Figure 1: Schematic of photoreactor for nitrate removal.

mathematically expressed in the following equations.

$$\eta = \frac{[NO_3^-]_0 - [NO_3^-]_t}{[NO_3^-]_0} \times 100, \quad (1)$$

$$\%S_{NO_2^-} = \frac{[NO_2^-]_t}{[NO_3^-]_0 - [NO_3^-]_t} \times 100, \quad (2)$$

$$\%S_{NH_4^+} = \frac{[NH_4^+]_t}{[NO_3^-]_0 - [NO_3^-]_t} \times 100, \quad (3)$$

$$\%S_{N_2} = \frac{[NO_3^-]_0 - [NO_3^-]_t - [NO_2^-]_t - [NH_4^+]_t}{[NO_3^-]_0 - [NO_3^-]_t} \times 100, \quad (4)$$

where $[X]_0$ is the initial concentration of X and $[X]_t$ is the concentration of X at time t.

3. Results and Discussion

3.1. Ag-TiO_2 Nanopowder Photocatalyst Characteristics. The results of transmission electron microscopy were used to examine the particle size and morphology of Ag nanoparticles on TiO_2 as well as the lattice information of both photocatalysts investigated by XRF. In comparison, the TEM image of nano-TiO_2 and nano-Ag-TiO_2 photocatalysts (Figure 2) showed a similar particle size and morphology with average particle size (in diameter) of approximately 15 nm (as the result of the average TiO_2 particle size before Ag doping). The results of the TEM analysis were not clearly distinguishable in terms of particle size and morphology although it was reported that Ag doping would slightly decrease the particle size of the larger TiO_2 powders [27].

The XRF patterns of TiO_2 and 1.0%Ag-TiO_2 nanopowder photocatalysts showed strong peaks of Ti, as shown in Figure 3. The XRF pattern of 1.0%Ag-TiO_2 photocatalyst indicated that Ag^+ dopant was effectively doped onto TiO_2 which is the same with the theoretical adding. The Ag dopant in Ag-TiO_2 phase was 0.99% for theoretical doping of 1.0% (Table 1). It was confirmed that Ag was effectively deposited on the surface of TiO_2 nanopowder. Specifically, Ag^+ ions were adsorbed onto the crystal structure of TiO_2 and subsequently formed Ag-TiO_2 [28, 29].

The BET specific surface areas of TiO_2 and 1.0%Ag-TiO_2 nanopowder photocatalysts were 1.164×10^2 and 1.124×10^2 m^2/g, and the corresponding pore volumes were 4.727×10^{-7} and 3.951×10^{-7} m^3/g. It was found that the specific surface area and pore volume of Ag-TiO_2 were decreased after doping. The findings were consistent with previous studies which doped TiO_2 nanopowder photocatalysts with varying dopants [4, 30, 31].

The slightly decreased BET surface areas and pore volume were due to the interference of Ag dopant on the formation of anatase crystallization [32, 33], and a marked influence on the microstructures was exhibited by calcination temperature [34]. However, the advantage of metal doping on semiconductor particles, Ag-TiO_2, was the prevention of recombination between electron and hole by trapping the electron on the metal surface resulting in increasing the lifetime of electron in conduction band, thus enhancing the efficiency of photocatalytic nitrate reduction [34].

3.2. NO_3^- Removal Using Photocatalytic Reduction. The NO_3^- removal efficiency (η) of photocatalytic reduction using TiO_2 and 1.0%Ag-TiO_2 photocatalysts under variable initial NO_3^- concentrations ($[NO_3^-]_0$; 10, 25, 50, 80, and 100 mg-N/L) and TiO_2 and 1.0%Ag-TiO_2 dosages (0.1, 0.5, 1.0, and 2.0 g) was determined by equation (1).

Table 2 tabulates the NO_3^- removal efficiency, nitrate concentration at termination ($[NO_3^-]_t$), ammonium ion selectivity ($\%S_{NH_4^+}$), and actual ammonium ion concentration ($[NH_4^+]_a$) of photocatalytic reduction under various $[NO_3^-]_0$ using TiO_2 and 1.0%Ag-TiO_2 photocatalysts. The NO_3^- removal efficiency of TiO_2 and 1.0%Ag-TiO_2 photocatalysts was 98.96-99.98%. The NO_3^- removal efficiency increased with the increase in photocatalyst dosage as the surface area for adsorption and reaction increased.

The ammonium ion selectivity ($S_{NH_4^+}$) and actual ammonium ion concentration ($[NH_4^+]_a$) increased with the increase in photocatalyst dosage for both TiO_2 and 1.0% Ag-TiO_2 photocatalysts. In addition, the initial nitrate concentration and $[NH_4^+]_a$ were positively correlated. In other words, low $[NO_3^-]_0$ resulted in low $[NH_4^+]_a$ and vice versa. Moreover,

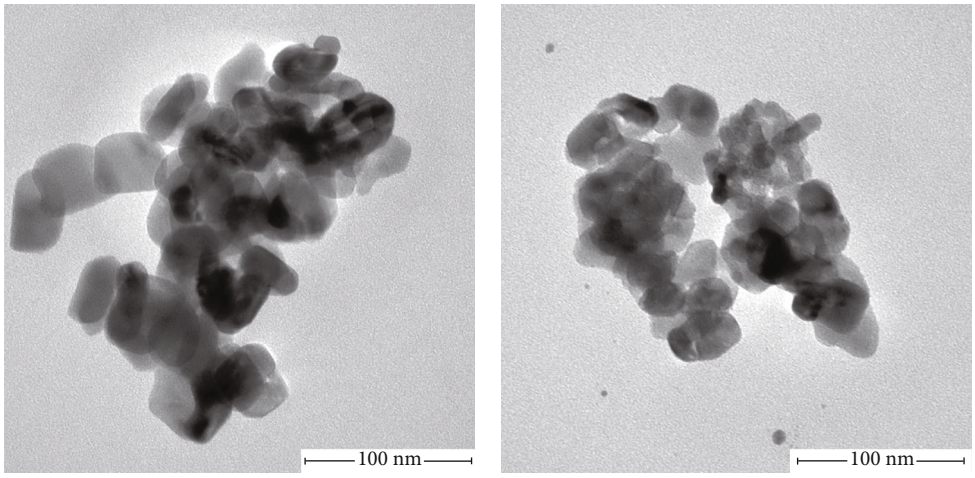

(a) TiO_2 (b) Ag-TiO_2

Figure 2: TEM image of (a) TiO_2 photocatalyst and (b) 1.0%Ag-TiO_2 photocatalyst.

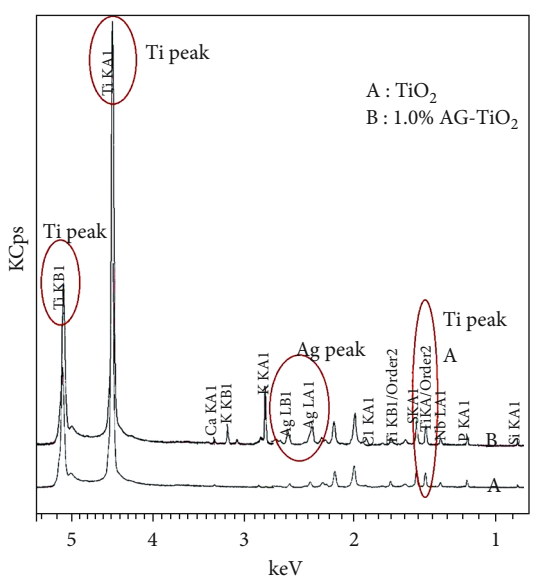

Figure 3: The XRF patterns of TiO_2 and 1.0%Ag-TiO_2 nanopowder photocatalysts.

$[NH_4^+]_a$ of 1.0% Ag-TiO_2 photocatalyst was higher than that of TiO_2 photocatalyst under all experimental conditions.

The NO_3^- reduction in photocatalytic process was a stepwise mechanism. When the photoinduced electrons (e^-) in valence band were excited onto conduction band, holes (h^+) appeared at valence band. This process was called electron-hole pairs photogeneration [32] (equation (5)). The photogenerated holes consumed $HCOO^-$, and $CO_2^{\cdot-}$ was generated [35] (equation (6)). The $CO_2^{\cdot-}$ is a strong reducing agent to reduce NO_3^- to either NH_4^+ or N_2 (equations (7)–(12)), in which nitrite (NO_2^-) was an intermediate product. The results of NO_2^-, NH_4^+, and N_2 in percent named the selectivity of NO_3^- reduction.

$$TiO_2 + h\nu \rightarrow e^- + h^+ \quad (5)$$

$$HCOO^- + h^+ \rightarrow H^+ + CO_2^{\cdot-} \quad (6)$$

$$NO_3^- + 2H^+ + 2e^- \rightarrow NO_2^- + H_2O \quad (7)$$

$$2NO_3^- + 12H^+ + 10CO_2^{\cdot-} \rightarrow N_2 + 6H_2O + 10CO_2 \quad (8)$$

$$NO_3^- + 10H^+ + 8CO_2^{\cdot-} \rightarrow NH_4^+ + 3H_2O + 8CO_2 \quad (9)$$

$$NO_2^- + 8H^+ + 6CO_2^{\cdot-} \rightarrow NH_4^+ + 2H_2O + 6CO_2 \quad (10)$$

$$2NO_3^- + 12H^+ + 10e^- \rightarrow N_2 + 6CO_2 \quad (11)$$

$$NO_3^- + 10H_2O + 8e^- \rightarrow NH_4^+ + 3H_2O \quad (12)$$

In the nitrate reduction experiments, 58 mmol of formic acid (FA) was used as a hole scavenger to improve the photocatalytic reduction reaction, while the pH of the solution increased from 2.28-2.42 to 2.41-5.5 due to the consumption of formic acid in the reaction and the generation of $[NH_4^+]$. In addition, the highly efficient conversion of NO_2^- to N_2 was also related to the initial acidity of the solution [36]. This was probably due to the specific absorption properties of NO_3^- and NO_2^- in varying pH solutions. Considering that the point of zero charge of the TiO_2 was 6.25 [37], in acidic solution, TiO_2 surface accumulated a net positive charge due to the increasing fraction of $TiOH_2^+$ sites on the surface and NO_2^- could be quickly adsorbed.

Figure 4 compares the nitrate concentrations of photocatalytic reduction under various $[NO_3^-]_0$ and photocatalytic dosages (TiO_2 and 1.0%Ag-TiO_2) from the start to end. In Figure 4, the NO_3^- removal was positively correlated with photocatalyst dosage due to the surface area effect, independent of photocatalyst type. Although at termination there were not much differences in final NO_3^- removal efficiencies, the NO_3^- removal rates of 1.0%Ag-TiO_2 photocatalyst were faster than those of TiO_2 photocatalyst for the comparable conditions. The faster removal rate of photocatalytic reduction activity was attributable to Ag^+ doping [33, 38]. The loading of TiO_2 with Ag^+ reduced the difference between

Table 1: Composition of TiO_2 and 1.0%Ag-TiO_2 photocatalysts.

Photocatalyst	Composition (%)						BET surface area (m^2/g)	Pore volume (m^3/g)
	TiO_2	Ag	SiO_2	P_2O_5	Nb_2O_5	Other		
TiO_2	96.8	—	0.44	0.15	0.11	2.50	1.164×10^2	4.727×10^{-7}
1.0%Ag-TiO_2	96.1	0.99	0.40	0.17	0.11	2.23	1.124×10^2	3.951×10^{-7}

Table 2: NO_3^- removal efficiency, $[NO_3^-]_t$, $\%S_{NH_4^+}$, and $[NH_4^+]_a$ of photocatalytic reduction using TiO_2 and 1.0%Ag-TiO_2 photocatalysts at termination.

Photocatalyst	$[NO_3^-]_0$ (mg-N/L)	Dosage (g)	NO_3^- removal (%)	$\%S_{NH_4^+}$	$[NH_4^+]_a$ (mg-N/L)	pH_t
TiO_2	10	0.1-2.0	98.96-99.48	25.81-34.00	2.55-3.38	2.41-2.84
	25	0.1-2.0	99.35-99.92	20.53-36.5	5.10-9.12	2.54-3.11
	50	0.1-2.0	99.84-99.92	9.53-26.40	4.76-13.18	2.80-3.61
	80	0.1-2.0	99.85-99.98	16.35-25.55	13.06-20.43	2.9-3.28
	100	0.1-2.0	99.90-99.95	17.13-22.56	17.12-22.55	2.93-3.3
1.0%Ag-TiO_2	10	0.1-2.0	99.60-99.62	19.71-64.09	1.96-6.38	2.50-2.51
	25	0.1-2.0	99.30-99.84	17.59-44.81	4.39-11.19	2.52-2.64
	50	0.1-2.0	99.78-99.90	14.97-45.98	7.47-22.97	2.72-3.03
	80	0.1-2.0	99.85-99.94	19.20-38.15	15.33-30.50	3.00-4.02
	100	0.1-2.0	99.82-99.96	16.12-38.10	16.09-38.10	3.06-5.50

Note: $\%S_{NH_4^+}$ is NH_4^+ selectivity (%), $[NH_4^+]_a$ is actual $[NH_4^+]$, and pH_t is pH at the end.

energy levels of the valence and conduction bands, resulting in the extension of light absorption wavelength into the visible light region. Ag^+ also acted as a trap site for excited electrons, giving rise to electron-hole separation. In addition, Ag^+ doping enhanced charge transport, prolonged the lifetime of electron-hole pairs, and reduced the charge recombination [39–42]. As a result, Ag^+ could be adopted for photocatalytic reduction process to improve NO_3^- removal.

Figure 5 illustrates the catalytic selectivity (%) of photocatalytic reduction using TiO_2 and 1.0%Ag-TiO_2 photocatalysts in which NO_3^- was transformed into NO_2^-, NH_4^+, and N_2. The results showed that overall N_2 accounted for the largest proportions of NO_3^- by-products, followed by NH_4^+ and NO_2^-.

In Figure 5, the photocatalyst types (TiO_2 and 1.0%Ag-TiO_2) and dosage played a role in the selectivity of the photocatalytic reduction scheme. This showed that the Ag dopant enhanced the photocatalytic reduction activity, and both the activity and $[NH_4^+]$ increased with 1.0%Ag-TiO_2 dosage increase. However, 1.0%Ag-TiO_2 photocatalyst dosage beyond 0.1 g (i.e., 0.5, 1.0, and 2.0 g) contributed to $[NH_4^+]$ in the treated wastewater exceeding that of TiO_2 photocatalyst (Table 2). NH_4^+ is harmful to aquatic life once in the natural waterways where it converts into NH_3.

The initial nitrate concentrations also played a role in $[NH_4^+]$ in the treated wastewater, independent of photocatalyst type (TiO_2 and 1.0%Ag-TiO_2). Specifically, higher $[NO_3^-]_0$ resulted in higher $[NH_4^+]$. Given 0.1 g of either TiO_2 or 1.0%Ag-TiO_2 photocatalyst, $[NH_4^+]$ was 1.96-16.09 mg-N/L, independent of $[NO_3^-]_0$. Assuming complete NH_4^+-to-NH_3 conversion, these were equivalent to 1.96-16.09 mg-N/L total ammonia nitrogen (NH_3-N), which is below 17 mg-N/L NH_3-N of the US EPA [16]. Meanwhile, the nitrate concentrations of the three control conditions (i.e., the controls) remained unchanged at the end of the experiment.

In Figure 5, the catalytic selectivity of NO_3^- into NO_2^- could also be observed. The remaining nitrite concentrations ($[NO_2^-]$) were negligible as NO_2^- was converted into NH_4^+ and N_2 during the photocatalytic reduction process [43].

To comparatively investigate the effect of initial nitrate concentration and photocatalyst dosage on the concentration of ammonium ion, the relationships between $[NH_4^+]$ and $[NO_3^-]_0$ and photocatalyst dosage (TiO_2 and 1.0%Ag-TiO_2) were established by using statistical multiple linear regression. $[NH_4^+]$, $[NO_3^-]_0$, and photocatalyst dosage are denoted by Y, X_1, and X_2, respectively. The multiple linear regression was expressed in equation (13), and Table 3 tabulates the regression results.

$$Y = b + \beta_1 X_1 + \beta_2 X_2 + \cdots + \varepsilon, \tag{13}$$

where b is the linear regression constant, β is the linear regression coefficient, and ε is the error constant.

In Table 3, β of the initial nitrate concentration ($[NO_3^-]_0$) was, respectively, 0.925 and 0.838 for TiO_2 and 1.0%Ag-TiO_2 photocatalysts ($p < 0.001$), indicating that $[NO_3^-]_0$ played the dominant role in NO_3^- removal efficiency and the remaining NH_4^+. Meanwhile, β of photocatalyst dosage was 0.407 and 0.288 for 1.0%Ag-TiO_2 and TiO_2 photocatalysts, suggesting that the photocatalyst dosage had considerably less effect on the remaining NH_4^+.

In reality, $[NO_3^-]_0$ varies from area to area. Given diverse $[NO_3^-]_0$, it is operationally practical to vary the

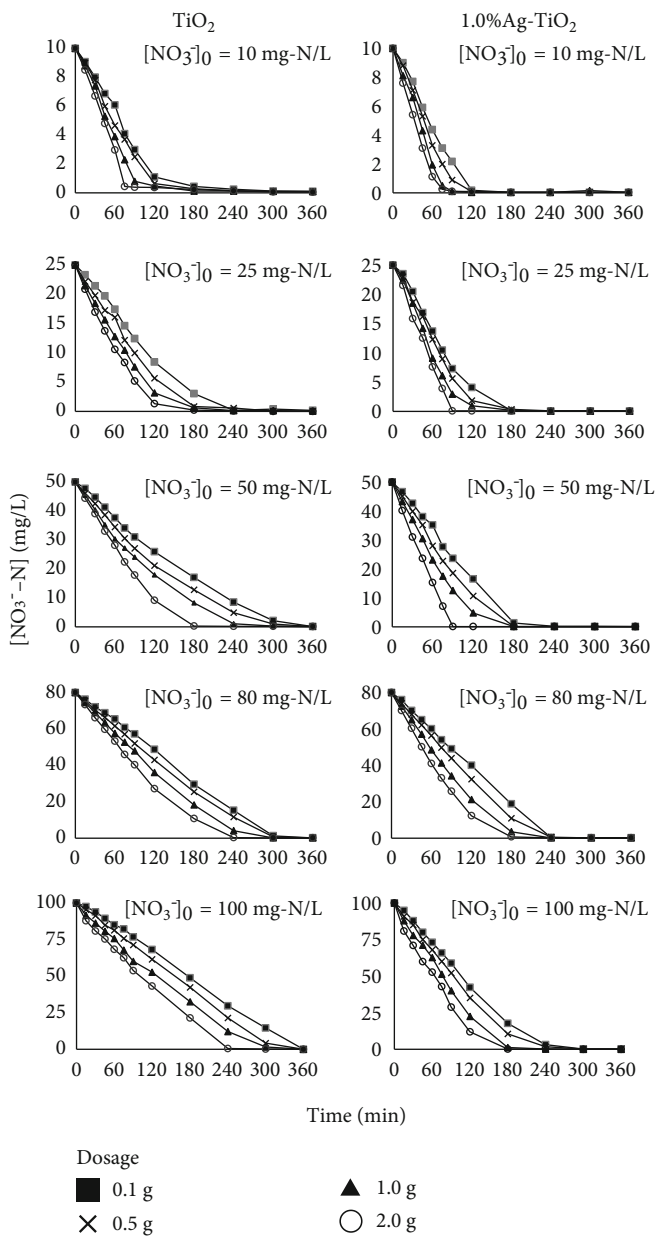

Figure 4: The concentrations of NO_3^- of the photocatalytic reduction scheme under various $[NO_3^-]_0$ and TiO_2 and 1.0%Ag-TiO_2 dosages.

photocatalyst dosage in the photocatalytic reduction scheme. Based on the experimental results, 0.1 g of Ag-TiO_2 photocatalyst is advisable due to efficient removal of NO_3^- (Figure 3).

To facilitate estimation of the remaining $[NH_4^+]$ in treated wastewater using photocatalytic reduction, the multiregression prediction equations of the theoretical remaining ammonium ion ($[NH_4^+]_T$), as a function of $[NO_3^-]_0$ and photocatalyst dosage, are expressed in equations (14) and (15), respectively.

The prediction equation for TiO_2 photocatalyst is

$$[NH_4^+]_T = -1.489 + 0.185[NO_3^-]_0 + 2.698\text{dosage}. \quad (14)$$

The prediction equation for 1.0%Ag-TiO_2 photocatalyst is

$$[NH_4^+]_T = -3.744 + 0.274[NO_3^-]_0 + 6.064\text{dosage}. \quad (15)$$

The relationships between $[NH_4^+]_T$, $[NO_3^-]$, and photocatalyst dosage, as shown in equations (7) and (8), could be further applied to estimate the remaining $[NH_4^+]$ under various $[NO_3^-]_0$ and photocatalyst dosages.

4. Conclusion

This research investigated the NO_3^- removal efficiency of photocatalytic reduction process under various $[NO_3^-]_0$ (10,

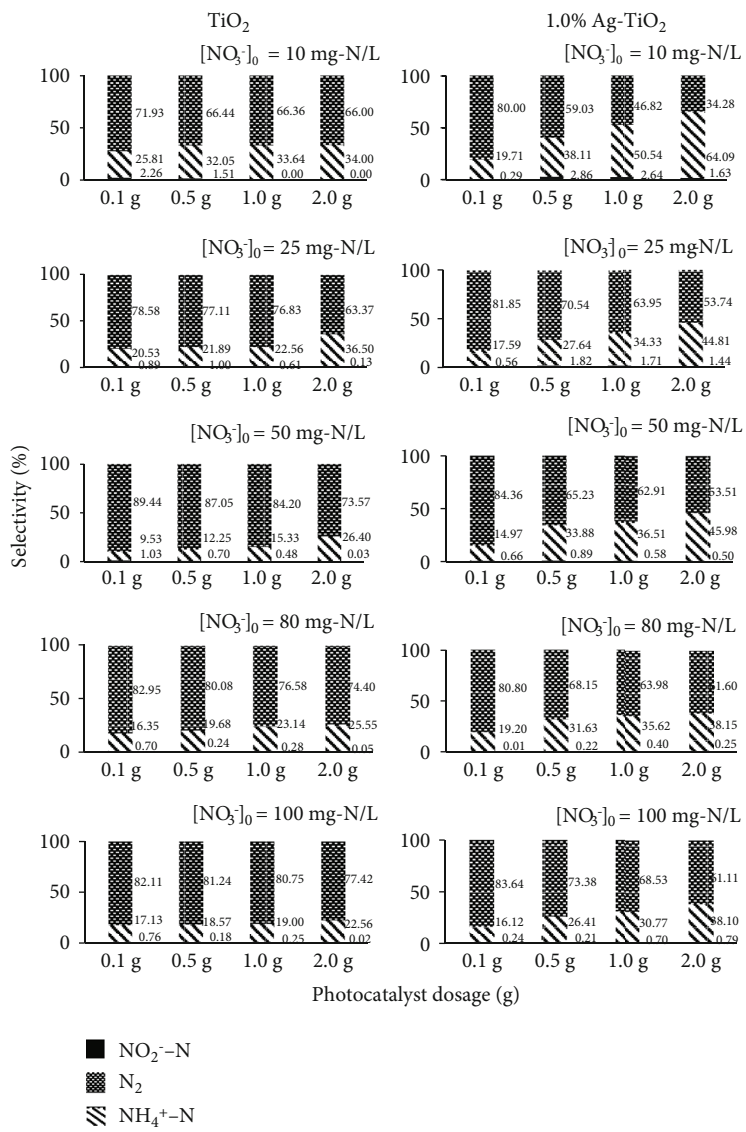

Figure 5: The catalytic selectivity of the photocatalytic reduction scheme under various $[NO_3^-]_0$ and TiO_2 and 1.0%Ag-TiO_2 dosages.

Table 3: Results of multiple linear regression analysis.

Photocatalyst	Independent variables	b	β	t value	p value
TiO_2	$[NO_3^-]_0$	6.879	0.925	15.395	0.000
	Dosage	0.184	0.288	4.787	0.000
	Constant	-1.489		-1.643	0.119
$R = 0.969$, $R^2 = 0.939$, $F = 129.955$, and p value < 0.001.					
1.0%Ag-TiO_2	$[NO_3^-]_0$	0.274	0.838	11.96	0.000
	Dosage	6.064	0.407	5.63	0.000
	Constant	-3.744		-2.16	0.045
$R = 0.955$, $R^2 = 0.911$, $F = 87.30$, and p value < 0.001.					

25, 50, 80, and 100 mg-N/L) and photocatalyst dosages (0.1, 0.5, 1.0, and 2.0 g) using nanoparticle TiO_2 and 1.0%Ag-TiO_2 photocatalysts under UVA. The NO_3^- removal efficiency of both photocatalysts under experimental $[NO_3^-]_0$ and photocatalyst dosages was between 98.96 and 99.98%. The catalytic selectivity products were NH_4^+, NO_2^-, and N_2, with N_2 accounting for a significant proportion of the selectivity. The doping of TiO_2 with Ag^+ improved the removal efficiency of NO_3^-. It was found that $[NO_3^-]_0$ played a more important role in the remaining NH_4^+ than the photocatalyst dosage. Specifically, higher $[NO_3^-]_0$ led to higher $[NH_4^+]$ in the treated wastewater. Multiple linear regression analysis confirmed the dominant role of $[NO_3^-]_0$ in the remaining NH_4^+.

Data Availability

The analysis data used to support the findings of this study are included within the supplementary information file(s).

Conflicts of Interest

The author(s) declare(s) that they have no conflicts of interest.

Acknowledgments

The authors would like to express sincere gratitude to the Faculty of Engineering, Kasetsart University, Thailand, for the technical support.

References

[1] N. Tong, Y. Wang, Y. Liu et al., "PdSn/NiO/NaTaO3:La for photocatalytic ammonia synthesis by reduction of NO3− with formic acid in aqueous solution," *Journal of Catalysis*, vol. 361, pp. 303–312, 2018.

[2] Y. A. Shaban, A. A. El Maradny, and R. K. Al Farawati, "Photocatalytic reduction of nitrate in seawater using C/TiO_2 nanoparticles," *Journal of Photochemistry and Photobiology A: Chemistry*, vol. 328, pp. 114–121, 2016.

[3] D. Sun, W. Yang, L. Zhou, W. Sun, Q. Li, and J. K. Shang, "The selective deposition of silver nanoparticles onto {1 0 1} facets of $_{TiO\ 2}$ nanocrystals with co-exposed {0 0 1}/{1 0 1} facets, and their enhanced photocatalytic reduction of aqueous nitrate under simulated solar illumination," *Applied Catalysis B: Environmental*, vol. 182, pp. 85–93, 2016.

[4] K. Doudrick, T. Yang, K. Hristovski, and P. Westerhoff, "Photocatalytic nitrate reduction in water: managing the hole scavenger and reaction by-product selectivity," *Applied Catalysis B: Environmental*, vol. 136-137, pp. 40–47, 2013.

[5] R. Lucchetti, L. Onotri, L. Clarizia et al., "Removal of nitrate and simultaneous hydrogen generation through photocatalytic reforming of glycerol over "in situ" prepared zero-valent nano copper/P25," *Applied Catalysis B: Environmental*, vol. 202, pp. 539–549, 2017.

[6] E. Bahadori, A. Tripodi, G. Ramis, and I. Rossetti, "Semi-batch photocatalytic reduction of nitrates: role of process conditions and co-catalysts," *ChemCatChem*, vol. 11, no. 18, pp. 4642–4652, 2019.

[7] Z. W. Lipsky and G. K. German, "Ultraviolet light degrades the mechanical and structural properties of human stratum corneum," *Journal of the Mechanical Behavior of Biomedical Materials*, vol. 100, article 103391, 2019.

[8] T. F. Anderson, "Artificial light sources," *Dermatologic Clinics*, vol. 4, no. 2, pp. 203–215, 1986.

[9] T. Rojviroon and S. Sirivithayapakorn, "E. coliBacteriostatic action using TiO2Photocatalytic reactions," *International Journal of Photoenergy*, vol. 2018, 12 pages, 2018.

[10] T. Rojviroon, O. Rojviroon, and S. Sirivithayapakorn, "Photocatalytic decolourisation of dyes using TiO2thin film photocatalysts," *Surface Engineering*, vol. 32, no. 8, pp. 562–569, 2016.

[11] M. Long, J. Wang, H. Zhuang, Y. Zhang, H. Wu, and J. Zhang, "Performance and mechanism of standard nano-TiO_2 (P-25) in photocatalytic disinfection of foodborne microorganisms – Salmonella typhimurium and Listeria monocytogenes," *Food Control*, vol. 39, pp. 68–74, 2014.

[12] J. Yuan, E. Wang, Y. Chen, W. Yang, J. Yao, and Y. Cao, "Doping mode, band structure and photocatalytic mechanism of B–N-codoped TiO_2," *Applied Surface Science*, vol. 257, no. 16, pp. 7335–7342, 2011.

[13] K. Nakata and A. Fujishima, "TiO_2 photocatalysis: design and applications," *Journal of Photochemistry and Photobiology C: Photochemistry Reviews*, vol. 13, no. 3, pp. 169–189, 2012.

[14] F. Zhang, R. Jin, J. Chen et al., "High photocatalytic activity and selectivity for nitrogen in nitrate reduction on $_{Ag/TiO}$ catalyst with fine silver clusters," *Journal of Catalysis*, vol. 232, no. 2, pp. 424–431, 2005.

[15] H. O. N. Tugaoen, S. Garcia-Segura, K. Hristovski, and P. Westerhoff, "Challenges in photocatalytic reduction of nitrate as a water treatment technology," *Science of The Total Environment*, vol. 599-600, pp. 1524–1551, 2017.

[16] EPA, *Final aquatic life ambient water quality criteria for ammonia-freshwater*, 2013, https://www.federalregister.gov/documents/2013/08/22/2013-20307/final-aquatic-life-ambient-water-quality-criteria-for-ammonia-freshwater-2013.

[17] L. Li, Z. Xu, F. Liu et al., "Photocatalytic nitrate reduction over Pt–Cu/TiO_2 catalysts with benzene as hole scavenger," *Journal of Photochemistry and Photobiology A: Chemistry*, vol. 212, no. 2-3, pp. 113–121, 2010.

[18] J. Sá, C. A. Agüera, S. Gross, and J. A. Anderson, "Photocatalytic nitrate reduction over metal modified TiO_2," *Applied Catalysis B: Environmental*, vol. 85, no. 3-4, pp. 192–200, 2009.

[19] T. Yang, K. Doudrick, and P. Westerhoff, "Photocatalytic reduction of nitrate using titanium dioxide for regeneration of ion exchange brine," *Water Research*, vol. 47, no. 3, pp. 1299–1307, 2013.

[20] K. Kobwittaya and S. Sirivithayapakorn, "Photocatalytic reduction of nitrate over TiO_2 and Ag-modified TiO_2," *Journal of Saudi Chemical Society*, vol. 18, no. 4, pp. 291–298, 2014.

[21] J. M. A. Freire, M. A. F. Matos, D. S. Abreu et al., "Nitrate photocatalytic reduction on TiO_2: metal loaded, synthesis and anions effect,," *Journal of Environmental Chemical Engineering*, vol. 8, no. 4, article 103844, 2020.

[22] S. Cao, R. Du, Y. Peng, B. Li, and S. Wang, "Novel two stage partial denitrification (PD)-Anammox process for tertiary nitrogen removal from low carbon/nitrogen (C/N) municipal sewage," *Chemical Engineering Journal*, vol. 362, pp. 107–115, 2019.

[23] L. M. Santos, W. A. Machado, M. D. França et al., "Structural characterization of Ag-doped TiO_2 with enhanced photocatalytic activity," *RSC Advances*, vol. 5, no. 125, pp. 103752–103759, 2015.

[24] S. Krejčíková, L. Matějová, K. Kočí et al., "Preparation and characterization of Ag-doped crystalline titania for photocatalysis applications," *Applied Catalysis B: Environmental*, vol. 111-112, pp. 119–125, 2012.

[25] K. Gupta, R. P. Singh, A. Pandey, and A. Pandey, "Photocatalytic antibacterial performance of TiO_2 and Ag-doped TiO_2 against S. aureus. P. aeruginosa and E. coli," *Beilstein Journal of Nanotechnology*, vol. 4, pp. 345–351, 2013.

[26] N. Krasae and K. Wantala, "Enhanced nitrogen selectivity for nitrate reduction on Cu–nZVI by TiO_2 photocatalysts under UV irradiation," *Applied Surface Science*, vol. 380, pp. 309–317, 2016.

[27] M. Ahamed, M. A. M. Khan, M. J. Akhtar, H. A. Alhadlaq, and A. Alshamsan, "Ag-doping regulates the cytotoxicity of TiO_2 nanoparticles via oxidative stress in human cancer cells," *Scientific Reports*, vol. 7, no. 1, p. 17662, 2017.

[28] Y. Luo, S. Yu, B. Li et al., "Synthesis of (Ag,F)-modified anatase TiO2nanosheets and their enhanced photocatalytic activity," *New Journal of Chemistry*, vol. 40, no. 3, pp. 2135–2144, 2016.

[29] R. Saravanan, D. Manoj, J. Qin et al., "Mechanothermal synthesis of Ag/TiO_2 for photocatalytic methyl orange degradation and hydrogen production," *Process Safety and Environmental Protection*, vol. 120, pp. 339–347, 2018.

[30] N. T. Minh and B.-K. Lee, "Feasibility of silver doped TiO_2/-glass fiber photocatalyst under visible irradiation as an indoor air germicide," *International Journal of Environmental Research and Public Health*, vol. 11, pp. 3271–3288, 2014.

[31] L. Lu, G. Wang, Z. Xiong et al., "Enhanced photocatalytic activity under visible light by the synergistic effects of plasmonics and Ti^{3+}-doping at the Ag/TiO2- heterojunction," *Ceramics International*, vol. 46, no. 8, pp. 10667–10677, 2020.

[32] A. Herissan, J. Meichtry, H. Remita, C. Colbeau-Justin, and M. Litter, "Reduction of nitrate by heterogeneous photocatalysis over pure andradiolytically modified TiO_2 samples in the presence of formic acid," *Catalysis Today*, vol. 281, 2016.

[33] L. Elsellami, F. Dappozze, A. Houas, and C. Guillard, "Effect of Ag^+ reduction on the photocatalytic activity of Ag-doped TiO_2," *Superlattices and Microstructures*, vol. 109, pp. 511–518, 2017.

[34] X. F. Lei, X. X. Xue, and H. Yang, "Preparation and characterization of Ag-doped TiO_2 nanomaterials and their photocatalytic reduction of Cr(VI) under visible light," *Applied Surface Science*, vol. 321, pp. 396–403, 2014.

[35] D. Zhang, B. Wang, X. Gong, Z. Yang, and Y. Liu, "Selective reduction of nitrate to nitrogen gas by novel Cu_2O-Cu_0@Fe_0 composite combined with HCOOH under UV radiation," *Chemical Engineering Journal*, vol. 359, pp. 1195–1204, 2019.

[36] W. Gao, R. Jin, J. Chen et al., "Titania-supported bimetallic catalysts for photocatalytic reduction of nitrate," *Catalysis Today*, vol. 90, no. 3-4, pp. 331–336, 2004.

[37] F. Zhang, Y. Pi, J. Cui, Y. Yang, X. Zhang, and N. Guan, "Unexpected selective photocatalytic reduction of nitrite to nitrogen on silver-doped titanium dioxide," *The Journal of Physical Chemistry C*, vol. 111, no. 9, pp. 3756–3761, 2007.

[38] S. Parastar, S. Nasseri, S. H. Borji et al., "Application of Ag-doped TiO2nanoparticle prepared by photodeposition method for nitrate photocatalytic removal from aqueous solutions," *Desalination and Water Treatment*, vol. 51, no. 37-39, pp. 7137–7144, 2013.

[39] J. Huang, L. Ding, Y. Xi et al., "Efficient silver modification of TiO_2 nanotubes with enhanced photocatalytic activity," *Solid State Sciences*, vol. 80, pp. 116–122, 2018.

[40] R. Qian, H. Zong, J. Schneider et al., "Charge carrier trapping, recombination and transfer during TiO_2 photocatalysis: an overview," *Catalysis Today*, vol. 335, 2018.

[41] S. Buda, S. Shafie, S. A. Rashid, H. Jaafar, and N. F. M. Sharif, "Enhanced visible light absorption and reduced charge recombination in AgNP plasmonic photoelectrochemical cell," *Results in Physics*, vol. 7, pp. 2311–2316, 2017.

[42] B. Xin, L. Jing, Z. Ren, B. Wang, and H. Fu, "Effects of simultaneously doped and deposited Ag on the photocatalytic activity and surface states of TiO_2," *The Journal of Physical Chemistry B*, vol. 109, no. 7, pp. 2805–2809, 2005.

[43] G. Tokazhanov, E. Ramazanova, S. Hamid, S. Bae, and W. Lee, "Advances in the catalytic reduction of nitrate by metallic catalysts for high efficiency and N_2 selectivity: a review," *Chemical Engineering Journal*, vol. 384, p. 123252, 2020.

Hindawi
International Journal of Photoenergy
Volume 2020, Article ID 8846644, 9 pages
https://doi.org/10.1155/2020/8846644

Research Article

Preparation of Graphene-Modified Anticorrosion Coating and Study on Its Corrosion Resistance Mechanism

Peng Wang and Dayong Cai

College of Materials Science and Engineering, Yanshan University, Qinhuangdao 066004, China

Correspondence should be addressed to Peng Wang; lrwp@ysu.edu.cn

Received 13 August 2020; Revised 15 October 2020; Accepted 16 October 2020; Published 2 November 2020

Academic Editor: Jinlong Liu

When aluminum alloy is present in a Cl^--rich environment, the surface oxide film is easily damaged, resulting in faster dissolution of the substrate. The application of graphene-modified anticorrosion coating can effectively prevent the occurrence of corrosion. In this study, to explore the corrosion resistance of graphene-modified anticorrosion coating on the surface of aluminum alloy, we prepared graphene-modified anticorrosion coating on the surface of aluminum alloy and investigated the corrosion resistance mechanism. Epoxy resin primer and polyurethane top coat were modified by predispersed reduced graphene oxide (rGO). Scanning electron microscope (SEM) and Raman spectrum were used to investigate the microstructure of graphene-modified anticorrosion coating, and it was found that the addition of rGO could effectively improve the porosity defect of epoxy resin primer. Electrochemical workstation was used to quickly characterize the corrosion resistance of graphene-modified anticorrosion coating, and the change of the electrochemical curve during soaking in 3.5% NaCl was investigated every 5 hours. It was found that the application of rGO to modify the anticorrosion coating could improve the corrosion resistance of the anticorrosion coating, and as the soaking time increased, the corrosion resistance of graphene-modified anticorrosion coating changed regularly. The study results indicated that when the content of rGO was 0.4%, the porosity of epoxy coating decreased from 1.54% to 0.33%, the porosity dropped by an order of magnitude, and the self-corrosion voltage was relatively positive (-0.72434 V). The self-corrosion current density was the lowest (1.948×10^{-6} A/cm^2), and at the low frequency, the impedance modulus was the highest (10^3). After the equivalent circuit fitting, the dispersion index was relatively high, the dispersion effect was relatively weak, and the corrosion resistance of the coating was improved. For graphene-modified anticorrosion coating, in the early stage of corrosion protection, the existence of pores and other defects in the coating might increase the dispersion effect, resulting in greatly decreased corrosion resistance of the coating. In the middle stage of corrosion protection, the pores in the coating would be completely filled by corrosive ions, resulting in a weakened dispersion effect. Therefore, the decrease in the corrosion resistance of the coating was slowed down and became stable.

1. Introduction

Aluminum alloy has been widely used in aircraft frames, skins, fuel tanks, landing gear struts and other structures due to its low density, high specific strength, good ductility, good workability and other characteristics. The strong chemical activity of aluminum alloy makes it easy to form oxide film on the surface, but the film is thin (usually 10-15 nm) and has uneven dispersion and poor compactness, leading to poor corrosion resistance of the film [1]. Therefore, it cannot play a good protective role. Especially in the marine atmospheric environment rich in Cl^-, the higher concentration of corrosive ions can easily penetrate the oxide film, leading to corrosion of the aluminum alloy substrate [2]. A series of protective measures have been developed worldwide for serious metal corrosion. As the simplest, efficient, and economical anticorrosion measure, organic coating protection has attracted wide attention. Common organic coatings mainly include epoxy resin coating, polyurethane resin coating, and fluorocarbon resin coating. Epoxy resin is characterized by greater hardness and higher adhesion, but cured coating has large porosity and poor acid resistance and UV

Table 1: 7075-T6 aluminum alloy composition.

Component	Zn	Mg	Cu	Si	Fe	Mn	Cr	Ti	Al	Others
Percentage	5.6	2.5	1.4	0.35	0.42	0.29	0.22	0.1	Allowance	0.15

resistance. Polyurethane resin has excellent flexibility, abrasion resistance, and mechanical properties, but its corrosion resistance will drop sharply after UV aging, which will seriously affect the protection of metallic substrate. Even though fluorocarbon resin has excellent UV resistance, its lower adhesion limits its future applications. Graphene is currently the lightest and thinnest material, and its microlamellar structure and small size effect have been found to be effective in improving the structure of the anticorrosion coating and increasing its corrosion resistance.

Graphene-modified anticorrosion coatings have the following characteristics:

(1) Light weight: the application of graphene to modify anticorrosion coatings can effectively reduce the thickness and improve the protection efficiency of coatings [3].

(2) Excellent barrier properties: graphene can be effectively filled in the micropores in coatings to improve the pores and other defects of anticorrosion coatings; moreover, the conjugated binary lamellar structure of graphene is superimposed in the coating to form a dense physical insulation layer, and the surface has excellent hydrophobic property after adsorbing alkanes and can greatly block the infiltration and penetration of water molecules and corrosive media into the coating [4].

(3) Excellent electrical conductivity: after the metallic substrate is corroded, it can quickly transfer electrons to the coating surface to prevent stacking of corrosion products on the substrate surface [5].

(4) Excellent mechanical properties: the C-C bond in the graphene structure makes graphene have good structural rigidity, which can effectively improve the flexibility and impact resistance of graphene-modified anticorrosion coatings [6].

To this end, researchers have conducted several studies [7–10]. Pourhashem et al. [11] used silane coupling agents APTES (KH550) and GPTMS (KH560) to prepare graphene oxide-modified epoxy resin coating and investigated its protective mechanism in stainless steel. Ye et al. [12] used covalent grafting to prepare functionalized graphene-modified epoxy resin coating and investigated its corrosion resistance in Q235 steel. Paul et al. [13] polymerized acrylic monomer solution to synthesize hydrophobic organosiloxane-acrylic resin and covalently bonded to fluorosilane-modified graphene nanosheets to prepare superhydrophobic (≥152°) anticorrosion coating, which improved the protection of LY12 aluminum alloy. In the above studies on graphene-modified anticorrosion coatings, graphene oxide (GO) was mostly used to modify anticorrosion coatings, and the protection mechanism was investigated in stainless steel substrates. However, the effects of graphene-modified anticorrosion coatings on aviation aluminum alloy substrates were rarely investigated. Therefore, the following contents were investigated in this paper:

After using rGO to modify the epoxy primer, its porosity dropped by an order of magnitude. After cooperating with the graphene-modified polyurethane coating, its self-corrosion voltage is relatively positive, the self-corrosion current density is low, the impedance modulus value is large at low frequency, and it has high corrosion resistance. With the extension of the immersion time in 3.5% NaCl solution, the weakening of the dispersion effect decreases, and the corrosion resistance of the coating decreases slowly. The corrosion resistance mechanism of aviation aluminum alloy is explored.

2. Experimental Section

2.1. Materials. The metal substrate used in the experiment was 7075-T6 aluminum alloy, and its composition is shown in Table 1. The coatings were epoxy resin primer and polyurethane resin top coat provided by the Marine Chemical Research Institute in China. Reduced graphene oxide was 1133 anticorrosion graphene produced by The Sixth Element (Changzhou) Materials Technology Co., Ltd. in China. The graphene dispersant was F463 dispersant produced by Foshan Aona Polymer Co., Ltd. The other chemical reagents used in the experiment were purchased from Aladdin.

2.2. Preparation of rGO Dispersion. Reduced graphene oxide, F463 dispersant, and xylene solution were mixed in a ratio of 1 : 0.1 : 10 and then ultrasonically treated in a 600 W water bath sonicator for 2 hours to obtain the uniform graphene dispersion.

2.3. Preparation of Anticorrosion Coatings. Before coating, the surface of 7075-T6 aluminum alloy was sandblasted with 120-mesh white corundum, ultrasonically degreased with acetone, dehydrated with absolute ethyl alcohol, and finally dried and placed in a dry vessel for later use. Epoxy resin, curing agent, and diluent were mixed in a ratio of 8 : 1 : 3, and then the prepared graphene dispersion was doped (rGO addition ratio was 0.4% wt). The epoxy resin doped with reduced graphene oxide was magnetically stirred for 20 minutes. Atmospheric spray technology was used to spray on the sandblasted surface of aluminum alloy and cured at 70°C for 1 hour (air pressure was maintained at 6-7 MPa during spraying, and the spraying distance was maintained at 15-20 cm). After the epoxy resin coating was completely dry, the above steps and addition ratio were repeated to prepare the polyurethane resin coating on the surface of epoxy resin primer. The total thickness of the anticorrosion coating was

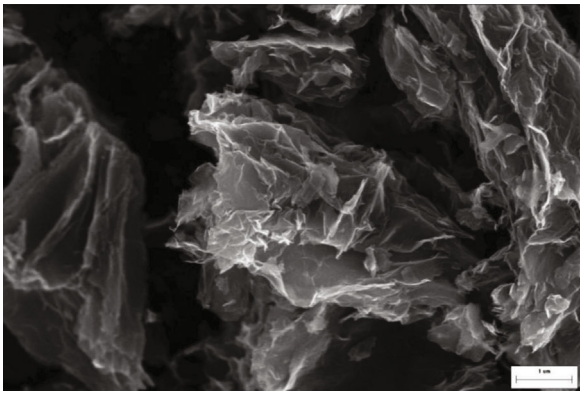

Figure 1: SEM image of rGO.

about 150 μm. The anticorrosion coating undoped with reduced graphene oxide was prepared in the same way as a blank control.

2.4. Characterization. A scanning electron microscope (7900F) was used to observe the microscopic morphology of the cross-section of coating. Raman spectrometer (wavelength 532 nm) was used to measure the Raman spectrum of the coating to investigate the microstructure of reduced graphene in the coating. Autolabe PGSTAT 302N electrochemical workstation (Metrohm, Switzerland) was used to determine the polarization curve and AC impedance of the anticorrosion coating and analyze the corrosion resistance of the anticorrosion coating and the change in the corrosion resistance of the graphene-modified anticorrosion coating after soaking in 3.5% NaCl. NOVA software was used to fit the electrochemical curve and draw the equivalent circuit. Before testing, it needed to be connected to a copper wire, and then, the sample was sealed with epoxy resin. The exposed coating area was fixed to 1 cm^2. The electrochemical measurement was performed with a three-electrode system: a 10×10 mm platinum sheet was used as the counter electrode, a saturated calomel electrode was used as the reference electrode, the test interval of the polarization curve was self-corrosion potential (±150 mV), the scanning speed was 1 mV/s, the frequency range of sine wave in the AC impedance test (EIS) was 0.01-100000 Hz, and the amplitude of loaded AC disturbance voltage was 10 mV.

3. Results and Discussion

3.1. Characterization of rGO

3.1.1. SEM of rGO. At present, the main methods for preparation of graphene include mechanical exfoliation, chemical vapor deposition, SiC epitaxial growth, and redox process. The rGO used in this experiment was prepared by redox process, and its microscopic morphology is shown in Figure 1. It can be seen from Figure 1 that the rGO sheet had a large number of layers and the edges were wrinkled. The reason was that the hydroxyl groups (including the hydroxyl groups formed by the conversion of various oxygen-containing functional groups) on the benzene ring branches during the preparation of rGO by redox process, new C=C double bonds were formed, and the electrostatic repulsion between graphene sheets was weakened, leading to intensified rGO agglomeration and increased edge defects [14, 15].

3.1.2. Dispersion of rGO. The comparison of rGO dispersion before and after standing for 20 days is shown in Figures 2(a) and 2(b) . It can be seen from Figures 2(a) and 2(b) that the color of rGO dispersion after standing for 20 days was not changed, and no rGO precipitation occurred, indicating that F463 dispersant can make rGO evenly dispersed in xylene. In the analysis of the dispersion mechanism, after ultrasound is used to predisperse rGO, the large van der Waals force of rGO makes its surface adsorb the chain-like polymer structure in the dispersant. And then relying on the physical barrier and electrostatic repulsion between polymers, the dispersion of rGO in the solution is achieved (as shown in Figure 2(c)).

The Raman spectrum of the prepared graphene-modified anticorrosion coating is shown in Figure 3. It could be seen from the figure that there were three characteristic peaks of graphene: D peak (near 1350 cm^{-1}), G peak (near 1580 cm^{-1}), and 2D peak (near 2690 cm^{-1}). D peak was a graphene defect peak, which required at least one defect to activate. The higher intensity of D peak in Figure 3 indicated that there were more edges and defects in the graphene. The 2D peak of single-layer graphene was located near 2690 cm^{-1} and sharp, and its peak intensity was about 4 times that of G peak. As the number of graphene layers increased, its location shifted to the right, the peak intensity decreased, and the peak width increased [16, 17]. When the graphene sheet reached ten layers or more, the shape of its 2D peak was basically the same as that of graphite. It was formed by the superposition of two peaks, and its intensity was about 1/4 or 1/2 of the G peak intensity, respectively. As shown in Figure 2, $I_{2D} : I_G$ was about 1 : 1, indicating that the dopant was graphene with more layers rather than graphite [18]. The grain size of rGO in the graphene-modified anticorrosion coating was about 12 nm, calculated by formula (1) [19] for graphene grain size.

$$\mathrm{La(nm)} = \left(2.4 \times 10^{-10}\right)\lambda^4 \left(\frac{I_D}{I_G}\right)^{-1}, \quad (1)$$

where λ is the wavelength of the excitation light source (532 nm).

3.2. Morphology of Anticorrosion Coatings. The cross-sectional micromorphology of original and graphene-modified anticorrosion coatings is shown in Figure 4. As can be seen from Figure 4, epoxy resin has excellent chemical stability and adhesion; it not only has anticorrosion effect on the aluminum alloy substrate but also strengthens the bonding of anticorrosion coating to aluminum alloy substrate. However, with the volatilization of diluent during high-temperature curing, more pores may occur. Pores are typical defects in anticorrosion coatings. As the corrosion progresses, corrosive ions enter the pores and defects of coatings

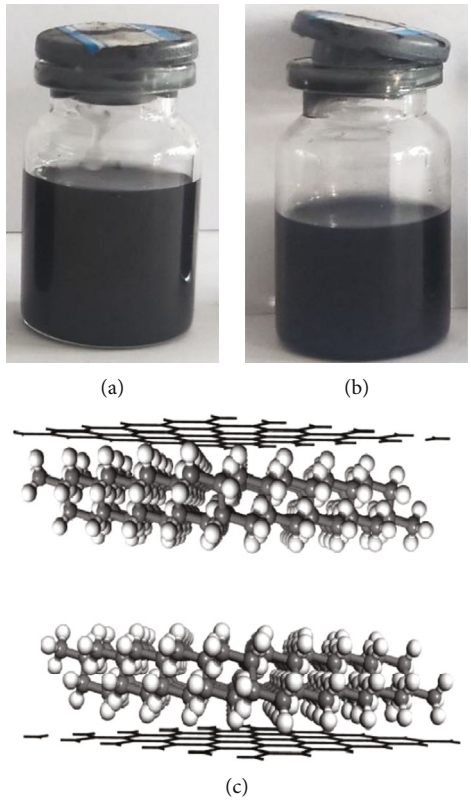

Figure 2: Dispersion of rGO ((a) 0d; (b) 20d; (c) dispersion mechanism).

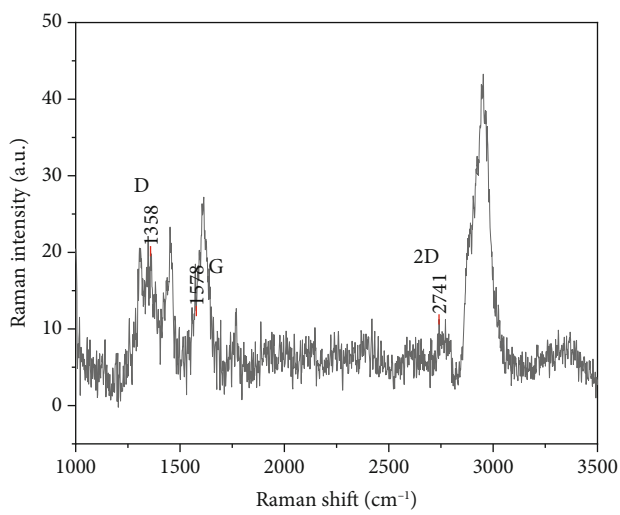

Figure 3: Raman of graphene-modified coating.

through diffusion, forming an ion pathway connecting the metal substrate with the outside. This not only destroys organic coatings but also accelerates the corrosion of the metal substrate [20, 21]. Polyurethane resin has low viscosity and good fluidity. The top coat formed after high-temperature curing has no large porosity, and corrosive media such as Cl^- and water cannot pass through easily. Therefore, Image-Pro software was used to calculate the porosity in epoxy resin primer (as shown in Table 2). From the data in Table 2, it could be seen that the porosity in the epoxy resin primer in graphene-modified anticorrosion coating was one order of magnitude lower than that of the original coating. And the anticorrosion coating defects were significantly improved. This is because the predispersed rGO surface adsorbs more organic polymers and the rGO is effectively dispersed after it is fully stirred with the polymer diluent. In the subsequent curing process, as the diluent volatilizes, rGO occupies the volatilized dilution. The location where the agent is located and relying on its own excellent microlamella structure and small size effect effectively prevent the penetration of corrosion ions (Cl^-) into the anticorrosion coating and reduce the formation of "water vapor pathway," thereby enhancing the corrosion resistance of coatings.

3.3. Electroactivity of Anticorrosion Coatings. The polarization curve of original and graphene-modified anticorrosion coatings is shown in Figure 5. Self-corrosion potential (E_{corr}, SCE) indicates the degree of difficulty of corrosion of the test sample, while self-corrosion current density (J_{corr}) is a favorable basis for quickly evaluating the corrosion resistance of coating. It could be seen from Figure 5 that when graphene-modified anticorrosion coating was compared with original anticorrosion coating, the self-corrosion potential was relatively positive. This indicates that graphene-modified anticorrosion coating is not prone to corrosion, and the addition of rGO hinders the anodic dissolution and cathodic formation occurring in oxide film on the aluminum alloy surface during polarization.

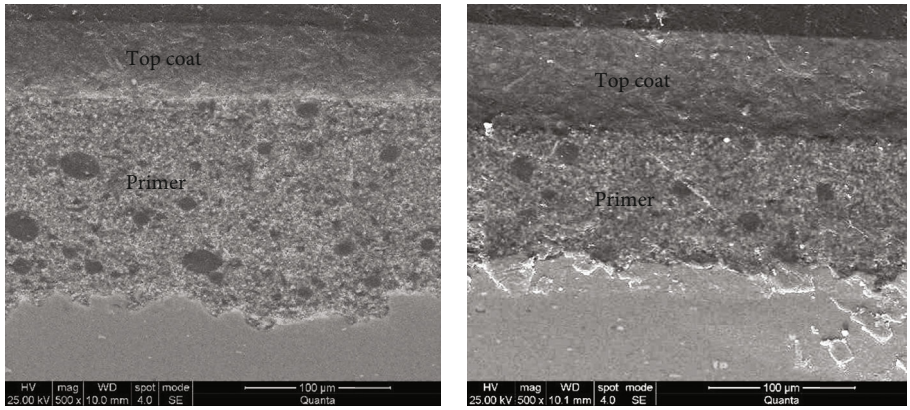

(a) (b)

Figure 4: SEM images of original and graphene-modified coatings ((a) original; (b) graphene-modified coating).

Table 2: Porosity of original and graphene-modified coatings.

Coatings	Original	Graphene-modified coating
Porosity (%)	1.54	0.33

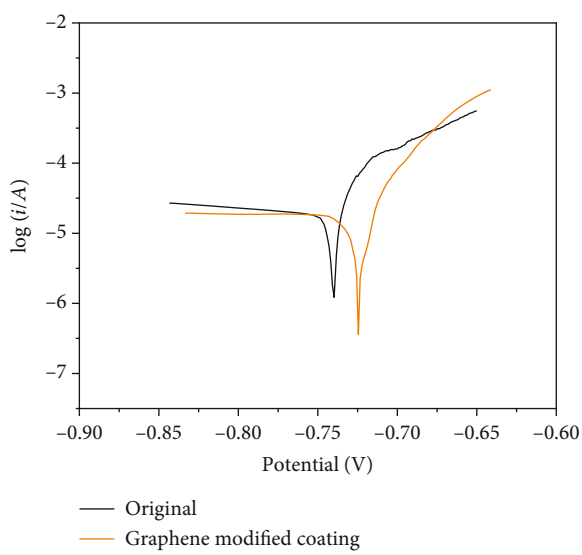

Figure 5: Tafel of original and graphene-modified coatings.

The results of the Tafel curve fitting using Nova software are shown in Table 3, where b_a is the Tafel slope of the anode, b_c is the Tafel slope of the cathode, and R_p is the polarization resistance calculated according to formula (2). It could be seen from the fitting data in Table 3 that the self-corrosion current density on graphene-modified anticorrosion coating decreased and the polarization resistance increased. The addition of rGO enlarged the transmission route of electrons in the anticorrosion coating, and the electrical resistance of the coating was increased, thereby improving the corrosion resistance of the coating.

$$R_p = \frac{b_a/b_c}{2.303(b_a + b_c)J_{\text{coor}}}. \quad (2)$$

The Bode curve of original and graphene-modified anticorrosion coatings is shown in Figure 6 ((a) impedance modulus diagram and (b) phase angle diagram). In the electrochemical corrosion test, the impedance modulus ($|Z|$) in the low-frequency region was used to compare the corrosion resistance of coatings. In Figure 6(a), $|Z|$ of graphene-modified anticorrosion coating at low frequency > 103 > $|Z|$ of original anticorrosion coating at low frequency indicates that graphene-modified anticorrosion coating has better corrosion resistance. This was consistent with the result shown in the polarization curve.

The Nyquist curve of the anticorrosion coating obtained by the electrochemical workstation is shown in Figure 7. The size of capacity reactance arc radius in the Nyquist curve indicates the diffusion speed of corrosion products and the easiness of charge transfer. The comparison of the capacity reactance arc radius in Figure 7 showed that corrosion products produced on the surface of aluminum alloy protected by graphene-modified anticorrosion coating were not easy to stack, the charge was easily transferred, and the corrosion of the aluminum alloy substrate was inhibited. In the original and graphene-modified anticorrosion coatings in Figure 7, there was inductive reactance arc in addition to capacity reactance arc. The appearance of inductive reactance arc was caused by the destruction of oxide film on the aluminum alloy surface, thereby activating the pitting corrosion [22]. In the phase angle curve in Figure 6(b), both the anticorrosion coatings had a peak and a trough. The equivalent circuit diagram was drawn according to the Nyquist curve, as shown in Figure 8 (where R_s is the solution resistance, Q_{dl} is the constant phase angle element, R_{ct} is the coating resistance, L is the inductance caused by pitting corrosion, and R_m is the oxide film resistance), and the data obtained by fitting the elements in the equivalent circuit with software are shown in Table 4 [23]. In Table 4, R_{ct} of graphene-modified anticorrosion coating was doubled compared with that of original anticorrosion coating. Graphene-modified anticorrosion coating had higher dispersion index and larger dispersion

Table 3: Results of Tafel curve fitting.

	E_{corr} (V)	J_{corr} (A/cm^2)	b_a	b_c	R_p (Ω)
Original	-0.74045	3.801×10^{-6}	0.0081057	0.010076	510.68
Graphene-modified coatings	-0.72434	1.948×10^{-6}	0.0073826	0.010325	1014.5

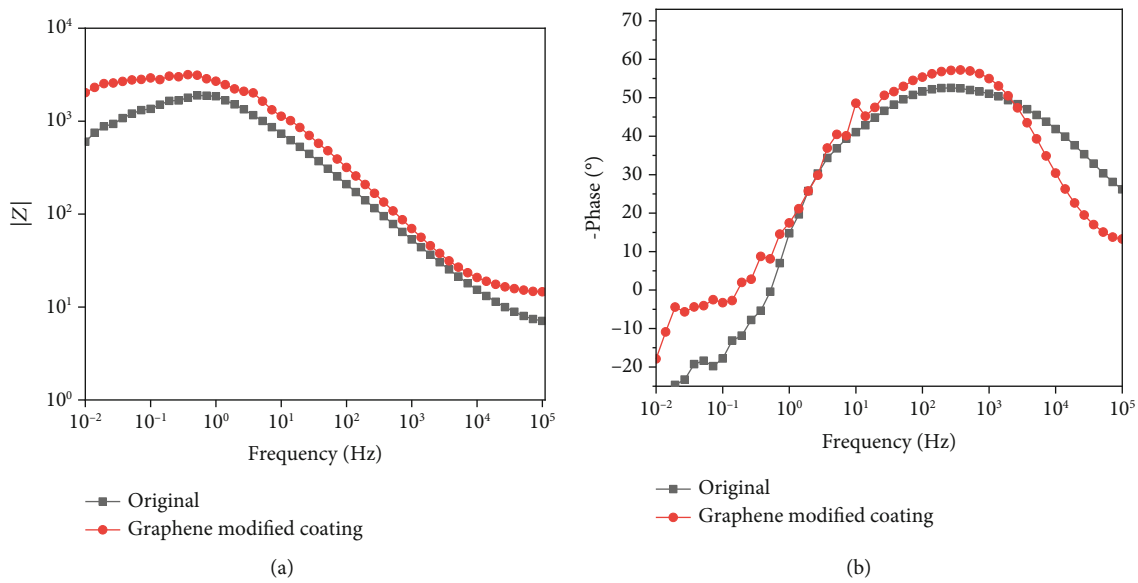

Figure 6: Bode of the original and graphene-modified coatings ((a) impedance modulus curve; (b) phase angle curve).

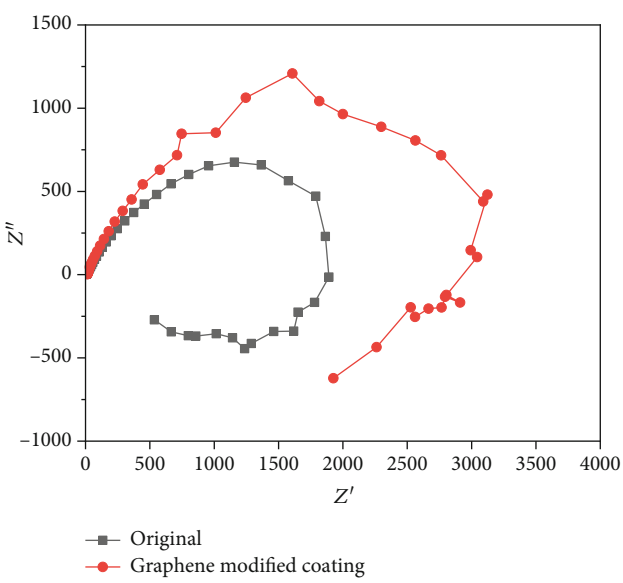

Figure 7: Nyquist of original and graphene-modified coatings.

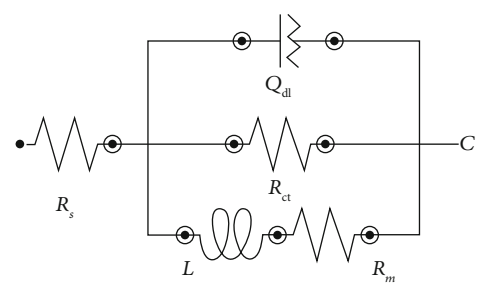

Figure 8: Equivalent circuit diagram.

Table 4: Fitting data of equivalent circuit components.

Coatings	R_s (Ω)	R_{ct} (Ω)	Q_{dl} Y_0	Q_{dl} N
Original	5.467	1067.2	5.071×10^{-5}	0.679
Graphene-modified coating	12.922	2768	3.076×10^{-5}	0.716

effect. The dispersion index tended to be 1. The surface of graphene-modified anticorrosion coating tended to be an electrical double-layer capacitor and had strong corrosion resistance [24].

The Bode curve of graphene-modified anticorrosion coating soaked in 3.5% NaCl for different times is shown in Figure 9. The equivalent circuit drawn according to Figure 8(b) (phase angle curve) and Figure 10 (Nyquist curve) was consistent with that Figure 8, and the fitting data of equivalent circuit components are shown in Table 5. In the impedance modulus curve shown in Figure 9(a), it could be seen that the $|Z|$ value did not change at low frequency in the early stage of soaking, and the corrosion resistance of graphene-modified anticorrosion coating did not decrease. After soaking for 10 hours, at low frequency, the $|Z|$ value

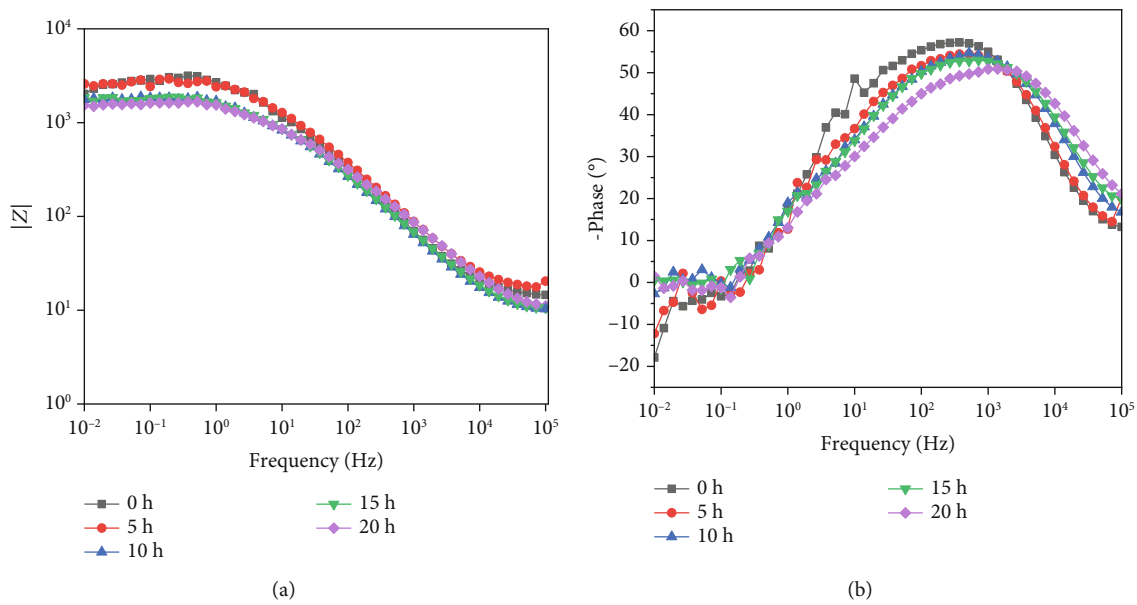

Figure 9: Bode of graphene-modified anticorrosion coating soaked in 3.5% NaCl for different times ((a) impedance modulus curve; (b) phase angle curve).

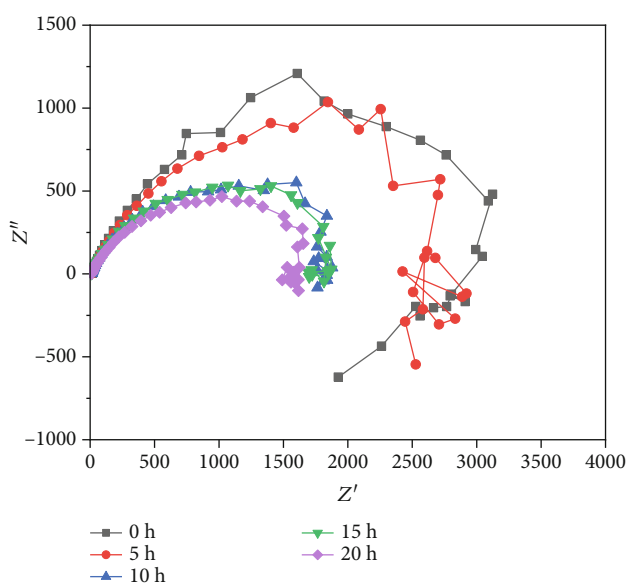

Figure 10: Nyquist of graphene-modified anticorrosion coating soaked in 3.5% NaCl for different times.

Table 5: Fitting data of equivalent circuit components.

Time	R_s (Ω)	R_{ct} (Ω)	Q_{dl}	
			Y_0	N
0 h	12.922	3768	3.076×10^{-5}	0.716
5 h	14.82	2734.9	3.025×10^{-5}	0.690
10 h	7.786	1861.9	5.128×10^{-5}	0.661
15 h	7.574	1851.4	5.0753×10^{-5}	0.6548
20 h	7.105	1638.2	5.152×10^{-5}	0.6261

decreased to a large extent, and the corrosion resistance of graphene-modified anticorrosion coating decreased greatly. Then, as the soaking time increased, the decrease of the $|Z|$ value at low frequency slowed down. The capacity reactance arc radius in the Nyquist curve and the dispersion index in the fitted data showed the same change. In the analysis of reason, corrosive ions were gradually filled into the pores and other defects of graphene-modified anticorrosion coating within 5 hours of soaking, thus realizing the invasion of corrosive ions to the surface of aluminum alloy. And then, as the pores and other defects were completely filled by corrosive ions, the dispersion effect of corrosive ions in graphene-modified anticorrosion coating decreased and became stable. The corrosive ions gradually destroyed the graphene-modified anticorrosion coating, and the area of corrosive ions in the graphene-modified anticorrosion coating was expanded. This reduces the corrosion resistance of the graphene-modified anticorrosion coating [25].

4. Conclusions

(1) rGO was used to prepare graphene-modified anticorrosion coating, and the cross-sectional micromorphology of graphene-modified anticorrosion coating and the microstructure of rGO in the coating were tested and analyzed. It is found that rGO could effectively improve the porosity of graphene-modified anticorrosion coating by relying on its microlamellar structure and small size effect and reduce it by an order of magnitude. rGO was prone to reagglomeration in the anticorrosion coating, and the rGO sheet in the graphene-modified anticorrosion coating reached more than 10 layers

(2) The electrochemical performance of anticorrosion coating was tested and analyzed, and it was found that compared with the original anticorrosion coating, the self-corrosion voltage of the graphene-modified anticorrosion coating was relatively positive, the self-corrosion current density was relatively low, the polarization resistance was relatively large, the impedance modulus at low frequency was relatively large, the dispersion effect in the equivalent circuit components was relatively weak, and the coating had better corrosion resistance

(3) The electrochemical curve of the graphene-modified anticorrosion coating soaked in 3.5% NaCl for different times was tested and analyzed, and it was found that corrosive ions showed a strong dispersion effect in a period of time due to the existence of pores and other defects in the graphene-modified anticorrosion coating in the early stage of soaking. As the pores and other defects were completely filled, the dispersion effect slowed down and became stable, thereby reducing the corrosion resistance of the graphene-modified anticorrosion coating

Data Availability

The data used to support the findings of this study are available from the corresponding author upon request.

Conflicts of Interest

The authors declare that they have no conflicts of interest.

References

[1] V. K. Beura, C. Kale, S. Srinivasan, C. L. Williams, and K. N. Solanki, "Corrosion behavior of a dynamically deformed Al–Mg alloy," *Electrochimica Acta*, vol. 354, p. 136695, 2020.

[2] M. A. Wahid, A. N. Siddiquee, and Z. A. Khan, "Aluminum alloys in marine construction: characteristics, application, and problems from a fabrication viewpoint," *Marine Systems & Ocean Technology*, vol. 15, no. 1, pp. 70–80, 2020.

[3] A. K. Geim and K. S. Novoselov, "The rise of graphene," *Nature Materials*, vol. 6, no. 3, pp. 183–191, 2007.

[4] H. Wu and L. T. Drzal, "Graphene nanoplatelet paper as a light-weight composite with excellent electrical and thermal conductivity and good gas barrier properties," *Carbon*, vol. 50, no. 3, pp. 1135–1145, 2011.

[5] P. Dhiraj, T. J. Carlos, R. Harl Robert, J. G. Kane, R. Rogers Bridget, and I. Bolotin Kirill, "Graphene: corrosion-inhibiting coating," *ACS Nano*, vol. 6, no. 2, pp. 1102–1108, 2012.

[6] M. A. Krishnan, K. S. Aneja, A. Shaikh et al., "Graphene-based anticorrosive coatings for copper," *RSC Advances*, vol. 8, no. 1, pp. 499–507, 2018.

[7] C. Cheng, S. Qiu, M. Cui et al., "Achieving high performance corrosion and wear resistant epoxy coatings via incorporation of noncovalent functionalized graphene," *Carbon*, vol. 114, pp. 7858–7862, 2017.

[8] Y. T. Hui, Z. Z. Hua, L. Jin et al., "Corrosion protection of aluminum alloy by epoxy coatings containing polyaniline modified graphene additives," *Materials and Corrosion*, vol. 70, no. 7, pp. 1298–1305, 2019.

[9] S. Lu, Y. Li, W. Zhao et al., "Tuning F-doped degree of rGO: restraining corrosion-promotion activity of EP/rGO nanocomposite coating," *Journal of Materials Science & Technology*, vol. 44, no. 9, pp. 121–132, 2020.

[10] H. Wang, L. Grabstanowicz, H. Barkholtz, D. Rebollar, and D.-J. Liu, "Impacts of imidazolate ligand on performance of zeolitic-imidazolate framework-derived oxygen reduction catalysts," *ACS Energy Letters*, vol. 4, no. 10, pp. 2500–2507, 2019.

[11] S. Pourhashem, A. Rashidi, M. R. Vaezi, and M. R. Bagherzadeh, "Excellent corrosion protection performance of epoxy composite coatings filled with amino-silane functionalized graphene oxide," *Surface & Coatings Technology*, vol. 317, pp. 1–9, 2017.

[12] Y. Ye, D. Zhang, T. Liu et al., "Superior corrosion resistance and self-healable epoxy coating pigmented with silanzied trianiline-intercalated graphene," *Carbon*, vol. 142, pp. 164–176, 2018.

[13] P. C. Uzoma, F. Liu, L. Xu et al., "Superhydrophobicity, conductivity and anticorrosion of robust siloxane-acrylic coatings modified with graphene nanosheets," *Progress in Organic Coatings*, vol. 127, pp. 239–251, 2019.

[14] C. C. Kiang and P. Martin, "Chemical reduction of graphene oxide: a synthetic chemistry viewpoint," *Chemical Society reviews*, vol. 43, no. 1, pp. 291–312, 2014.

[15] S. Stankovich, D. A. Dikin, R. D. Piner et al., "Synthesis of graphene-based nanosheets via chemical reduction of exfoliated graphite oxide," *Carbon*, vol. 45, no. 7, pp. 1558–1565, 2007.

[16] R. Thomsen, "Double resonant Raman scattering in graphite," *Physical Review Letters*, vol. 85, no. 24, pp. 5214–5217, 2000.

[17] N. T. An, L. Jae-Ung, Y. Duhee, and C. Hyeonsik, "Excitation energy dependent Raman signatures of ABA- and ABC-stacked few-layer graphene," *Scientific reports*, vol. 4, no. 7, article 4630, 2014.

[18] R. J. Nemanich and S. A. Solin, "First- and second-order Raman scattering from finite-size crystals of graphite," *Physical Review B*, vol. 20, no. 2, pp. 392–401, 1979.

[19] L. G. Cancado, K. Takai, T. Enoki et al., "General equation for the determination of the crystallite size La of nanographite by Raman spectroscopy," *Applied Physics Letters*, vol. 88, no. 16, 2006.

[20] A. Meroufel, C. Deslouis, and S. Touzain, "Electrochemical and anticorrosion performances of zinc-rich and polyaniline powder coatings," *Electrochimica Acta*, vol. 53, no. 5, pp. 2331–2338, 2007.

[21] E. Rocca, C. Juers, and J. Steinmetz, "Corrosion behaviour of chemical conversion treatments on as-cast Mg–Al alloys: electrochemical and non-electrochemical methods," *Corrosion Science*, vol. 52, no. 6, pp. 2172–2178, 2010.

[22] A. Venugopal and V. S. Raja, "AC impedance study on the activation mechanism of aluminium by indium and zinc in 3.5% NaCl medium," *Corrosion Science*, vol. 39, no. 12, pp. 2053–2065, 1997.

[23] G. Bierwagen, D. Tallman, J. Li, L. He, and C. Jeffcoate, "EIS studies of coated metals in accelerated exposure," *Progress in Organic Coatings*, vol. 46, no. 2, pp. 149–158, 2003.

[24] J. D. Scantlebury and K. Galić, "The application of AC impedance to study the performance of lacquered aluminium specimens in acetic acid solution," *Progress in Organic Coatings*, vol. 31, no. 3, pp. 201–207, 1997.

[25] S. Syed, "Influence of the environment on atmospheric corrosion of aluminiumCorrosion engineering," *Science and Technology*, vol. 45, no. 4, pp. 282–287, 2010.

Hindawi
International Journal of Photoenergy
Volume 2020, Article ID 8835737, 8 pages
https://doi.org/10.1155/2020/8835737

Research Article

Study of the Protection of Aluminum Alloy Surfaces by a Graphene-Modified Fluorocarbon Anticorrosive Coating

Peng Wang and Dayong Cai

College of Materials Science and Engineering, Yanshan University, Qinhuangdao 066004, China

Correspondence should be addressed to Peng Wang; lrwp@ysu.edu.cn

Received 15 August 2020; Revised 18 September 2020; Accepted 5 October 2020; Published 23 October 2020

Academic Editor: Yimin Wu

Graphene-modified anticorrosion coatings have become a hot spot in the field of metal protection due to the large-scale promotion of aluminum alloys, which are prone to corrosion in marine and atmospheric environments. The protection of aluminum alloy surfaces by a graphene-modified anticorrosive coating was explored in this study by applying a graphene-modified anticorrosive coating to an aluminum alloy surface to test its resistance to corrosion. Dispersion-treated reduced graphene oxide (rGO) was used to modify the epoxy resin and fluorocarbon resin. It was found, by using a scanning electron microscopy (SEM) and the microstructure of the coating made by the Raman Spectroscopy Institute, that the addition of rGO could effectively improve the porosity of the epoxy primer, and the electrochemical workstation was able to resist the graphene-modified anticorrosive coating. The corrosion performance was quickly characterized, the polarization curve and the AC impedance curve were fitted, and it was found that the self-corrosion current density (J_{corr}) of the graphene-modified anticorrosive coating was the smallest (1.190×10^{-7} A/cm^2) when 0.6% of rGO was added; the impedance modulus ($|Z|$) was the largest (10^4), the capacitive reactance arc radius was the largest, and the coating resistance was the largest after fitting (15517 Ω). When 0.8% of rGO was added, the dispersion coefficient was large, and it had a good physical insulation performance. The main reason for the reduction of the corrosion resistance was that the agglomeration of rGO made the aluminum alloy matrix and the external corrosive environment form a highly conductive circuit, thereby accelerating the corrosion of the aluminum alloy matrix.

1. Introduction

In a space shuttle, the most serious corrosion is found in the structure of the aircraft body. A large amount of condensation forms on the surface and inside of the aircraft fuselage during the takeoff and climb phase due to the difference in temperature between the ground and the high altitude. When the relative humidity of the atmosphere in the external environment exceeds 65%, a film of water about 0.001 μm thick is deposited on the surface of the aircraft body and structural parts [1]. The thickness of the water film gradually increases with the increase of the external relative humidity, and when the humidity of the external environment reaches 100%, condensation forms on the surface of the aircraft body. Corrosion is caused by the saturated Cl^- ion, O_2, and other corrosive media coming into contact with the aluminum alloy structural parts of the aircraft. The common types of corrosion of the aluminum alloy structural parts of aircraft currently include the following: (1) pit-like corrosion: in a neutral aqueous solution or humid environment, corrosion pits appear on the surface of the aluminum alloy. Their depth and diameter increase rapidly, and they continue to develop inside the aluminum alloy. In a marine atmosphere, Cl^- ions can accelerate the corrosion of aluminum alloy, and the surface of aluminum alloy is prone to a galvanic effect; (2) crevice corrosion: the aluminum alloy undergoes a reduced reaction of anode solvent and cathode oxygen in the gap between the interface, resulting in an accumulation of corrosion products, blocking the transmission of corrosive media, leading to differences in the corrosive media and concentration inside and outside the crevice, and then evolving into "occluded battery corrosion"; and (3) friction corrosion: corrosion products are formed by chemical and electrochemical reactions on the contact surfaces of two aluminum alloy

structural parts. The friction between the contact surfaces causes the corrosion products to fall off, and the newly exposed aluminum alloy surface corrodes again and again, which causes damage to the aluminum alloy structural parts. Organic coating protection is the simplest, most efficient, and economical anticorrosion method in the industry [2].

The level of development of heavy-duty anticorrosion coatings is a measure of the advanced level of a country's coatings industry. A series of heavy-duty anticorrosion coatings have been developed at home and abroad in response to the phenomenon that aluminum alloys are prone to corrosion. These mainly include the following: (1) epoxy heavy-duty anticorrosion coatings, an epoxy resin macromolecule chain, which contains two or more epoxy groups. Thermosetting resin is highly adhesive and extremely hard. As such, it is widely used for building materials. However, epoxy resin is extremely porous, It is easily corroded by oxygen, water, and chloride ions and has poor acid resistance. Other disadvantages include poor ultraviolet rays and brittle paint film; (2) polyurethane heavy-duty anticorrosive coating; this is extremely flexible and highly adhesive and has excellent wear resistance due to the reactive cyanate group (-NCO) on the macromolecular chain. It is often used as a topcoat in the field of heavy anticorrosion to protect the substrate due to its mechanical properties, but its UV resistance is poor, and its anticorrosion performance is greatly reduced after ultraviolet aging; (3) fluorocarbon coatings that contain a large amount of C, with a bond energy of up to 485.6 kJ/mol F-bonded fluorocarbon resin, have excellent chemical and UV resistance. They are widely used in ships, pipelines, and aerospace fields, but their adhesion and pigment wetting are poor [3, 4].

These reasons have led to much research by scientific researchers. For example, Pourhashem and others [5] used silane coupling agents APTES (KH550) and GPTMS (KH560) to prepare graphene oxide-modified epoxy resin coatings to test their ability to protect stainless steel. Ye et al. [6] used covalent grafting to prepare functionalized graphene-modified epoxy resin coating and explored the corrosion resistance of Q235 steel; Uzoma et al. [7] used a solution polymerization of acrylic monomer to synthesize hydrophobic organic. The siloxane-acrylic resin and fluorosilane-modified graphene nanosheets were connected by covalent bonds to prepare a superhydrophobic (≥152°) anticorrosion coating, which improved the protection of LY12 aluminum alloy. In the above research on graphene-modified anticorrosion coatings, graphene oxide (GO) was used to modify anticorrosion coatings, the protection mechanism of stainless steel was explored, and the modified anticorrosion coatings of reduced graphene oxide were used on aviation aluminum alloy substrates [8, 9]. Therefore, due to the limited exploration, the contents defined below are addressed in this article.

A polymer dispersant is used to produce an rGO surface to prepare for graphene dispersion; then, rGO is used to modify the epoxy primer and fluorocarbon resin topcoat; and atmospheric spray technology is used to apply a graphene-modified anticorrosive coating to the surface of aviation aluminum alloy. An electron microscope and Raman spectroscopy are used to scan, test, and characterize the microstructure of the graphene-modified anticorrosive coating; and an electrochemical workstation is used to test and characterize the corrosion resistance of the graphene-modified anticorrosive coating. The corrosion resistance mechanism of the anticorrosive coating is explored by fitting an equivalent circuit to explore its ability to resist the corrosion of aviation aluminum alloy.

2. Experimental Section

2.1. Materials. The metal matrix used in the experiment is 7075-T6 aluminum alloy, and its composition is shown in Table 1. The coating is epoxy resin primer and fluorocarbon resin topcoat provided by the Beijing Institute of Aeronautical Materials. The reduced graphene oxide is 1133 anticorrosive graphene produced by the China Changzhou Sixth Element Material Technology Co., Ltd. The graphene dispersant used is F431 type dispersant produced by the Foshan Aona Polymer Co., Ltd. The other chemical reagents used throughout the experiment were purchased from Aladdin.

2.2. Preparation of Anticorrosion Coatings. Firstly, the reduced graphene oxide, F431 dispersant, and xylene solution were mixed in a ratio of 1 : 0.1 : 10 and then ultrasonically treated in a 600 W water bath sonicator for 2 hours to obtain a uniform graphene dispersion. Before being painted, the surface of the 7075-T6 aluminum alloy was sandblasted using 120-mesh white corundum. Then, it was ultrasonically degreased with acetone, dehydrated with ethanol, and finally dried and placed in a desiccator for use. The epoxy resin, curing agent, and diluent were mixed at 8 : 1 : 3. After mixing the paint, the prepared graphene dispersion (rGO addition ratio was 0.4% wt) was doped with reduced graphene oxide. The epoxy resin was magnetically stirred for 20 minutes using atmospheric spraying technology, sprayed on the sandblasted aluminum alloy surface, and cured at 70°C for 1 hour (air pressure was maintained at 6-7 MPa during spraying, and the spraying distance was maintained at 15~20 cm). When the epoxy resin coating was completely dry, the above steps were repeated and proportions were added to prepare a polyurethane resin coating on the surface of the epoxy primer. The total thickness of the anticorrosive coating was about 150 μm. The anticorrosive coating doped with nonreduced graphene oxide was prepared in the same way as a blank comparison reference.

2.3. Characterization. A scanning electron microscope (7900F) was used to observe the microscopic morphology of the coating cross-section; a Raman spectrometer (wavelength 532 nm) was used to measure the Raman spectrum of the coating to study the microstructure of the reduced graphene in the coating; an Autolab PGSTAT 302N electrochemical workstation (Switzerland Wantong) was used to determine the polarization curve and the AC impedance of the anticorrosion coating to analyze the corrosion resistance of the anticorrosion coating and the change of the law of the corrosion resistance of the graphene-modified anticorrosion coating after being soaked in 3.5% NaCl. NOVA software

Table 1: 7075-T6 aluminum alloy composition.

Composition	Zn	Mg	Cu	Si	Fe	Mn	Cr	Ti	Al	Else
Percentage (%)	5.6	2.5	1.4	0.35	0.42	0.29	0.22	0.1	Margin	0.15

was used to fit the electrochemical curve to draw the equivalent circuit. It had to be connected to the copper wire and then sealed with epoxy resin before being tested. The exposed coating area was fixed to 1 cm^2. The electrochemical measurement selected a three-electrode system: 10×10 mm. The platinum sheet was the counter electrode, the saturated calomel electrode was the reference electrode, the polarization curve test interval was relative to the self-corrosion point ± 150 mV, the scanning speed was 1 mV/s, the AC impedance test (EIS) sine wave frequency range was 0.01 Hz ~100000 Hz, and the load AC disturbance voltage amplitude was 10 mV.

3. Results and Discussion

3.1. Morphology of rGO in Anticorrosion Coatings. There are three characteristic peaks in the Raman spectrum of melene: the D peak (near 1350 cm^{-1}), the G peak (near 1580 cm^{-1}), and the 2D peak (near 2690 cm^{-1}). Peak D is a defect peak and requires at least one defect to activate; the 2D peak of a single-layer graphene is located near 2690 cm^{-1}. It is sharp, and its intensity is about 4 times that of peak G. As the number of graphene layers increases, its position will shift to the right. The peak intensity decreases, and the peak width grows. When the graphene sheet reaches more than ten layers, its 2D peak shape is basically the same as graphite, but the 2D peak of graphite is composed of two peaks, 2D1 and 2D2, and the peak intensity is about 1/4 and 1/2 of the G peak [10].

F431 is a dispersant, and the Raman spectrum of the graphene-modified anticorrosive coating with 0.2% rGO addition is shown in Figure 1. It can be seen from Figure 1 that the intensity of the D peak is higher, indicating more rGO edges and defects; I2D : IG is 1 : 1, indicating that the dopant is rGO with more layers instead of graphite. This is due to the strong van der Waals force on the surface of rGO that makes rGO agglomerate inside the coating, which is consistent with the phenomenon observed by the scanning electron microscopy [11].

3.2. Morphology of Anticorrosion Coatings. Figures 2(a)–2(d) show the microscopic cross-sectional morphology of graphene-modified anticorrosion coatings with rGO additions of 0.2%, 0.4%, 0.6%, and 0.8%. It can be seen from Figures 2(a)–2(c) that there are fewer pores in the cross-section of the epoxy primer when less than 0.6 of rGO is added, which indicates that a small amount of rGO can effectively improve the pores in the epoxy primer. As the corrosion progresses, it can effectively prevent the intrusion of water molecules, chloride ions, and other corrosive media; reduce the accumulation of corrosive ions; greatly reduce the amount of "water" in the graphene-modified anticorrosive coating; and increase the probability of forming an "air passage"; and the pores in the epoxy primer cross-section increase sharply with 0.8% of rGO [12, 13]. As the corrosion progresses, the corrosive media accumulate in the pores, reducing the graphene-modified anticorrosive coating. The corrosion resistance of the layer accelerates the corrosion of the aluminum alloy substrate, and the dispersion of rGO in the cross-section of the polyurethane resin topcoat in each graphene-modified anticorrosive coating is relatively uniform. No microcracks appear as the amount of rGO is increased. The rGO in the anticorrosive coating can accelerate the electron transfer speed in the corrosion process, increase the conduction path of electrons, and effectively utilize the anticorrosive filler in the polyurethane resin topcoat [14, 15].

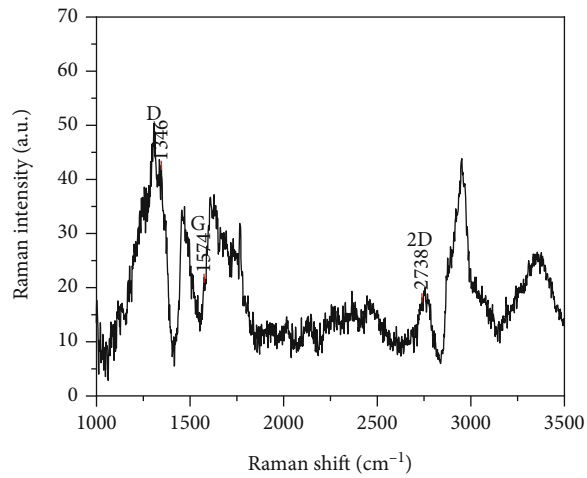

Figure 1: Raman of graphene-modified coatings.

The statistical results of the porosity of the graphene-modified anticorrosive coatings with 0.2%, 0.4%, 0.6, and 0.8% of the coatings in the prepared state and with F431 as the dispersant and 0.8%, respectively, are shown in Table 2 using Image-Pro software. It can be seen that the porosity of the primer coating tended to first decrease and then increase when less than 0.6% of rGO was added. The porosity of the primer coating was smallest at 0.12% when 0.6% of rGO was added, and the topcoat was defective when 0.8% of rGO was added [16]. This shows that the dispersion of rGO in the coating affects its microscopic morphology. The better the dispersion effect of rGO, the greater the effect of its microlamellar structure. The addition of an excessive amount of rGO will cause the rGO agglomeration phenomenon to continue to increase until the graphene-modified anticorrosion coating becomes defective, thereby reducing its ability to resist corrosion [17].

3.3. Electroactivity of Anticorrosion Coatings. The polarization curves of the prepared state and F431 as a dispersant with rGO at 0.2%, 0.4%, 0.6%, and 0.8% graphene-modified

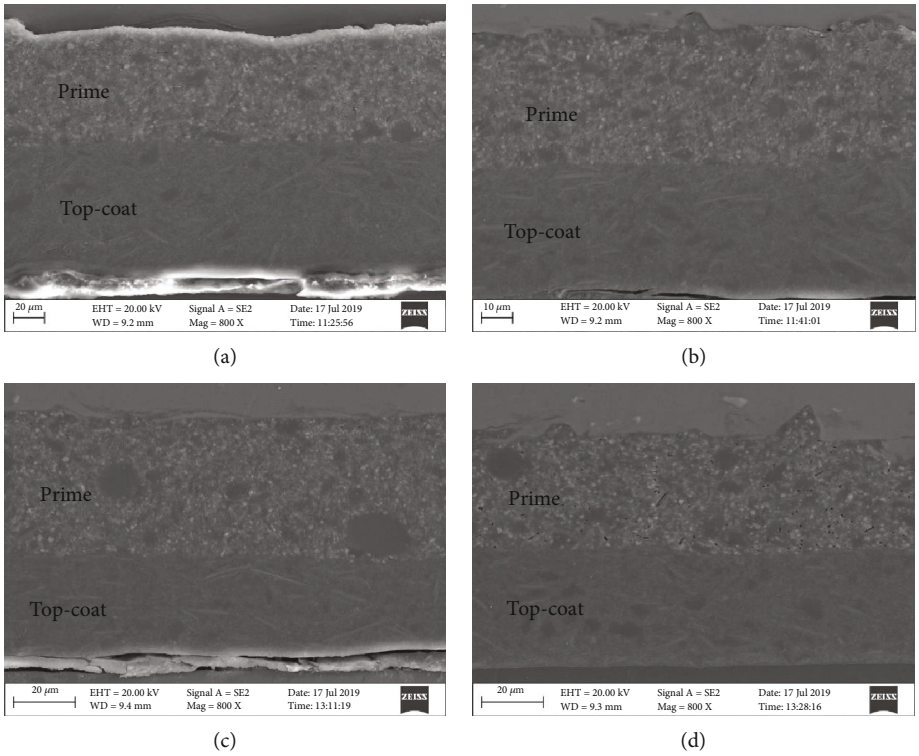

Figure 2: SEM of graphite-modified anticorrosive coatings with different percentages of rGO dispersed by F431 (a–d); the additional rGO are 0.2%, 0.4%, 0.6%, and 0.8%.

Table 2: Porosity of original and graphene-modified coatings.

Coatings	rGO-0.2%	rGO-0.4%	rGO-0.6%	rGO-0.8%
Porosity (%)	0.18	0.12	0.05	0.63

anticorrosive coating are shown in Figure 3. The size of the self-corrosion potential shows the degree of difficulty of its corrosion, and the self-corrosion current density is an important basis for characterizing its resistance to corrosion [18]. It can be seen from Figure 3 that the self-corrosion potential of the coating first appears with an increase in the amount of rGO. After the movement, the negative trend reached the most positive value when the amount of rGO was 0.6%, which was -0.19 V. Then, the corrosion potential quickly became negative at -0.65 V with the increase in the amount of rGO. The excellent conductivity of rGO accelerated the circulation of the electrons, increased the conduction path of the electrons inside the coating, and changed the oxide film on the aluminum alloy surface during the polarization process, which hindered the anode reaction to varying degrees (dissolution of the aluminum alloy matrix) and the cathodic reaction (oxygen absorption corrosion), leading to changes in the anode Tafel slope and the cathode Tafel slope, resulting in a positive or negative shift of the potential of self-corrosion [19, 20].

The results of the Tafel curve fitting using Nova software are shown in Table 3, where b_a was the Tafel slope of the anode, b_c was the Tafel slope of the cathode, and R_p was the polarization resistance calculated based on a ratio of 3.1. It can be seen from the fitting data in Table 3 that the

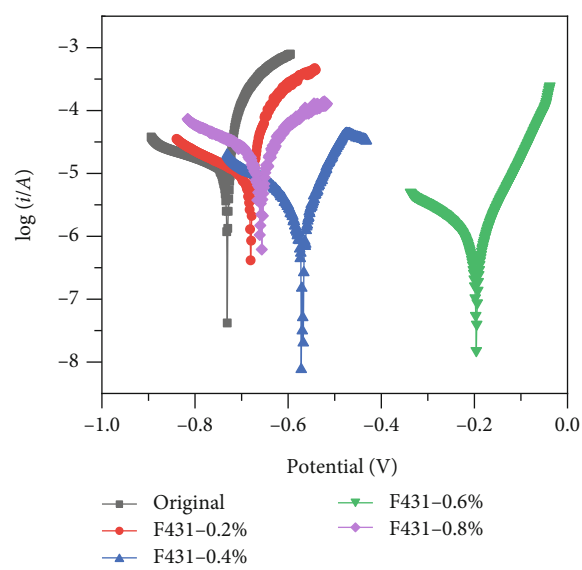

Figure 3: Tafel curves of original and graphene additions of 0.2%, 0.4%, 0.6%, and 0.8% anticorrosion coatings. Original, no graphene added.

coating self-corrosion current density decreased and the polarization resistance value increased when the addition of rGO increased. The self-corrosion current density (J_{corr}) reaches the minimum when 0.6% of rGO was added, the value was 1.19×10^{-7} A/cm^2, and the polarization resistance was the largest at 29831 Ω. The self-corrosion current density

Table 3: Results of Tafel curve fitting.

	E_{corr} (V)	J_{corr} (A/cm^2)	b_a	b_c	R_p (Ω)
Original	-0.7313	2.147×10^{-6}	0.012724	0.007797	977.8
F431-0.2%	-0.6805	1.580×10^{-6}	0.008116	0.009737	1220.8
F431-0.4%	-0.56789	4.633×10^{-7}	0.017767	0.033082	10836
F431-0.6%	-0.1956	1.190×10^{-7}	0.014154	0.019352	29831
F431-0.8%	-0.6592	1.758×10^{-6}	0.013298	0.013453	1651.9

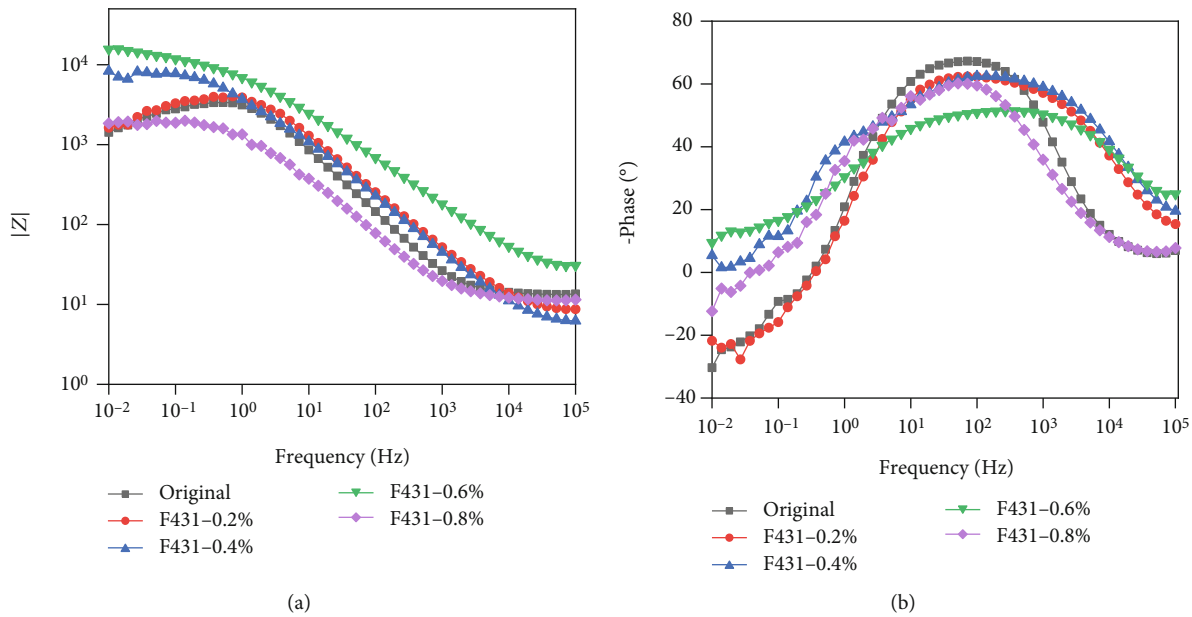

Figure 4: Bode of original and graphene additions of 0.2%, 0.4%, 0.6%, and 0.8% to anticorrosion coatings.

(J_{corr}) increased to 1.75×10^{-6} A/cm^2 when 0.8% of rGO was added, the polarization resistance value decreased to 1657.9 Ω, and the corrosion resistance of the graphene-modified anticorrosion coating dropped sharply. This is because the addition of rGO increases the conduction path of the electrons in the anticorrosion coating, thereby increasing its corrosion resistance performance. When 0.8% of rGO is added, it will accumulate in the coating to form a conductive path to connect to the external corrosive environment and accelerate the exchange of electrons between the aluminum alloy surface and the metal ions in the corrosive environment, thereby reducing the corrosion resistance of the coating performance [20, 21].

$$R_p = \frac{b_a/b_c}{2.303(b_a + b_c)J_{corr}}. \quad (1)$$

The Bode curves of the prepared state and F431 as a dispersant with the addition of rGO at 0.2%, 0.4%, 0.6%, and 0.8% to the graphene-modified anticorrosive coating are shown in Figure 4. It can be seen from Figure 4(a) that the impedance modulus value of the graphene-modified anticorrosive coating is at low frequency when F447 is used as the dispersant and the amount of rGO added is increased from 0.2% to 0.8%. $|Z|$ shows a tendency to increase first and then decrease. When the amount of rGO added is 0.6%, the impedance modulus value at low frequency is the largest, about 105, indicating that the corrosion resistance of the anticorrosive coating is the best at this time, and the polarization curve results are consistent [22, 23].

The prepared state and F431 as a dispersant and the Nyquist curve of the graphene-modified anticorrosion coating with 0.2%, 0.4%, 0.6%, and 0.8% of added rGO are shown in Figure 5, and the equivalent circuit was analyzed using Nova software. The middle components are fitted (Figure 6(a) is the equivalent circuit diagram of the prepared state when the amount of rGO is 0.2% and 0.8%, and Figure 6(b) is the equivalent circuit diagram when the amount of rGO is 0.4% and 0.6%); R_s is the solution resistance; Q_{dl} is the constant phase angle element; R_{ct} is the coating resistance; L is the inductance caused by pitting corrosion; R_m is the oxide film resistance, and the equivalent circuit component values are shown in Table 4. It can be seen by combining the AC impedance spectroscopy with the fitted coating resistance

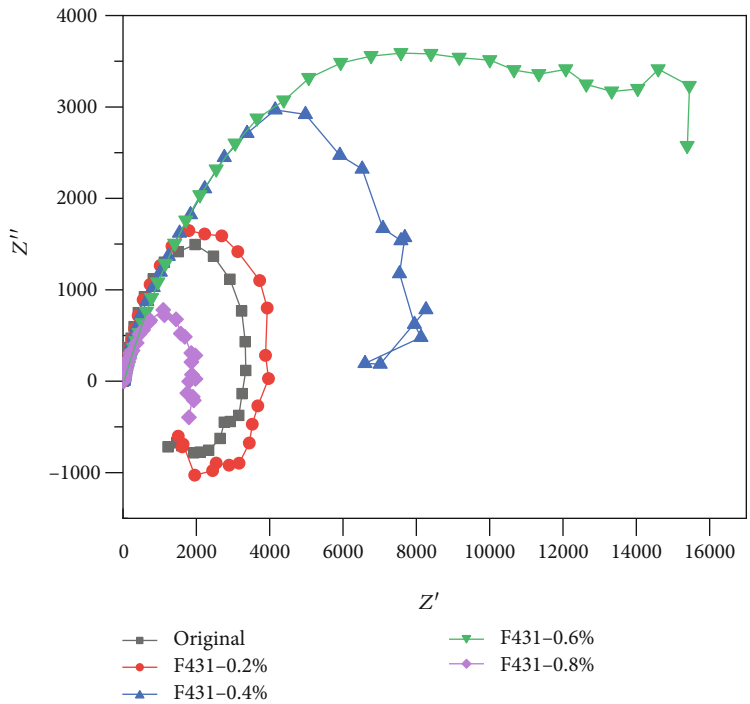

Figure 5: Nyquist of original and graphene additions of 0.2%, 0.4%, 0.6%, and 0.8% anticorrosion coatings. Original, no added graphene; (1–4) 0.2%, 0.4%, 0.6%, and 0.8% added graphene.

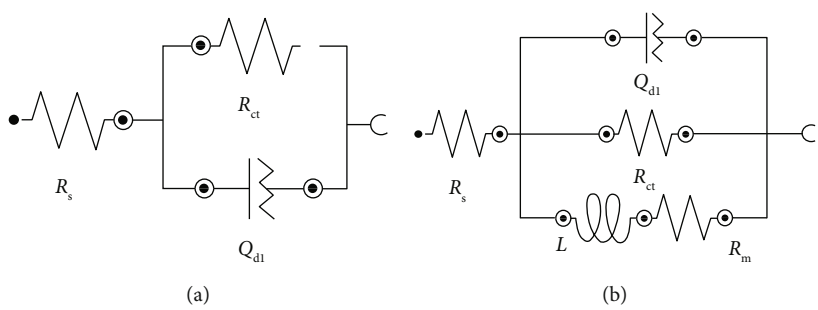

Figure 6: Equivalent circuit diagram.

Table 4: Fitting data of equivalent circuit components.

Coatings	R_s (Ω)	R_{ct} (Ω)	Q_{dl} Y_0	Q_{dl} N
Original	13.372	2230.4	2.614×10^{-5}	0.870
F431-0.2%	8.072	2532.1	2.410×10^{-5}	0.776
F431-0.4%	4.749	8177.1	4.857×10^{-5}	0.704
F431-0.6%	17.863	15517.0	3.212×10^{-5}	0.595
F431-0.8%	10.944	1957.7	1.147×10^{-4}	0.744

data that F431 is a dispersant, and the capacitive arc radius in the Nyquist curve first increases and then decreases when the amount of rGO is increased from 0.2% to 0.8%. The capacitive arc radius is the largest when the amount of rGO is 0.6%. At this time, the resistance of the graphene-modified anticorrosion coating is 15517 Ω, and the graphene-modified anticorrosion coating has better corrosion resistance, which is consistent with the polarization curve. The inductive arc resistance appears in the Nyquist curve in the preparation state and the addition of rGO at 0.2% and 0.8%, indicating that the corrosion ion Cl^- has appeared on the surface of the oxide film of the aluminum alloy substrate [24, 25].

4. Conclusions

(1) The excellent microsheet structure of graphene improves defective anticorrosive coating. The porosity of the graphene-modified anticorrosive coating is the smallest when 0.6% of rGO is added. The agglomeration of rGO becomes serious as more is added, and rGO with low surface energy cannot be fully mixed with organic coatings; therefore, new defects will occur after the coating has been cured

(2) The self-corrosion current density (J_{corr}) of the graphene-modified anticorrosive coating is the smallest (1.190×10^{-7} A/cm^2) when 0.06% of rGO is added, and the impedance modulus ($|Z|$) is the largest (10^4). In terms of the capacitive reactance, the arc radius is the largest, and the coating resistance is the largest (15517 Ω) after fitting. The corrosion resistance is the best at this time, mainly because the graphene is doped into the coating, extending the conduction path of electrons inside the coating, increasing the resistance of the coating, and decelerating corrosion

(3) The rGO agglomeration phenomenon in the graphene-modified anticorrosive coating is serious when 0.8% of rGO is added, the coating defects increase, the self-corrosion current density (J_{corr}) is larger (1.758×10^{-6} A/cm^2), and the coating is resistant. The corrosion performance is poor, but its dispersion coefficient is large, and it has a good physical insulation performance. Its corrosion resistance is reduced mainly because the agglomeration of rGO makes the aluminum alloy matrix, and the external corrosive environment forms a highly conductive circuit, thereby accelerating the corrosion of the aluminum alloy matrix

Data Availability

The data used to support the findings of this study are available from the corresponding author upon request.

Conflicts of Interest

The authors declare no conflict of interest.

References

[1] V. K. Beura, C. Kale, S. Srinivasan, C. L. Williams, and K. N. Solanki, "Corrosion behavior of a dynamically deformed Al-Mg alloy," *Electrochimica Acta*, vol. 354, article 136695, 2020.

[2] H. Zhu, L. Yue, C. Zhuang et al., "Fabrication and characterization of self-assembled graphene oxide/silane coatings for corrosion resistance," *Surface & Coatings Technology*, vol. 304, pp. 76–84, 2016.

[3] J. Mondal, L. Aarik, J. Kozlova et al., "Functionalization of Titanium Alloy Surface by graphene and Metal Oxides: Corrosion Inhibition," *Journal of Nanoscience and Nanotechnology*, vol. 15, no. 9, pp. 6533–6540, 2015.

[4] B. Zhang, V. R. Patlolla, D. Chiao, D. K. Kalla, H. Misak, and R. Asmatulu, "Galvanic corrosion of Al/Cu meshes with carbon fibers and graphene and ITO-based nanocomposite coatings as alternative approaches for lightning strikes," *The International Journal of Advanced Manufacturing Technology*, vol. 67, no. 5-8, pp. 1317–1323, 2013.

[5] S. Pourhashem, A. Rashidi, M. R. Vaezi, and M. R. Bagherzadeh, "Excellent corrosion protection performance of epoxy composite coatings filled with amino-silane functionalized graphene oxide," *Surface & Coatings Technology*, vol. 317, pp. 1–9, 2017.

[6] Y. Ye, D. Zhang, T. Liu et al., "Superior corrosion resistance and self-healable epoxy coating pigmented with silanzied trianiline-intercalated graphene," *Carbon*, vol. 142, pp. 164–176, 2019.

[7] P. C. Uzoma, F. Liu, L. Xu et al., "Superhydrophobicity, conductivity and anticorrosion of robust siloxane-acrylic coatings modified with graphene nanosheets," *Progress in Organic Coatings*, vol. 127, pp. 239–251, 2019.

[8] S. Syed, "Influence of the environment on atmospheric corrosion of aluminium," *Corrosion Engineering, Science and Technology*, vol. 45, no. 4, pp. 282–287, 2013.

[9] P. A. Okafor, J. Singh-Beemat, and J. O. Iroh, "Thermomechanical and corrosion inhibition properties of graphene/epoxy ester–siloxane–urea hybrid polymer nanocomposites," *Progress in Organic Coatings*, vol. 88, pp. 237–244, 2015.

[10] L. Cancado, K. Takai, T. Enoki et al., "General equation for the determination of the crystallite size La of nanographite by Raman spectroscopy," *Applied Physics Letters*, vol. 88, no. 16, pp. 163106–163113, 2006.

[11] R. R. Laleh, H. Savaloni, F. Abdi, and Y. Abdi, "Corrosion inhibition enhancement of Al alloy by graphene oxide coating in NaCl solution," *Progress in Organic Coatings*, vol. 127, pp. 300–307, 2019.

[12] S. Nezamdoust and D. Seifzadeh, "rGO@APTES/hybrid sol-gel nanocomposite for corrosion protection of 2024 aluminum alloy," *Progress in Organic Coatings*, vol. 109, pp. 1–9, 2017.

[13] L. Xiong, J. Liu, M. Yu, and S. Li, "Improving the corrosion protection properties of PVB coating by using salicylaldehyde@ZIF-8/graphene oxide two-dimensional nanocomposites," *Corrosion Science*, vol. 146, pp. 30386–30410, 2018.

[14] S. Asaldoust and B. Ramezanzadeh, "Synthesis and characterization of a high-quality nanocontainer based on benzimidazole-zinc phosphate (ZP-BIM) tailored graphene oxides; a facile approach to fabricating a smart self-healing anti-corrosion system," *Journal of Colloid and Interface Science*, vol. 564, pp. 230–244, 2020.

[15] A. K. Behera, R. Chandran, S. Sarkar, and A. Mallik, "An exploration on the use of in-house synthesized reduced few layer graphene particles as a reinforcement during sono-electroplating of Cu matrix composite films," *Journal of Alloys and Compounds*, vol. 817, p. 152713, 2020.

[16] W. Chang, P. Wang, Y. Zhao, C. Ren, B. N. Popov, and C. Li, "Characterizing corrosion properties of graphene barrier layers deposited on polycrystalline metals," *Surface & Coatings Technology*, vol. 398, p. 126077, 2020.

[17] D. S. Chauhan, M. A. Quraishi, K. R. Ansari, and T. A. Saleh, "Graphene and graphene oxide as new class of materials for corrosion control and protection: Present status and future scenario," *Progress in Organic Coatings*, vol. 147, p. 105741, 2020.

[18] Y. Ding, J. Zhong, P. Xie et al., "Protection of Mild Steel by Waterborne Epoxy Coatings Incorporation of Nanowires/-Graphene," *Polymers*, vol. 11, no. 12, p. 1998, 2019.

[19] S. Chhetri, S. Ghosh, P. Samanta, N. C. Murmu, and T. Kuila, "Effect of Fe3O4-decorated N-doped reduced graphene oxide nanohybrid on the anticorrosion performance of epoxy composite coating," *ChemistrySelect*, vol. 4, no. 46, pp. 13446–13454, 2019.

[20] A. Dehghani, G. Bahlakeh, and B. Ramezanzadeh, "Designing a novel targeted-release nano-container based on the silanized graphene oxide decorated with cerium acetylacetonate loaded

beta-cyclodextrin (β -CD-CeA-MGO) for epoxy anti-corrosion coating," *Chemical Engineering Journal*, vol. 400, pp. 89548–89563, 2020.

[21] L. T. Duy and H. Seo, "Construction of stretchable supercapacitors using graphene hybrid hydrogels and corrosion-resistant silver nanowire current collectors," *Applied Surface Science*, vol. 521, p. 146467, 2020.

[22] A. A. Javidparvar, R. Naderi, and B. Ramezanzadeh, "Manipulating graphene oxide nanocontainer with benzimidazole and cerium ions: application in epoxy-based nanocomposite for active corrosion protection," *Corrosion Science*, vol. 165, pp. 1–61, 2020.

[23] Q. Liu, X. Zhang, W. Zhou et al., "Improved anti-corrosion behaviour of an inorganic passive film on hot-dip galvanised steel by modified graphene oxide incorporation," *Corrosion Science*, vol. 174, p. 108846, 2020.

[24] K. K. Pandey, A. Islam, R. Kumar, R. Ghosh, V. Arjunan, and A. K. Keshri, "Role of the hybrid addition of carbon nanotubes and graphene nanoplatelets on the corrosion behavior of plasma-sprayed aluminum oxide nanocomposite coating," *Advanced Engineering Materials*, vol. 22, no. 3, pp. 1–9, 2020.

[25] Q. Zhu, E. Li, X. Liu et al., "Epoxy coating with in-situ synthesis of polypyrrole functionalized graphene oxide for enhanced anticorrosive performance," *Progress in Organic Coatings*, vol. 140, pp. 1–23, 2020.

Hindawi
International Journal of Photoenergy
Volume 2020, Article ID 8818136, 7 pages
https://doi.org/10.1155/2020/8818136

Research Article

Study on the Creep Behavior of a Ni_3Al-Based Single Crystal Alloy at 850°C/450 MPa

Liwu Jiang,[1,2] **Yu Yang**,[1] **Meiling Wu**,[3] **and Min Cai**[4]

[1]*National Center for Materials Service Safety, University of Science and Technology Beijing, Beijing 100083, China*
[2]*NCS Testing Technology Co., Ltd., Beijing 100081, China*
[3]*Beijing Institute of Aeronautical Materials, Beijing 100095, China*
[4]*Avic Manufacturing Technology Institute, Beijing 100024, China*

Correspondence should be addressed to Liwu Jiang; lwjiang@ustb.edu.cn

Received 13 August 2020; Revised 21 September 2020; Accepted 22 September 2020; Published 13 October 2020

Academic Editor: Yimin Wu

The creep behaviors of Ni_3Al-based single crystal alloy IC6SX with [001] and [111] orientations under the condition of 850°C/450 MPa were investigated. The effect of crystal orientation on the creep lives, fracture morphology, fracture mechanism, and dislocation evolution of the alloys with different orientations was analyzed systematically. The results showed that the creep lives of the alloy were closely related to the crystal orientation under the condition of 850°C/450 MPa. The creep lives of the single crystal alloys with [001] and [111] orientations were 56.3 h and 126.9 h, respectively. Moreover, the fracture morphologies of the two alloys with [001] and [111] orientations were different. The results showed that some holes formed at the fracture surface of the alloy with [111] rather than [001] orientation. Furthermore, the surface near the fracture of the two alloys with [001] and [111] orientations was serrated. Therefore, the fracture mechanism of the single crystal alloys with [001] and [111] orientations was ductile fracture. In addition, a large number of dislocations cut into the γ' phase. Therefore, the cutting mechanism of dislocations in the alloys with [001] and [111] orientations was the creep deformation mechanism.

1. Introduction

With the development of the turbine vanes of aero-engines, the working temperature and content of precious metals of superalloy turbine blades are increased continuously [1–6]. Ni_3Al-based single crystal alloy has the following advantages, such as low density, strong oxidation resistance, stable structure, and strong creep resistance. Therefore, the alloy has become the most potential material for turbine blades [7–13].

Gui found that the creep resistance of Ni-based single crystal alloy with [111] orientation was better than that with [001] orientation from 1000°C to 1100°C [14]. Other studies showed that the creep resistance and creep rate of Ni-based single crystal alloys with different orientations were different [15–20]. The creep properties of single crystal alloy DD6 were studied by Wang et al. [21]. They pointed that, under the same test condition, the creep life of single crystal alloy DD6 decreased in order of [111], [001] and [011] orientations at 760°C, which was consistent with alloy DD499 under the condition of 1040°C/165 MPa [22]. Su and Tian showed the effect of the crystal orientation on the microstructure of Ni-based single crystal alloy. It was found that the γ' phases of the single crystal alloys with [001], [011] and [111] orientations were transformed into N-type rafted structure, stripe-like rafted structure, and mesh-like rafted structure under 1040°C/137 MPa, respectively [23, 24]. It has also been found that the dendrite morphologies, fracture mechanism, and dislocation evolution of Ni-based single crystal alloys with different orientations were different [25–30]. It is necessary to investigate the creep lives, fracture morphology, and dislocation evolution of the single crystal alloy IC6SX with different crystal orientations.

In this paper, the relationship between creep properties and crystal orientation of Ni_3Al-based single crystal alloy IC6SX at 850°C/450 MPa has been explored. The fracture mechanism, microstructure, and dislocation evolution of

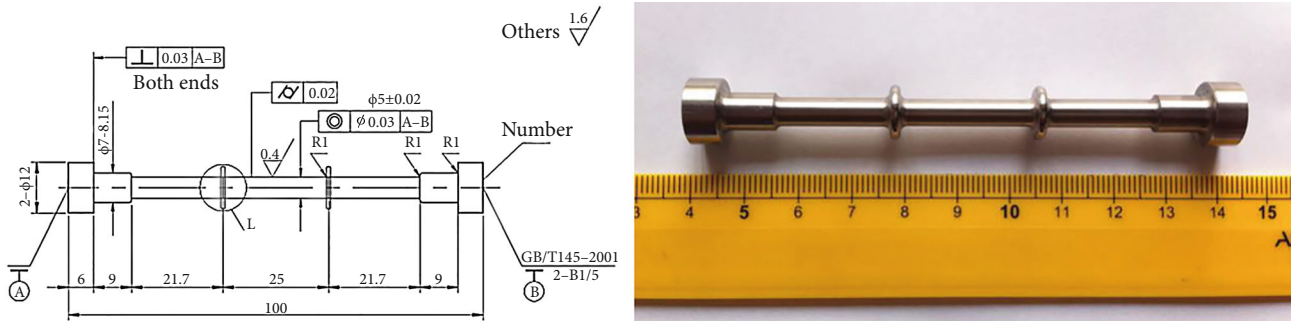

Figure 1: Schematic diagram of processed creep specimen and photo of high-temperature creep specimen.

the Ni_3Al-based single crystal alloys with different orientations were investigated, providing a theoretical basis for the application of Ni_3Al-based single crystal alloy IC6SX.

2. Experimental

The material used for the present study was a Ni_3Al-based single crystal alloy IC6SX, with a nominal composition of Ni-7.4~8.0Al-13.5~14.3Mo-0.02~0.03B (wt%). The single crystal alloy test bars with different crystal orientations were produced by screw selection crystal method in the DZG-0.025 directional solidification furnace. All the test bars were calibrated for crystal orientation by X-ray backscattering Laue method. The bars with orientation deviation less than 10° and without defects were selected for experimental study.

Figure 1 shows that the single crystal alloy was processed into a high-temperature creep specimen after the heat treatment under the condition of 1260°C/10 h + 870°C/32 h. The uniaxial constant load tensile creep tests for the single crystal alloys with [001] and [111] orientations were carried out under the condition of 850°C/450 MPa by the GWT504 high-temperature durable creep testing machine.

The microstructure of creep specimens was analyzed by the ZEISS Axio Imager A2m optical microscope (OM) and ZEISS SUPRA55 scanning electron microscope (SEM). The dislocation morphology of creep specimens was investigated by the Tecnai F30 transmission electron microscope (TEM).

3. Results and Discussion

3.1. Effect of Crystal Orientation on Creep Properties of Single Crystal Alloy. Figure 2 shows the creep curves of the single crystal alloy IC6SX with [001] and [111] orientations at 850°C/450 MPa, and the partial enlarged graph of the region marked by the arrow is shown in the top left corner.

It can be seen from Figure 2 that the creep curves of the single crystal alloy IC6SX were composed of the transient primary creep stage, steady creep stage, and accelerating creep stage. The initial strain of the single crystal alloys with [001] and [111] orientations at 850°C/450 MPa were 0.44% and 0.14%, respectively. The creep lives of the single crystal alloys with [001] and [111] orientations were 56.3 h and 126.9 h, respectively. The minimum steady creep rate of the alloys with [001] and [111] orientations were 1.03×10^{-5} and 1.04×10^{-5}, respectively. The elongation of the alloys

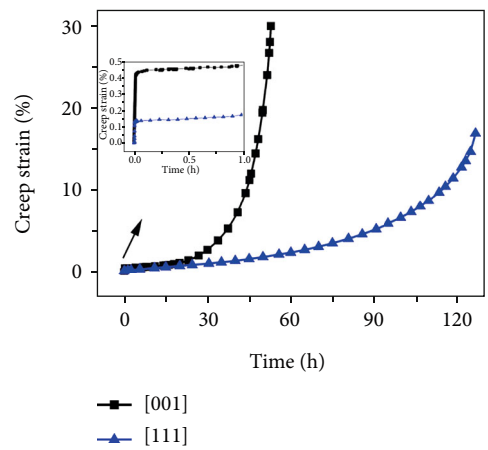

Figure 2: Creep curves of the single crystal alloy IC6SX with [001] and [111] orientations at 850°C/450 MPa.

with [001] and [111] orientations were 31.0% and 19.5%, respectively. Compared with the single crystal alloy with [001] orientation, the creep life of the alloy with [111] orientation was obviously increased, while the elongation was obviously decreased.

3.2. Fracture Morphology and Longitudinal Section Microstructure of Single Crystal Alloys with Different Orientations after Creep Test

3.2.1. Single Crystal Alloy with [001] Orientation. Figure 3 shows the sample photo and the fracture morphology of the single crystal alloy IC6SX with [001] orientation after being crept for 56.3 h and then up to fracture at 850°C/450 MPa.

Figure 3(a) shows that positions A, B, C, and D were the exposed core, transition section B, transition section C, and gauge length of the creep specimen, respectively. As shown in Figure 3(a), in the three positions A, B, and C which were outside the gauge length, there was no obvious deformation. However, a certain degree of the plastic deformation occurred in position D. The surface of the specimen was slightly black and green, which indicated that the surface of the specimen had a slight degree of oxidation in the process of creep. In Figure 3(b), the fracture shape of the specimen changed from circle to ellipse, with the ellipticity (major axis : minor axis) of 1.5. Figure 3(c) is a partial enlarged picture of position A in Figure 3(b), showing a certain number

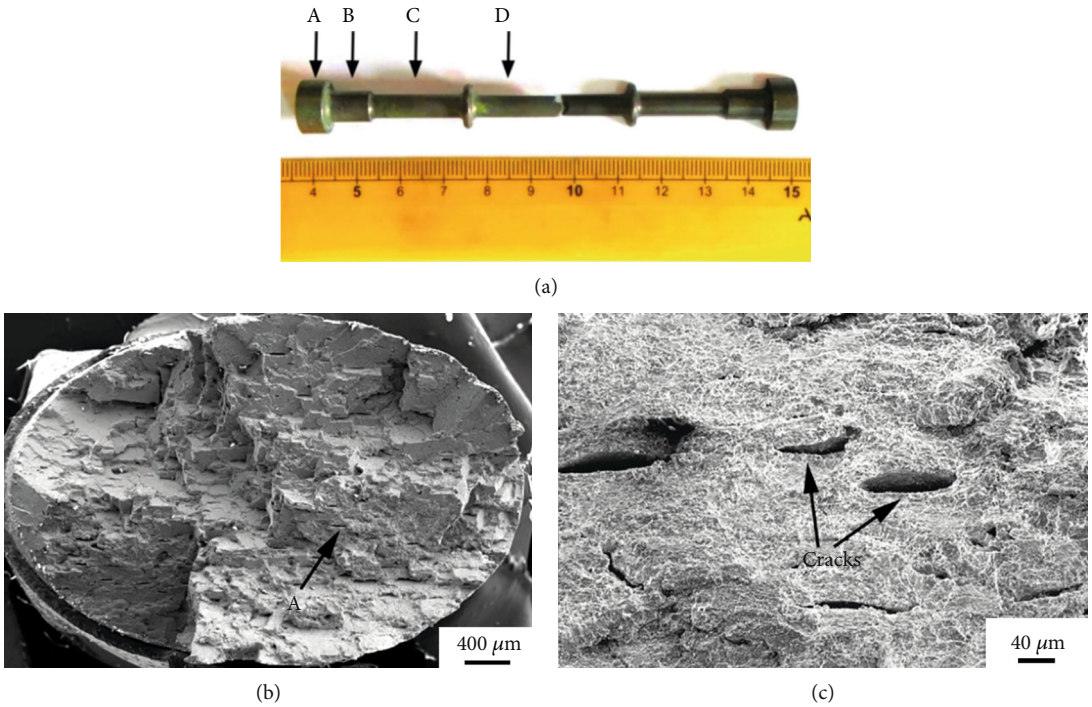

Figure 3: Sample photo and SEM images of the fracture morphology of the single crystal alloy IC6SX with [001] orientation after being crept for 56.3 h and then up to fracture at 850°C/450 MPa. (a) Fracture specimen photo; (b) low multiple fracture morphology; (c) partial enlarged image of position A from (b).

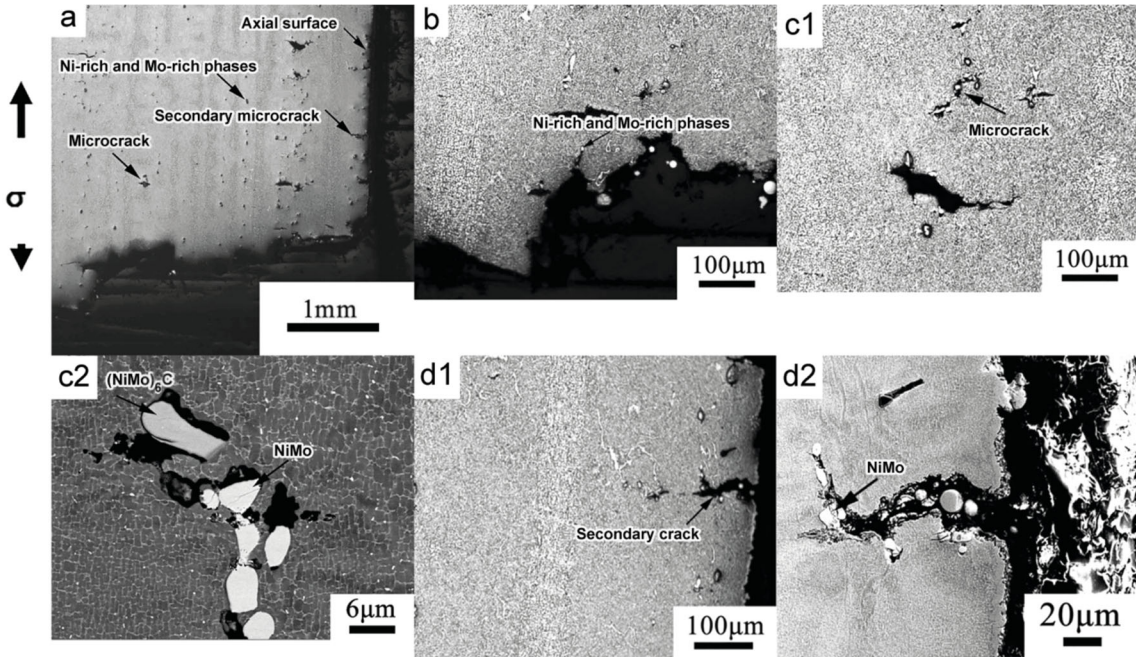

Figure 4: Microstructures of the fracture longitudinal section of the single crystal alloy IC6SX with [001] orientation after being crept for 56.3 h and then up to fracture at 850°C/450 MPa. (a) Macroscopic metallographic structure (OM image); (b) fracture surface cracks (OM image); (c1) microcracks in the interior of the matrix (OM image); (c2) microcracks in the interior of the matrix (SEM image); (d1) secondary crack on the axial surface (OM image); (d2) secondary crack on the axial surface (SEM image).

of cracks on the fracture surface, as shown by the arrow in Figure 3(c).

Figure 4 shows the microstructures of the fracture longitudinal section of the single crystal alloy IC6SX with [001] orientation after being crept for 56.3 h and then up to fracture under the condition of 850°C/450 MPa. It can be seen from Figure 4(a) that creep fracture edge of the single crystal alloy with [001] orientation was approximately

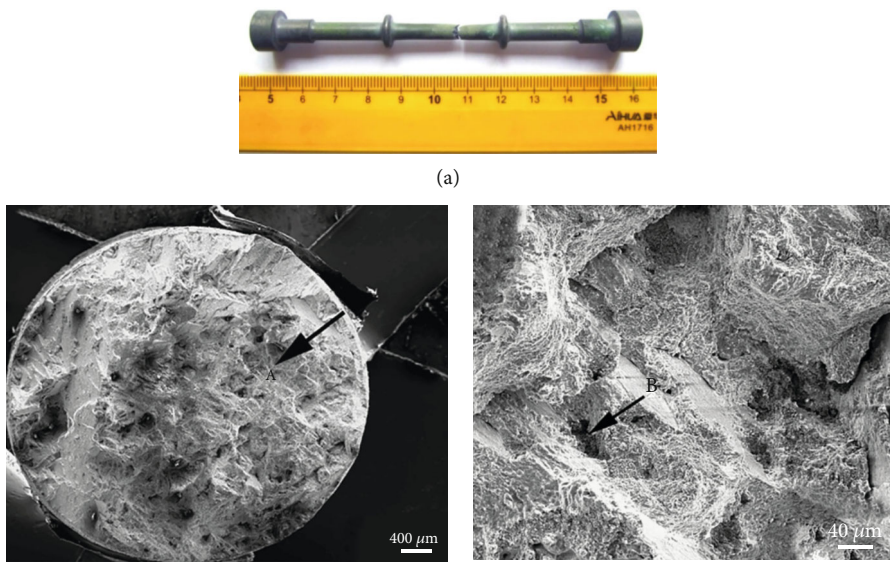

Figure 5: Sample photo and SEM images of fracture morphology of the single crystal alloy IC6SX with [111] orientation after being crept for 126.9 h and then up to fracture at 850°C/450 MPa. (a) Fracture specimen photo; (b) low multiple fracture morphology; (c) partial enlarged image of position A from (b).

perpendicular to the stress axis. The analysis of the macroscopic metallographic structure showed that a large number of microcracks existed at the region near the fracture in the interior of the specimen. In addition, the microcracks, which were distributed along the growth orientation of [001], formed at Ni-rich and Mo-rich phases in the interdendrite region. With the increase of the distance to the fracture surface, the number and size of microcracks decreased gradually. Furthermore, there were a certain number of secondary cracks on the axial surface, and the length of the secondary cracks decreased gradually from the surface near the fracture to the interior of the specimen. Moreover, the directions of microcracks and secondary cracks were perpendicular to the stress axis. From Figure 4(b), it was found that the surface near the fracture was serrated, showing ductile fracture, and the surface cracks near the fracture propagated along the Ni-rich and Mo-rich phases from the fracture to the interior of the alloy. Figures 4(c1) and 4(c2), respectively, show the optical image and SEM image of microcracks within the matrix near the fracture. In addition, Figure 4(c1) indicates that microcracks formed in the interior of the alloy near the fracture. These microcracks generated, connected, and grew at the interface between the Ni-rich, Mo-rich and the matrix, as shown in Figure 4(c2). Figures 4(d1) and 4(d2) show the optical image and SEM image of the surface secondary crack near the fracture, respectively. It can be seen from Figure 4(d1) that under the action of tensile stress the secondary cracks along the axial surface were perpendicular to the stress axial and propagated to the interior of the specimen. Due to the existence of Ni-rich and Mo-rich phases near the axial surface in the alloy, the direction of the secondary cracks changed. Moreover, the secondary cracks connected with the microcracks around the Ni-rich and Mo-rich phases, as shown in Figure 4(d2).

3.2.2. Single Crystal Alloy with [111] Orientation. Figure 5 shows the sample photo and the fracture morphology of the single crystal alloy IC6SX with [111] orientation after being crept for 126.9 h and then up to fracture at 850°C/450 MPa.

It can be seen from Figure 5(b) that the fracture shape of the specimen was approximately circle, and the enlarged photo of position A is shown in Figure 5(c). Figure 5(c) indicates that there were some holes in the fracture surface, as shown by arrow B in Figure 5(c).

Figure 6 indicates the microstructures of fracture longitudinal section of the single crystal alloy IC6SX with [111] orientation after being crept for 126.9 h and then up to fracture at 850°C/450 MPa. It can be seen from Figure 6(a) that the angle between the creep fracture edge of the alloy and the stress axis was about 45°. The analysis of the macroscopic metallographic structure showed that within the specimen a certain number of microcracks existed at the region near the fracture. In addition, the microcracks formed in the interdendritic region of the Ni-rich and Mo-rich phases and were distributed diffusely. The number and the size of microcracks decreased gradually from the fracture surface to the interior of the specimen. There was a certain angle between the direction of the microcracks and the stress axis. A few secondary cracks with the small length existed on the axial surface. Figure 6(b) is the enlarged picture of region A in Figure 6(a). Figure 6(b) indicates that the surface near the fracture was serrated, which was a ductile fracture. In addition, the surface crack near the fracture propagated to the interior of the specimen along the Ni-rich, Mo-rich phases and dendritic arm. Figures 6(c1) and 6(c2) show the optical image and SEM image of internal microcracks within the matrix near the fracture surface, respectively. In addition, Figure 6(c1) indicates that a few microcracks formed in the alloy near the fracture, and Figure 6(c2) shows that the cracks generated, connected, and grew at the interface between the

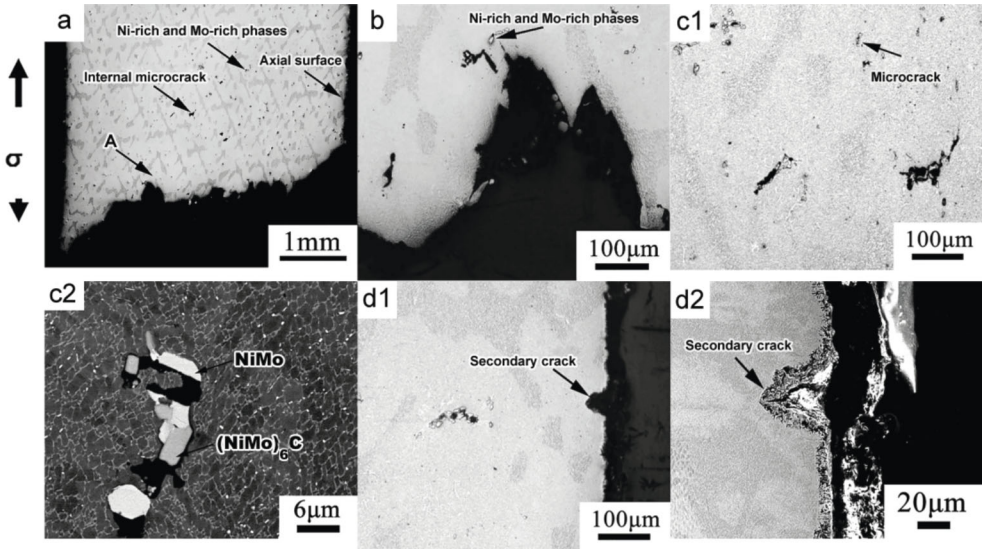

Figure 6: Microstructures of fracture longitudinal section of the single crystal alloy IC6SX with [111] orientation after being crept for 126.9 h and then up to fracture at 850°C/450 MPa. (a) Macroscopic metallographic structure (OM image); (b) fracture surface cracks (OM image); (c1) microcracks in the interior of the matrix (OM image); (c2) microcracks in the interior of the matrix (SEM image); (d1) secondary crack on the axial surface (OM image); (d2) secondary crack on the axial surface (SEM image).

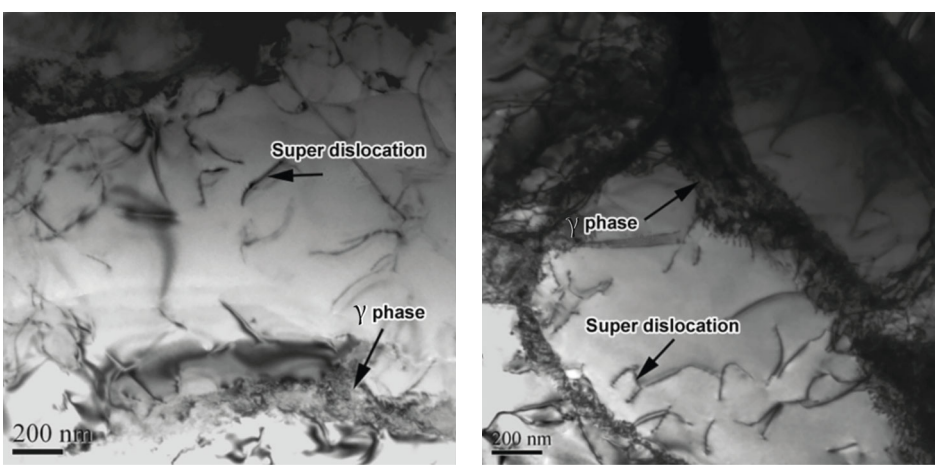

(a) (b)

Figure 7: Dislocation configuration of the single crystal alloy with different orientations after creep rupture at 850°C/450 MPa: (a) [001] orientation; (b) [111] orientation.

Ni-rich, Mo-rich phases and the matrix. Figures 6(d1) and 6(d2) show the optical image and SEM image of the surface secondary cracks near the fracture, respectively. Moreover, Figure 6(d1) indicates that under the action of tensile stress, there were secondary cracks along the surface. It can be seen from Figure 6(d2) that the crack propagated along the direction perpendicular to the stress axial to the interior of the specimen, and the crack tip was obviously oxidized, causing passivation of the crack tip.

3.3. Evolution of Dislocations during Creep of Single Crystal Alloys with Different Crystal Orientations. Figure 7 shows the dislocation configuration of the single crystal alloys with [001] and [111] orientations after creep rupture at 850°C/450 MPa. It can be seen that the dislocation configuration of the single crystal alloy with [001] orientation was similar to that with [111] orientation after creep fracture. In addition, a large number of dislocations generated in the γ channels, cutting into the γ' phase. Consequently, the cutting mechanism of dislocations in the alloys with [001] and [111] orientations under high stress was the main creep deformation mechanism.

3.4. Analysis and Discussion. Due to the low temperature and high stress, the dislocations move in slip mode. However, in addition to the relative displacement of the slip plane, the single crystal slip is often accompanied by the rotation of the crystal planes, leading to the elliptical deformation of the alloy. Owing to primary NiMo phase and $(NiMo)_6C$ phase

with incomplete solid solution which are both the hard brittle phase existed within the single crystal alloys with different orientations, the dislocations will pile up and result in stress concentration when reaching the hard brittle phase. When the stress concentration reaches a certain level, the cracks form in and around the primary NiMo phase and $(NiMo)_6C$ phase. Moreover, under the action of the tensile stress, the cracks connect with each other and extend to the interior of the specimen.

Therefore, within the gauge length, due to the large deformation of the specimen, a large number of dislocations pile up at the interdendritic interface between the primary NiMo phase and matrix phase or between the $(NiMo)_6C$ phase and matrix phase near the fracture, causing the crack formation around the interface. In addition, the elongation direction of the cracks is approximately perpendicular to the stress axis. However, the cracks hardly form in the gauge length away from the fracture. At the same time, a certain number of secondary cracks are also found on the surface near the fracture of the specimen, and there are hard and brittle phases at the crack tip. Due to the high temperature during creep, the surface of the specimen is easy to oxidize. Under the action of the tensile stress, dislocations are easy to pile up near the hard and brittle oxides, resulting in stress concentration. When the stress concentration reaches a certain level, the microcracks form and further propagate to the interior of the specimen in the direction perpendicular to the tensile stress. When extending to a certain extent, the cracks meet with the microcracks which were formed around the hard and brittle phases between dendrites, which accelerate the microcrack propagation, further leading to the fracture of the specimen.

Because the fracture shape of the alloy with [001] orientation changes from circle to ellipse, the deformation degree of the alloy with [001] orientation is larger than that of the alloy with [111] orientation within the gauge length. A certain number of cracks of the two alloys with [001] and [111] orientations form at the interface between the primary NiMo phase or $(NiMo)_6C$ phase and the matrix phase near the fracture. However, the total number of cracks of the alloy with [001] orientation is obviously larger than that of the alloy with [111] orientation. Therefore, the creep life of the alloy with [001] orientation is shorter than that of the alloy with [111] orientation. In addition, it is found that the surfaces near the fracture of the [001] and [111] orientations are serrated. Therefore, the fracture mechanisms of the two alloys are ductile fracture.

4. Conclusion

(1) The creep life of the single crystal alloy IC6SX with [111] orientation is longer than that of the alloy with [001] orientation. In addition, the cracks form at the interdendritic interface between the primary NiMo phase and the matrix or between the $(NiMo)_6C$ phase and the matrix phase near the fracture, with the elongation direction of the cracks approximately perpendicular to the stress axis

(2) Under the condition of 850°C/450 MPa, the fracture morphology of the single crystal alloy with [001] orientation is ellipse, while that with [111] orientation is circle. The fracture mechanisms of the two alloys with [001] and [111] orientations are ductile fracture

(3) Under the condition of 850°C/450 MPa, the creep deformation mechanism of dislocations is mainly dislocation cutting mechanism in the alloys with [001] and [111] orientations

Data Availability

The research data used to support the findings of this study are included within the article.

Conflicts of Interest

No conflict of interest exists in the submission of this manuscript.

Acknowledgments

This research was supported by the National Science and Technology Major Project (Grant No. 2017-VI-0012-0084, 2017-VI-0011-0083), the Fundamental Research Funds for the Central Universities (Grant No. FRF-GF-19-029B) and the National Natural Science Foundation of China (Grant No. 51471022).

References

[1] J. Zhang, L. Wang, D. Wang et al., "Recent progress in research and development of nickel-based single crystal superalloys," *Acta Metallurgica Sinica*, vol. 55, no. 9, p. 1077, 2019.

[2] G. Liu, L. Liu, Z. H. Han, G. J. Zhang, and J. Zhang, "Solidification behavior of Re-and Ru-containing Ni-based single-crystal superalloys with thermal and metallographic analysis," *Rare Metals*, vol. 36, no. 10, p. 792, 2016.

[3] R. C. Reed, T. Tao, and N. Warnken, "Alloys-by-design: application to nickel-based single crystal superalloys," *Acta Materialia*, vol. 57, no. 19, pp. 5898–5913, 2009.

[4] J. Y. Chen, L. M. Cao, M. Xue, and L. J. Liu, "Microstructure and stress rupture property of an experimental single crystal Ni-base superalloy with different heat treatments," *Rare Metals*, vol. 33, no. 2, pp. 144–148, 2014.

[5] K. D. Xu, Z. M. Ren, and C. J. Li, "Progress in application of rare metals in superalloys," *Rare Metals*, vol. 33, no. 2, pp. 111–126, 2014.

[6] W. Y. Ma, Y. F. Han, S. S. Li, Y. R. Zheng, and S. K. Gong, "Effect of Mo content on the microstructure and stress rupture of a Ni-based single crystal superalloy," *Acta Metallurgica Sinica*, vol. 42, no. 11, p. 1191, 2006.

[7] Z. G. Kong and S. S. Li, "Effects of temperature and stress on the creep behavior of a Ni_3Al base single crystal alloy," *Progress in Natural Science: Materials International*, vol. 23, no. 2, pp. 205–210, 2013.

[8] Y. F. Han, "Development of Ni_3AI and its alloys," *Journal of Aeronautical Materials*, vol. 10, no. 1, p. 53, 1990.

[9] Q. Gao, Y. D. Gong, and Y. G. Zhou, "Experimental study on surface roughness in micro-milling of single crystal Ni_3AI-

based superalloy," *China Mechanical Engineering*, vol. 27, no. 6, p. 801, 2016.

[10] R. Q. Wang, B. Zhang, and D. Y. Hu, "Creep constitutive model of Ni_3Al-based single crystal superalloy," *Journal of Aerospace Power*, vol. 33, no. 3, p. 657, 2018.

[11] Y. X. Wu, H. Zhang, F. L. Li, S. S. Li, S. K. Gong, and Y. F. Han, "Kinetics and microstructural evolution during recrystallization of a Ni_3Al-based single crystal superalloy," *Transactions of Nonferrous Metals Society of China*, vol. 22, no. 9, pp. 2098–2105, 2012.

[12] L. W. Jiang, S. S. Li, Z. C. Qiu, and Y. F. Han, "Effects of withdrawal rate on microstructure and stress rupture properties of a Ni_3Al-based single crystal superalloy IC6SX," *Acta Metallurgica Sinica*, vol. 45, no. 5, p. 547, 2009.

[13] J. Yang, W. Kao, and C. Liu, "Development of nickel aluminide matrix composites," *Materials Science and Engineering A*, vol. 107, pp. 81–91, 1989.

[14] Z. L. Gui, "Status of the study on anisotropy of single crystal superalloys in Russia," *Aviation Maintenance and Engineering*, vol. 1, p. 20, 1997.

[15] F. Latief, K. Kakehi, and H. Murakami, "Anisotropic creep behavior of aluminized Ni-based single crystal superalloy TMS-75," *Materials Science and Engineering A*, vol. 567, pp. 65–71, 2013.

[16] V. Sass and M. Feller-Kniepmeier, "Orientation dependence of dislocation structures and deformation mechanisms in creep deformed CMSX-4 single crystals," *Materials Science and Engineering A*, vol. 245, no. 1, pp. 19–28, 1998.

[17] P. Lukas, J. Cadek, V. Sustek, and L. Kunz, "Creep of CMSX-4 single crystals of different orientations in tension and compression," *Materials Science and Engineering A*, vol. 208, no. 2, pp. 149–157, 1996.

[18] V. Sass, U. Glatzel, and M. Feller-Kniepmeier, "Anisotropic creep properties of the nickel-base superalloy CMSX-4," *Acta Materialia*, vol. 44, no. 5, pp. 1967–1977, 1996.

[19] P. Nörtershäuser, J. Frenzel, A. Ludwig, K. Neuking, and G. Eggeler, "The effect of cast microstructure and crystallography on rafting, dislocation plasticity and creep anisotropy of single crystal Ni-base superalloys," *Materials Science & Engineering A*, vol. 626, pp. 305–312, 2015.

[20] P. Y. Wei, Z. G. Yang, X. M. Cheng, Z. G. Zhong, C. Li, and S. Z. Liu, "Tensile creep anisotropy of single crystal superalloy DD3," *Journal of Aeronautical Materials*, vol. 19, no. 3, p. 7, 1999.

[21] K. G. Wang, J. R. Li, S. Z. Liu, Y. Li, and C. X. Cao, "Study on creep properties of DD6 single crystal superalloy at 760°C," *Journal of Materials Engineering*, vol. 5, p. 7, 2004.

[22] G. M. Han, J. J. Yu, X. F. Sun, H. R. Guan, and Z. Q. Hu, "Anisotropic stress rupture behavior of a nickel-based single crystal superalloy," *Rare Metal Materials and Engineering*, vol. 4, p. 673, 2011.

[23] Y. Su, S. G. Tian, H. C. Yu, D. L. Shu, and S. Liang, "Microstructure evolution and its effect on creep behavior of single crystal Ni-based superalloys with various orientations," *Materials Science and Engineering A*, vol. 668, p. 243, 2016.

[24] S. G. Tian, Y. Su, H. C. Yu, and D. L. Shu, "Microstructure evolution and creep properties of a single crystal nickel-based superalloy with various orientations," *Materials Science Forum*, vol. 4074, no. 1758, p. 1951, 2017.

[25] C. B. Yang, L. Liu, X. B. Zhao, Y. F. Li, J. Zhang, and H. Z. Fu, "Dendrite morphology and evolution mechanism of nickel-based single crystal superalloys grown along the <001> and <011> orientations," *Progress in Natural Science: Materials International*, vol. 22, no. 5, pp. 407–413, 2012.

[26] J. L. Liu, T. Jin, J. H. Zhang, and Z. Q. Hu, "Influence of crystal orientation on microstructure and segregation of Ni base single crystal superalloy," *The Chinese Journal of Nonferrous Metals*, vol. 12, no. 4, p. 764, 2002.

[27] C. B. Yang, L. Liu, X. B. Zhao, G. Liu, J. Zhang, and H. Z. Fu, "Dendrite arm spacings and microsegregations in (001) and (011) orientated single crystal superalloys DD407," *Acta Metallurgica Sinica*, vol. 47, no. 10, p. 1246, 2011.

[28] X. B. Zhao, S. F. Gao, C. B. Yang et al., "Influence of crystal orientation on microstructure and mechanical properties and its control for nickel-base single crystal superalloys," *Rare Metals Letters*, vol. 32, no. 1, p. 24, 2013.

[29] S. G. Tian, L. L. Yu, S. Zhang, H. C. Yu, B. J. Qian, and L. Xiao, "Influence of crystal orientations on creep behaviors of single crystal nickel-based superalloy," *The Chinese Journal of Nonferrous Metals*, vol. 21, no. 2, p. 356, 2011.

[30] Z. K. Zhang, B. Z. Wang, D. S. Liu, Z. X. Wen, and Z. F. Yue, "Creep properties and fracture mechanism of DD6," *Journal of Materials Science and Engineering*, vol. 30, no. 3, p. 375, 2012.

Hindawi
International Journal of Photoenergy
Volume 2020, Article ID 8896666, 9 pages
https://doi.org/10.1155/2020/8896666

Research Article

Dynamical Properties of the New Ternary Fission in Collisions of $^{197}Au+^{197}Au$ at 15 *MeV/Nucleon*

Xian Li,[1] **Chengqian Wang**,[1] **and Yaohui Xu**[2]

[1]*Instiute of Mathematics and Physics, Leshan Normal University, Leshan, 614000 Sichuan, China*
[2]*Instiute of Electronics and Materials Engineering, Leshan Normal University, Leshan, 614000 Sichuan, China*

Correspondence should be addressed to Chengqian Wang; wangchengqiancqx@163.com

Received 20 July 2020; Revised 3 September 2020; Accepted 13 September 2020; Published 6 October 2020

Academic Editor: Jiangwei LIU

The dynamical properties of the new ternary fission in heavy ^{197}Au+^{197}Au at 15 MeV/nucleon have been investigated by using the improved quantum molecular dynamics model. The dependencies of the production probability, lifetime, the time interval, and angular distribution on the impact parameter are carefully studied. The calculation results show that the characteristics of these are very different between the small and the large impact parameter. Comparing the theoretical results with the experimental data, one can obtain that the fast ternary breakup likely occurs at the impact parameter region b = 7-9 fm. The nonisotropic of angular distribution and the short time interval among two fissions indicates that the fast ternary fission is a nonequilibrium and violent process.

1. Introduction

Heavy-ion collisions have been paid much attention for several decades, and multifragmentation is a common phenomenon in the intermediate-energy heavy-ion collisions. In the low incident energy region, middle-mass nucleus-nucleus systems predominantly lead to these reactions: fusion, fusion-fission, quasi-fission, deep-inelastic, and quasi-elastic scattering with the two heavy fragments produced in the exit channel. Also, the normal ternary fission, which has two bigger fragments and a light-charged particle emitted from the neck, occurs on the peripheral collision. However, for the very heavy collision system at the incident energy around 20 MeV/nucleon, there exists a new ternary reseparation mode which is very different from the normal ternary fission, and many experiments have verified this reaction mode in heavy nuclear reaction system [1, 2]. This ternary fission of the new fission mode is considered as a transition from the low-energy fusion-fission collision to the high-energy multifragmentation. Studying this questions can reveal some very interesting phenomena of the dynamical and energy dissipation mechanisms [1–3] in the heavy-ion collisions.

The experimental researches on collisions of a very heavy system ^{197}Au+^{197}Au have been carried out at energy of 15 MeV/nucleon, by using the CHIMERA multidetector array arranged in 4π geometry at the Laboratori Nazionali del Sud (LNS) in Catania. Their preliminary result showed that a violent process of reseparation into three fragments with comparable size was founded in this heavy system. This ternary fission was called fast ternary breakup [4, 5] and clearly different from normal ternary fission. Then, a series of deep experiments and analyses have demonstrated that the fragments of this ternary breakup are almost exactly aligned and the time scale of these two separations is very short, about 70-80 fm/c [6–8].

In order to understand and observed the new ternary fission mechanism, it is necessary to use suitable dynamical model of nucleus-nucleus collision from the many theoretical simulation model [3, 9–11]. For example, the Los Alamos finite-range macroscopic dynamical description [3] is static and concludes that the ternary fission only happens on strong two-body dissipation existed. Then in the low energies, the classical dynamical model HICOL of Feldmeier [9] based on the one-body dissipation dynamics is widely used for analysis of deep-inelastic reactions.

But for the ternary fission in heavy reaction system at low energy, there seems still having some unsuitable when studying the energy dissipation mechanism. In addition, the quantum molecular dynamics (QMD) code of Lukasik was used to the Au+Au system and failed to reproduce the characteristic of the collinear emission pattern of the ternary fission [12, 13], maybe because of the lack of important improvements on the nucleon-nucleon interaction term. Finally, the improved quantum molecular dynamics (ImQMD) model, which both the mean-field and the nucleon-nucleon collisions as well as the Pauli principle are treated properly and may be a suit way to simulate the nuclear action in low energy. Both the experimental and the theoretical studies on the new ternary fission indicate that it is worthwhile and meaningful to research the dynamical mechanism of the new ternary fission.

In this paper, ImQMD model has been applied to simulate the heavy ^{197}Au+^{197}Au collisions at 15 MeV/nucleon, and the new ternary fissions are selected. The dynamical properties of them are comprehensive studied, such as the fission modes and their probabilities, the angular distributions of fragments, and the time scale of the secondary fission.

2. Theoretical Approach

For the reader's convenience, let us first briefly introduce our model. The QMD model is a microscopic transport model based on a molecular dynamics picture and has been successfully used in intermediate energy heavy-ion collisions [14, 15]. By making serious improvements, it has been extended to apply to heavy-ion collisions at low energies near barrier and called the ImQMD model. The main improvements include the three terms: the surface and surface symmetry energy terms, which are introduced in the potential energy density functional in the mean field; a system-size-dependent wave packet width, which is introduced in order to consider the evolution of the wave packet width; and an approximate treatment of antisymmetry, which is carried out by the phase space occupation constrain [15, 16].

In the ImQMD model, each nucleon is expressed by a Gaussian wave packet

$$\phi_i\left(\vec{r}\right) = \frac{1}{\left(2\pi\sigma_r^2\right)^{3/4}} \exp\left[-\frac{\left(\vec{r}-\vec{r}_i\right)^2}{4\sigma_r^2}\right] \exp\left[\frac{i\vec{p}_i\cdot\vec{r}}{\hbar}\right], \quad (1)$$

where $\vec{r}_i, \vec{p}_i$ are the centers of ith wave packet in coordinate and momentum space, respectively. σ_r is the spread of the wave packet. Through a Wigner transformation, the one-body phase space distribution function for N-distinguishable particles is given by

$$f_i\left(\vec{r},\vec{p}\right) = \frac{1}{(\pi\hbar)^3} \exp\left[-\frac{\left(\vec{r}-\vec{r}_i\right)^2}{2\sigma_r^2}\right] \exp\left[-\frac{\left(\vec{p}-\vec{p}_i\right)^2}{2\sigma_p^2}\right], \quad (2)$$

where σ_p is the width of wave packet in momentum space, and σ_r, σ_p satisfy the minimum uncertainty relation

$$\sigma_r \cdot \sigma_p = \frac{\hbar}{2}. \quad (3)$$

The phase space distribution function of the whole system is described as

$$f\left(\vec{r},\vec{p}\right) = \sum_i f_i\left(\vec{r},\vec{p}\right). \quad (4)$$

Then the density distribution of the system can be obtained.

$$\rho\left(\vec{r}\right) = \int f\left(\vec{r},\vec{p}\right)d\vec{p} = \frac{1}{\left(2\pi\sigma_r^2\right)^{3/2}} \sum_i \exp\left[-\frac{\left(\vec{r}-\vec{r}_i\right)^2}{2\sigma_r^2}\right]. \quad (5)$$

The propagation of nucleons in reaction system under a self-consistently generated mean-field is governed by Hamiltonian equations of motion:

$$\dot{\vec{r}} = \frac{\partial H}{\partial \vec{p}_i}, \dot{\vec{p}}_i = -\frac{\partial H}{\partial \vec{r}_i}. \quad (6)$$

The Hamiltonian H consists of the kinetic energy T, the nuclear local interaction potential energy U_{loc}, and Coulomb interaction potential energy U_{coul} and is expressing as

$$H = T + U_{\text{loc}} + U_{\text{coul}}, \quad (7)$$

where

$$T = \sum_i \frac{p_i^2}{2m_i}, \quad (8)$$

in which $\vec{p}_i$ is the center of ith wave packet in momentum space and m_i is the mass of ith nucleon.

And

$$\begin{aligned} U_{\text{loc}} &= \int H_{\text{loc}}\left(\vec{r}\right)d\vec{r} = \int\left\{\frac{\alpha}{2}\frac{\rho^2}{\rho_0} + \frac{\beta}{\gamma+1}\frac{\rho^{\gamma+1}}{{\rho_0}^{\gamma}} + \frac{g_0}{2}(\nabla\rho)^2 \right. \\ &\quad \left. + g_\tau\frac{\rho^{\eta+1}}{{\rho_0}^{\eta}} + \frac{C_s}{2\rho_0}\left[\rho^2 - \kappa_s(\nabla\rho)^2\right]\delta^2\right\}d\vec{r}, \\ U_{\text{coul}} &= \frac{1}{2}\int \rho_p\left(\vec{r}\right)\frac{e^2}{\left|\vec{r}-\vec{r}\,'\right|}\rho_p\left(\vec{r}\,'\right)d\vec{r}\,d\vec{r}\,' \\ &\quad - e^2\frac{3}{4}\left(\frac{3}{\pi}\right)^{1/3}\int \rho_p\left(\vec{r}\right)^{4/3}d\vec{r} \end{aligned} \quad (9)$$

where $\delta = \rho_n - \rho_p/\rho_n + \rho_p$ is the isospin asymmetry. ρ, ρ_n, ρ_p are the nucleon, neutron, and proton densities, respectively.

Table 1: The IQ2 parameters used in ImQMD model.

α	β	γ	g_0	g_τ	η	C_S	κ_S	ρ_0
MeV	MeV		MeVfm^2	MeV		MeV	fm^2	fm^{-3}
-356	303	7/6	7.0	12.5	2/3	32.0	0.08	0.165

In the local interaction potential energy equation, the first and second terms are two-body and three-body parts, the g_0, g_τ terms are the surface and momentum-dependent terms, and the last part is the symmetry energy. The parameters named IQ2 in the Hamiltonian energy density function are shown in Table 1 [17]. In addition, we adopt a system-size-dependent wave packet width in our simulation:

$$\sigma_r = 0.09A^{1/3} + 0.88\text{fm}. \tag{10}$$

3. Results and Discussions

Making the initial nuclei in the real ground state is crucial important, because unreal nucleon emission of initial nuclei will affect the production in the nuclear reaction. By using the ImQMD model with IQ2 parameters, we selected 20 projectile and target initial nuclei. Their binding energies were 7.92 ± 0.05MeV/nucleonand the root-mean-square radii 5.35 ± 0.2fm, respectively. The bound of the nuclei evolved stably without spurious emission within 6000 fm/c. We have simulated more than 200,000 bombarding events, by rotating these projectile and target nuclei around their centers of mass with a Euler angle chosen randomly. For each small impact parameter (0-3 fm), we have simulated 4000-7000 reactions, 10000-15000 reactions for each medium impact parameter (4-6 fm), and 20000-30000 reactions for each peripheral impact parameter (7-12 fm).

As the same with the experiment research [7], a class of ternary fissions were selected under the condition:

$$A_{\text{projectile}} + A_{\text{target}} - 70 \le A_1 + A_2 + A_3 \le A_{\text{projectile}} + A_{\text{target}}, \tag{11}$$

where A_1, A_2, and A_3 are the masses of three fragments in a ternary fission, respectively. This condition showed the characteristics of the nuclear reactions were that the nearly complete balance of mass allowing for up to 70 mass units to be lost because of the evaporation of undetected nucleons and α particles. Conditions on the balance of longitudinal and transversal momenta are imposed:

$$\left|\sum_{i=1}^{3} \vec{p}_{\text{long}}(i)\right| > 0.8p_0, \left|\sum_{i=1}^{3} \vec{p}_{\text{trans}}(i)\right| < 0.04p_0, \tag{12}$$

where p_0 is the momentum of ^{197}Au projectiles.

In our previous work [18], we have calculated the mass distributions of fragments in the new ternary fission of ^{197}Au+^{197}Au collisions at 15 MeV/nucleon and compared with experimental result [4]. We can find that the theoretical results are in good agreement with experimental data. In addition, the result is shown in the data supplement part of figures S1. The results show that the ImQMD is suitable to study the heavy nuclear reaction of ^{197}Au+^{197}Au system at an energy of 15 MeV/nucleon.

3.1. The Modes and Production Probabilities of New Ternary Fissions. In our simulation, we have found the production probability of the new ternary fission is different at each impact parameter, and it is worthwhile to clarify this question. The dependence of the production probability about the new ternary fission on the impact parameter is shown in Figure 1. In small parameter region (0-2 fm), the production probability nearly rises up, then appears a plateau in the region (3-6 fm), and decreases rapidly after b = 7 fm almost to zero. This result implies the new ternary fissions of ^{197}Au+^{197}Au system mainly happen in the semicentral region of impact parameter.

Further experimental studies [7, 8] indicate that any new ternary fission of ^{197}Au+^{197}Au collision will break up into projectile-like (PLK) and target-like (TLK) fragments in first separation, and then the PLK or TLK will break into two fragments in the second separation. The time interval between these two separations of all the ternary fissions is not the same. If the time interval between the two separations is less than 100 fm/c, then we call it a direct ternary fission, and if not, call it a sequential ternary fission. To discover the characteristics of these two breakup modes, we have drawn and analyzed the snapshots of the time evolution of several typical ternary fissions by using the same method in Ref. 18. The results show that there exist two preformed necks already in the direct mode before the first breakup of reaction system; thus, the time interval will be very short in the following reaction process. However, for a sequential mode ternary fission that has no feature and after the first separation, the reaction system needs more time to form another neck and breaks up again. These snapshots are shown in the data supplement part of figures S2, S3.

Figure 2 shows the dependence of the production probabilities for the direct and sequential ternary fissions on impact parameter in reaction ^{197}Au+^{197}Au at 15 MeV/nucleon. From this figure, we can see that the sequential mode reaction dominates in the central and semiperipheral region of the impact parameters, and the direct mode likely appears at large impact parameters. The impact parameter b = 6 fm is a turning point; after that, the tendency of the black-dot line is declining; meanwhile, the red-triangle line is rising.

3.2. The Lifetime and the Time Scale of the Second Fission. It is very important and interesting to estimate when the primary breakup happens and how long will elapse from the primary fission to the second separation in a new ternary fission. And it can provide us with significant valuable physical insights on mechanism of heavy nuclear reactions. For the convenience, we define the lifetime as the passing time from the sticking time point of projectile and target nuclei to the primary breakup, and Δt is the time interval elapsing from the primary separation to the second fission. It is necessary to study the relationship of the lifetime or Δt with the impact parameter, and the average value of them is shown in

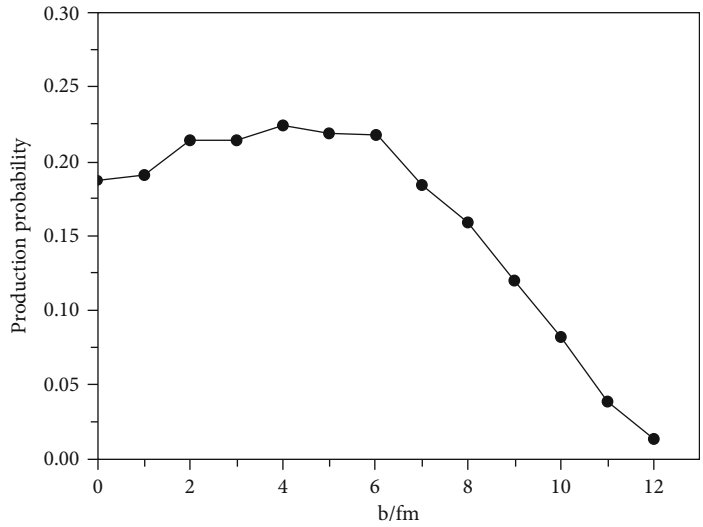

Figure 1: The dependence of the production probability on the impact parameter about the new ternary fission of ^{197}Au+^{197}Au system at an energy of 15 MeV/nucleon.

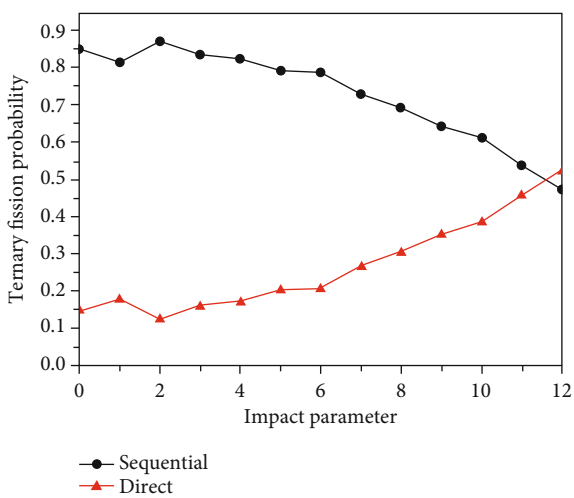

Figure 2: The dependence of the production probabilities about the direct and sequential ternary fissions on the impact parameter in ^{197}Au+^{197}Au system at an energy of 15 MeV/nucleon.

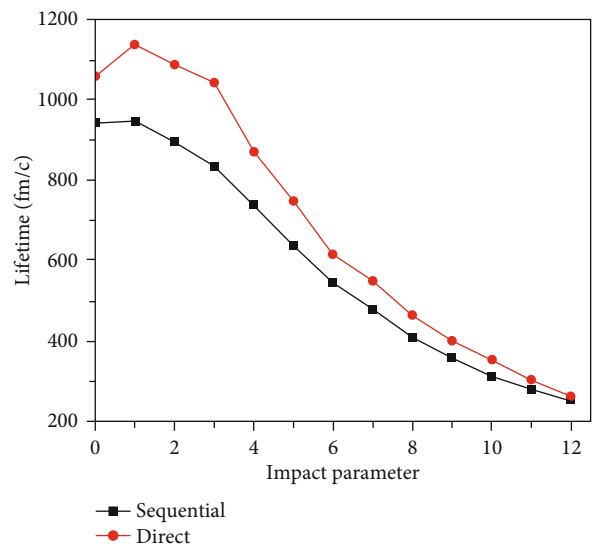

Figure 3: Correlation between the lifetime of the new ternary fissions and the impact parameter. The black solid-square line is the lifetimes of the composite system of the sequential ternary fission at all impact parameters, and the red solid-dot line represents that of the direct ternary fission.

Figures 3 and 4, respectively. From Figure 3, one can see that the lifetimes in both the direct and sequential ternary fissions decrease with the impact parameter increases and also find that the lifetime of direct ternary reaction is longer than that of the sequential mode, and their gap reduces rapidly along with the impact parameter rising. The longer lifetime of direct mode is due to the two necks that are formed at the breakup time point, and it needs more time to rearrange nucleons to be in a lower energy configuration. However, the difference nearly disappears at large impact parameter; this is because more nucleons take part in the reaction at small impact parameter and fewer nucleons at large impact parameter, that is to say, the spectator effect becomes more and more obvious. Then, the difference between the direct and sequential mode will be small before the separation. In Figure 4, the time interval Δt also falls down quickly from 550 fm/c till the impact parameter b = 6 fm, then gets slower when b = 7, 8 fm, and it remains unchanged after b = 9 fm, about 170 fm/c.

Moreover, according to the analysis dependance of Δt on impact parameters, we deduce that the fast sequential ternary reaction, mentioned in Ref. 4–6, probably happens at peripheral collision, so we change the time step of ImQMD code in our previous simulation and choose a smaller time step as 10 fm/c and calculate the fission time scale in the sequential ternary reactions at b = 7 fm again, and the time distributions of the primary and second separations are shown in Figure 5. The red line is the primary fission moment, and the blue line is

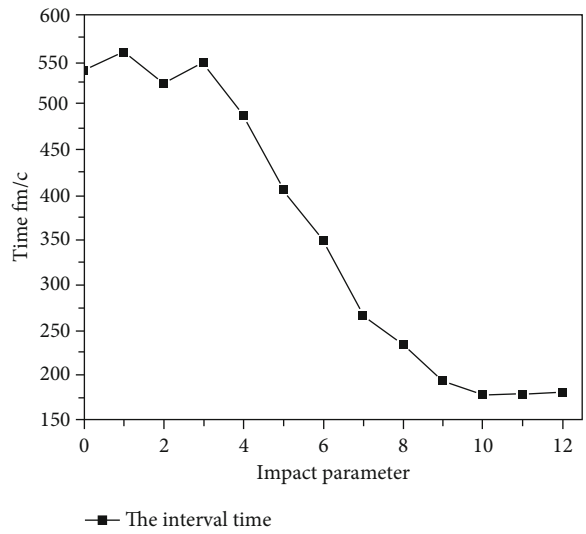

Figure 4: Correlation between the time interval Δt and the impact parameter.

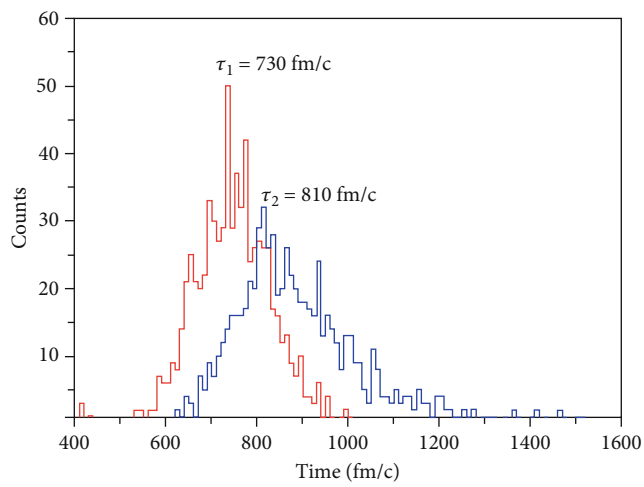

Figure 5: The distribution of the fission moment in sequential ternary fissions of ^{197}Au+^{197}Au system at b = 7 fm. The red line is the primary fission moment, and the blue line is the second breakup moment.

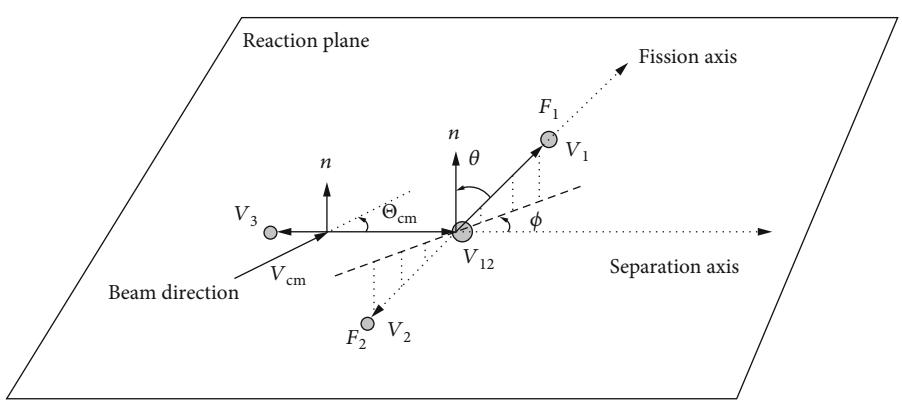

Figure 6: The schematic view of the reaction in a sequential ternary fission, in which a TLF and PLF are formed in the primary deep-inelastic process and followed by a consecutive breakup process from one of these two fragments. The definitions of the in-plane (ϕ), the out-of-plane (θ), and (Θ_{cm}) angles are shown. The normal direction $\vec{n}$ is the unit vector of reaction plane. The beam, separation and fission axes, and their orientations are displayed, and the orientation of the fission axis is given by the larger z-axis velocity $v_{1z} \geq v_{2z}$.

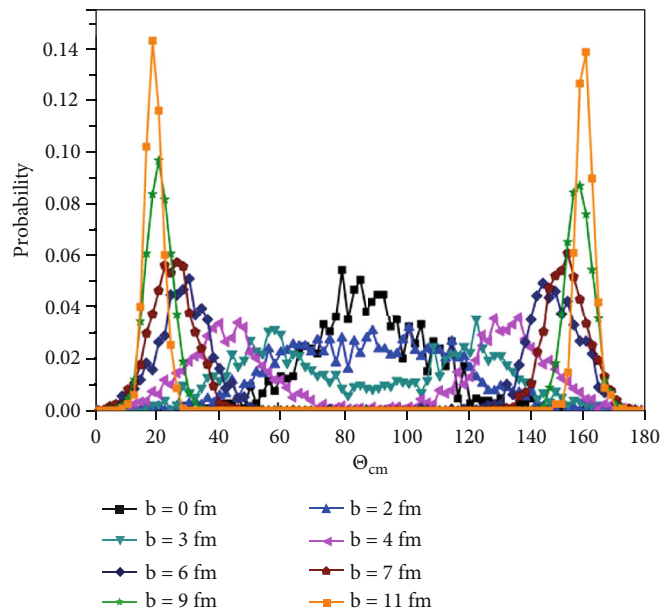

Figure 7: The dependence of angular distributions about Θ_{cm} on the impact parameter with respect to sequential ternary fissions in ^{197}Au +^{197}Au system at an energy of 15 MeV/nucleon.

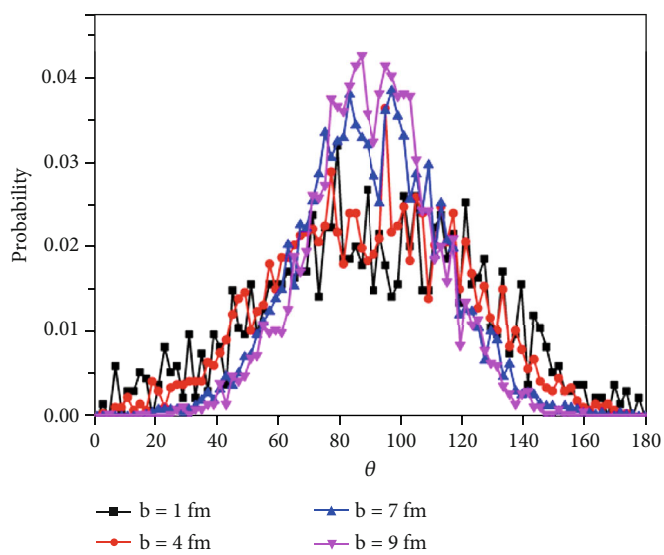

Figure 8: The dependence of angular distributions about θ on the impact parameter with respect to sequential ternary fissions in ^{197}Au+^{197}Au system at an energy of 15 MeV/nucleon.

the second breakup moment. The peaks of the distributions correspond to the time of $\tau_1 = 730$fm/c and $\tau_2 = 810$fm/c, respectively, and the interval time τ_2-τ_1 of the twice fissions is 80 fm/c, which is consistent with the time scale reported in Ref. 6. This simulation result supports the conclusion that the fast ternary reaction is a violent process, takes place in a very short time, and likely happens in peripheral collision.

3.3. Angular Distributions and the Correlation with the Impact Parameter. To further understand the dynamical and energy dissipation mechanism [19, 20] of the new ternary fission in^{197}Au+^{197}Au system nuclear reaction, we study their angular distributions. For clarity, we first give the definition of the angles, similar as in Ref. [1]. The velocity of the primary fragment survived in second fission is written as $\vec{v}_3$, and the velocity of the other fragment separated in the second fission is denoted as $\vec{v}_{12}$. The fragments and their velocities formed in second breakup are called F_1, $\vec{v}_1$ and F_2, $\vec{v}_2$, respectively. And their velocities' projections onto z-axis satisfying this relation $v_{1z} \geq v_{2z}$. $\vec{v}_{cm}$ is the velocity of the center-of-mass of the total system. Then, we define the

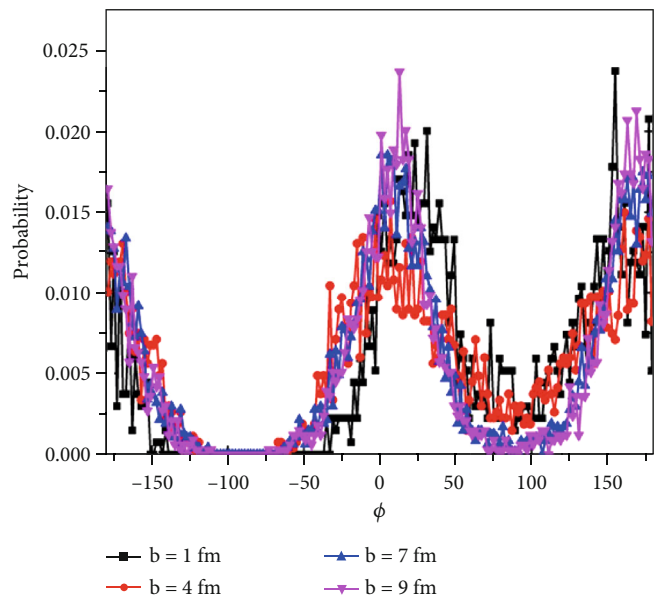

Figure 9: The dependence of angular distributions about ϕ on the impact parameter with respect to sequential ternary fissions in ^{197}Au +^{197}Au system at an energy of 15 MeV/nucleon.

beam axis, the separation axis (the first separation), and the fission axis (the second separation) by $\vec{v}_{cm}$, $(\vec{v}_{12} - \vec{v}_3)$, and $(\vec{v}_1 - \vec{v}_2)$, respectively. The reaction plane is defined by the beam and separation axes, and the normal direction $\vec{n}$ of reaction plane is the unit vector of the cross product $(\vec{v}_{12} - \vec{v}_3) \times \vec{v}_{cm}$. The out-of-plane angle θ specifies the deflection of the fission axis with respect to the normal direction $\vec{n}$. The in-plane-angle ϕ is the angle between the separation axis and the projection of fission axis onto the reaction plane. Θ_{cm} is the angle between separation axis and beam axis, also called the center-of-mass scattering angle. The schematic view of the reaction in a sequential ternary fission and the angles of θ, Θ_{cm}, and ϕ are shown in Figure 6.

The distributions of θ, Θ_{cm}, and ϕ in sequential ternary fissions are displayed in Ref. 21. These figures are shown in the data supplement part of figures S4. Both the theoretical results and experimental data are normalized. In order to make a comparison with the experimental data, only the PLK ternary fissions are chosen and analyzed. The distributions of the out-of-plane angle θ are peaked at 90° in both the experimental and ImQMD results, which indicates that the fission axes of ternary fissions lie in or are very close to the reaction plane at most times. The distribution of Θ_{cm} is peaking around 26°. The distribution of the in-plane angle ϕ both theoretical and experimental curves has two peaks, 15° and -165°, corresponding to the fragments F_1 and F_2 separately. It is worthwhile to clarify the question that the new ternary fission is a statistical or dynamical fission process at low bombarding energies. From this figure, we have found that the angular distribution of ϕ is anisotropic, and the peaked angles mean that the separated fragment proceeds a nonequilibrium reaction and still retains a memory of its creation.

For deeper study, the dependence of angular distributions on the impact parameters with respect to both PLF and TLF sequential ternary fissions are discussed systematically in^{197}Au+^{197}Au system at an energy of 15 MeV/nucleon. In Figure 7, the dependence of angular distributions about Θ_{cm} on the impact parameter is shown. From this figure, we can see that the distributions of Θ_{cm} are peaked at 90° in small impact parameter, such as b = 1.2 fm, and this indicates that the separation axis (the direction of the first separation) is likely vertical to the beam direction. With the impact parameter increases, when b ≥ 3fm, the angular distribution curve appears two complementary peaks, which correspond to PLK ternary fissions for $\Theta_{cm} < 90°$ and TLK ternary fissions for $\Theta_{cm} > 90°$, and also the curve of the distribution becomes narrow, sharp, and shifts. The probabilities of the two value are similar because the collision system is symmetric. The peak angle tends to be steady at 26° or 154°, which agrees with the "grazing angle" of the classical deflection function for binary dissipation collision [22, 23], indicating that the first separation is a deep inelastic scattering process.

In Figure 8, the dependence of angular distributions about θ on the impact parameter with respect to sequential ternary fissions is displayed. In small impact parameter region, such as b = 1, 4 fm, the distributions are more likely to be isotropic; for large parameters, it will have two peaks on symmetrical positions around 90°, and they are 85° and 95°, respectively. It means that the fission axis more likely very close to the reaction plane and not lies in it. Moreover, the angular distributions of ϕ on the impact parameters concerning sequential ternary fissions are drawn in Figure 9. In this figure, we can see that there are three peaks in the distributions: the middle peak represents the direction of F_1 in PLK ternary fission, and the other two peaks correspond to F_1 in TLK ternary fission, and the fragments of F_2 are in the complementary direction of themselves. Also, we can

observe that the three peaks of the distribution move along with the impact parameter increases, such as the middle peak moves from 26° (b = 1 fm) to 15° (b = 9 fm), and the distributions turn sharper at the same time. The distribution of ϕ is nonisotropic and strongly means the fission is very nonstatistical. The peaks of distribution ϕ about F_1 are 15° or 165°, and this means the fission axes are very close to the separation axes. Therefore, we can conclude that the secondary fission should be completed in a short time and the three fragments will be collinear.

4. Summary

The new ternary fission of the very heavy ^{197}Au+^{197}Au system at the incident energy of 15 MeV/nucleon has been studied by using the ImQMD model. Primarily, its production probability depends on the impact parameter, and it mainly occurs at central and semiperipheral collision region. The impact parameter b = 6 fm is a turning point; after that, the tendency of sequential mode is declining; meanwhile, the direct mode is rising. In addition, its lifetime decreases with impact parameter increasing, and the lifetime of direct mode is longer than that of the sequential mode; also, their difference reduces rapidly along with impact parameter rising. The time interval Δt between two breakups of sequential mode also falls down quickly before b = 6 fm and remains unchanged after b = 9 fm, about 170 fm/c. Especially, the value of Δt at b = 7 fm is estimated 80 fm/c, which is a very short time and indicates that this breakup occurs violently and is a nonequilibrium process.

To further study, the angular distributions for both PLF and TLF ternary fissions are analyzed. It is found that the distribution of Θ_{cm} is strongly dependent on the impact parameter, which appears isotropic at small impact parameters and presents obvious orientation at the range b > 3 fm, peaking at 25°. The distribution of θ is approximately isotropic at smaller impact parameter and peaks around 90° (90° ± 5°) when b > 7 fm. Then, the distribution of ϕ is weakly correlated with b, and ϕ distributes in a narrow range round 15° and 165° when b > 7 fm. At last, one can conclude that the new ternary fission in ^{197}Au+^{197}Au is a nonstatistical and collinear process.

In conclusion, this work has studied the dynamical properties of the new ternary fission, and their dependencies on the impact parameter also obtained the fast ternary fission which the fragments are comparable in size and collinear in space, more likely occurs at the range of b > 7 fm.

Data Availability

For theoretical data in this paper, ImQMD model has been applied to simulate the heavy ^{197}Au+^{197}Au collisions at 15 MeV/nucleon. Experimental data is part of the references in this paper.

Conflicts of Interest

The authors declare that they have no conflicts of interest.

Acknowledgments

This work is partly supported by the Funds of Talent Program of Leshan Normal University under Grant No. Z1166 and the Funds of Cultivating Program of Leshan Normal University under Grant No. Z1317.

Supplementary Materials

The supplementary data are shown in the file of "supplement data", which figures are results of our previous papers, and cited for confirming some description in this paper. *(Supplementary Materials)*

References

[1] A. A. Stefannini, G. Casini, P. R. Maurenzig et al., "Analysis of the sequential fission observed in collisions of ^{100}Mo + ^{100}Mo and ^{120}Sn + ^{120}Sn around 20 A·MeV," *Zeitschrift für Physik A Hadrons and Nuclei*, vol. 351, no. 2, pp. 167–186, 1995.

[2] R. J. Charity, R. Freifelder, A. Gobbi et al., "Results on two-, three-, and four-body events from the ^{100}Mo + ^{100}Mo and ^{120}Sn + ^{120}Sn collisions around E/A = 20 MeV," *Zeitschrift für Physik A Hadrons and Nuclei*, vol. 341, no. 1, pp. 53–73, 1991.

[3] N. Cârjan, K. Siwek-Wilczyńska, I. Skwira-Chalot, and J. Wilczyński, "Macroscopic dynamical description of rotating Au + Au system," *International Journal of Modern Physics E*, vol. 17, no. 1, pp. 53–59, 2008.

[4] I. Skwira-Chalot, K. Siwek-Wilczyńska, J. Wilczyński et al., "Dynamical evolution of the ^{197}Au + ^{197}Au system at 15 MeV/nucleon," *International Journal of Modern Physics E*, vol. 15, no. 2, pp. 495–499, 2006.

[5] I. Skwira-Chalot, K. Siwek-Wilczyńska, J. Wilczyński et al., "Ternary reactions in ^{197}AU + ^{197}AU collisions revisited," *International Journal of Modern Physics E*, vol. 16, no. 2, pp. 511–515, 2007.

[6] I. Skwira-Chalot, K. Siwek-Wilczyńska, J. Wilczyński et al., "Fast ternary and quaternary breakup of the ^{197}Au + ^{197}Au system in collisions at 15 MeV/nucleon," *Physical Review Letters*, vol. 101, no. 26, article 262701, 2008.

[7] J. Wilczyński, I. Skwira-Chalot, and K. Siwek-Wilczyńska, *International Journal of Modern Physics E*, vol. 17, no. 41, 2008.

[8] J. Wilczyński, I. Skwira-Chalot, K. Siwek-Wilczyńska et al., "Aligned breakup of heavy nuclear systems as a new type of deep inelastic collisions at small impact parameters," *Physical Review C*, vol. 81, no. 6, article 067604, 2010.

[9] H. Feldmeier, "Transport phenomena in dissipative heavy-ion collisions: the one-body dissipation approach," *Reports on Progress in Physics*, vol. 50, no. 8, pp. 915–994, 1987.

[10] H. Li and Z. Ding, "Hydrogen coverage dependent C C hydrogenation activity on Rh(111)," *Chemical Physics Letters*, vol. 746, article 137287, 2020.

[11] Z. Ding, X. Zhao, and L. L. Shaw, "Reaction between LiBH4 and MgH2 induced by high-energy ball milling," *Journal of Power Sources*, vol. 293, pp. 236–245, 2015.

[12] J. Lukasik, *QMD-CHIMERA code, [Ph.D. thesis]*, Jagellonian University, Cracow, Poland, 1993.

[13] J. Lukasik and Z. Majka, "QMD-CHIMERA code," *Acta Physica Polonica B*, vol. 24, p. 1959, 1993.

[14] J. Aichelin and H. Stöcker, "Quantum molecular dynamics — a novel approach to N-body correlations in heavy ion collisions," *Physics Letters B*, vol. 176, no. 1-2, pp. 14–19, 1986.

[15] N. Wang, Z. Li, X. Wu, J. Tian, Y. X. Zhang, and M. Liu, "Further development of the improved quantum molecular dynamics model and its application to fusion reactions near the barrier," *Physical Review C*, vol. 69, no. 3, article 034608, 2004.

[16] N. Wang, Z. Li, and X. Wu, "Improved quantum molecular dynamics model and its applications to fusion reaction near barrier," *Physical Review C*, vol. 65, no. 6, article 064608, 2002.

[17] N. Wang, Z. Li, X. Wu, and E. Zhao, "Search for possible way of producing super-heavy elements: dynamic study on damped reactions of ^{244}Pu + ^{244}Pu, ^{238}U + ^{238}U and ^{197}Au + ^{197}Au," *Modern Physics Letters A*, vol. 20, no. 34, pp. 2619–2627, 2005.

[18] J. L. Tian, X. Li, X. Z. Wu, Z. X. Li, and S. W. Yan, "Possible Mechanisms of Ternary Fission in the 197 Au+ 197 Au System at 15 A MeV," *Chinese Physics Letters*, vol. 26, no. 6, article 062502, 2009.

[19] Z. Ding, P. Wu, and L. Shaw, "Solid-state hydrogen desorption of 2 MgH2 + LiBH4 nano-mixture: A kinetics mechanism study," *Journal of Alloys and Compounds*, vol. 806, pp. 350–360, 2019.

[20] Z. Ding, H. Li, and L. Shaw, "New insights into the solid-state hydrogen storage of nanostructured LiBH4-MgH2 system," *Chemical Engineering Journal*, vol. 385, article 123856, 2020.

[21] X. Li, J. Tian, S. Yan, J. Cheng, and X. Jiang, "Angular distributions of fragments produced in ternary reaction of ^{197}Au + ^{197}Au at 15 A MeV," *Modern Physics Letters A*, vol. 26, no. 6, pp. 449–460, 2011.

[22] I. Skwira-Chalot, K. Siwek-Wilczynska, J. Wilczyński et al., "Dynamics of "binary" ^{197}Au + ^{197}Au collisions as a test of energy dissipation mechanism," *Acta Physica Polonica B*, vol. 38, p. 1509, 2007.

[23] J. Wilczynski, "Nuclear molecules and nuclear friction," *Physics Letters B*, vol. 47, no. 6, pp. 484–486, 1973.

Hindawi
International Journal of Photoenergy
Volume 2020, Article ID 8852665, 6 pages
https://doi.org/10.1155/2020/8852665

Research Article

Elastic, Mechanical, and Phonon Behavior of Orpiment Arsenic Trisulfide under Pressure

Liwu Jiang,[1,2] **Meiling Wu**,[3] **Peng Shi**,[1] **and Chuanhui Zhang**[1]

[1]*National Center for Materials Service Safety, University of Science and Technology Beijing, Beijing 100083, China*
[2]*NCS Testing Technology Co. Ltd., Beijing 100081, China*
[3]*Beijing Institute of Aeronautical Materials, Beijing 100095, China*

Correspondence should be addressed to Liwu Jiang; lwjiang@ustb.edu.cn

Received 13 August 2020; Revised 20 August 2020; Accepted 8 September 2020; Published 19 September 2020

Academic Editor: Jiangwei LIU

Arsenic trisulfide (As_2S_3) has been found to be an excellent glass former at high temperature and pressure. However, there is still some scarcity for the elastic and phonon behavior of the orpiment phase. By using the Dreiding force field of the geometry optimization computations, we investigated the elastic constants, mechanical moduli, and the phonon dispersion of orpiment As_2S_3 under the pressure from 0 to 5 GPa. Some results of the elastic parameters of orpiment-As_2S_3 at 0 GPa are consistent with the experimental data. The phonon dispersions for orpiment As_2S_3 under pressure are also reasonable with previous calculations.

1. Introduction

The computational simulation of materials has been a successful and rapid tool to understand the complex physical problems of materials. In addition, predicting the good elastic and mechanical properties of materials is a necessary demand for recent solid-state physics and science. And these mechanical properties at high pressure and temperature are also important for the development of modern technologies [1–4].

Arsenic trisulfide (As_2S_3) is the most studied compound due to its properties like large glass-forming ability, excellent infrared radiation transmission, and structural and mechanical properties [5, 6]. Under normal conditions, the stable phase is an orpiment layered structural semiconductor material. In its lattice, each As atom is surrounded by three S atoms, whereas each S atom is surrounded by two As atoms. At normal conditions, no other crystalline metastable phases of As_2S_3 could be artificially synthesized for a long time. The structure properties of arsenic sulfides were studied by the density functional theory [7], tight binding method [8], and nonempirical localized approach method [9]. The density of valence states of crystalline arsenic sulfides was investigated by using X-ray photoemission spectroscopy [10]. The optical and transport properties and electronic structure of Ni-doped arsenic sulfides were also studied [11]. Only one new phase of As_2S_3 named anorpiment has been naturally discovered recently [12]. It has low symmetry with triclinic structure and is made of covalently bonded layers of As and S atoms with a similar coordination arranged in a different stacking sequence by van der Waals force.

The high-pressure technique implies the active use of pressure as the fundamental thermodynamic variable for innovative material design. M. Güler and E. Güler reported that the classical force field can describe the surface, elastic, and phonon properties of wurtzite ZnS accurately, and the calculated data were in good agreement with the related experimental results [4]. Another previous work [13] pointed out that bonding disorder can be expected under high pressure in As_2S_3 glass, changing structural, vibrational, and optical properties. For example, using high-precision compressibility measurement and in situ high-energy X-ray diffraction to high pressure, the enhanced refractive index of the recovered As_2S_3 glass is promising for optical applications with improved functionalities [14]. A nearly permanent red shift in optical absorption after decompression can be used in high-impact-force optical sensors. In order to expand its application in the industrial field, it is necessary

and interesting to study the elastic constants, mechanical moduli, and the phonon dispersion of orpiment As_2S_3 under high pressure.

In this paper, we provided the details of theoretical calculations with the employed interatomic potential in Section 2. Then, we discussed our results with the available experimental results in Section 3. Finally, we presented the main findings in Conclusions.

2. Computational Methods

The most significant feature of material modeling is the choice of the interatomic potentials. A proper interatomic potential can describe the physical properties of materials sufficiently and accurately. The empirical potentials are the modelling tools for materials because they can yield reasonable results. These kinds of potentials can provide reasonable results of the structures, energies, and elastic and mechanical properties of alloys [15, 16] and many other materials [17, 18].

In this work, all the theoretical calculations were carried out with the General Utility Lattice Program (GULP) molecular dynamics code [19]. This versatile code allows the concerned structures to be optimized at constant pressure (all internal and cell variables are included) or at constant volume (unit cell remains frozen). The Dreiding force field [20] was chosen to be the empirical potentials for simulations. It is widely used in research describing the properties of organic and inorganic materials [21, 22]. To avoid the constraints, constant pressure optimization was applied to the geometry of o-As_2S_3 cells with the Newton-Raphson method based on the Hessian matrix calculated from the second derivatives. In Figure 1, the cell geometry of o-As_2S_3 was assigned as $a = 10.779$ Å, $b = 3.304$ Å, $c = 13.565$ Å, and $\alpha = \beta = \gamma = 90^\circ$ with space group PNMA. In the geometry optimization calculations, the Hessian matrix was recursively updated with the BFGS [23] algorithm. The phonon and associated properties of o-As_2S_3 were also analyzed as a function of pressure within the ranges between 0 GPa and 5 GPa in steps of 1 GPa. We captured the phonon density of states and dispersions for a material after specifying a shrinking factor with phonon computations. Furthermore, phonons are described by calculating their values at points in a reciprocal space within the first Brillouin zone of the given crystal. To achieve the Brillouin zone integration and obtain the PDOS, we used a standard and reliable scheme developed by Monkhorst and Pack [24] with $6 \times 6 \times 6$ k-point mesh.

3. Results and Discussion

As people know the volume of the crystal materials decreases, the density increases straightly under pressure. The density curve of o-As_2S_3 under pressure is shown in Figure 2. Under zero temperature, o-As_2S_3 has the lowest density value of 3.38 g/cm^3 at 0 GPa and has the highest density value of 3.80 g/cm^3 at 5 GPa. These results are consistent with the experimental value of 3.49 g/cm^3 [25]. So our prediction crystal structure of o-As_2S_3 under pressure is accurate.

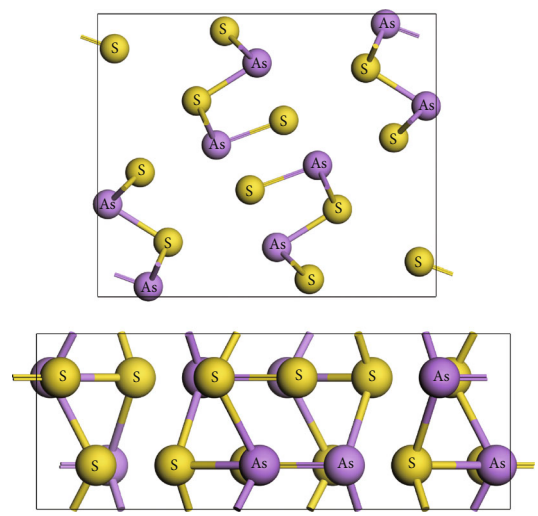

Figure 1: The crystal structure of orpiment As_2S_3. The yellow and purple atoms represent the S and As elements, respectively.

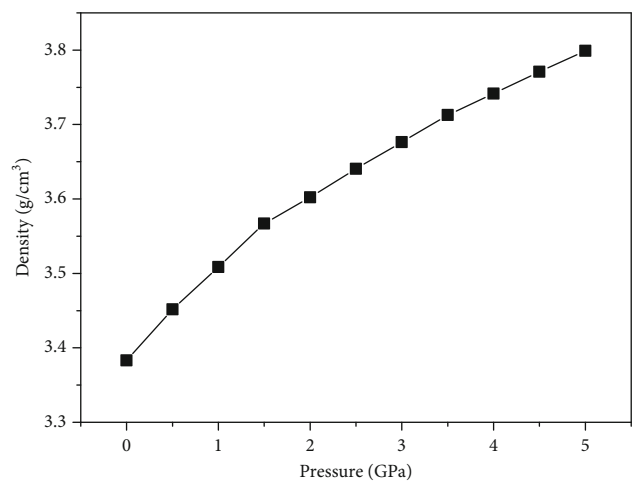

Figure 2: The density of orpiment As_2S_3 under pressure.

Then, we continued to compute the elastic and mechanical properties of o-As_2S_3 under pressure, such as the elastic constants (C_{ij}), bulk modulus (B), shear modulus (G) and Young moduli (E), and elastic wave velocities (V_L and V_S). The elastic constants were obtained by the second derivatives of the energy density with respect to strain. And the mechanical parameters were obtained by the linear combination of elastic constants using Voigt, Reuss, and Hill (VRH) approximations [26, 27].

Elastic constants deliver clear perceptions about the mechanical and other associated properties of materials. Though the elastic constants we obtained belong to the monocrystalline, these results also have important guiding significance for polycrystalline materials [28, 29]. For orthorhombic crystals, seven well-known elastic constants exist, which are specified as C_{11}, C_{12}, C_{13}, C_{22}, C_{23}, C_{33}, and C_{44} [30]. Figure 3 shows the results of C_{11}, C_{12}, C_{13}, C_{22}, C_{23}, C_{33}, and C_{44} constants for o-As_2S_3 under pressures between 0 GPa and 5 GPa. The calculated elastic constants are in the range of $C_{22} > C_{11} > C_{33} > C_{13} > C_{23} > C_{12} > C_{44}$. The elastic

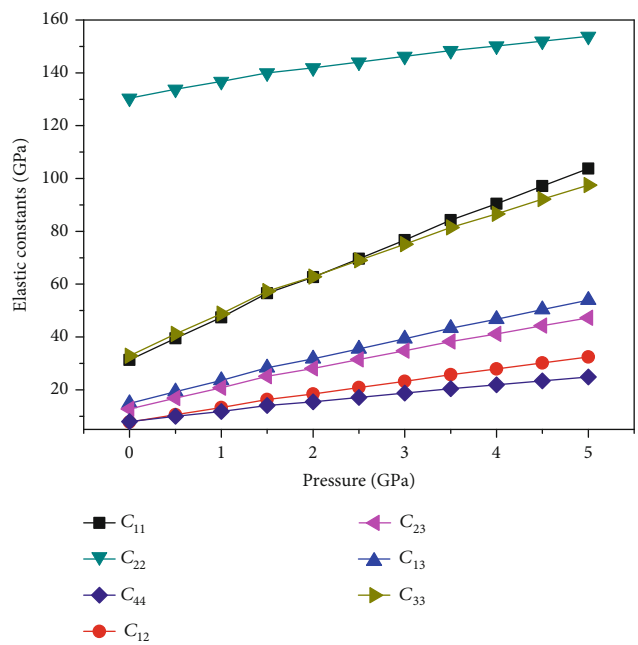

FIGURE 3: The elastic constants of orpiment As_2S_3 under pressure.

constants C_{11} and C_{33} represent the longitudinal elastic character, and they increase under pressure for the reason of elastic wave propagation occurs easily under pressure. The values of C_{11} and C_{33} are similar to each other at 0 GPa, and the difference between them exists as the pressure increases. The elastic constant C_{44} represents the shear elastic response to retarded wave propagation, and it also increases with the increasing pressure. In Table 1, our results for C_{13}, C_{33}, and C_{44} of o-As_2S_3 at 0 GPa are consistent with the experimental results of McNeil et al. [31], but C_{11} and C_{22} are larger than the data in Ref. [31]. The reason is due to the anisotropy of o-As_2S_3 and the measuring technology of Brillouin scattering and the size of samples. McNeil's measurement sample was made a natural crystal from Macedonia, and it was in the form of a thin plate roughly 5 mm square and 1 mm thick with only two good-quality surfaces (both perpendicular to the [010] axis). However, we used an orthorhombic crystal cell to do the simulation. So the anisotropy of o-As_2S_3 would influence the results of elastic parameters between us and the McNeil's.

According to stability, the mechanical stability criterion for orthorhombic crystals is $C_{11} > 0, C_{44} > 0$, $C_{11} + C_{22} > 2C_{12}$, and $C_{11} + C_{22} + C_{33} + 2(C_{12} + C_{13} + C_{23}) > 0$ [30]. Our calculated results of elastic constants of o-As_2S_3 obey the mechanical stability criterion, which consequently indicates that the o-As_2S_3 is mechanically stable in its ground state.

The bulk modulus represents an essential elastic constant connected to the bonding strength and is used as a primary parameter for the calculation of a material's hardness. The shear modulus represents the resistance to reversible deformations upon shear stress, while Young's modulus is defined as the ratio of the tensile stress to the corresponding tensile strain. Figure 4 shows the B, G, and E of o-As_2S_3 under pressure, and they all increase with the increasing pressure. However, the increase of B and E is obviously stronger than that of G. This result points that o-As_2S_3 is an isotropic material, so the external pressure produces a uniform volume compression effect and much less effect on the shear deformation of the material. Usually, brittle materials display a considerable resistance to the deformation before fracture, whereas ductile materials would be deformed easily. Ductility is a mechanical property of the material that represents the ability to plastically deform before it undergoes the fracture. Brittleness refers to the nature of fracture failure of materials without obvious plastic deformation when the external force reaches a certain limit. Ductility and brittleness are important for the production of the desired materials, so we continued to study the ductile and brittle behaviors of o-As_2S_3 under pressure. The Pugh ratio evaluation (G/B) [32], C for ductile and brittle performances of materials, was considered in this section. A low G/B value is associated with ductility, whereas a higher one corresponds to the brittle nature. The critical value which separates ductile and brittle materials is around 0.5. Our results show that G/B values decrease from 0.42 ($P = 0$ GPa) to 0.32 ($P = 5$ GPa) at zero temperature for o-As_2S_3 as inserted in Figure 4. Therefore, o-As_2S_3 is a kind of a ductile material for the entire pressure range.

It is known that the longitudinal (V_L) and shear elastic (V_S) waves may arise in solids at low temperatures due to vibrational excitations originating from the acoustic modes [33]. And the pressure behavior of the V_L and V_S of o-As_2S_3 pressure at $T = 0$ K is shown in Figure 5. The V_L indicates the longitudinal elastic wave velocity, and the V_S indicates the shear wave velocity. We can see that V_L has a significant increment compared to V_S, and this is the most common case for materials. The reason is that the bulk modulus and Young's modulus compared to the shear modulus have the same trend.

The ground state phonon dispersions of o-As_2S_3 were analyzed by using Dreiding potential quantitatively and compared in Reference [34] with theoretical results. We calculated the partial ground state phonon density of states (PDOS) of o-As_2S_3 to explain the contribution of As and S elements to the total phonon density of state (TDOS) of the material and showed them in Figure 6. The PDOS and TDOS appear with some separated regions corresponding to the longitudinal acoustic mode, transverse acoustic mode, longitudinal optic, and transverse optic mode of o-As_2S_3. Besides, the contribution of the As element to acoustic phonon modes is the same as that of S element, but in the high-frequency area, the case is different, and the contribution of the S element is dominant to optical modes. There is a big gap of 200 cm^{-1} (between the frequencies 300 cm^{-1} and 500 cm^{-1}) originating from the mass differences of As and S elements of o-As_2S_3.

In addition, Figure 7 shows the phonon dispersion of o-As_2S_3 along the chosen Γ-A path (the same as with original Ref [29]) in a reciprocal space for pressures 0 GPa and 5 GPa. It is seen that the pressure at 5 GPa shifts the phonon dispersion curves to higher frequency values. The reason is the atoms of o-As_2S_3 move towards each other and have to locate in the steeper potential wells under high pressures. In Figure 8, the corresponding PDOS curves of five pressures

Table 1: The present calculated results and experimental results of the elastic and mechanical parameters of As_2S_3 at 0 pressure.

Parameter	C_{11} (GPa)	C_{12} (GPa)	C_{13} (GPa)	C_{22} (GPa)	C_{23} (GPa)	C_{33} (GPa)	C_{44} (GPa)
Present	31.3	7.8	14.8	130.4	12.8	32.9	7.9
EXP. [30]	99.6	–	20.6	27.1	–	21.9	1.1
Parameter	B (GPa)	G (GPa)	E (GPa)	V_S (km/s)	V_L (km/s)		
Present	25.8	10.7	58.3	1.8	3.4		

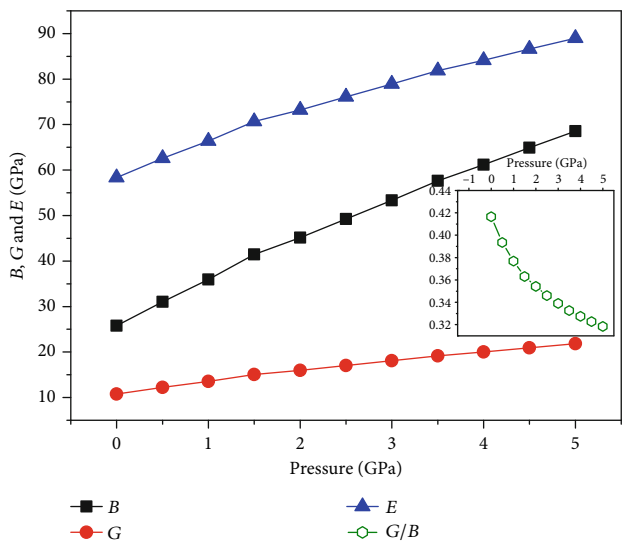

Figure 4: The mechanical moduli of orpiment As_2S_3 under pressure. The inserted picture shows the Pugh ratio evaluation (G/B).

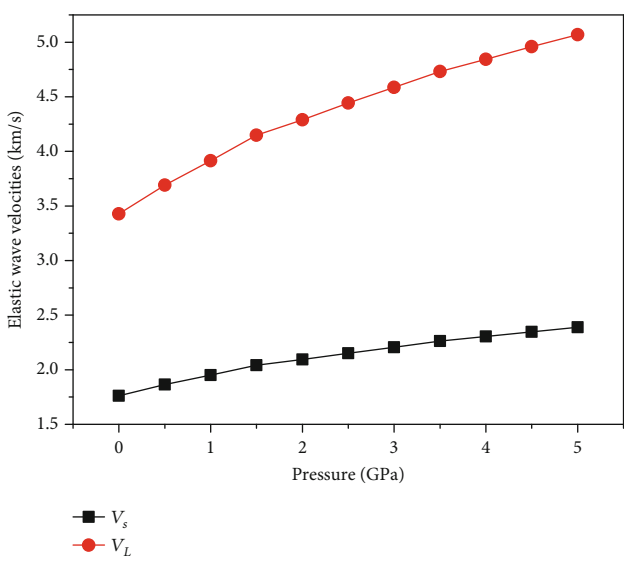

Figure 5: The longitudinal (V_L) and shear wave (V_S) velocities of orpiment As_2S_3 under pressure.

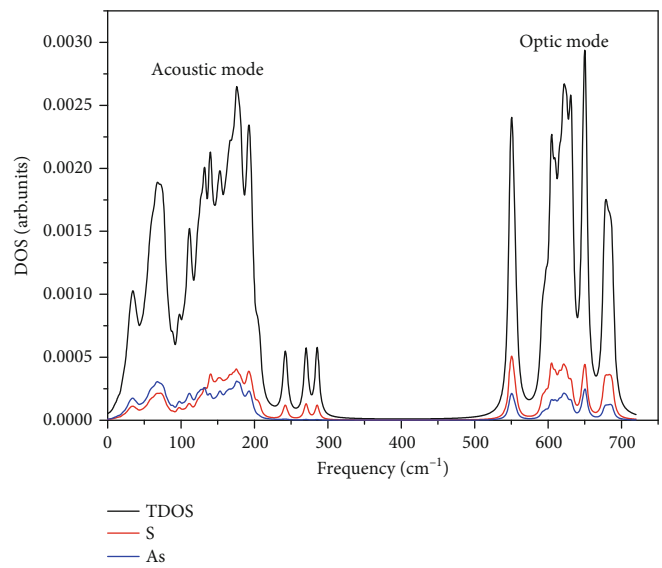

Figure 6: The partial density of states (PDOS) and total phonon density of states (TDOS) of orpiment As_2S_3 at 0 GPa pressure.

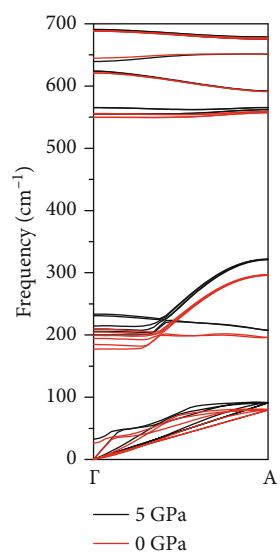

Figure 7: The phonon dispersion curve of orpiment As_2S_3 at 0 GPa and 5 GPa pressure.

(0 GPa, 1 GPa, 2 GPa, 3 GPa, 4 GPa, and 5 GPa) are presented. The increasing pressure increases the PDOS peaks of o-As_2S_3 under the high pressures, and the gap between acoustic and optical modes also shifts to higher frequencies from 350 cm^{-1} to 500 cm^{-1}.

In summary, the calculated parameters of o-As_2S_3 in this work are consistent with experiments and those of some published theoretical data. And some of the elastic constants and phonon properties of o-As_2S_3 at 0 GPa demonstrate fair accordance with the experimental and theoretical data. We

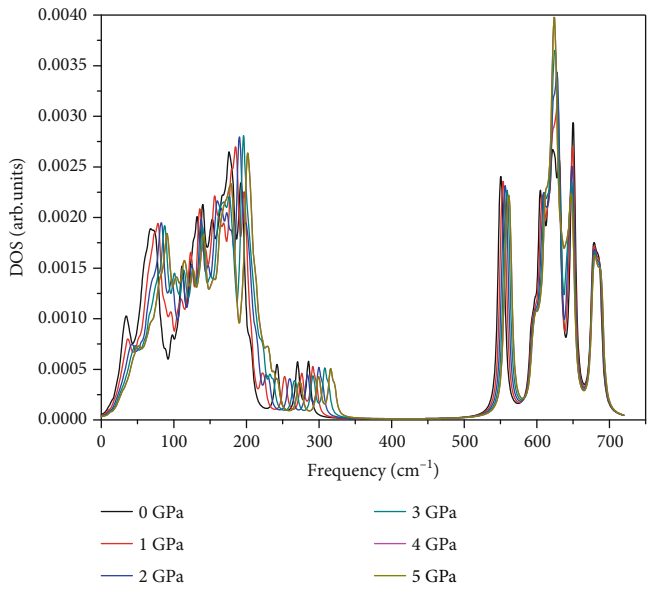

Figure 8: The total phonon density of states (TDOS) of orpiment As_2S_3 under pressure.

hope that our results add value to the forthcoming researches about o-As_2S_3 under pressure.

4. Conclusions

In this paper, we applied the Dreiding interatomic potential for the geometry optimization on the structural properties of o-As_2S_3 and studied both the ground state and pressure-dependent elastic, mechanical, and phonon dispersions of o-As_2S_3. The present results for the ground state of o-As_2S_3 were former experiments for the elastic constants, and the phonon characteristics were consistent with the published theoretical data. Moreover, we presented the effect of pressure on o-As_2S_3 and obtained some reasonable results. The mechanical properties of bulk modulus, shear modulus, Young's modulus, and longitudinal elastic character were increments under pressure. The o-As_2S_3 exhibits ductile character under high pressure. At last, the increasing pressure increases the PDOS peaks of o-As_2S_3 under the high pressures, and the gap between acoustic and optical modes also shifts to higher frequencies from 350 cm^{-1} to 500 cm^{-1}.

Data Availability

The research data used to support the findings of this study are included in the article.

Conflicts of Interest

We declare that we have no conflict of interest about the manuscript.

Acknowledgments

This research was supported by the National Science and Technology Major Project (Grant No. 2017-VI-0012-0084), the Fundamental Research Funds for the Central Universities (Grant No. FRF-GF-19-029B), and the National Natural Science Foundation of China (Grant No. 51471022).

References

[1] O. Boudrifa, A. Bouhemadou, N. Guechi, S. Bin-Omran, Y. Al-Douri, and R. Khenata, "First-principles prediction of the structural, elastic, thermodynamic, electronic and optical properties of $Li_4Sr_3Ge_2N_6$ quaternary nitride," *Journal of alloys and compounds*, vol. 618, pp. 84–94, 2015.

[2] D. Duan, X. Huang, F. Tian et al., "Pressure-induced decomposition of solid hydrogen sulfide," *Physical Review B*, vol. 91, no. 18, article 180502, 2015.

[3] Z. Zeng, C. S. Garoufalis, S. Baskoutas, and G. Bester, "Excitonic optical properties of wurtzite ZnS quantum dots under pressure," *The Journal of Chemical Physics*, vol. 142, no. 11, article 114305, 2015.

[4] M. Güler and E. Güler, "Theoretical analysis of elastic, Mechanical and Phonon Properties of Wurtzite Zinc Sulfide under Pressure," *Crystals*, vol. 7, no. 6, 2017.

[5] V. V. Brazhkin, Y. Katayama, M. V. Kondrin, A. G. Lyapin, and H. Saitoh, "Structural transformation yielding an unusual metallic state in liquid As_2S_3 under high pressure," *Physical Review B*, vol. 82, no. 14, article 140202, 2010.

[6] G. V. Gibbs, A. F. Wallace, R. Zallen et al., "Bond paths and van der Waals interactions in orpiment, As_2S_3," *The Journal of Physical Chemistry. A*, vol. 114, no. 23, pp. 6550–6557, 2010.

[7] P. Srivastava, H. Singh Mund, and Y. Sharma, "Investigation of electronic properties of crystalline arsenic chalcogenides: theory and experiment," *Physica B: Condensed Matter*, vol. 406, no. 15-16, pp. 3083–3088, 2011.

[8] Y. Watanabe, H. Kawazoe, and M. Yamane, "Imperfections in amorphous chalcogenides. III. Interacting-lone-pair model for localized gap states based on a tight-binding energy-band calculation for As_2S_3," *Physical Review B*, vol. 38, no. 8, pp. 5677–5683, 1988.

[9] D. W. Bullett, "Electronic structure of arsenic chalcogenides," *Physical Review B*, vol. 14, no. 4, pp. 1683–1692, 1976.

[10] S. G. Bishop and N. J. Shevchik, "Densities of valence states of amorphous and crystalline As_2S_3, As_2Se_3, and As_2Te_3: X-ray photoemission and theory," *Physical Review B*, vol. 12, no. 4, pp. 1567–1578, 1975.

[11] Y. Sharma and P. Srivastava, "Optical and transport properties and electronic structure of nickel doped arsenic chalcogenides," *Computational Materials Science*, vol. 53, no. 1, pp. 451–459, 2012.

[12] A. R. Kampf, R. T. Downs, R. M. Housley, R. A. Jenkins, and J. Hyrsl, "Anorpiment, As_2S_3, the triclinic dimorph of orpiment," *Mineralogical Magazine*, vol. 75, no. 6, pp. 2857–2867, 2011.

[13] C. Y. Yang, M. A. Paesler, and D. E. Sayers, "Chemical order in the glassy As_xS_{1-x} system: an X-ray-absorption spectroscopy study," *Physical Review B*, vol. 39, no. 14, pp. 10342–10351, 1989.

[14] E. Soignard, O. B. Tsiok, A. S. Tverjanovich et al., "Pressure-Driven Chemical Disorder in Glassy As_2S_3 up to 14.7 GPa, Postdensification Effects, and Applications in Materials Design," *The Journal of Physical Chemistry B*, vol. 124, pp. 430–442, 2020.

[15] C. H. Zhang, S. Huang, J. Shen, and X. N. Chen, "Chen's lattice inversion embedded-atom method for Ni Al alloy," *Chinese Physics B*, vol. 21, no. 11, article 113401, 2012.

[16] C. H. Zhang, S. Huang, J. Shen, and X. N. Chen, "Structural and mechanical properties of Fe-Al compounds: an atomistic study by EAM simulation," *Intermetallics*, vol. 52, pp. 86–91, 2014.

[17] L. C. He, S. S. Guo, J. C. Lei, Z. D. Sha, and Z. S. Liu, "The effect of stone-thrower-Wales defects on mechanical properties of graphene sheets – a molecular dynamics study," *Carbon*, vol. 75, pp. 124–132, 2014.

[18] C. H. Zhang, Y. Wang, and D. B. Sun, "The molecular dynamics simulation on the mechanical properties of Ni glass with external pressure," *International Journal of Modern Physics B*, vol. 31, no. 20, article 1750138, 2017.

[19] J. D. Gale and A. L. Rohl, "The General Utility Lattice Program (GULP)," *Molecular Simulation*, vol. 29, no. 5, pp. 291–341, 2003.

[20] S. L. Mayo, B. D. Olafson, and W. A. Goddard, "DREIDING: a generic force field for molecular simulations," *The Journal of Physical Chemistry*, vol. 94, no. 26, pp. 8897–8909, 1990.

[21] R. Devanathan, A. Venkatnathan, and M. Dupuis, "Atomistic simulation of nafion membrane: I. Effect of hydration on membrane nanostructure," *The Journal of Physical Chemistry. B*, vol. 111, no. 28, pp. 8069–8079, 2007.

[22] P. G. Boyd, S. M. Moosavi, M. Witman, and B. Smit, "Force-field prediction of materials properties in metal-organic frameworks," *Journal of Physical Chemistry Letters*, vol. 8, no. 2, pp. 357–363, 2017.

[23] R. Fletcher, "A new approach to variable metric algorithms," *The Computer Journal*, vol. 13, no. 3, pp. 317–322, 1970.

[24] H. J. Monkhorst and J. D. Pack, "Special points for Brillouin-zone integrations," *Physical Review B*, vol. 13, no. 12, pp. 5188–5192, 1976.

[25] D. J. E. Mullen and W. Nowacki, "Refinement of the crystal structures of realgar, AsS and orpiment, As_2S_3," *Zeitschrift für Kristallographie - Crystalline Materials*, vol. 136, no. 1-2, pp. 48–65, 1972.

[26] W. Voigt, *Lehrbuch der Kristallphysik (mit Ausschluss der Kristalloptik)*, Vieweg+Teubner Verlag, 1928.

[27] A. Reuss, "Berechnung der Fließgrenze von Mischkristallen auf Grund der Plastizitätsbedingung für Einkristalle," *ZAMM-Journal of Applied Mathematics and Mechanics/Zeitschrift für Angewandte Mathematik und Mechanik*, vol. 9, no. 1, pp. 49–58, 1929.

[28] S. Hirsekorn, "Elastic properties of polycrystals: a review," *Textures and Microstructures*, vol. 12, no. 1-3, pp. 1–14, 1990.

[29] R. L. Fleischer, "Substitutional solutes in AlRu-I. Effects of solute on moduli, lattice parameters and vacancy production," *Acta Metallurgica et Materialia*, vol. 41, no. 3, pp. 863–869, 1993.

[30] L. E. McNeil and M. H. Grimsditch, "Elastic constants of As_2S_3," *Physical Review B*, vol. 44, no. 9, pp. 4174–4177, 1991.

[31] S. F. Pugh, "XCII. Relations between the elastic moduli and the plastic properties of polycrystalline pure metals," *Philosophical Magazine*, vol. 45, no. 367, pp. 823–843, 1954.

[32] B. G. Dick and A. W. Overhauser, "Theory of the dielectric constants of alkali halide crystals," *Physics Review*, vol. 112, no. 1, pp. 90–103, 1958.

[33] S. Radescu, A. Mujica, P. R. Hernandez et al., "Study of the orpiment and anorpiment phases of As2S3under pressure," *Journal of Physics: Conference Series*, vol. 950, article 042018, no. 4, 2017.

[34] R. Hill, "The elastic behaviour of a crystalline aggregate," *Proceedings of the Physical Society. Section A*, vol. 65, no. 5, pp. 349–354, 1952.